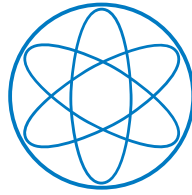


PHYSIK DEPARTMENT



# Development and Characterisation of New High-Rate Muon Drift Tube Detectors

Dissertation

von

Bernhard Bittner

28.06.2012



Max-Planck-Institut für Physik  
(Werner-Heisenberg-Institut)

# TECHNISCHE UNIVERSITÄT MÜNCHEN

Max-Planck-Institut für Physik  
(Werner-Heisenberg-Institut)

## Development and Characterisation of New High-Rate Muon Drift Tube Detectors

Bernhard Korbinian Bittner

Vollständiger Abdruck der von der Fakultät für Physik der Technischen Universität München zur Erlangung des akademischen Grades eines

Doktors der Naturwissenschaften (Dr. rer. nat.)

genehmigten Dissertation.

Vorsitzender: Univ.-Prof. Dr. A. Ibarra

Prüfer der Dissertation:

1. Priv.-Doz. Dr. H. Kroha
2. Univ.-Prof. Dr. L. Oberauer

Die Dissertation wurde am 28. Juni 2012 bei der Technischen Universität München eingereicht und durch die Fakultät für Physik am 25. Juli 2012 angenommen.



# Contents

<b>I</b>	<b>Introduction</b>	<b>1</b>
1	Outline	3
2	The Large Hadron Collider	5
2.1	Detectors at the LHC . . . . .	5
2.2	LHC Upgrade Scenarios . . . . .	7
3	The ATLAS Detector	9
3.1	The Detector Components . . . . .	9
3.2	The ATLAS Trigger and DAQ System . . . . .	13
3.3	Upgrade Scenarios . . . . .	14
4	The ATLAS Muon Spectrometer	15
4.1	Layout . . . . .	15
4.2	Background Radiation . . . . .	17
4.3	Alignment . . . . .	17
4.4	The Monitored Drift Tube Chambers . . . . .	19
4.5	Upgrade Scenarios . . . . .	29
<b>II</b>	<b>The sMDT Technology</b>	<b>33</b>
5	Motivation for 15 mm Diameter Drift Tubes	35
5.1	Limitations of the 30 mm Diameter Drift Tubes . . . . .	35
5.2	Advantages of 15 mm Diameter Drift Tubes . . . . .	37
5.3	Expected Performance of the sMDT Technology . . . . .	38
5.4	Summary . . . . .	43
6	sMDT Prototype Chamber	47
6.1	Drift Tubes and Gas Distribution System . . . . .	47
6.2	Chamber Construction . . . . .	50
6.3	Summary . . . . .	51
7	Sense Wire Position Measurement	53
7.1	Measurement Setup . . . . .	53
7.2	Monte-Carlo Simulation of the Teststand . . . . .	53
7.3	Wire Position Determination . . . . .	55
7.4	The Cosmic Ray Data . . . . .	64
7.5	Horizontal Wire Coordinate Reconstruction . . . . .	67

7.6	Summary . . . . .	72
<b>8</b>	<b>Test Beam Measurements</b>	<b>77</b>
8.1	The Beam Line . . . . .	77
8.2	Goals of the Beam Test . . . . .	79
8.3	Experimental Setup . . . . .	79
8.4	Data Taking and Preparation . . . . .	80
8.5	Single Tube Resolution . . . . .	85
8.6	Single Tube Efficiency . . . . .	90
8.7	Track Segment Resolution . . . . .	91
8.8	Tests with Trigger Chambers . . . . .	96
<b>9</b>	<b>Performance under Gamma Irradiation</b>	<b>99</b>
9.1	The Gamma Irradiation Facility at CERN . . . . .	99
9.2	Test Setup for the 15 mm Diameter Drift Tubes . . . . .	99
9.3	Data Preparation . . . . .	102
9.4	Data Analysis . . . . .	114
9.5	Results . . . . .	116
9.6	Summary and Outlook . . . . .	118
<b>10</b>	<b>Conclusions</b>	<b>123</b>
<b>III</b>	<b>Appendix</b>	<b>125</b>
<b>A</b>	<b>Readout Scheme of the sMDT Prototype Chamber</b>	<b>127</b>
<b>B</b>	<b>Calibration of the ADC of the MDT Readout Electronics</b>	<b>131</b>

# **Part I**

## **Introduction**



# Chapter 1

## Outline

During the two years of operation of the Large Hadron Collider (LHC), since the startup in 2009, the experiments ATLAS and CMS have already accumulated about  $5 \text{ fb}^{-1}$  of data at a centre of mass energy of 7 TeV,  $0.045 \text{ fb}^{-1}$  in 2010 and  $4.5 \text{ fb}^{-1}$  in 2011. For 2012 another increase of the integrated luminosity to a total of about  $15 \text{ fb}^{-1}$  is planned, which may allow for the discovery of the Higgs boson or for excluding it. No new phenomena beyond the Standard Model have been found so far.

In order to extend the search for new physics processes and to measure the properties of new particles with even higher accuracy, the design luminosity of LHC might not be enough. For these reasons it is planned to increase the luminosity of the LHC to about 7 times the design value. This upgrade project is called the High Luminosity LHC (HL-LHC) and is planned for the years beyond 2022. A first step towards higher luminosities at and above the design value will already be made in 2018.

The higher interaction rate will create new challenges for the experiments: a much higher particle density and rate in the detectors. Besides the necessity of higher trigger selectivity for events containing hints of new physics, there are other aspects that have to be studied. The detector components were designed and tested for counting rates expected for the LHC design luminosity. Increasing the hit rate can lead to efficiency loss and a degradation of the spatial resolution. An other important aspect is the radiation hardness of the readout electronics. Ionizing particles can damage the electronic chips or change memory bits corrupting the data. To make sure that the detector can continue taking high quality data after the LHC upgrades, all parts of the detector are tested under the expected conditions. It is already obvious that parts of the detector have to be replaced by new detector technologies developed to withstand the harsh environment at HL-LHC.

The limitations of the ATLAS muon spectrometer in the light of the LHC upgrade are discussed in chapter 4. This thesis presents a new muon chamber technology suitable to be installed in regions where the current system will not be sufficiency any more. Chapter 5 motivates the technology choice. The construction of a prototype chamber is described in chapter 6. The chapters 7 to 9 describe the tests performed to verify that the required spatial resolution and detection efficiency is achieved.



# Chapter 2

## The Large Hadron Collider

The Large Hadron Collider (LHC) is the latest in a long sequence of powerful accelerators developed and built at CERN. In 2011 it reached a new world record of 7 TeV center-of-mass energy of two colliding proton beams. To make this enormous energy possible, a huge infrastructure is necessary. After the shut down of the Large Electron Positron Collider (LEP) at the end of 2000, the space in the accelerator tunnel was used to build a new accelerator: the LHC. The pre-accelerators already existing could be reused, from the LINAC2 followed by the Proton Synchrotron (PS) operating since 1959 to the powerful Super Proton Synchrotron (SPS). An overview of the whole CERN accelerator complex is shown in Figure 2.1.

The main challenge during the development of the LHC was the design and construction of the beam bending magnets. Within a space of only 20 cm two 7 T magnetic fields of opposite orientation have to be realized. All LHC experiments rely on the ability of the accelerator to provide a high quality beam. Besides the beam energy, two properties are important: the luminosity and the life time of the beam. The instantaneous luminosity is defined as the number of particles per unit area and time

$$\mathcal{L} = \frac{\text{particles}}{\text{cm}^2\text{s}}. \quad (2.1)$$

It determines the number of collisions per time interval. The design value for the LHC is  $\mathcal{L}_0 = 10^{34} \text{ cm}^{-2}\text{s}^{-1}$  at 7 TeV beam energy. The beam is not continuous but consists of up to 2808 bunches containing  $1.15 \cdot 10^{11}$  protons each. The design value of the bunch crossing rate is 40 MHz corresponding to a bunch separation time of 25 ns. At one bunch crossing up to 28 proton pairs collide at the design luminosity. A higher number of collisions gives a larger number of events for the experiments to analyse increasing the sensitivity for rare processes.

### 2.1 Detectors at the LHC

There are four main experiments at the LHC: ALICE<sup>1</sup>, ATLAS<sup>2</sup>, CMS<sup>3</sup> and LHCb<sup>4</sup>. Their locations are indicated in Figure 2.1. Two of them (ATLAS and CMS) are designed to

---

<sup>1</sup>Website: <http://aliceinfo.cern.ch/>

<sup>2</sup>Website: <http://atlas.ch/>

<sup>3</sup>Website: <http://cms.web.cern.ch/>

<sup>4</sup>Website: <http://lhcb-public.web.cern.ch/lhcb-public/>

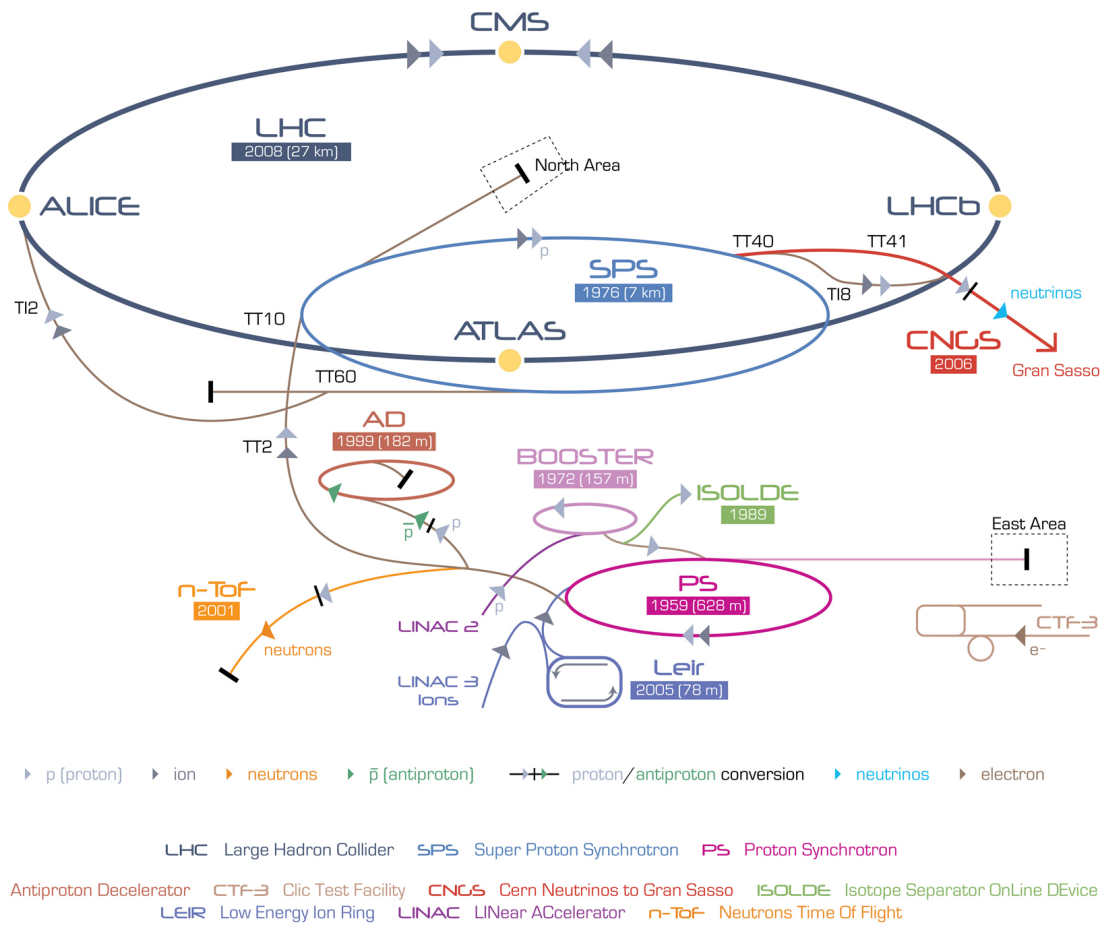


**Figure 2.1:** Overview of the CERN accelerator complex. The year of the first beam and the circumference of the accelerator rings are indicated.

exploit the whole range of physics accessible at the LHC. Their main goal is the search for the Higgs boson and the search for new physics beyond the Standard Model like supersymmetry or extra dimensions. ALICE studies the formation of a quark-gluon-plasma in the collisions of lead nuclei and LHCb b-hadron physics and related CP violation.

In addition, three smaller detectors are installed: LHCf<sup>5</sup>, TOTEM<sup>6</sup> and MoEDAL<sup>7</sup>. LHCf measures particles created in beam direction 140 m away from the interaction point in the ATLAS detector to improve the understanding of cosmic ray interactions and the associated shower production in the atmosphere. TOTEM uses detectors installed close to the beam between 10 and 220 m away from the CMS interaction point in order to study elastic proton scattering and diffractive processes. The goal of MoEDAL is to search for the magnetic monopoles and other highly ionizing stable (or pseudo-stable) massive particles (SMPs).

## 2.2 LHC Upgrade Scenarios

Shortly after the startup of the LHC in 2008 a magnet quench [CER08] resulted in more than 50 damaged dipole magnets. During the repair after this incident not all faulty magnet connections were replaced to allow for an earlier start of the physics program. The main repair program was postponed to the long 15 month shut down LS1 starting end of 2012. After the shut down, the LHC will restart with 6.5 TeV beam energy.

Another long shut down, LS2, is foreseen for the year 2018. It will mainly be used to adapt the LHC components to allow for higher instantaneous luminosity. One limiting factor is the injector chain. To realize the plans of a High Luminosity LHC (HL-LHC) with up to seven times the instantaneous design luminosity, parts of the pre-accelerators have to be replaced. The new LINAC 4 which will replace the LINAC2 as proton source for the BOOSTER storage ring which will already be ready for the restart in 2014. The new proton source allows for higher beam currents and is necessary for all intended luminosity upgrades of LHC. Changes to the LHC beam optics or magnet layout will also be necessary. For a detailed overview see [CER12].

The long shutdowns will also be used by the experiments to adapt their detectors to the expected running conditions and replace broken parts or components that have reached the maximum of their life time. The implications of the luminosity upgrade for the ATLAS muon spectrometer and the development of new detector components to operate under the new conditions are discussed in this thesis.

---

<sup>5</sup>Website: <http://public.web.cern.ch/public/en/lhc/LHCf-en.html>

<sup>6</sup>Website: <http://totem-experiment.web.cern.ch/totem-experiment/>

<sup>7</sup>Website: <http://moedal.web.cern.ch/>



# Chapter 3

## The ATLAS Detector

The ATLAS detector is with 44 m length and 25 m height and the largest of the LHC experiments. It has a weight of about 7,000 tones. The assembly of the detector started in 2003 with the installation of the support structures and was finished end of 2008. This chapter gives a brief description of the detector components and of the trigger and readout system of the ATLAS detector. A more detailed description can be found in [ATL08].

### 3.1 The Detector Components

The ATLAS detector consists of several layers of subdetectors. A cut-away view of the detector is shown in Figure 3.1. The innermost part provides particle tracking with very high resolution, the adjacent calorimeters measure the energies of particles and outermost layer, the muon spectrometer, measures the momentum of muons with high precision.

#### 3.1.1 The Inner Detector

The Inner Detector (ID) starts at a radial distance of 4.6 centimetres from the proton beam axis, extends to a radius of 1.2 metres, and is seven metres in length along the beam. The ID can determine track coordinates with an accuracy better than  $20\ \mu\text{m}$  in the  $r\text{-}\phi$  plane perpendicular to the beam. With this high accuracy it is possible to associate the detected particles to a common vertex.

The ID is build inside a superconducting solenoid magnet. From the measured track curvature the momentum of the charged particles can be calculated. To fulfil this task at the LHC, the detector has to cope with very high track densities and event rates. At the nominal luminosity of  $10^{34}\ \text{m}^{-2}\text{s}^{-1}$ , 28 proton-proton interactions every 25 ns are expected, each event consisting of up to about 2000 particles. This requires a very fast detector with high granularity.

The ID is a combination of three subsystems: two segmented silicon detector trackers (the Pixel Detector and the Semiconductor Tracker (SCT) ) and a gas tracking detector, the Transition Radiation Tracker (TRT).

The Pixel Detector is the innermost part of the ID. Its 80 million electronics channels are distributed over 1744 modules with about 47,000 pixels each. The resolution in the *precision plane*<sup>1</sup> is as small as  $10\ \mu\text{m}$  for the three track points.

---

<sup>1</sup>The so-called *precision plane* is the  $r\text{-}\phi$  plane, providing the measurement of the important transverse

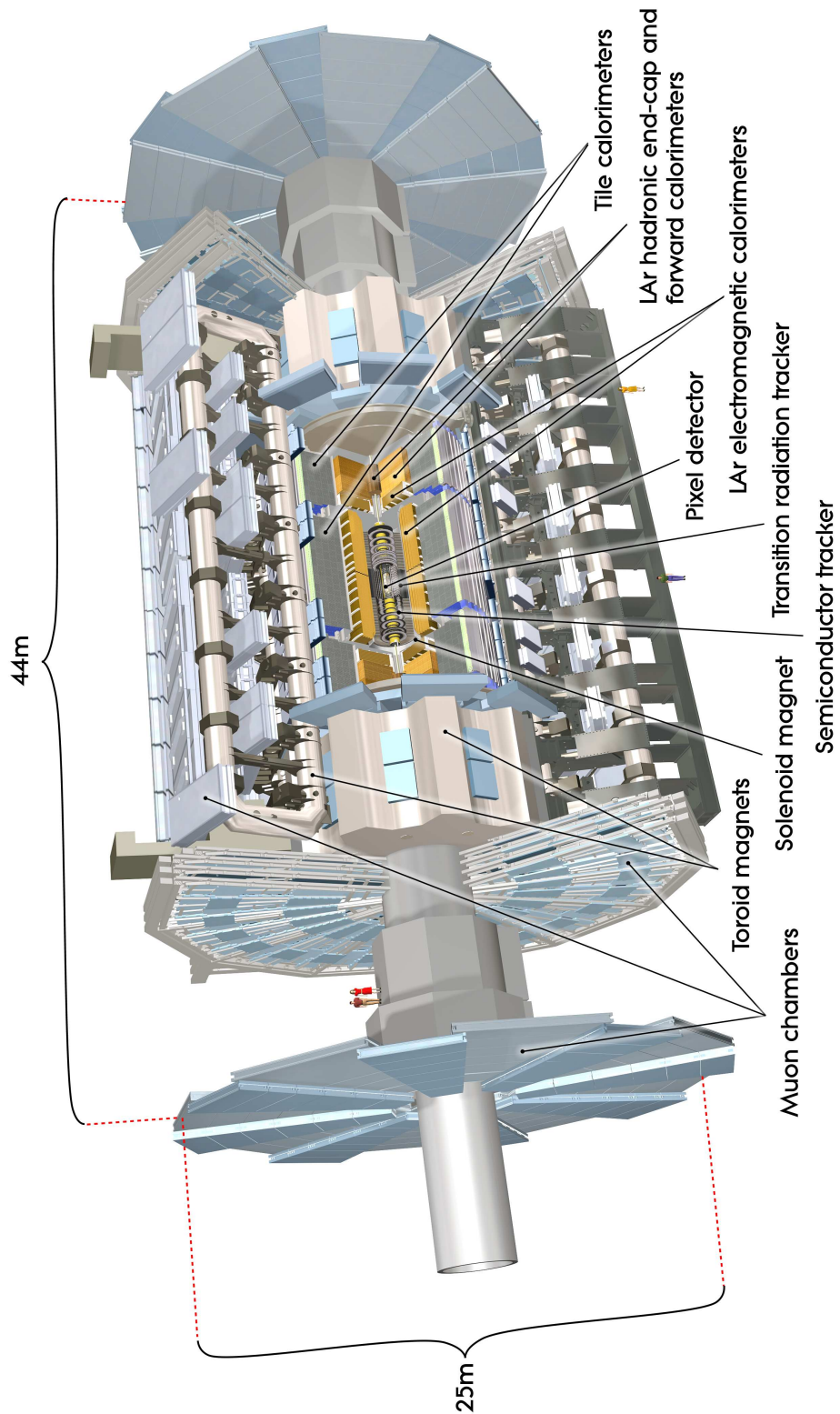


**Figure 3.1:** Cut-away view of the ATLAS detector. The weight of the detector is approximately 7000 tons [ATL09].

It is surrounded by the SCT. This detector covers a larger  $\eta$  area, namely  $|\eta| < 2.5$ . The resolution in the precision plane is with  $17\ \mu\text{m}$  almost as good as for the Pixel Detector, and it provides track points over a large volume. The modules are equipped with silicon strip detectors. Each strip has a width of  $80\ \mu\text{m}$  and a length of  $12.6\ \text{cm}$ .

Subsequent is the TRT, a combination of straw-tube tracker and transition radiation detector. It consists of straw tubes (tiny drift tubes) and a transition medium inbetween and provides on average 36 space-points per track with a resolution of about  $170\ \mu\text{m}$ . Electrons are identified by their characteristic transition radiation.

### 3.1.2 The Calorimeters

The calorimeters are located after the solenoid magnet, beginning at a distance of 1.5 meters from the beam axis. Their purpose is the determination of the total energy of a particle or jet. This is done by stopping the particles and their decay products and measuring the deposited energy in the calorimeters. Since the interaction of hadrons, leptons and photons with matter is very different, there is one part dedicated to measure hadron energies and another part designated to determine the energy of mostly electromagnetically interacting particles, such as photons and  $e^\pm$ .

Except for muons, which have a very low interaction with matter, all detectable particles are absorbed in the calorimeters.

#### The Liquid Argon Calorimeter

The *Liquid Argon* (LAr) Calorimeter is divided into several components: an electromagnetic sampling calorimeter with 'accordion-shaped' lead absorbers in the barrel and in the endcaps, a hadronic calorimeter using flat copper electrodes in the endcaps, and a forward calorimeter close to the beam pipe in the endcaps made of copper and tungsten as absorber material. In addition, LAr presampling calorimeters in front of the electromagnetic calorimeter help to correct for the energy loss in front of the calorimeter (mainly due to LAr cryostat walls and the barrel solenoid).

#### The Tile Calorimeter

The *Tile Calorimeter* is a large hadronic sampling calorimeter which uses steel as absorber material and scintillating plates read out by wavelength shifting fibres as active medium. It covers the central region  $|\eta| < 1.7$ . A special feature in its design is the orientation of the scintillating tiles which are placed in planes perpendicular to the colliding beams and are staggered in depth resulting in a good sampling homogeneity. The thickness of the calorimeter is equivalent to a total of about two hadronic interaction lengths. It has a cylindrical structure with an inner radius of 2.3 m and an outer radius of 4.2 m and is subdivided into a 5.6 m long central barrel and two 2.9 m long extended barrel parts. The total number of readout channels is about 10,000.

### 3.1.3 The Muon Detectors

The muon spectrometer forms the outermost layer of the ATLAS detector. The fact that muons are the only long living known and detectable particles that are not stopped in the

---

momentum  $p_T$  of a track.

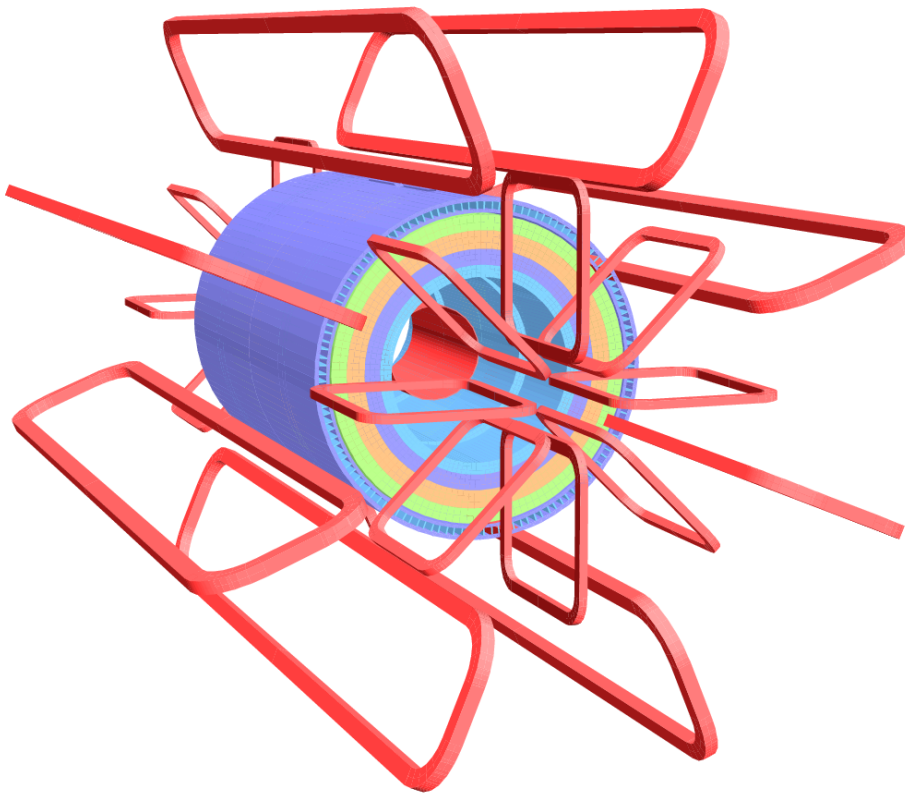


**Figure 3.2:** Geometry of the magnet coils and tile calorimeter steel. The eight race-track shaped barrel toroid coils, with the end-cap coils interleaved, are visible. The solenoid magnet is located inside the cylindrical calorimeter volume. The tile calorimeter serves also as the return yoke of the solenoid magnet [ATL08].

calorimeters, is used for particle identification. A toroidal magnetic field with a maximum strength of 1.5 T bends the muon tracks a second time after the ID and provides the possibility to independently determine the momentum of the particle. The toroidal magnet system consists of a barrel part and two endcap magnets. The outer endcap parts of the muon spectrometer are outside the magnetic field (see fig. 3.2).

ATLAS uses four different muon detector types in the muon spectrometer: Monitored Drift Tube chambers (MDT), Resistive Plate Chambers (RPC), Thin Gap Chambers (TGC) and Cathode Strip Chambers (CSC). RPCs and TGCs are used as trigger chambers as they have a very good time resolution and can detect a muon within 25 ns, thus allowing the bunch crossing identification of the event. The number of readout channels and therefore the achieved spatial resolution is chosen to allow the measurement of the o-called second coordinate<sup>2</sup> with an accuracy of about 1 cm. RPCs are used in the barrel part, TGCs in the endcaps. The more than 1000 MDT chambers provide a very high spatial resolution of better than 60  $\mu\text{m}$  in the track bending plane, but are relatively slow with a maximum drift time of 700 ns. These detectors allow the good reconstruction of the muons and the precise momentum measurement. In the very forward region of the endcap region the MDT chambers are replaced by CSCs. They have a higher tolerance for background radiation and can work in harsh conditions in the area close to the beam line. The combination of all four detector types provides the desired resolution in space and time for the muon trajectory and momentum.

The main topic of this thesis is the development of new muon detectors for the areas with very high background radiation levels. Therefore this part of ATLAS is discussed in more detail in the next section.

## 3.2 The ATLAS Trigger and DAQ System

The ATLAS trigger system is used to select interesting events out of the more than 40 million collisions every second. This is necessary because the bandwidth of the electronic and PCs handling the outgoing data is limited and it is therefore not possible to store every single event.

The event selection is done in three steps:

**Level 1** The first level is completely realized in hardware to keep latencies small. The trigger decision is based on a subset of detectors and searches for predefined patterns like leptons with a high  $p_T$  track or missing energy in the calorimeters. The electronics defines regions of interest (ROI) based on the measured hits. The maximum rate for this stage is 100 kHz with a latency of less than 2.5  $\mu\text{s}$ .

**Level 2** The second level is a PC farm that analysed the hits in the ROIs in more detail. A first track reconstruction is performed and the result compared to the defined trigger settings. The maximum rate is 3.5 kHz with a latency of about 40 ms.

**Event Filter** The last stage has a rate of only 200 Hz and takes about 4 s per event. Here the information from the whole detector is combined and analysed with off-line analysis tools. One event has a total size of about 1.3 MB.

---

<sup>2</sup>The direction perpendicular to the precision plane.

Events selected by the events filter are then written to the TIER 0 data centre at CERN. The total data output of data all LHC experiments is about 10 to 14 PB per year. Storing this huge amount of data is already a challenge, but making the data available to all involved physicists worldwide is even more complicated. To tackle this problem a world wide computing network, the LHC Computing Grid (LCG), was set up [Eck05].

### 3.3 Upgrade Scenarios

Following a future upgrade of the LHC some parts of the ATLAS detector have to be replaced or improved. There are three main limitations for the currently installed detectors:

- The lifetime of components,
- Increased background and particle counting rates and
- Radiation hardness of the detector and electronic components.

Some replacements have been foreseen already in the initial design because the life time of a few components is reached after 10 years of normal LHC running. This is the case for the silicon tracking detectors in the ID. Other parts of ATLAS were designed for the expected background counting rates of the initial LHC design luminosity and will have a low efficiency in a HL-LHC scenario. This is for example the case for the innermost layer of the forward muon spectrometer. Details of this problem are discussed in section 4.5.

One of the constrains for all upgrade activities is the tight LHC shut-down schedule. The machine down time foreseen for the 2018 shut-down is only one year. This short time window allows no failures. Therefore it is necessary to have all components ready at least one year before the installation date and perform an extensive test run of the assembled system. This allows to spot all problems and repair them before the installation in ATLAS.

An overview of the upgrade activities and plans can be found in [ATL11].

# Chapter 4

## The ATLAS Muon Spectrometer

After the quick overview of all subsystems in ATLAS, the muon spectrometer shall now be discussed in detail. ATLAS puts much emphasis on a very precise muon reconstruction and trigger since there are many physics processes with muons in the final state. A very nice example is the fully leptonic Higgs channel  $H \rightarrow ZZ \rightarrow \mu\mu\mu\mu$  which provides a very clean signal signature with low background. The muon spectrometer is also the largest part of ATLAS and responsible for the huge dimensions of the detector (see Fig. 3.1).

### 4.1 Layout

The muon spectrometer consists of 3 layers of chambers in the barrel and in the endcaps as shown in Figure 4.1. There are also additional chambers (e.g. mounted on the endcap toroids) to close acceptance gaps. The structures in forward direction are called wheels, one small and two big ones called BW and EO. The chambers in the central area, the barrel, are sorted into layers, called the inner, middle and outer layer.

The magnet system of the muon spectrometer contains no iron in order to minimize scattering of the muons. With a solid iron core it would have been possible to achieve a stronger magnetic field, but at the cost of much higher deflection of muon tracks due to multiple scattering. The muon system of the other multi purpose detector CMS did choose this approach.

Without contribution from the inner detector the aim for the momentum resolution of the muon spectrometer is

$$\frac{\Delta p_T}{p_T} < 3\% \quad \text{for } E_\mu < 200 \text{ GeV} \quad \text{and} \quad \frac{\Delta p_T}{p_T} \approx 10\% \quad \text{for } E_\mu \approx 1 \text{ TeV}. \quad (4.1)$$

The muon momentum is determined from the sagitta of the muon track and the magnetic field strength along the track. For a 1 TeV muon the expected sagitta is at the order of 500  $\mu\text{m}$ . To achieve the desired momentum resolution the muon chambers have to provide a spatial resolution of about 40  $\mu\text{m}$  and the relative positions of the chambers have to be known with an accuracy of about 30  $\mu\text{m}$  in the bending plane.

The precision tracking detectors of the ATLAS muon spectrometer are more than 1000 drift-tube detectors, the so-called *Monitored Drift Tube* (MDT) chambers. A small forward region of the spectrometer is covered by CSCs<sup>1</sup> because the expected background rates are above the limit for an efficient operation of the MDT chambers.

---

<sup>1</sup>Cathode Strip Chambers

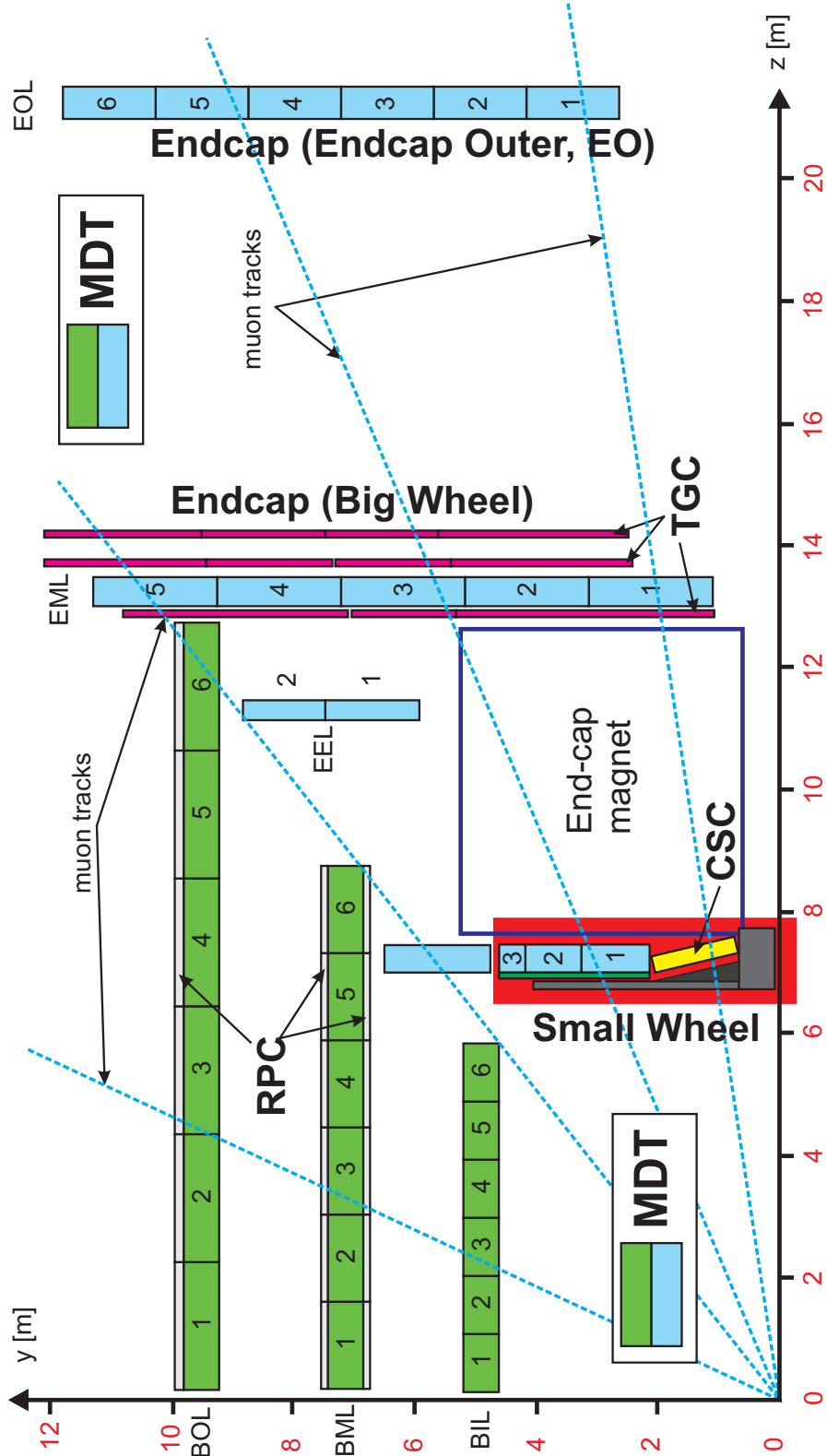


**Figure 4.1:** Schematic view of one quadrant of the muon system in the  $r$ - $z$  plane (track bending plane). The dashed lines indicate tracks of muons with infinite momentum. They typically traverse three muon stations allowing for a track sagitta measurement (see text). The different detector types in the muon system, MDT, CSCs, RPCs and TGCs are indicated.

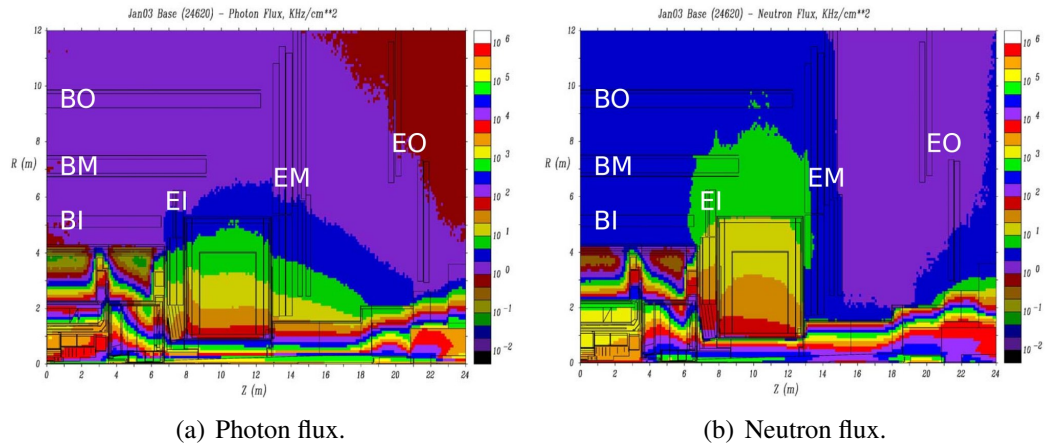


**Figure 4.2:** Simulated flux of photons and neutrons in the ATLAS muon spectrometer for the LHC design luminosity of  $10^{34} \text{ cm}^{-2}\text{s}^{-1}$  [Bar05].

MDT chambers provide a very good spatial resolution in the precision plane, but cannot measure the second coordinate or provide a trigger signal. These tasks are performed by the RPCs<sup>2</sup> in the barrel region and the TGCs<sup>3</sup> in the endcap regions.

## 4.2 Background Radiation

The main background radiation in the ATLAS muon spectrometer is due to low energy photons and thermal neutrons originating from interactions of the collision products in the detector, the shielding and the support structures. Detailed simulations [Bar05] show that especially the regions around the end-cap toroid magnets between the EI and EM endcap muon chamber layers are affected by neutron and photon background (see Figure 4.2).

The high background radiation fluence puts high demands on the rate capability of the muon detectors and on their radiation hardness. The background radiation can also cause defects in the electronic chips or corrupt stored information. If the data is corrupted by so-called single event upsets, the software has to spot and discard the damaged data. It is also possible that the firmware of the central readout electronics board, the Chamber Service Module (CMS), gets corrupted. This has to be spotted by the detector control system and the firmware has to be restored. In the worst case, the chips are permanently damaged and need to be replaced.

For the detectors the challenge arises from the high counting rates. A high background occupancy increases the risk of losing real muon hits. Also the spatial resolution of the drift tubes is deteriorated by the background radiation. The rate limitations of the drift tubes used in the muon spectrometer are discussed in detail in the next chapter.

## 4.3 Alignment

In the previous section the necessities of a relative alignment of about  $30 \mu\text{m}$  between different layers was discussed. This accuracy is reached by an optical alignment system

<sup>2</sup>Resistive Plate Chambers

<sup>3</sup>Thin Gap Chambers

**Table 4.1:** Different types and sources of misalignment. For 2D plots the distributions are fitted with a polynomial  $y = m \cdot x + b$ , the interesting variable is then represented by  $m$ .

Misalignment	Type	Histogram
$\Delta\alpha$	Rotation	Distribution of $\Delta\alpha = \alpha_1 - \alpha_2$
$\Delta\beta$	Rotation	$\Delta z$ shift vs. $x$ position
$\Delta\gamma$	Rotation	$\Delta y$ vs. $x$
$\Delta x$	Movement	$\Delta x = x_1 - x_2$ from trigger chambers
$\Delta y$	Movement	$\Delta y = y_1 - y_2$ from MDT chambers
$\Delta z$	Movement	$\Delta y$ vs. $\alpha$

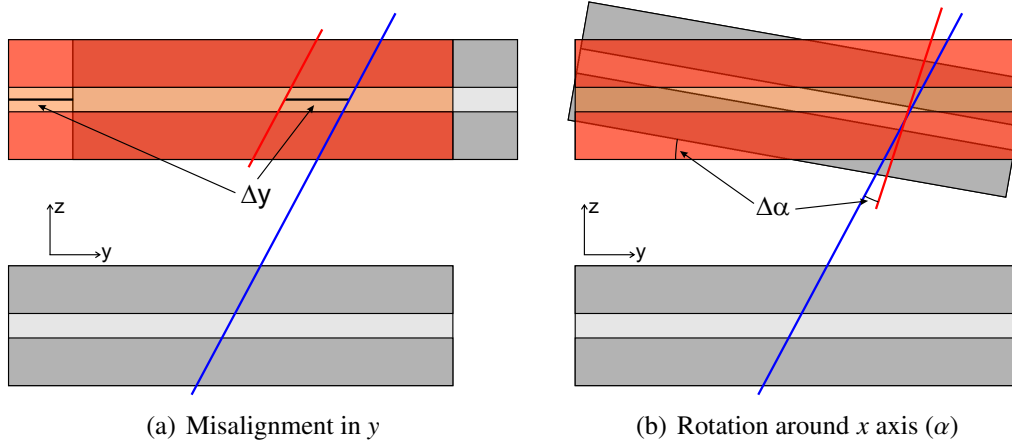


**Figure 4.3:** Effects of chamber misalignment on the track reconstruction. The real chamber positions are marked in gray, the assumed position (if different) is indicated in red. The real muon track has a blue color, the reconstructed segment in the misaligned chamber is red.

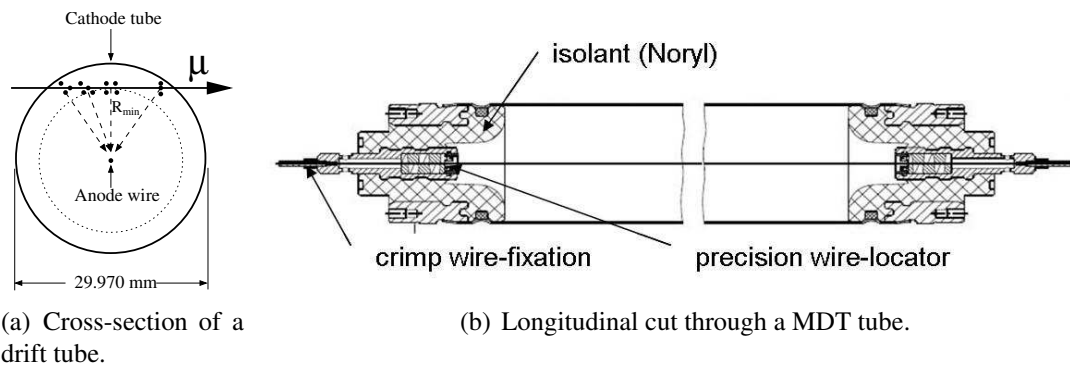
connection the whole spectrometer, but it can only monitor relative movements in the barrel region where an initial alignment of the chambers is performed with tracks. In the endcap region the optical system can provide an absolute alignment.

Different methods for a track based alignment were already discussed in [Bit08]. The main aspect is the comparison of the reconstructed muon track in different chambers. Relative rotations or movements can be seen in different distributions (see Table 4.1). The cases  $\Delta y$  and  $\Delta\alpha$  are illustrated in Figure 4.3.

The monitoring by optical sensors (discussed in detail in chapter 4.4.6) serves for the measurement of torsions and expansions induced by temperature changes, respectively. The CSCs are also included in the optical alignment system. The trigger chambers do not need this high precision in the alignment because of their limited spatial resolution. They were aligned during the assembly of the muon spectrometer relative to the MDT chambers.

**Table 4.2:** Parameters of the drift tubes in the ATLAS MDT chambers.

Parameter	Design value
Tube material	Aluminium
Outer tube diameter	29.970 mm
Tube wall thickness	0.4 mm
Wire material	gold plated W/Re (97/3)
Wire diameter	50 $\mu\text{m}$
Gas mixture	Ar:CO <sub>2</sub>
Gas pressure	3 bar (absolute)
Gas gain	$2 \cdot 10^4$
Wire potential	3080 V
Maximum drift time	$\approx 700$ ns
Average drift tube resolution (with time slewing corrections)	$\approx 80$ $\mu\text{m}$

**Figure 4.4:** A MDT tube in different views [ATL08].

## 4.4 The Monitored Drift Tube Chambers

Almost all chambers consist of 2 multilayers of drift tubes, each with 3 tube layers for the middle and outer chambers and 4 tube layers for the inner chambers, respectively. Design parameters of the drift tubes are shown in Table 4.2. The mechanical structure of a MDT chamber is shown in Figure 4.5.

### 4.4.1 The Principle of Drift Tubes and MDT Chambers

When a muon passes through the tube, some gas atoms along the path get ionised. After the ionisation, the resulting free electrons drift through the gas and ionise more gas atoms until they have lost all their energy. The range of these free electrons is very short, resulting in localised ionisation clusters in the gas along the path of the muon. For a muon with an energy of 100 GeV on average 100 clusters/cm are generated in Ar-based gases at 3 bar. The mean free path length of the muon is therefore about 100  $\mu\text{m}$  [Ale99].

Due to the potential difference between the tube wall and the anode wire, the primary ionisation electrons drift to the wire, whereas the ions drift to the tube wall (cp. Fig. 4.4(a)). The drift velocity of the electrons usually depends on the local electric field. The velocity of the ions is mainly determined by their low mobility and has usually no

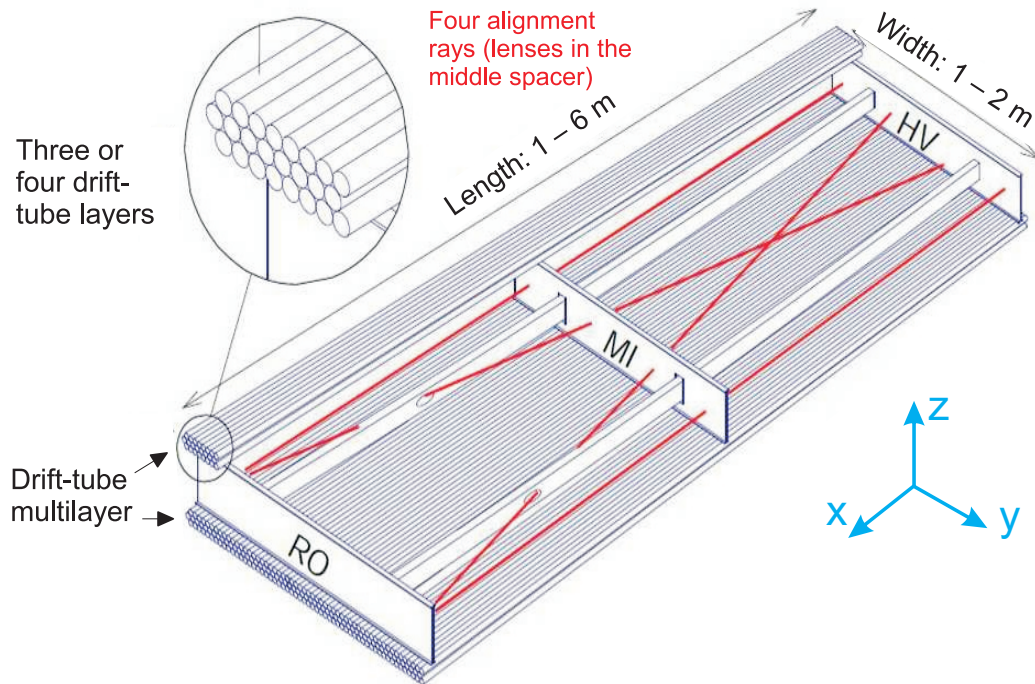


**Figure 4.5:** Mechanical structure of a MDT chamber [ATL08]. Three cross plates connected by longitudinal beams form an aluminium space frame carrying two multilayers of three or four drift tube layers. Four optical alignment rays, two parallel to the tubes and two diagonal, allow for monitoring of the internal geometry of the chamber. RO and HV designate the location of the readout electronics and of the high voltage distribution boards, respectively. The local coordinate system of the chamber is defined by the wire direction ( $x$  axis), the  $y$  axis perpendicular to the tubes pointing away from the interaction point and parallel to the tube layers and the  $z$  axis perpendicular to the tube layers.

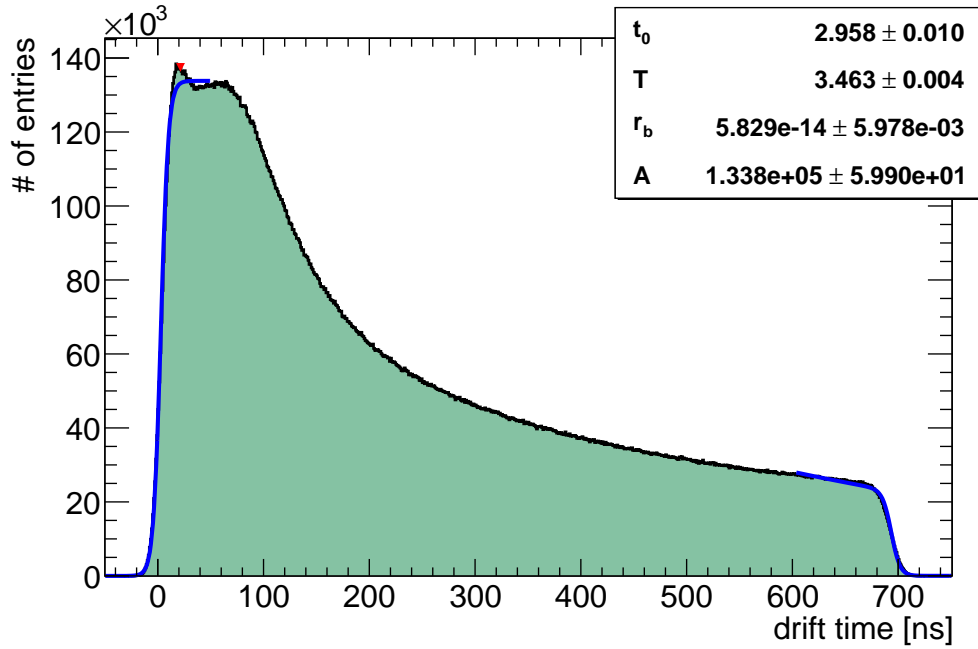


**Figure 4.6:** Drift time spectrum of the ATLAS MDT tubes measured in the cosmic ray teststand in Garching.

strong dependence on the electric field. Due to the cylindrical geometry, the field gets stronger closer to the wire. At a distance of about  $150\ \mu\text{m}$  from the wire, the field is strong enough that the energy gained by the electrons between two collisions allows for the ionisation of the gas molecules. This leads to an avalanche of secondary electrons. For the ATLAS MDT chambers, the gas amplification, defined as the number of electrons at the wire resulting from one primary ionisation, is  $2 \cdot 10^4$ .

The readout electronics measures the time between the trigger signal and the charge pulse arriving at the wire end on the readout side. From the drift time measurement of the first electrons arriving at the wire and crossing the signal threshold one can determine the minimal distance  $R_{\min}$  between the muon track and the wire (see Fig. 4.4(a)) after offline correction for the time of flight of the muon from the interaction point to the chamber and for the signal propagation time along the wire. The second coordinate information from the trigger chambers is used to calculate the propagation time of the signal along the wire.

#### 4.4.2 Response to Muons

Figure 4.6 shows a typical drift time spectrum for an uniformly illuminated 30 mm diameter ATLAS MDT tube. This distribution contains information about the drift properties of the gas. Close to the wire the drift velocity is high in the strong electric field. With increasing distance to the wire the drift velocity drops. This behaviour is seen in the slow fall of the drift time spectrum. A detailed discussion of the drift time spectrum can be found in [Hor05]. Here only the properties relevant for this thesis are discussed. The rising edge can be fitted with a Fermi function:

$$f(t) = \frac{A}{1 + \exp\left\{-\frac{t-t_0}{T}\right\}} + r_b. \quad (4.2)$$

$t_0$  is the turning point of the fitted function  $f(t)$  and the parameter  $T$  is a measure of the slope at this point.  $4T$  is the rise time of the spectrum from 10% to 90%. The parameter  $r_b$  describes a positive constant background for example due to noise or background radiation. The value of  $t_0$  is in general different for each tube because of different signal paths and is therefore determined for each channel separately to achieve a common timing for the whole chamber. The drift time is defined as

$$t_{\text{drift}} = t - t_0 . \quad (4.3)$$

The falling edge at the end of the drift time spectrum is defines the maximum drift time in the tube. Here a function composed of two Fermi functions, where one is multiplied by an exponential, is used to account for the slow fall towards the edge of the spectrum:

$$g(t) = A \frac{1 + A_{\text{top}} \exp \left\{ -\frac{(t-t_{\text{max}})}{T_t} \right\}}{1 + \exp \left\{ -\frac{t-t_{\text{max}}}{T_b} \right\}} + r_b . \quad (4.4)$$

The slope at the edge now depends on two parameters,  $T_t$  and  $T_b$ . This is in contrast to the function used in [Hor05]. The reason for the modification is discussed in Section 5.3.4.

The length of the drift time spectrum depends on environmental parameters, such as temperature, gas mixture, magnetic field and background hit rate. Since the accurate determination of the relation between drift time and drift radius depends on the maximum drift time measurement, the quality of the fit of the falling edge is very important for the drift tube spatial resolution.

### 4.4.3 The Space-to-Drift-Time Relation

The drift time  $t$  is linked to the drift radius  $r$  by the so-called space-to-drift time relationship  $r(t)$ . This relation depends on environmental parameters such as temperature, gas mixture and density, magnetic field, high voltage and background hit rate which might vary with time. To obtain a precise  $r(t)$  relationship, the chambers have to be calibrated at regular time intervals of about one day (cp. [Bag08]).

A first estimate for the  $r(t)$  relation can be computed from the drift time spectrum. The  $r(t)$  relation is defined as

$$r_i = r(t_i) = \int_0^{t_i} \dot{r}(t) dt \quad \text{with} \quad 0 \leq t_i \leq t_{\text{max}} , \quad (4.5)$$

where  $t_{\text{max}}$  is the maximum drift time. At a constant muon rate  $dN/dr$  per tube section ( $r, r + dr$ ) and the muon rate  $dN/dt$  per drift time interval ( $t, t + dt$ ) are linked via

$$\frac{dN}{dr} = \frac{dN}{dt} \frac{dt}{dr(t)} = \frac{dN}{dt} \frac{1}{\dot{r}(t)} = c . \quad (4.6)$$

Integrating relation (4.6) leads to

$$r(t_i) \approx \frac{1}{c} \int_0^{t_i} \frac{dN}{dt} dt . \quad (4.7)$$

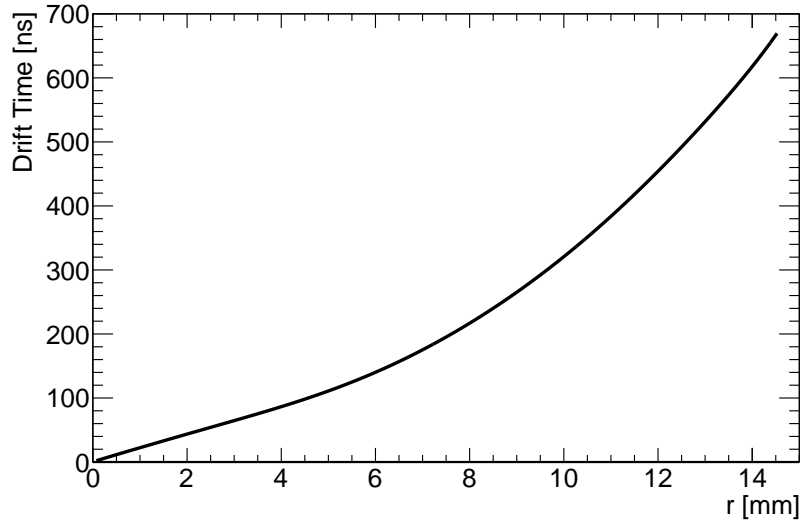


**Figure 4.7:** Measurement of a typical  $r(t)$  relation for an ATLAS MDT tube.

The integral is approximated by a sum of the bin contents  $dN_k$  of the drift time spectrum up to the bin  $i$  containing the drift time  $t_i$ :

$$r(t_i) = \frac{1}{c} \sum_{k=0}^i \delta N_k . \quad (4.8)$$

The constant  $c$  is defined by the fact that the maximum drift time corresponds to a drift radius equal to the inner tube radius  $R$  and the total number of muon counts  $N_{\text{total}}$  in the drift time spectrum:  $r(t_{\text{max}}) = N_{\text{total}}/c = R$ .

This first estimate can be improved by the so-called auto-calibration. The basic principle of this calibration method is the minimization of the residuals of tracks in the chamber for the correct  $r(t)$  relation. Starting with the initial  $r(t)$  relation, tracks are reconstructed and the residuals, the difference of reconstructed track position and measured drift radius, are calculated (see next section for details). Then the  $r(t)$  relation is varied and a optimum of the residual distribution (centred around zero) is searched for iteratively [Dei00, Loe07].

Figure 4.7 shows a typical  $r(t)$  relation for the ATLAS MDTs. The features of the drift time spectrum (Fig. 4.6), and the behaviour of the drift velocity, are reflected in this plot. For small distances to the wire the drift velocity is almost constant, resulting in the linear part of the drift time spectrum and the linear section of the  $r(t)$  relation. For larger radii the drift velocity decreases with the electric field resulting in a falling drift time spectrum and a curved  $r(t)$  relation.

With the  $r(t)$  auto calibration method an average single tube spatial resolution of  $80 \mu\text{m}$  is achieved (taking into account the time slewing corrections to the drift time measurement, see Section 8.4.2). It is limited by fluctuation in the generation of the ionisation clusters along the track and due to the diffusion of the electron clusters during the drift to the anode wire. Also, ionisation charge from background radiation, such as thermal neutrons and protons in the ATLAS cavern, deteriorate the resolution because of shielding of the electric field near the wire and consequently reduction of the gas gain and because of fluctuations in the space charge and therefore of the local electric field in the tubes.

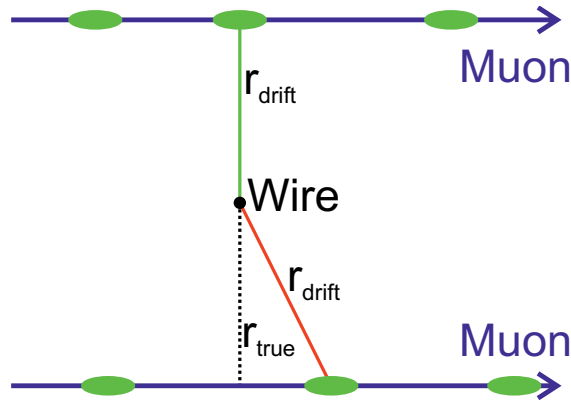


**Figure 4.8:** Influence of the ionisation cluster position on the measured drift radius.  $r_{\text{true}}$  is the distance of the muon track from the wire and  $r_{\text{drift}}$  the measured drift radius, which can be larger than  $r_{\text{true}}$  depending on the cluster position with respect to the wire.

#### 4.4.4 Single Tube Resolution and Efficiency

##### Single Tube Resolution

The single tube resolution  $\sigma(r)$  depends on several parameters:

- Overall ionization charge collected at the wire (signal height),
- mean distance between primary ionisation clusters,
- widening of the electron clouds due to diffusion.

The second point is very important for tracks close to the wire. As illustrated in Figure 4.8, there can be different measured drift radii for tracks with the same distance to the wire depending on the positions of the ionisation clusters with respect to the wire. This effect deteriorates and limits the spatial resolution near the wire. The RMS value of  $(r_{\text{drift}} - r_{\text{true}})/r_{\text{drift}}$  is still 1% for tracks closer than 700  $\mu\text{m}$  to the wire.

For larger drift radii, the signal height has a significant impact on the single tube resolution. The threshold crossing time varies with the signal height. This so called time slewing effect is discussed in detail in Section 8.4.2. Figure 4.9 shows the spatial resolution of a drift tube before and after correction for this effect.

The final limitation is the diffusion of the primary electron clusters in the gas. This effect depends on the parameters of the drift gas and the drift velocity. A fast drift gas leads to stronger diffusion and therefore to a larger uncertainty on the drift time. A slower gas (e.g. with higher pressure) results in less diffusion and allows for a better time and spatial resolution, but results in a higher occupancy of the detector.

The average single tube resolution is defined as the quadratic mean of the resolution of  $N$  radial intervals:

$$\sigma_m = \sqrt{\sum_{i=1}^N \frac{\sigma_i^2}{N}}. \quad (4.9)$$

Applying this formula to the  $r$ -dependent resolution measurement shown in Figure 4.9, obtained for the ATLAS MDT drift tubes using the standard operating parameters of

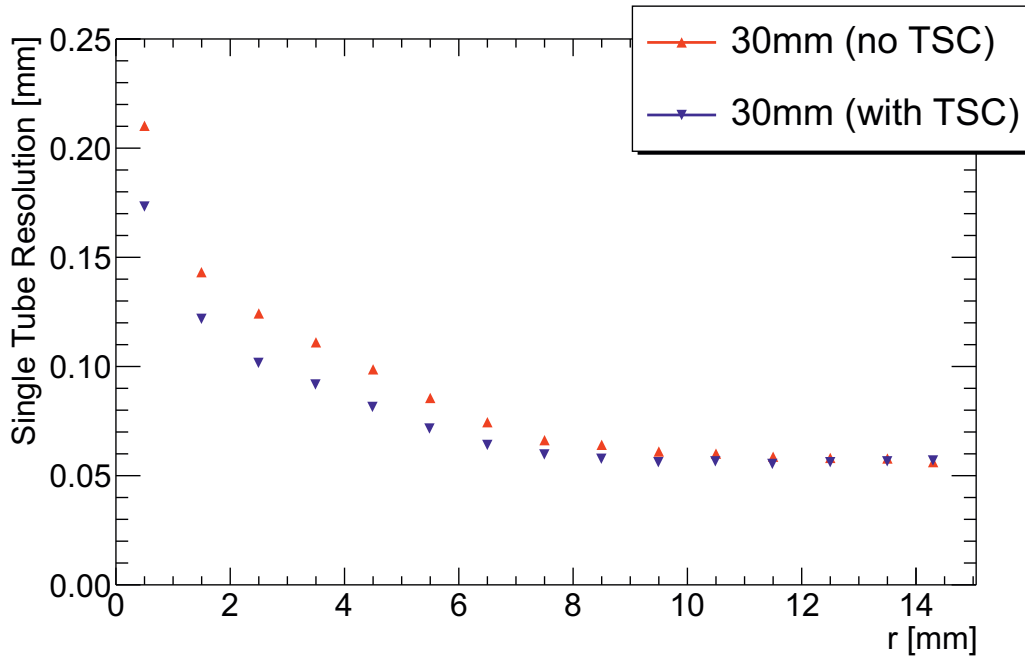


**Figure 4.9:** Spatial resolution of the 30 mm diameter drift tubes before and after the time slewing correction (TSC, cp. Sec. 8.4.2) [Kor12].

3080 V wire potential and 3 bar absolute pressure of the Ar:CO<sub>2</sub> (93:7) mixture at 20°C, gives an average single tube resolution of  $\sigma_m = (98 \pm 2) \mu\text{m}$  without the time slewing correction. After applying this correction, the average resolution is  $(84 \pm 2) \mu\text{m}$ .

### Single Tube Efficiency

Since every muon track ionizes the gas sufficiently in order to induce a signal above the discriminator threshold the detection efficiency is 100% except for tracks very close to the tube wall which have a very short path length in the tube. If the path length is smaller than the average distance between two charge clusters it is possible that there will be no ionisation at all.

However, the efficiency of muon hits usable for muon track reconstruction, defined as the probability that the hit is within 3 times the local drift tube resolution of the reconstructed muon track ( $3\sigma$  efficiency) is deteriorated due to the following facts:

- $\delta$ -electrons created by the muons,
- dead time of the readout electronics (in the presence of  $\delta$ -electrons or of background radiation).

$\delta$ -electrons might be released from the tube walls by the incoming muons leaving an ionization trail in the gas. They reduce the efficiency because they can create hits closer to the wire ( $r_{\delta e}$ ) than the muon hits ( $r_\mu$ ) masking their detection (see Figure 4.10).

Another ingredient determining the efficiency is the dead time of the readout electronics. After a hit is registered in the MDT ASD chip (see Sec. 4.4.7 for details) it can not process the next hit immediately which then might be lost. The dead time of the ASD chip is adjustable between 180 ns and 780 ns. The  $3\sigma$  efficiency for the minimum and maximum dead-time settings shown in Figure 4.11, taking into account all hits within the

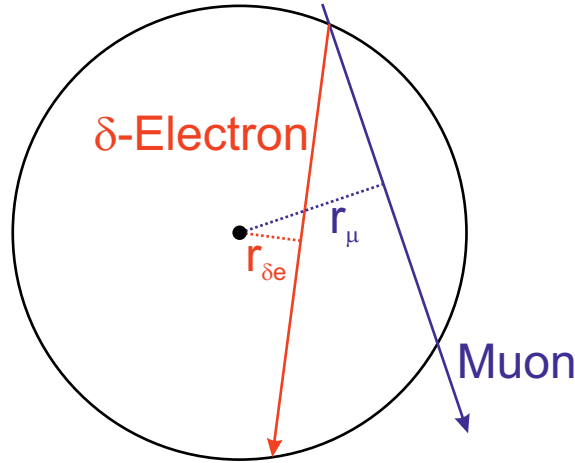


**Figure 4.10:** Masking of muon hits by  $\delta$ -electrons.

drift time spectrum. In the presence of  $\delta$ -electrons the short dead-time allows to detect a muon hit if it arrives more than 180 ns after a  $\delta$ -electron signal, resulting in a higher efficiency for large track radii compared to the setting with 780 ns electronics dead-time. The average  $3\sigma$  single tube efficiency is  $\varepsilon_{\text{long}} = (92.8 \pm 0.9)\%$  for the 780 ns dead-time and  $\varepsilon_{\text{short}} = (93.8 \pm 0.5)\%$  for the shortest possible dead-time setting.

The short dead time has the disadvantage of higher data rate and readout bandwidth requirement. Furthermore the average number of threshold crossing induced by a signal in the tube is larger than one. To reduce this effect the standard dead time setting for ATLAS operation is 780 ns, resulting in a lower efficiency at longer radii. But it ensures that the counting rate per channel stays below the 500 kHz limit of the electronics in the presence of background radiation.

#### 4.4.5 Track Reconstruction

Figure 4.12 illustrates the principle of the track reconstruction in the drift tube chambers. The track in the MDT chamber is parametrized as

$$y = mz + b. \quad (4.10)$$

The distance  $r_t$  between the track and the wire with the coordinates  $(y, z)$  is given by

$$r_t = \left| \frac{b + mz - y}{\sqrt{1 + m^2}} \right|. \quad (4.11)$$

The track reconstruction is performed by a  $\chi^2$  minimisation of the sum of the squares of the deviations of the track radii  $r_t$  from the measured drift radii  $r_d$  for  $N$  tubes along a track:

$$\chi^2(m, b) = \sum_{w=0}^N \left( \frac{r_{d,w} - r_{t,w}}{\sigma_w(r_{d,w})} \right)^2 = \sum_{w=0}^N \left( \frac{r_{d,w} - \left| \frac{b + mz_w - y_w}{\sqrt{1 + m^2}} \right|}{\sigma_w} \right)^2 \quad (4.12)$$

$\sigma_w(r_d)$  is the drift tube resolution.

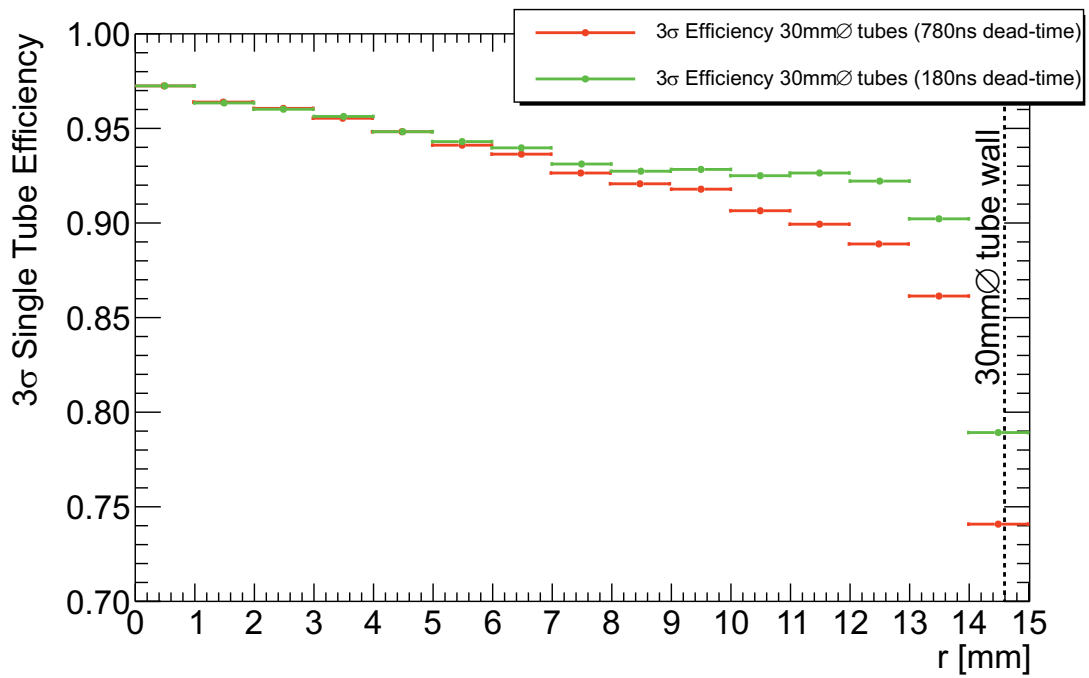


**Figure 4.11:**  $3\sigma$  single tube efficiency for the 30 mm diameter drift tubes for 780 ns and 180 ns dead-time settings of the readout electronics [Kor12].

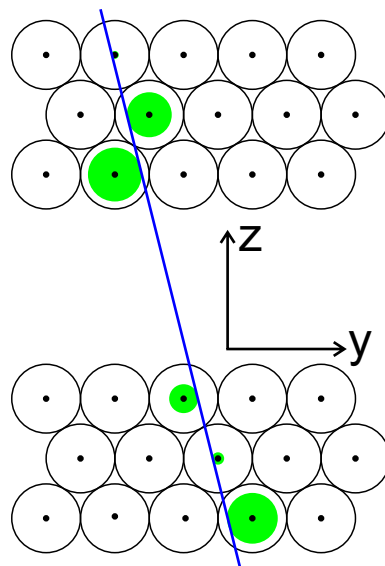


**Figure 4.12:** Principle of the track reconstruction in the drift tube chambers. The track is fitted to the measured drift circles.

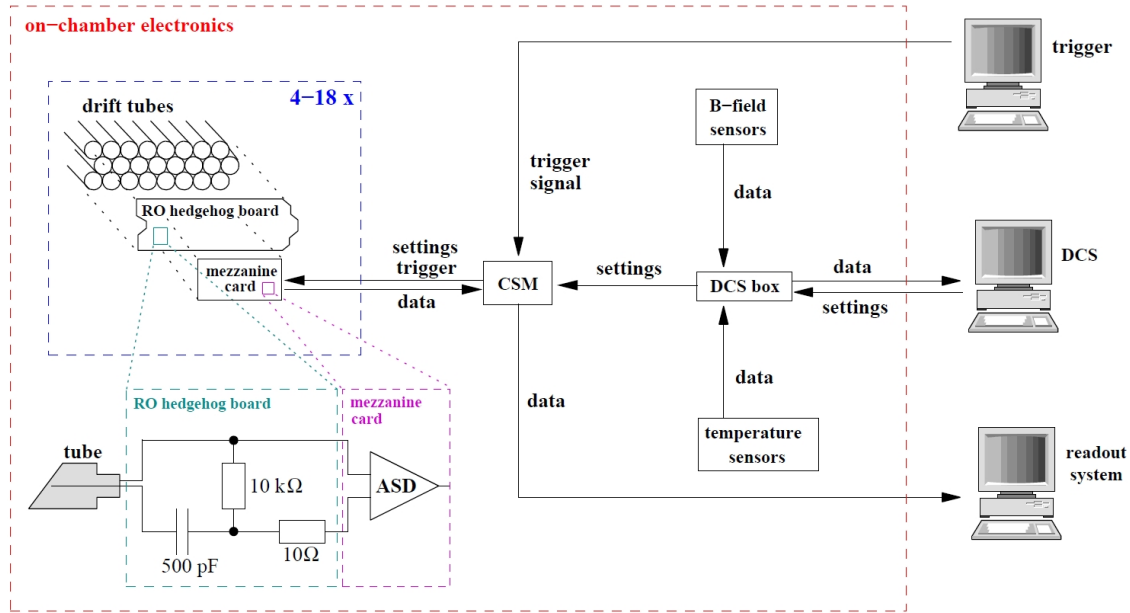


**Figure 4.13:** The readout electronics scheme of a MDT chamber. The Chamber Service Module (CSM) controls all components.

#### 4.4.6 MDT Chamber Monitoring

Each MDT chamber has its own internal optical monitoring system to measure mechanical deformations. As indicated in Figure 4.5, there are 4 optical alignment rays built into the frame of the chamber: two along the tubes and two diagonal. With this system, it is possible to monitor deformations with an accuracy of few micrometers [ATL08]. This system was also used to adjust for the gravitational tube sag by correcting the measured chamber deformation of up to  $500 \mu\text{m}$  in order to centre the wires inside the tubes not only at the end-plugs but over the full length of the chamber.

#### 4.4.7 MDT Chamber Readout Electronics

Each chamber is provided with a high voltage (HV) between wires and tube walls, with low voltage (LV) for the readout electronics, with connections to the central Trigger and Timing Control (TTC) and Data Acquisition (DAQ) system and with a connection to the Detector Control System (DCS).

##### High Voltage Supply

The high voltage for the drift tubes is distributed via a HV splitter box to each of the tube layers. The two multilayers of the chambers are served by separate channels of the HV power supplies. Within a layer, the tubes are connected serially via the so-called HV hedgehog boards.

##### Readout of the Chambers

The central part of the MDT chamber readout electronics is the Chamber Service Module (CSM). It has connections to the mezzanine cards carrying the front-end electronic chips, the TTC system, an optical link to the readout system and a connection to the Detector

Control System (DCS) used to program the electronics and monitoring of the chambers. A schematic illustration of the electronic components on a chamber is given in Figure 4.13.

The mezzanine cards are mounted on read-out (RO) hedgehog boards. These boards are similar to the HV hedgehog boards, but with the purpose to connect the tubes to the Amplifier–Shaper–Discriminator (ASD) chips, decoupling the readout electronics capacitively from the HV. Each ASD chip contains eight channels, three chips are mounted on each mezzanine card. When the signal exceeds the programmable threshold which can be adjusted separately for each ASD chip, the ASDs send digital signals to the TDC<sup>4</sup> on the mezzanine card and analogue signals to an ADC<sup>5</sup>.

The signal arrival time measurement by the TDC is started by the trigger signal of the LHC and stopped when a signal from the ASD chips arrives. After the muon time-of-flight correction, the start signal provides the time when the muon crossed the chamber. The time measured by the TDC is the drift time of the electrons in the tube together with the signal propagation time along the wire.

The ADC measures the charge of the signal pulse within a certain time window after the discriminator threshold is crossed (typically 20 ns long). The information can be used to distinguish between real muon and electronic noise hits, since muons give a higher signal. It is also used to correct for variations of the threshold crossing time depending on the signal height, the so called time slewing effect.

The information from the TDC and the ADC is transferred to the CSM if a trigger signal was generated. If the module receives a trigger signal from the central ATLAS trigger, the data is sent via an optical fibre to the central DAQ system.

The MDM (Muon DCS Module) on the chamber is connected to the MDT CAN<sup>6</sup> bus system of ATLAS. On this bus the readout electronics is programmed (e.g. the thresholds and dead time settings, new firmware versions etc) and initialized. Also the temperature and B-field sensors on the chambers are read out via this bus.

## 4.5 Upgrade Scenarios

The ATLAS muon detectors have been designed for operation up to the design luminosity of LHC. After the upgrade to HL-LHC the background counting rates in the muon spectrometer will rise above the design parameters. [ATL11] provides an overview of the upgrade plans.

### 4.5.1 Muon Trigger Rates

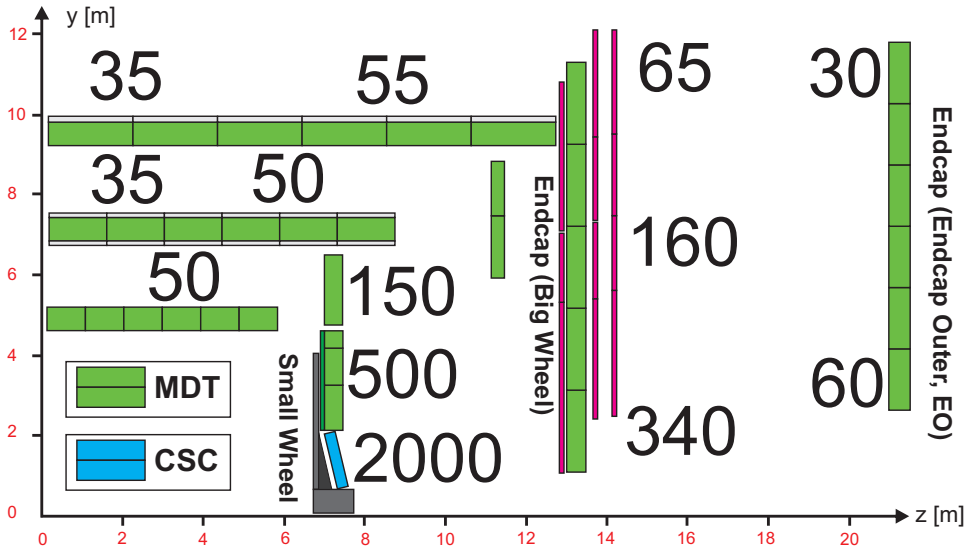
The ATLAS muon trigger selects muons above certain transverse momentum  $p_T$  thresholds. Due to the limited momentum resolution of the trigger system the rejection of low  $p_T$  muons at high trigger thresholds is limited. Figure 4.15 shows the trigger efficiencies for different threshold settings. When setting the threshold to  $p_T = 40$  GeV, there is still a large efficiency for muons below this limit. Since the muon spectrum at the LHC (see Figure 4.16) contains a large contribution of soft muons, there is a considerable trigger rate for muons below threshold. This is acceptable as long as the Level 1 rates do not

---

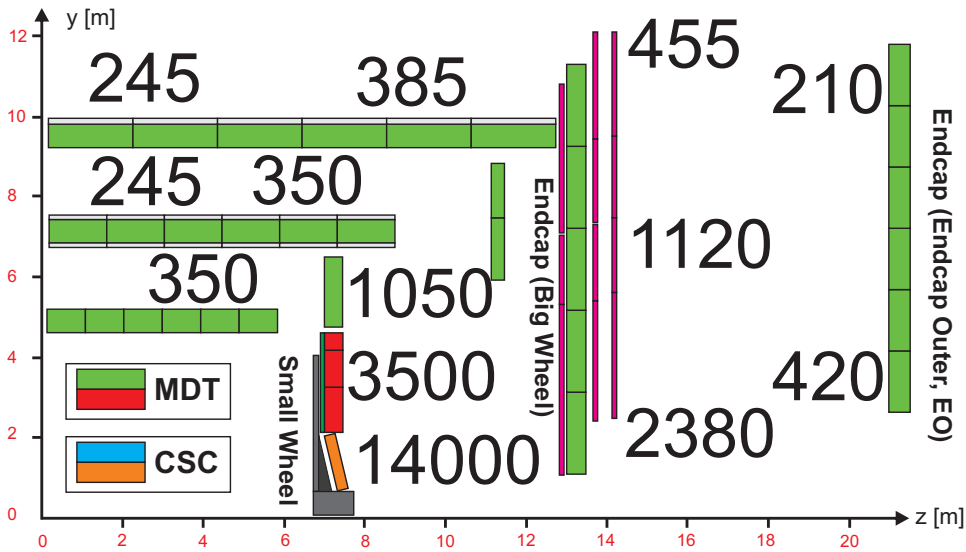
<sup>4</sup>Time-to-Digital-Converter

<sup>5</sup>Analog-to-Digital-Converter

<sup>6</sup>Controller Area Network.



(a) Counting rates in  $\text{Hz}/\text{cm}^2$  for  $\mathcal{L} = 1 \cdot 10^{34} \text{cm}^{-2}\text{s}^{-1}$  (nominal LHC luminosity including a safety factor of 5 from simulation). All chambers are within their design range of 300 kHz per tube.



(b) Counting rates in  $\text{Hz}/\text{cm}^2$  for  $\mathcal{L} = 7 \cdot 10^{34} \text{cm}^{-2}\text{s}^{-1}$  (7 times nominal LHC luminosity estimated from background measurements in the ATLAS detector). The rate capabilities of the chambers in the small wheel (red/orange) is exceeded.

**Figure 4.14:** Expected background rates in the muon spectrometer for nominal LHC and maximum HL-LHC luminosity. Where the rates exceed the limit for the MDT chamber operation the chambers are marked with red/orange color.

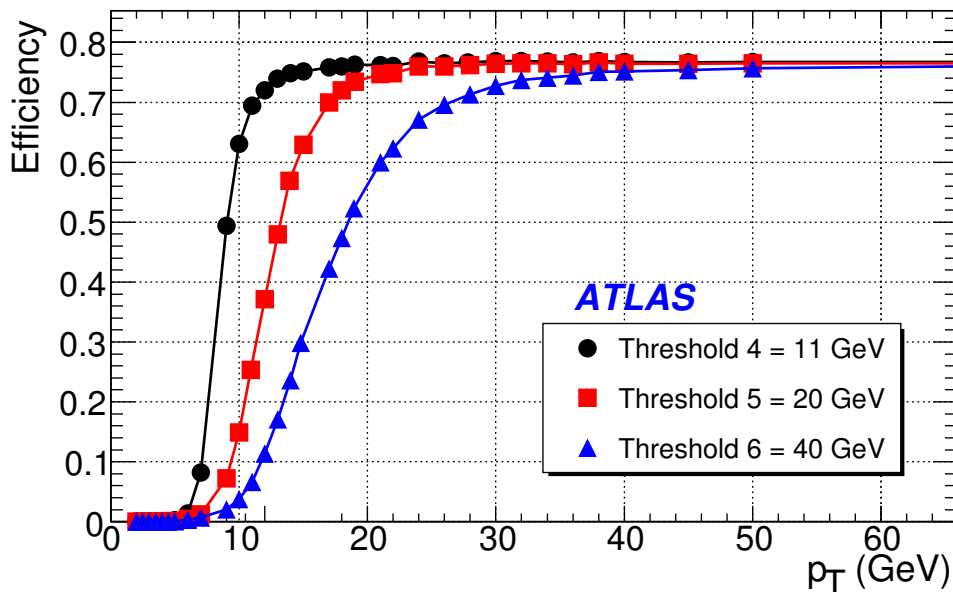


**Figure 4.15:** Efficiency of the Level-1 muon trigger vs.  $p_T$  for three typical trigger thresholds. At the high muon rates from proton–proton collisions at HL-LHC the turn-on ranges of the efficiency curves to the maximum efficiency are too wide in order to sufficiently suppress low  $p_T$  muon triggers even at high thresholds. The momentum resolution on the muon trigger chambers needs to be improved [Dub10].

exceed the limitations (see Sec. 3.2). This will however, be the case at HL-LHC at least in the endcap regions of the ATLAS muon spectrometer.

Therefore it is necessary to increase the momentum resolution of the muon trigger for the LHC upgrade. This can be achieved by using improved trigger chambers with a better spatial and angular resolution and by including the high-resolution MDT chambers in the trigger. Details of the trigger upgrade scenarios can be found in [Dub10].

## 4.5.2 The ATLAS Muon Small Wheel Upgrade

In the barrel part of the muon spectrometer the radiation levels at HL-LHC will still be below the limit of  $500 \text{ kHz/cm}^2$  for the existing MDT chambers as shown in Figure 4.14. But in the endcap regions in the Small and Big Wheels the acceptable limits are exceeded. The only solutions are to improve the shielding and to replace the detectors concerned, in particular to build complete **New Small Wheels (NSW)**. The demands on the new muon tracking detector technology for the NSW are greater than 99% tracking efficiency and high spatial chamber resolution of better than  $60 \mu\text{m}$  (and an angular resolution of better than  $0.5 \text{ mrad}$  precise in the Level 1 muon trigger). All requirements have to be fulfilled up to the highest expected rates of  $14 \text{ kHz/cm}^2$ . The different detector types in consideration are described in [ATL11].

The upgrade schedule of the LHC leaves only a short time window for the installation of the NSWs in the muon spectrometer in 2018. This thesis will discuss one very promising detector technology based on the MDT chamber design which has been demonstrated to fulfil all requirements and can be constructed within the given time limits.

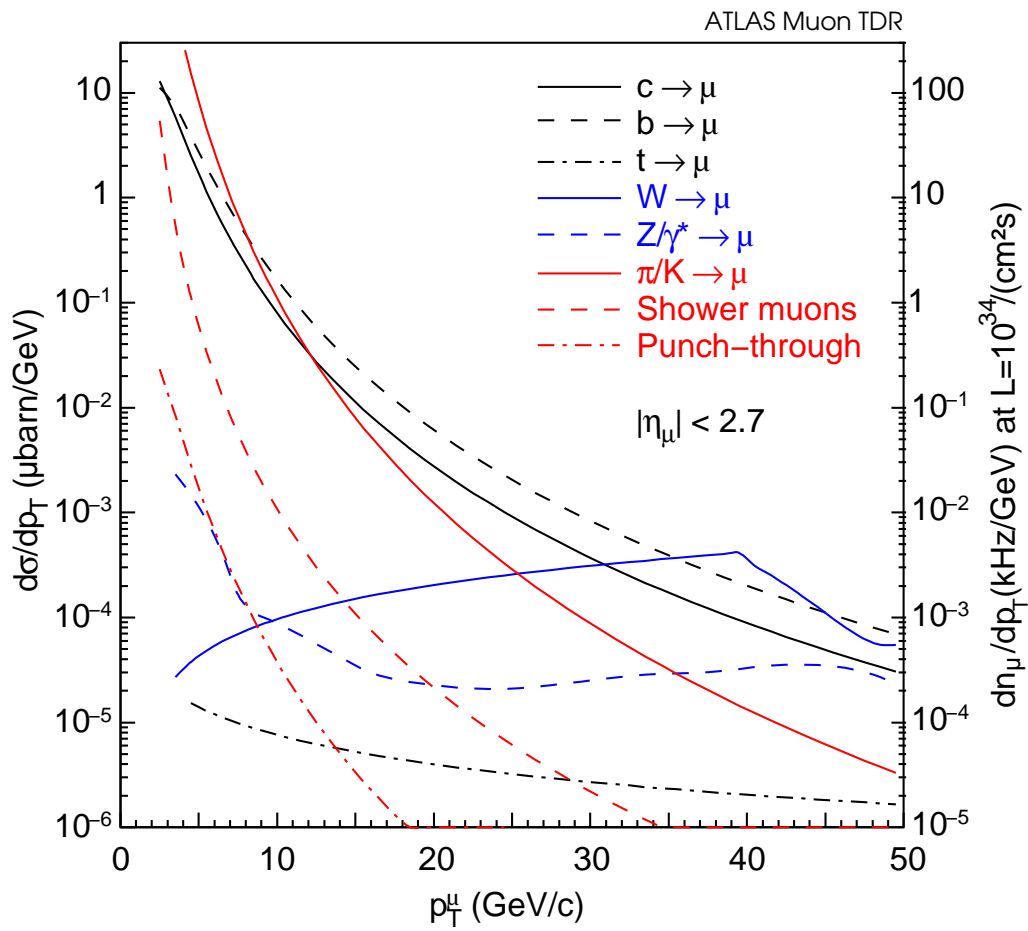


**Figure 4.16:** Muon production cross-sections and rates in the ATLAS detector as a function of the muon  $p_T$  [ATL02].

# **Part II**

## **The sMDT Technology**



# Chapter 5

## Motivation for 15 mm Diameter Drift Tubes

The drift tubes chambers installed in ATLAS show very good performance. In this chapter the limitations of the 30 mm diameter drift tube operation at background rates expected at HL-LHC are discussed. A new detector technology for replacement of the existing muon chambers in the critical ATLAS detector regions with respect to background rates is introduced.

### 5.1 Limitations of the 30 mm Diameter Drift Tubes

The 30 mm diameter drift tubes have been studied extensively before installing them in the ATLAS muon spectrometer [Ale99, Hor04]. They show very good efficiency and resolution up to the highest background rates expected at the LHC design luminosity. The  $3\sigma$  efficiency was already discussed in Section 4.4.4. Efficiency loss originates from background hits masking the muon hits. The track segment reconstruction efficiency in a MDT chamber is above 95% at the highest expected background rates as shown in Figure 5.1.

Figure 5.2(a) and 5.2(b) show the degradation of the average single tube resolution and of the chamber resolution with 6 tube layers, respectively, with increasing background hit rate.

The radial dependence of the drift tube resolution is shown in Figure 5.3 for increasing background rates. Two radial regions can be distinguished: one close to the wire with drift radii below about 7 mm and the region above 7 mm. The region between 4 and 7 mm shows the smallest degradation with the background rate. The region close to the wire suffers from gas gain loss due to shielding of the wire potential by the ion space charge which increases with the background flux. Smaller signals show larger variations of the threshold crossing time and, therefore, worse time resolution. For large drift radii, fluctuations of the space charge cause variations of the electrical field and therefore of the drift velocity in the Ar:CO<sub>2</sub> (93:7) gas which has a field dependent drift velocity, especially at large drift distances. Both effects have a statistical nature and vary with time even for a constant radiation background.

When the LHC instantaneous luminosity increases above the design value of  $10^{34}$  per cm<sup>2</sup>s, the efficiency and spatial resolution of the 30 mm diameter drift tubes will not be sufficient anymore in the highest radiation regions of the ATLAS muon spectrometer.

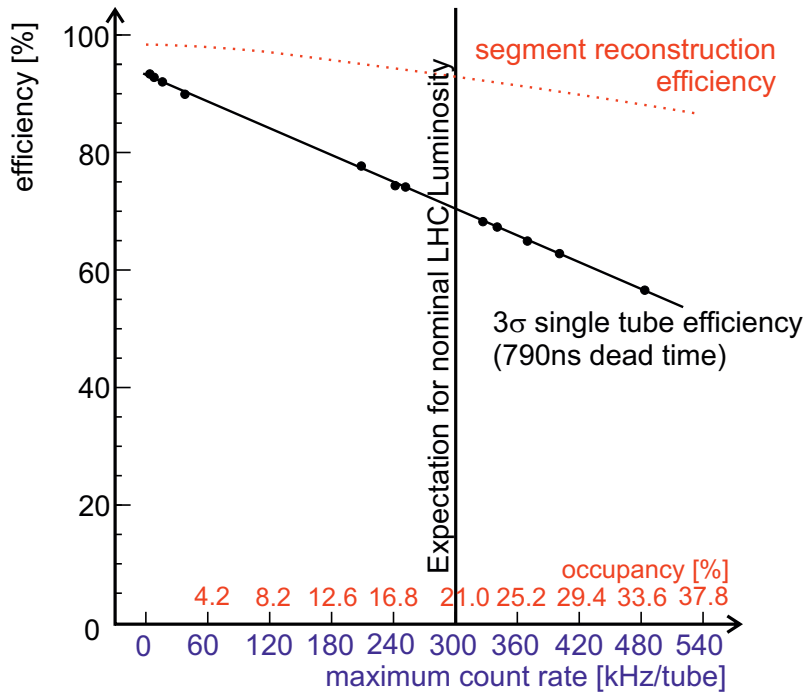
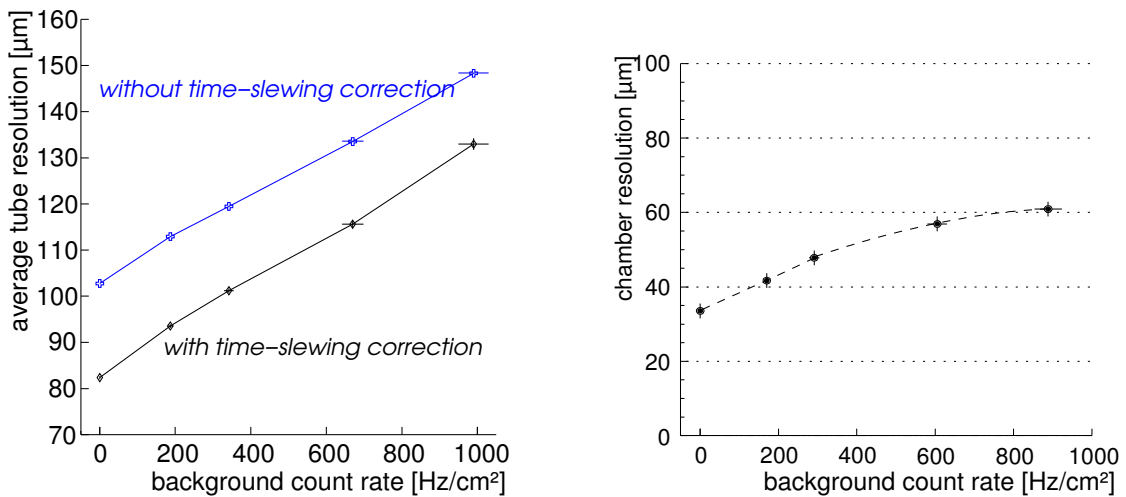


**Figure 5.1:**  $3\sigma$  efficiency of 30 mm diameter drift tubes as a function of the background counting rate for the maximum deadtime of 780ns of the readout electronics. The corresponding track segment reconstruction efficiency in MDT chamber with 6 tube layers is also shown. The expected maximum background rate in MDT chambers in ATLAS at the LHC design luminosity is 300 kHz/tube in the Small Wheels of the ATLAS muon spectrometer [Hor06].



(a) Average single tube resolution as a function of the background hit rate.

(b) Chamber resolution as a function of the background hit rate.

**Figure 5.2:** Effect of the  $\gamma$  background hit rate on the spatial resolution for 30 mm $\varnothing$  drift tubes [Hor06]. 500 Hz/cm<sup>2</sup> background flux corresponds to 300 kHz/tube counting rate in 2 m long tubes.

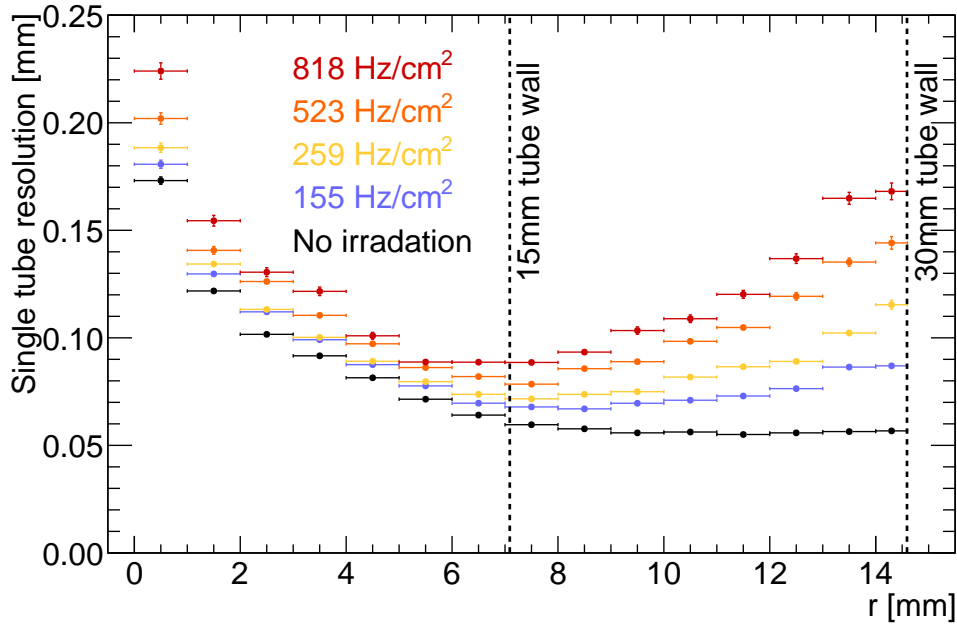


**Figure 5.3:** Spatial resolution of 30 mm $\varnothing$  drift tubes as a function of the drift radius for different  $\gamma$  background hit rates [Hor06]. 500 Hz/cm<sup>2</sup> is the maximum expected background hit rate in ATLAS at the LHC design luminosity.

New muon chamber technologies are under development to replace the detectors in the critical regions (see Section 4.5).

## 5.2 Advantages of 15 mm Diameter Drift Tubes

The effect of space charge fluctuations on the spatial resolution is small for drift radii below 7 mm. This is one of the reasons for reducing the outer radius of the drift tubes to 7.5 mm, the other is the shorter maximum drift time. Since the wall thickness cannot be reduced below 400  $\mu\text{m}$ , the inner radius of the smaller diameter tubes is 7.1 mm. The operating parameters, gas mixture, gas pressure and gas gain, are kept unchanged.

The smaller drift tube diameter has also other advantages compared to the standard ATLAS MDT drift tubes using the same operating parameters:

- Reduction of the gain loss caused by space charge effects in the presence of background radiation which dominates close to the wire.
- 4.3 times lower occupancy due to the shorter drift time and therefore lower data rate in the presence of background radiation.
- Higher redundancy and track segment reconstruction efficiency due to the up to two times larger number of tube layers fitting into the same detector volume.

The expected performance of muon chambers built of 15 mm diameter drift tubes, called small Muon Drift Tube Chamber or sMDT chamber, with the same Ar:CO<sub>2</sub> (93:7) gas mixture and the same gas gain as the ATLAS MDT chambers is discussed in the next section.

A non-negligible advantage of the new drift-tube detector solution with smaller tube diameter is the simple integration into the existing ATLAS detector system. The existing detector services can be re-used:

**The gas system** providing Ar:CO<sub>2</sub> (93:7) at 3 bar absolute pressure.

**The HV supplies:** the requirements with respect to voltage are similar to the ones for the MDT chambers regarding voltage and current. The current needed for one chamber will be higher because of the increased granularity and background counting rate but distributing the HV supply for one chamber on more power supply channels than before can be done without having to integrate new parts in the existing system.

**Active readout electronics:** since the signal height and shape of the drift tube signals does not change it is possible to reuse the MDT readout electronics. A new electronics development is foreseen because of chip availability, higher radiation hardness and bandwidth requirements, but will use the same principles.

**Chamber layout, alignment and track reconstruction:** the general chamber layout will not change and the optical alignment monitoring system and track reconstruction in ATLAS can be easily adopted.

Using the same drift gas has several additional advantages: this gas has already been extensively tested with respect to ageing and drift properties including resolution and efficiency and behaviour in a high background environment.

The Ar:CO<sub>2</sub> (93:7) gas at a relatively low gas gain of  $2 \cdot 10^4$  has been chosen in order to reduce the risk of ageing. The same gas gain is also the baseline for the smaller diameter tubes. Since the gain depends on the electric field at the wire the HV has to be adjusted when reducing the tube diameter.

## 5.3 Expected Performance of the sMDT Technology

### 5.3.1 Gas Gain and Spatial Resolution

To keep the gas gain the same it is necessary to adjust the high voltage between the anode wire and the tube wall when reducing the tube diameter. The electric field of a cylindrical capacitor with charge per unit length  $\lambda = \frac{Q}{L}$  is given by

$$E(r) = \frac{\lambda}{2\pi\epsilon_0 r} . \quad (5.1)$$

The potential between the wire with radius  $r_w$  and the tube with an inner radius of  $r_t$  is given by

$$U = \lambda \frac{1}{2\pi\epsilon_0} \ln \frac{r_t}{r_w} . \quad (5.2)$$

The electric field at the wire has to be the same for the 15 mm $\varnothing$  tubes as for the 30 mm $\varnothing$  tubes in order to achieve the same gain, i.e.

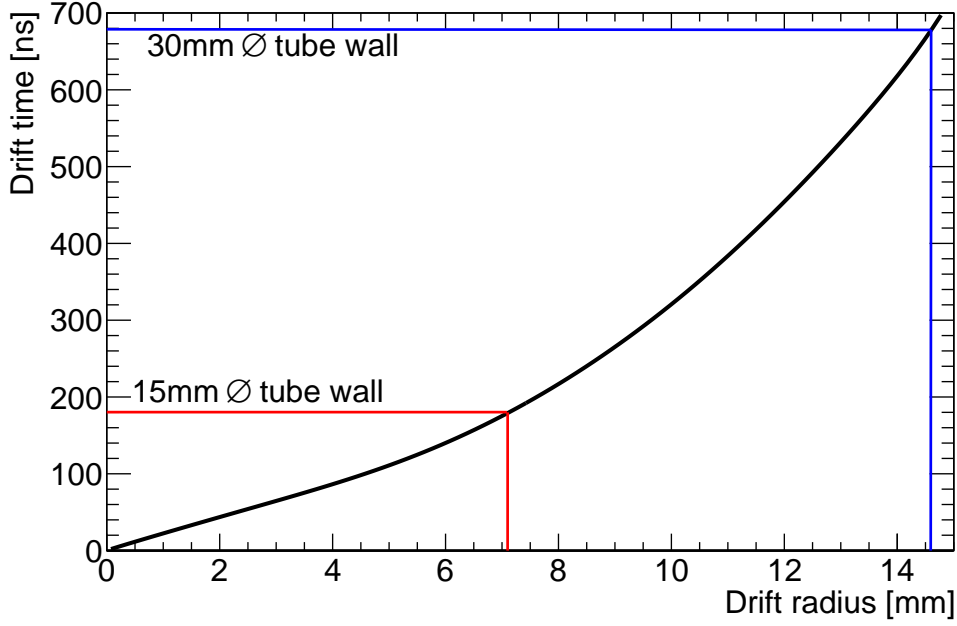


**Figure 5.4:** Space-to-drift-time relation of the ATLAS MDT drift tubes. The 15 mm $\varnothing$  tubes show the same behaviour at drift radii below 7.1 mm because of the same operating conditions.

$$E_{30}(r_w) = E_{15}(r_w), \quad (5.3)$$

$$\frac{U_{30}}{\ln \frac{r_{t,30}}{r_w}} = \frac{U_{15}}{\ln \frac{r_{t,15}}{r_w}}. \quad (5.4)$$

From equation 5.4, the voltage to be applied to the 15 mm $\varnothing$  tubes can be calculated. Inserting the unchanged wire radius  $r_w = 25 \mu\text{m}$ , the inner radius  $r_{t,30} = 14.6 \text{ mm}$  of the 30 mm $\varnothing$  tubes, the inner radius of the 15 mm tubes  $r_{t,15} = 7.1 \text{ mm}$  and  $U_{30} = 3080 \text{ V}$  used for the large diameter tubes to achieve a gas gain of  $2 \cdot 10^4$  gives

$$U_{15} = \frac{\ln \frac{r_{t,15}}{r_w}}{\ln \frac{r_{t,30}}{r_w}} U_{30} = 2730 \text{ V}. \quad (5.5)$$

As one can see in Figure 5.3, the largest degradation of the single-tube resolution with increasing background rate occurs for drift radii above  $\sim 7 \text{ mm}$ . Therefore, an important contribution to the resolution degradation due to space charge fluctuations at high background rates is eliminated for 15 mm $\varnothing$  tubes. The  $r(t)$  relation for drift radii below 7 mm is almost linear (see Fig. 5.4), implying that the drift velocity is almost independent of the electric field and will have little sensitivity to variations in the electric drift field caused by induced space charge fluctuations.

For 15 mm $\varnothing$  tubes, the gain drop due to ion space charge build-up is the dominant degradation effect of the background radiation on the drift-tube resolution. The gain of a

drift tube can be parametrized by the Diethorn formula [Die56]:

$$G(V, \rho) = \left( \frac{V}{A(\rho)} \right)^{\frac{V}{B}} \quad (5.6)$$

with the gas density  $\rho$  ( $\rho_0$  is the normal gas density) and the anode potential  $V$ .  $A(\rho)$  is defined as

$$A(\rho) = r_w \ln \left( \frac{r_t}{r_w} \right) E_{\min} \left( \frac{\rho}{\rho_0} \right), \quad (5.7)$$

with the wire radius  $r_w$ , the tube inner radius  $r_t$ .  $B$  is defined as

$$B = \frac{\ln \left( \frac{r_t}{r_w} \right) \Delta V}{\ln 2}. \quad (5.8)$$

$\Delta V$  and  $E_{\min}$  are gas parameters:  $e\Delta V$  is the minimum ionisation energy and  $E_{\min}$  is the minimum field strength needed for the electrons to reach the ionisation energy. With this formula it is possible to calculate the gas gain reduction for the space charge created at a given background hit rate. The details of the calculation for the 30 mm $\varnothing$  ATLAS MDT tubes are described in [Ale99]. Performing the same calculations for the smaller drift tube diameter shows that the gain drop is strongly reduced. The gain drop for both tube diameters is shown in Figure 5.5 as a function of the background hit rate. For neutral background particles, like photons and neutrons, converting mostly in the tube walls, and in linear approximation, the voltage drop corresponding to the gain loss is proportional to  $r_t^3$ , i.e. it is lower by a factor of  $(14.6 \text{ mm})^3 / (7.1 \text{ mm})^3 = 8.7$  for 15 mm $\varnothing$  compared to 30 mm $\varnothing$  tubes. For charged background particles directly ionizing the gas, the path length in the gas also enters and the voltage drop scales with  $r_t^4$ .

Since without background radiation the average resolution of the ATLAS MDT tubes profits from the higher resolution at increasing radius, the average resolution of unirradiated 15 mm $\varnothing$  tubes is worse. It is possible to estimate the average resolution of 15 mm $\varnothing$  tubes from the measured radial dependence of the resolution without background radiation of the ATLAS MDT tubes (see Fig. 5.3). Calculating the average resolution only for drift radii smaller than 7.1 mm results in an average single tube resolution of  $\sigma_m = (106 \pm 2) \mu\text{m}$ , compared to the average up to 14.6 mm of  $(84 \pm 2) \mu\text{m}$  without radiation background. To achieve the same chamber resolution more 15 mm $\varnothing$  tube layers per chamber can be used. Measurements of the single 15 mm $\varnothing$  tube and of the track segment resolution are shown in section 8. Figure 5.6 shows that the 15 mm $\varnothing$  single tube resolution is expected to be better than 150  $\mu\text{m}$  up to the highest rates expected at the HL-LHC.

### 5.3.2 Efficiency

For tracking purposes the so called  $3\sigma$  efficiency is relevant: the probability of finding a hit in the tube within 3 times the single tube resolution ( $3\sigma$ ) at the position of the muon track. For given resolution, if all hits within the readout window are accepted, this efficiency is determined by the dead-time the readout electronics during which the tube is

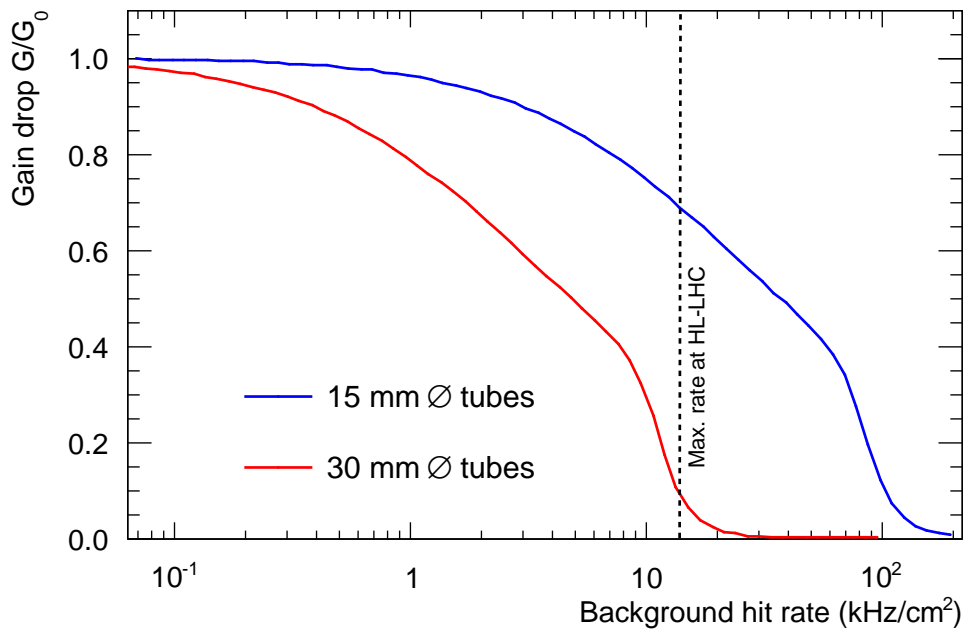


**Figure 5.5:** Gas gain  $G$  relative to the nominal gain  $G_0$  as a function of the background hit rate of  $\gamma$ -rays for 15 mm and 30 mm diameter tubes [Sch12a]. The dashed line marks the maximum expected background hit rate in the drift tubes at HL-LHC of 14 kHz/cm<sup>2</sup> [ATL11].

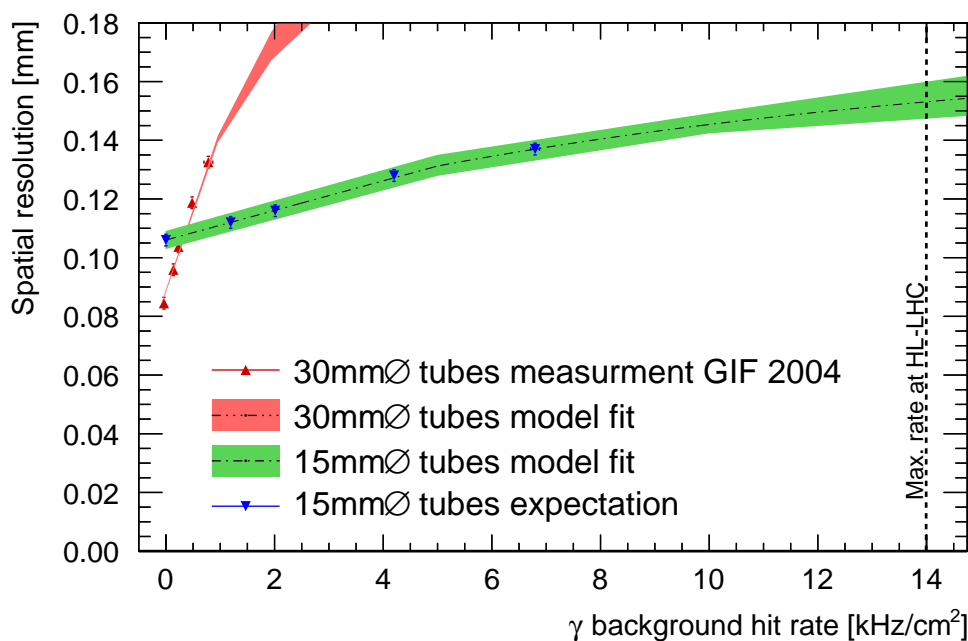


**Figure 5.6:** Expectation for the average resolution of 15 mm diameter tubes (green) derived from the measurement for the 30 mm diameter tubes (red) as a function of the background hit rate by calculating the average resolution for radii less than 7.1 mm and multiplying the corresponding rates of the 30 mm diameter tube measurements by 8.7 (see text) [Sch12a].

inefficient. The two times smaller drift tube diameter also reduces the background hit rate in a tube of a given length by a factor of two.

Overall the occupancy of the drift tubes is reduced by a factor given by the value of the maximum drift-time for the 30 and 15 mm diameter drift tubes (see Sec. 5.3.4) times the factor two of the background hits rate reduction, i.e. by a factor of

$$\frac{\text{occupancy}(30 \text{ mm}\varnothing)}{\text{occupancy}(15 \text{ mm}\varnothing)} = \frac{t_{\text{max}}^{30}}{t_{\text{max}}^{15}} \cdot 2 = \frac{685 \text{ ns}}{180 \text{ ns}} \cdot 2 = 7.6 \quad (5.9)$$

The occupancy is relevant for the track segment reconstruction efficiency in a chamber.

For the 30 mm $\varnothing$  tubes a dead-time larger than the maximum drift-time is chosen to suppress multiple threshold crossings of signals and to reduce the required readout bandwidth because of limitations in the DAQ system. Since the maximum drift-time for the smaller diameter tubes is about 3.8 times shorter (for the 30 mm $\varnothing$  tubes filled with Ar:CO<sub>2</sub> 93:7 gas mixture at 3 bar pressure the maximum drift time varies between 675 ns and 695 ns [Rau05], the 15 mm $\varnothing$  tubes have a maximum drift time between 175 ns and 185 ns, see Fig. 5.8 [Sch10]) it is possible to use a shorter readout window and a shorter dead-time for the available bandwidth limitations.

A lower counting rate per channel is also an important consideration for the readout electronics. The current TDC on the ATLAS front-end cards, the mezzanine cards, accepts a maximum rate of 500 kHz per channel [Pos07]. For the sMDT chambers, new electronics is under development with rate capability matching the expectation for the regions in the ATLAS muon spectrometer with the highest background counting rates.

### 5.3.3 Tracking Redundancy

With smaller tube diameter it is possible to fit a larger number of tube layers into the same available detector volume. Reducing the tube diameter by a factor 2 results in a 4 times denser tube grid. Details of the new sMDT chamber design are discussed in the next chapter. A larger number of tube layers increases the segment finding efficiency, especially in an environment with a high background counting rate (see Fig. 5.7).

For a chamber with  $t$  tube layers the probability  $p$  to find at least  $m$  hits on the segment is given by the Poisson distribution

$$p = \sum_{h=m}^t \binom{t}{h} (1 - \varepsilon)^{t-h} \varepsilon^h \quad (5.10)$$

for a single tube  $3\sigma$  efficiency  $\varepsilon$ . ATLAS requires a segment reconstruction efficiency of better than 95% for tracking. This corresponds to a minimum  $3\sigma$  single tube efficiency  $\varepsilon = 84.7\%$  when requiring at least 4 hits in a 6-layer chamber. When requiring at least 7 hits in a 12-layer chamber, a single tube efficiency of only 75.5% is sufficient.

More hits on a track improve the chamber spatial resolution. The average track segment spatial resolution  $\sigma_{\text{track}}$  with  $N$  hits per track depends on the average single tube resolution  $\sigma_{\text{tube}}$  and the relative wire positioning accuracy  $\sigma_{\text{pos}}$  in the chamber according to (see Section 8.7):

$$\sigma_{\text{track}} = \sqrt{\frac{\sigma_{\text{tube}}^2 + \sigma_{\text{pos}}^2}{N}}. \quad (5.11)$$

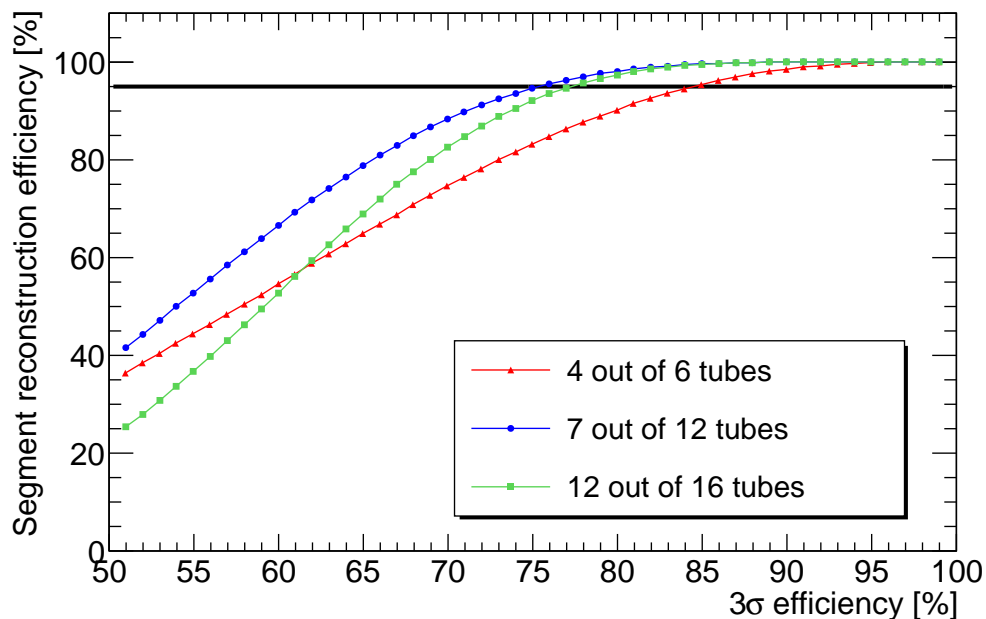


**Figure 5.7:** Track segment reconstruction efficiencies as a function of the  $3\sigma$  efficiency for different numbers of tube layers and minimum number of required hits per track segment.

### 5.3.4 Drift Time Spectrum

Since most of the operating parameters are kept unchanged, the drift time spectrum of the 15 mm diameter tubes is very similar to the drift time spectrum for the 30 mm diameter tubes for drift radii below 7.1 mm. Figure 5.8 compares the two spectra. Reducing the tube diameter by a factor of two reduces the maximum drift time by about a factor of 3.8 because the electron drift velocity in the Ar:CO<sub>2</sub> (93:7) gas decreases with decreasing electrical field (increasing distance to the wire, compare Fig. 5.4 and Sec. 4.4.3). Another difference is the shape of the falling edge: the slope of the falling edge of the drift time spectrum is much steeper for the 15 mm $\varnothing$  tubes than for the 30 mm $\varnothing$  tubes. Therefore the fitting function for determining the maximum drift time was modified as discussed in section 4.4.2.

## 5.4 Summary

The rate capability of the standard ATLAS MDT chambers will be exceeded in the high-rate forward regions of the ATLAS muon spectrometer when the luminosity of the LHC is raised above the design value. Reducing the diameter of the drift tubes by a factor of 2 while keeping the other operating parameters unchanged offers an attractive solution. The parameters of the ATLAS MDT system are shown in Table 5.1, in comparison with the parameters of the new sMDT system. The occupancy of the drift tubes is reduced by a factor of 7.6 due to the smaller tube diameter and the shorter drift time. The shorter maximum drift time allows also for reducing the electronics dead time without exceeding the bandwidth limitations. Reducing the dead-time results in a significantly higher single tube  $3\sigma$  efficiency in the presence of background radiation, because the probability of

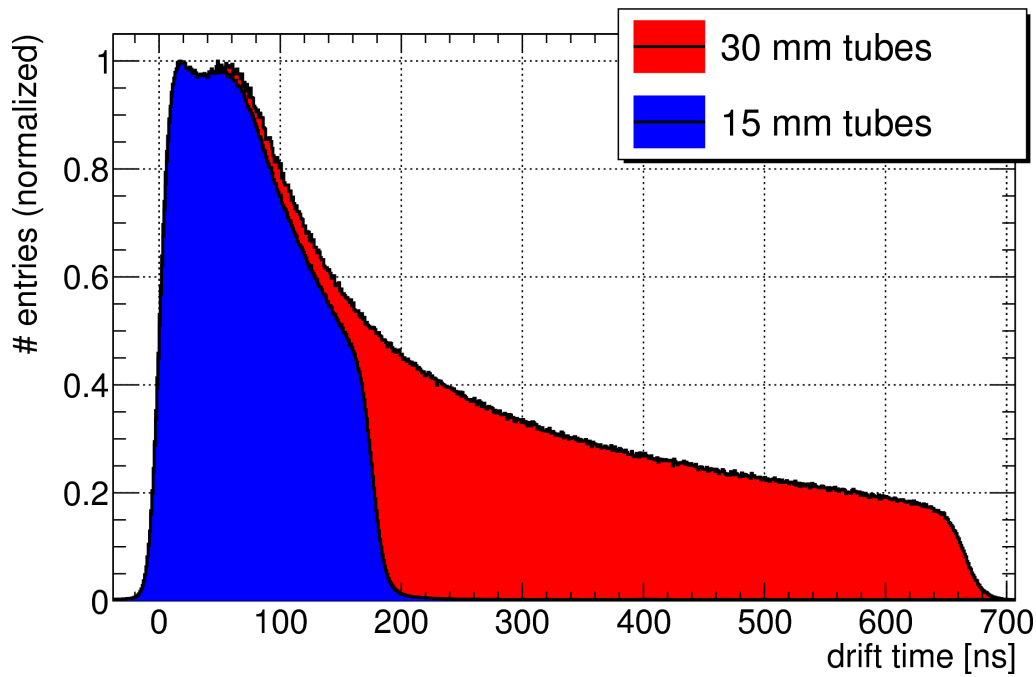


**Figure 5.8:** Comparison of the drift time spectra of 30 mm $\varnothing$  and 15 mm $\varnothing$  tubes. The difference between 100 ns and 160 ns is caused by the different temperatures of the 15 mm $\varnothing$  and 30 mm $\varnothing$  tubes (see Sec. 7.14(a)).

masking of a muon hit by a background hit becomes smaller. Also the gain drop and, therefore, the degradation of the spatial resolution with increasing background hit rate are considerably reduced compared to the standard ATLAS MDT tubes. Both improvements allow for achieving the required spatial resolution and tracking efficiency even at the highest expected background rates at HL-LHC.

The construction and performance tests of a full-size sMDT prototype chamber with 15 mm diameter drift tubes are discussed in the following chapters.

**Table 5.1:** Comparison of the parameters of the drift tubes in the ATLAS MDT and in the sMDT chambers.

Parameter	Design value	
	MDT drift tubes	sMDT drift tubes
Outer tube diameter	29.970 mm	15.0 mm
Tube material	Aluminum	
Tube wall thickness	0.4 mm	
Wire material	gold plated W/Re (97/3)	
Wire diameter	50 $\mu\text{m}$	
Gas mixture	Ar:CO <sub>2</sub> (93:7)	
Gas pressure	3 bar (absolute)	
Gas gain	$2 \cdot 10^4$	
Wire potential	3080 V	2730 V
Fitted maximum drift time (21°C)	(685 $\pm$ 10) ns	180 $\pm$ 5 ns
Average drift tube resolution (without background radiation and with time slewing corrections)	(84 $\pm$ 2) $\mu\text{m}$	(106 $\pm$ 2) $\mu\text{m}$



# Chapter 6

## sMDT Prototype Chamber Design and Construction

In this chapter the design and construction of a sMDT prototype chamber is discussed. Since the tube diameter is reduced by a factor of 2 and, therefore, the tube grid is 4 times denser compared to the ATLAS MDT chambers all parts (gas distribution system, hedgehog boards, etc.) for the chamber have to be redesigned. Also the glueing procedure of the tubes into layers was optimized in order to speed it up for assembly of up to twice the number of tube layers compared to the ATLAS MDT chamber construction. Details of the new design can also be found in [Sch10].

### 6.1 Drift Tubes and Gas Distribution System

The 15 mm diameter aluminium tubes have the same wall thickness of 400  $\mu\text{m}$  as the 30 mm diameter tubes. Reducing the thickness is not possible without sacrificing the stability. Changing the outer diameter of the tubes from 30 mm to 15 mm reduces the inner radius from 14.6 mm to 7.1 mm, i.e. by a factor of 2.06.

The tube endplug had to be redesigned completely. Figure 6.1 shows an exploded view of all components of the new drift tubes. The main part of the endplug is the plastic insulator surrounding the brass insert holding the wire via a copper crimp tubelet. An important part of the endplug is the wire locating piece, the twister, inserted into the brass insert on the inside of the tube which is used to center the wire with respect to the external precision surface on the brass insert of the endplug with an accuracy of a few  $\mu\text{m}$ . The brass insert also provides via the signal caps the electrical connections to the readout electronics and to the HV supply.

The plastic gas connector is part of the new modular gas distribution system shown in more detail in Figure 6.2. The grounding pin is screwed into the space left between three neighbouring tubes during assembly of the chamber reducing the number of ground connections between the tubes while connecting all tube walls to ground. The assembly and the quality control tests of the drift tubes are described in [Sch10].

#### 6.1.1 The Hedgehog Boards

The functionality of the HV and readout hedgehog boards of the sMDT chamber has already been discussed in section 4.4.7. The new boards contain the same circuits, but on a 4 times smaller area. The only solution for a HV stable design is placing the components

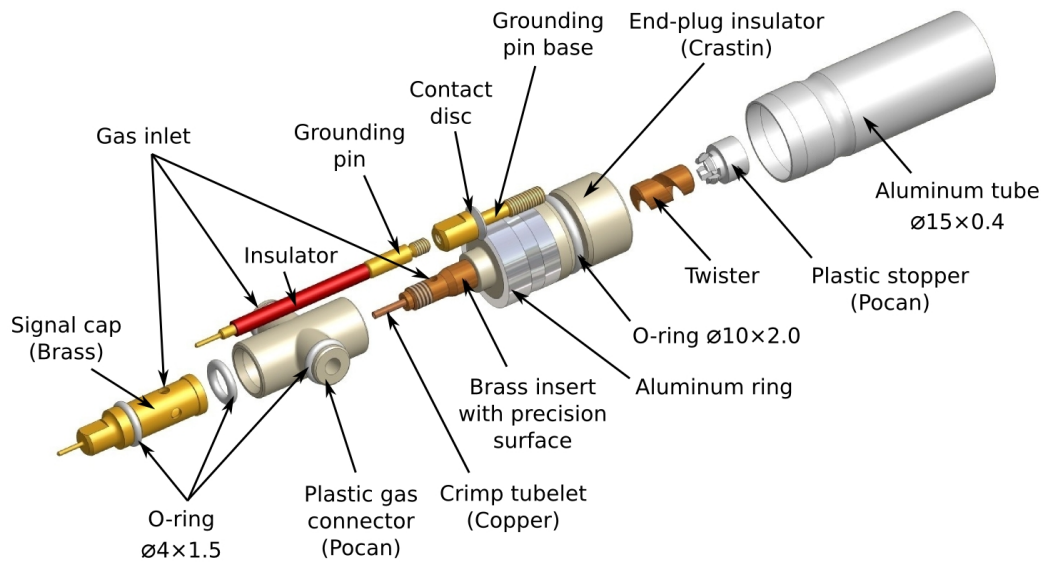


**Figure 6.1:** Blow-up view of the endplug parts and the gas system connection.

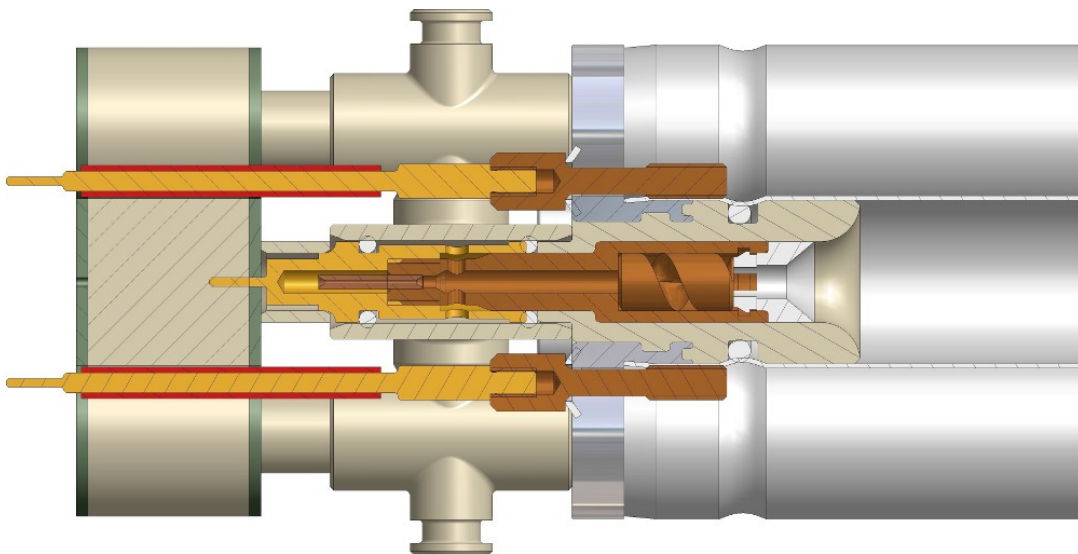
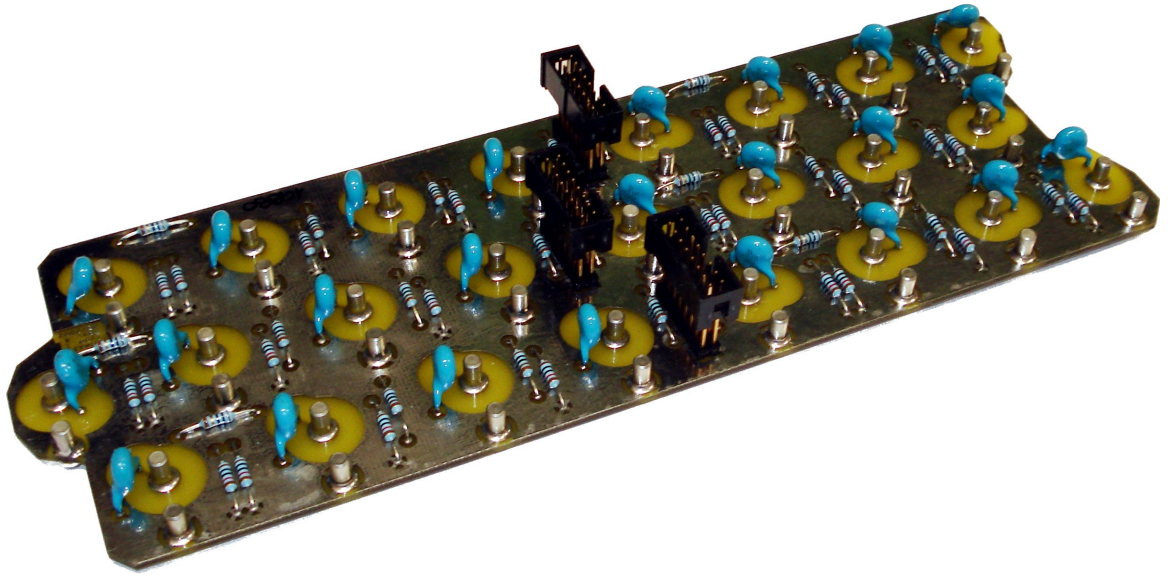
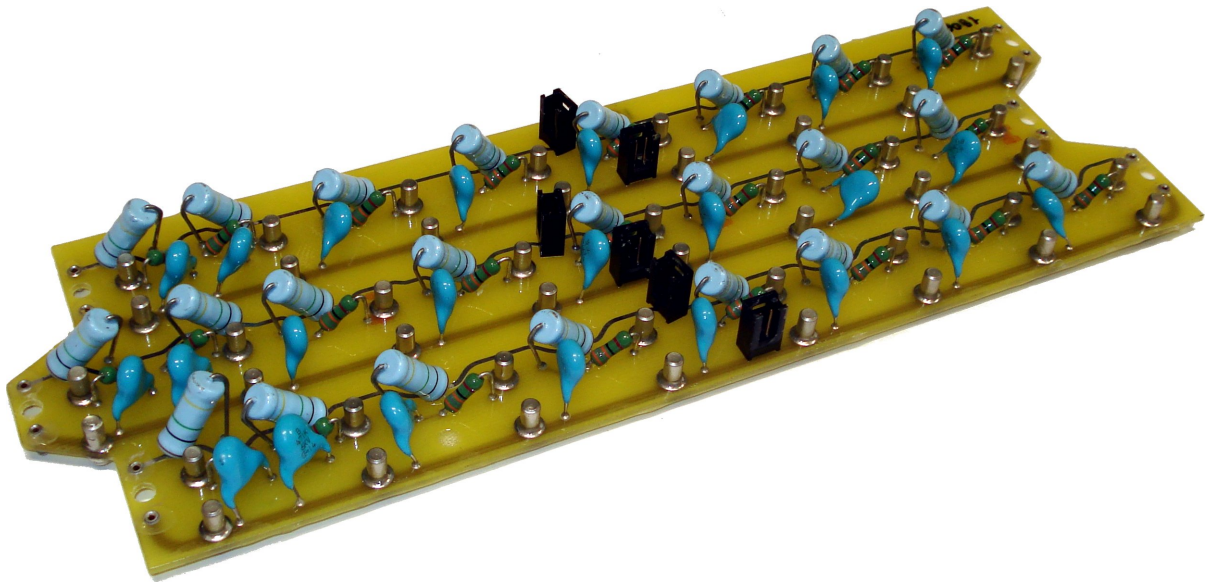


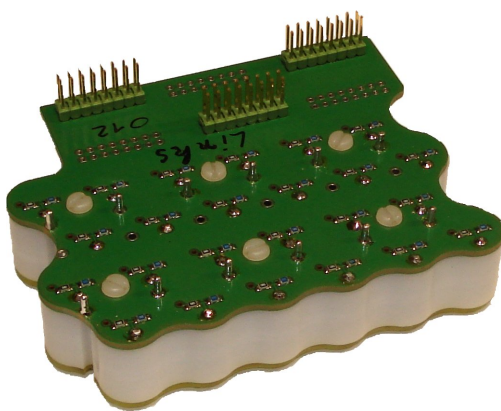
**Figure 6.2:** Illustration of the gas distribution system to the individual tubes and connection through an assembled endplug. The hedgehog card is visible on the left-hand side.



(a) ATLAS MDT chamber readout board.



(b) ATLAS MDT chamber high voltage board.



(c) sMDT readout board.



(d) sMDT high voltage board.

**Figure 6.3:** The different hedgehog boards for the ATLAS MDT and the sMDT chambers in comparison.

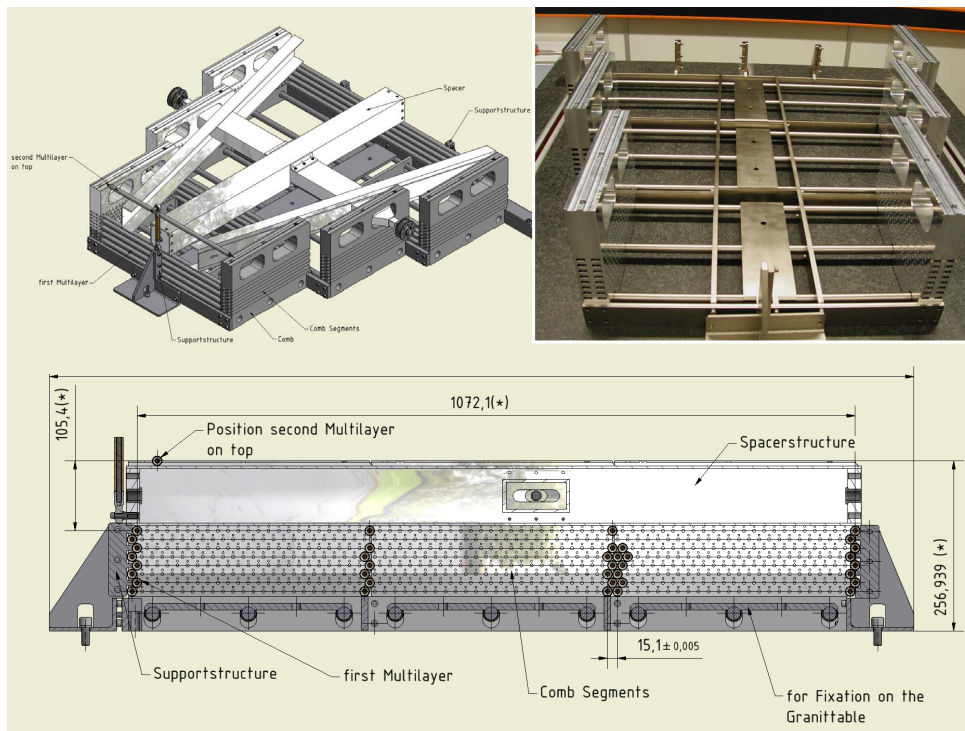


**Figure 6.4:** The jigs holding the tubes in the grid during chamber assembly.

on several layers of boards. The high-voltage decoupling capacitors in the readout side and the resistors on the HV side are enclosed in HV insulating plastic cylinders. Figure 6.3 compares the ATLAS MDT hedgehog boards to the new sMDT boards. After assembly, the boards are cleaned and coated with lacquer to minimize leakage currents. The maximum allowed leakage current on the HV boards is set to 25 nA at 3500 V.

## 6.2 Chamber Construction

After the tubes passed the quality control tests they are placed in a jig and glued together. The jig structure is shown in Figure 6.4. From equation (5.11), the accuracy of the sense wire positions is an important ingredient of the track point resolution. To achieve the needed wire positioning accuracy of  $20\ \mu\text{m}$  (rms), the glueing jig has been fabricated with an accuracy of  $\pm 5\ \mu\text{m}$ . After one layer of tubes is placed in the combs they are fixed by the next set of combs and glue is applied. Then the next tube layer is placed in the jig. This is repeated until the whole multilayer with up to 8 layers is assembled. The second multilayer is assembled in the same way. Finally, both multilayers are glued to the spacer structure. The relative alignment of the two multilayers is ensured by notches in the support structure. It is possible to complete this cycle within three days. Compared to the construction of the ATLAS MDT chambers where the glueing of one tube layer required one day this is a substantial improvement.

After the glueing is finished, the gas distribution system is mounted on the chamber and the hedgehog boards are installed on the signal caps. After closing the Faraday cage, the final quality control measurements of the gas leak rate and of the HV leakage currents

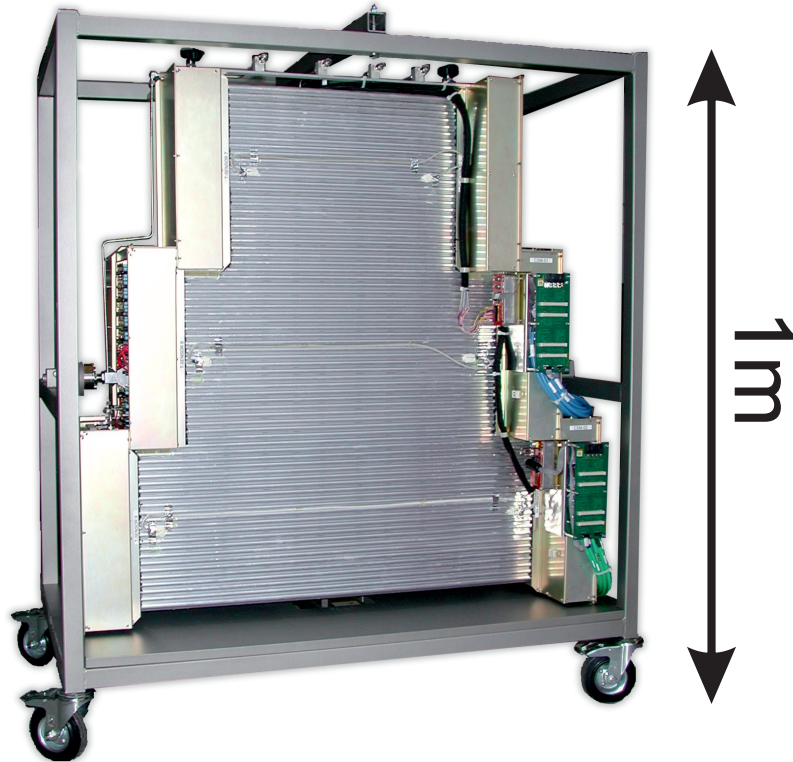


**Figure 6.5:** The full-size prototype chamber.

are performed. Afterwards the readout electronics are added and the noise rate of the chamber, i.e. the counting rate without HV applied, is measured. A too high noise rate indicates non perfect grounding or shielding by the Faraday cage. Figure 6.5 shows a photograph of the fully equipped large prototype chamber. Compared to a typical ATLAS MDT chamber the number of tubes is 3 times higher, the number of tube layers increased from 6 to 16.

### 6.3 Summary

The design of the sMDT chambers with a four times denser tube grid compared to the ATLAS MDT chambers was a very challenging effort. The production of the drift tubes and of the hedgehog boards with the required quality and performance required several iterations. Several smaller prototype chambers have been build.

The final full-sized prototype chamber with 16 layers of 72 tubes would fit into the Small Wheel of the ATLAS muon spectrometer. It was used for the verification of the construction procedure for large chambers and served as test chamber in test beam and *gamma*-irradiation experiments. The following chapters discuss the first measurements performed with this chamber.



# Chapter 7

## Sense Wire Position Measurement

This chapter describes the measurement of the sense wire positioning accuracy of the prototype chamber. An accuracy of  $20\ \mu\text{m}$  (rms) is required in order to achieve the desired chamber resolution.

### 7.1 Measurement Setup

To measure the mechanical wire position accuracy of the prototype chamber, a cosmic ray test-stand at LMU Munich in Garching was used which was installed in order to perform the same measurements for the ATLAS MDT chambers during their production in Munich. The setup and the measurement for the ATLAS MDT chambers are described in detail in [Kor02] and [Rau05].

The layout of the teststand is shown in Figures 7.1 and 7.2. The principle of the measurement is the comparison of cosmic muon ray tracks reconstructed in two reference chambers with accurately known wire positions with hits in the prototype chamber. The reference chambers were X-rayed at CERN to measure the wire positions with an accuracy of a few  $\mu\text{m}$ . The chambers provide reference tracks with  $< 0.4\ \text{mrad}$  angular and  $< 20\ \mu\text{m}$  spatial resolution.

The trigger is provided by a coincidence of two layers of scintillators, one above the chambers and one below. The segmentation of the trigger hodoscope along the tubes allows for the determination of the second coordinate ( $x$  direction) of the muon track. The trigger logic includes a pattern finding unit to ensure that only tracks inside one tower (see Figure 7.2) are triggered in order to limit the inclination angle of the muon track in the  $x$ - $z$  plane and optimize the reconstruction.

The lower scintillator layer is shielded by a 30 cm thick iron absorber which stops muons below  $600\ \text{MeV}/c$  [Kor02] rejecting low energy muon tracks with a high multiple scattering. The magnitude of multiple scattering was estimated by comparing the reconstructed track segments in the two reference chambers. If the difference of the track parameters, slope and offset, is too large, the event is rejected. The cut values are optimised using Monte-Carlo simulation as described in section 7.2.1.

### 7.2 Monte-Carlo Simulation of the Teststand

A full Monte-Carlo simulation is used to optimize the data analysis of the cosmic ray teststand. The simulation is based on GEANT 4 [Ago03, Kor00] using a custom interface

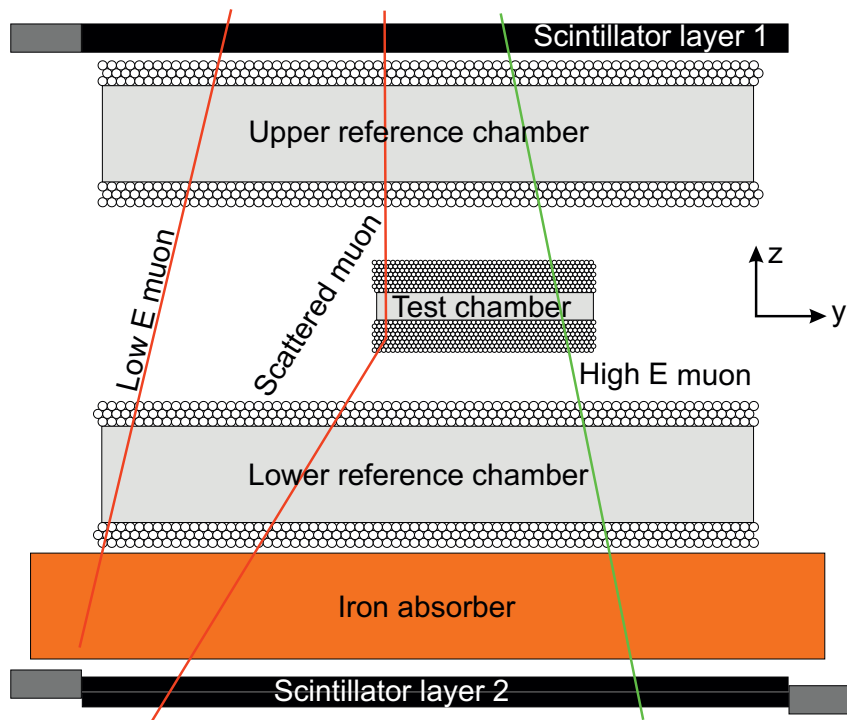


**Figure 7.1:** The cosmic ray test setup in the  $y$ - $z$  plane. Muons with a momentum of less than  $600 \text{ MeV}/c$  are stopped in the iron absorber.

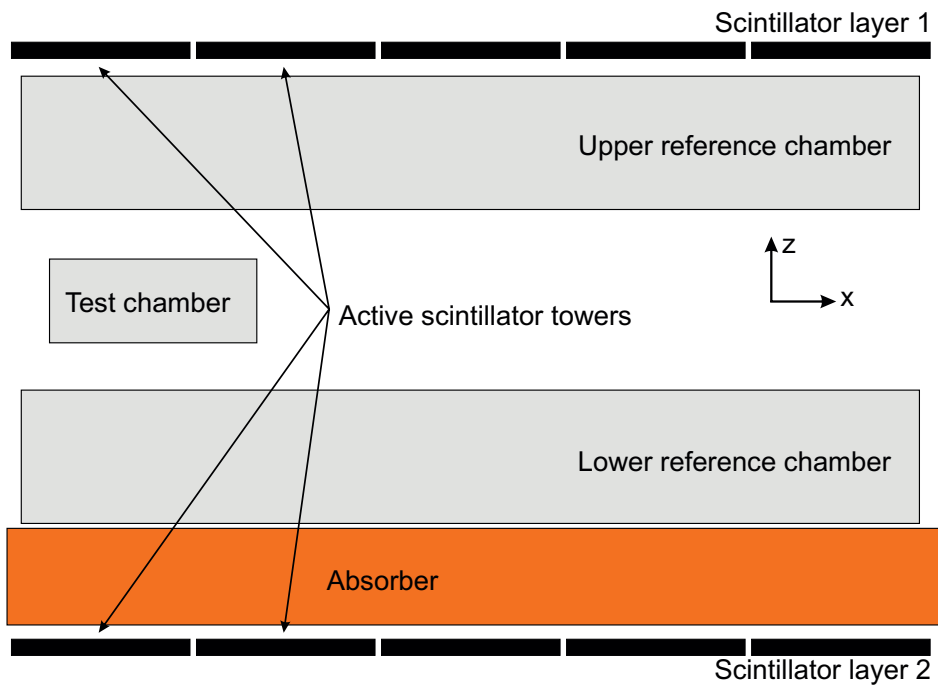


**Figure 7.2:** View of the cosmic ray test setup the  $x$ - $z$  plane. The 5 trigger towers are visible.

**Table 7.1:** Monte-Carlo data sets used for studying the teststand data analysis.

Dataset	Events	Energy distribution	$E_{\min}$	$E_{\max}$
<b>Cosmic</b>	$6.0 \cdot 10^6$	$1/E^2$	100 MeV	100 GeV
<b>Flat</b>	$733 \cdot 10^3$	1	100 MeV	100 GeV

for the implementation of the detector geometry [Kor02].

In addition to the detector components also 4 debugging planes are included in the simulation where the information for each particle crossing them is recorded. This information contains particle identification and energy and the three dimensional velocity vector. The data from the debug planes is used to reconstruct and select the muons tracks in the teststand and to study multiple scattering effects depending on the muon energy.

Two different data sets were used as described in Table 7.1. The difference between the two data sets is the initial momentum distribution for the incoming muons. In the first data set data set a  $1/E^2$  dependence was used, close to the energy distribution of cosmic muons.

The second data set has a flat energy distribution between 100 MeV and 100 GeV. This data set contains a much higher number of high-energy muons and was used to understand the multiple scattering effects also for higher muon energies and to optimize the reconstruction algorithm for straight tracks.

### 7.2.1 Muon Momentum Selection

To minimize track extrapolation errors due to multiple scattering, the measured deflection angle between the two reference chambers in the plane perpendicular to the drift tubes is used. From the simulated data sets, the relation between muon momentum and scattering angle is determined to find a suitable cut on the scattering angle to select high momentum muons and minimize the multiple scattering uncertainty.

Using the debug information the true scattering angle of a muon track  $\Delta m_{\text{MC}}$  can be determined. The measured angle  $\Delta m_{\text{fit}}$  is calculated from the difference of the slopes of reconstructed track segments in the two reference chambers. Figure 7.3 shows the difference  $\Delta m_{\text{MC}} - \Delta m_{\text{fit}}$  between the measured and the expected scattering angle from the MC simulation, between the reference MDT chambers in the teststand. The width of the distribution is a measure of the angular resolution of the teststand. A Gaussian fit to the central region of the distribution gives a standard deviation of  $\sigma = 0.46$  mrad. Tracks for the wire position measurement are selected in a  $\Delta m_{\text{fit}}$  window of  $1.6\sigma$  around zero with an efficiency of 49.6% both in the data and in the cosmic Monte-Carlo simulation.

## 7.3 Wire Position Determination

### 7.3.1 Event Selection

To determine the wire positions in the prototype chamber, the distances of the wires from the track extrapolated from the reference chambers are compared to the measured drift radii in the test chamber. Events fulfilling the following criteria are selected:

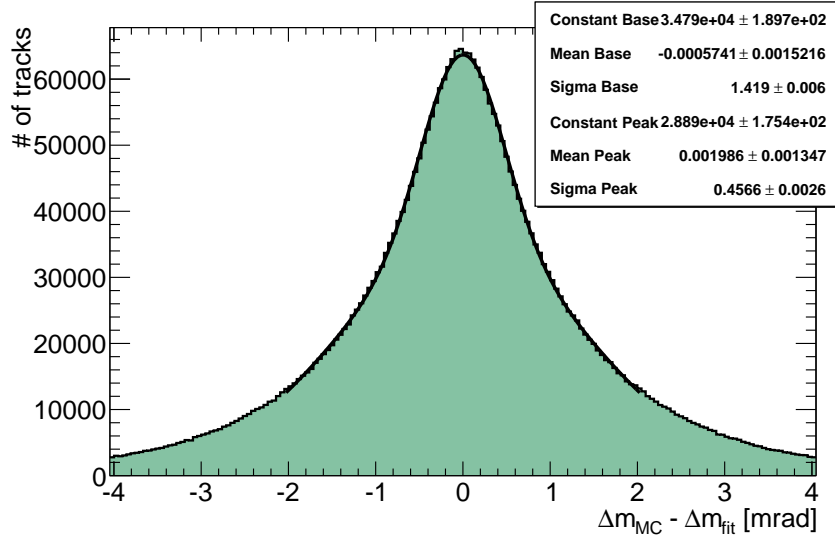


**Figure 7.3:** Difference between the scattering angles between the reference MDT chambers in the teststand from Monte-Carlo prediction ( $\Delta m_{MC}$ ) and from measurement ( $\Delta m_{fit}$ ).

- hits in the scintillator hodoscope allowing for a second coordinate measurement,
- reconstructed track segments in both reference chambers,
- Scattering angle of the muon  $\leq 1.6 \cdot 0.46 \text{ mrad} = 0.74 \text{ mrad}$ .

The detailed cut flow is shown in Figure 7.4 for the cosmic MC data set and the experimental data. The strictest requirement is the scattering angle cut. A track in the test chamber is not required because the track from the reference chambers are only compared with hits in individual tubes of the prototype chamber. Tracks in the test chamber are, however, needed for the alignment of the test chamber with respect to the reference chambers as discussed in section 7.4.2.

The difference between data and MC in the efficiencies of the hodoscope hits and the track in the second reference chamber requirements can be explained by the slightly different trigger requirements in the MC simulation. Muons without hit in the bottom scintillator layer are accepted in the simulation and the angular distribution of good MC muons tracks is slightly different from the data, resulting in additional tracks missing the second reference chamber.

### 7.3.2 Wire Position Reconstruction

The wire displacements in the  $y$ - $z$  plane perpendicular to the tubes from the expected positions are defined as (see Figure 7.5):

$$\delta_y = y_m - y_e \quad \text{and} \quad \delta_z = z_m - z_e, \quad (7.1)$$

$d_e$  and  $d_m$  are the distances of the track to the expected and to the measured wire coordinates  $(y_e, z_e)$  and  $(y_m, z_m)$ , respectively. The drift radius  $r_m$  determined from the measured

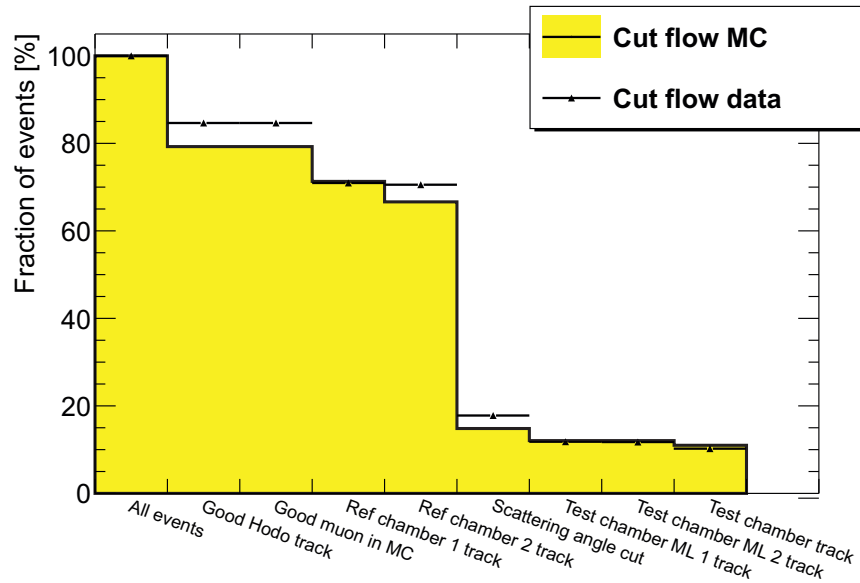


**Figure 7.4:** Comparison of the cut flows for the cosmic MC events set and the data taken with the test cosmic ray teststand. The last step of the event selection is the cut on the scattering angle, the amount of tracks in the test chamber is only shown for comparison.

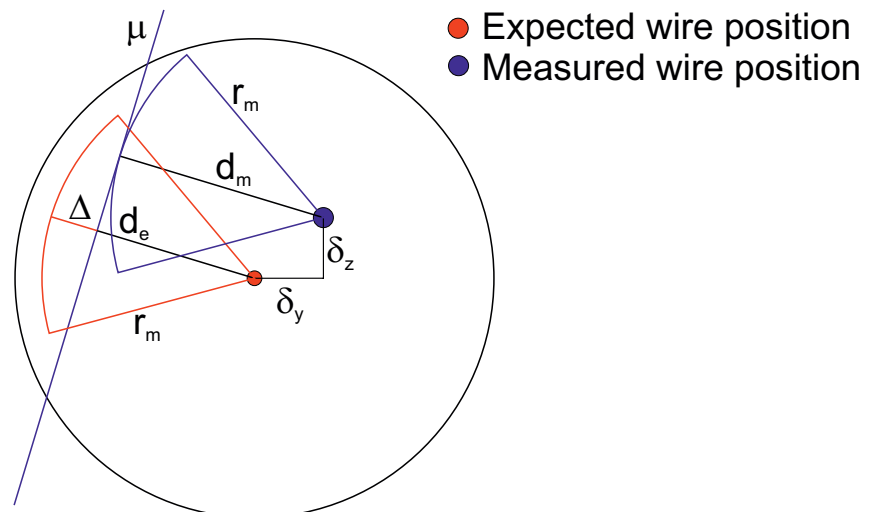


**Figure 7.5:** Effect of wire displacement on the track coordinate measurement. The drift radius  $r_m$  is determined from the measured drift time (see text).

drift time gives the absolute value of  $d_m$ :  $|d_m| = r_m$ . The track residual is defined as

$$\Delta = |d_e| - |d_m| = |d_e| - r_m . \quad (7.2)$$

A straight track in the  $y$ - $z$ -plane is parametrized by  $y = mz + b$ . The expected drift radius  $r_e$  for a wire with expected position  $(y_e, z_e)$  is the distance of closest approach of the track to the wire given by

$$d_e = \frac{b + mz_e - y_e}{\sqrt{1 + m^2}} . \quad (7.3)$$

Similarity for the measured drift radius:

$$d_m = \frac{b + mz_m - y_m}{\sqrt{1 + m^2}} . \quad (7.4)$$

$d_e$  and  $d_m$  are positive for tracks on the right-hand side of the wire ( $y > 0$ ) and negative for tracks on the left-hand side ( $y < 0$ ).

To simplify the equations, only vertical tracks with track angle  $\alpha < 0.05$  rad are selected and therefore  $1 + m^2 \approx 1$ . Inserting equations (7.3) and (7.4) into equation (7.2) and using equation (7.1) results in

$$\Delta = |d_e| - |d_m| = (y_m - y_e) - m(z_m - z_e) = \delta_y - m\delta_z . \quad (7.5)$$

Since  $\delta_z$  is multiplied by  $m$ , its contribution to  $\Delta$  is very small and  $\delta_y$  and  $\delta_z$  can be determined independently. To measure the positions of the wires at both ends of the tubes it is necessary to separate the events according to the  $x$  position in the chamber and skip events with muon tracks close to the middle of the tubes. This will reduce the available statistic to less than 1/3 for each wire end compared to using all events for the measurement. But the necessary accuracy of better than  $6 \mu\text{m}$  for a wire is only achievable when using all available data (see Sec. 7.4). For this reason all data available for a single tubes are combined. The measured displacement is therefore a convolution of both displacements on the two wire ends. The measured resolution for one wire is therefore  $\sqrt{2}$  times larger than for only one wire end.

### 7.3.3 Horizontal Wire Positions

There are two methods for determining the wire displacements:

- A From the shift of the residual distribution .
- B From the shift of the V-Plot: measured drift-time vs. expected drift radius.

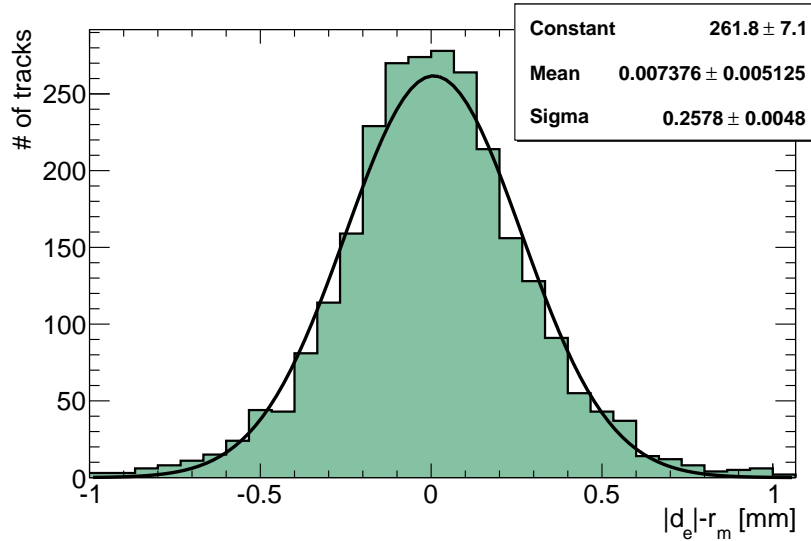


**Figure 7.6:** Track residual distribution for one tube in the Monte-Carlo simulation. The shift of the distribution is determined from a Gaussian fit.

### Method A: Residuals

Because of the selection of vertical tracks the mean of the distribution of the residuals in Equation (7.5) can be approximated by ( $\langle m \rangle \approx 0$ ):

$$\langle \Delta \rangle = \langle |d_e| - |d_m| \rangle = \langle \delta_y - m\delta_z \rangle \approx \langle \delta_y \rangle \quad (7.6)$$

The shift of the residual distribution is determined using a peak finding algorithm [ROO] and then fitting a Gaussian in order to refine the mean value. The residual distribution for a typical tube in the Monte-Carlo simulation is shown in Figure 7.6.

For Monte-Carlo data without wire displacement, the mean of the measured displacements for all 1152 tubes with respect to the wire positions used in the simulation in the prototype chamber is  $(-0.4 \pm 0.17) \mu\text{m}$  with a resolution of  $(5.7 \pm 0.13) \mu\text{m}$  (see Fig. 7.9) for the combination of both wire ends, equivalent to  $(4.0 \pm 0.1) \mu\text{m}$ .

### Method B: V-Plot

Plotting the expected track distance to the wire  $d_e$  against the measured drift time  $t$  results in a V-shaped plot (see Fig. 7.8). Since the  $r(t)$  relationship is not linear, only the central part of the plot is fitted with a linear function

$$t(d_e) = s |d_e - \delta_y| + t_0, \quad (7.7)$$

neglecting again  $\delta_z$  and determining  $\delta_y$  as the shift of the V-shaped function. The slope  $s$  is proportional to the inverse of the drift velocity.  $t_0$  is an offset.

The accuracy of this method is not as good as the one of method **A**, but it provides a good cross check. While method **A** is optimal for small wire displacements, large displacements are easier spotted with method **B** providing the starting values for method **A**.

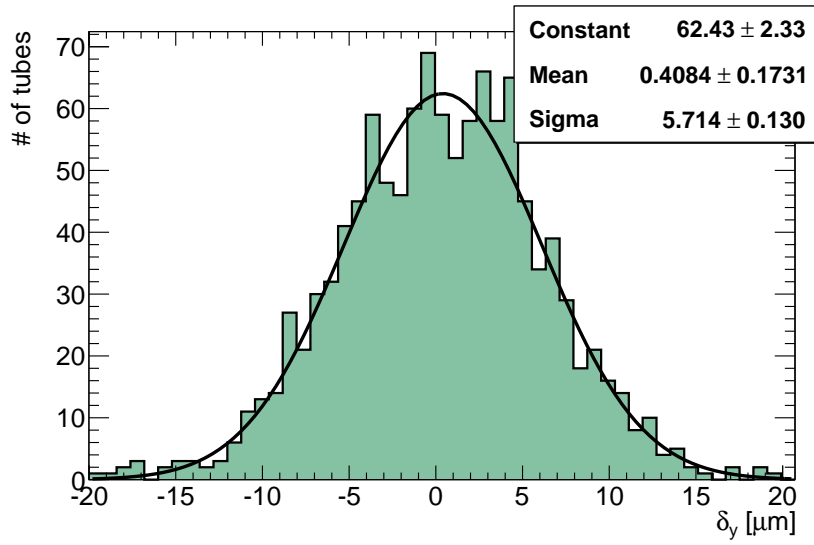


**Figure 7.7:** Distribution of  $\delta_y$ , the horizontal wire displacement, for Monte-Carlo data with ideal wire positions.

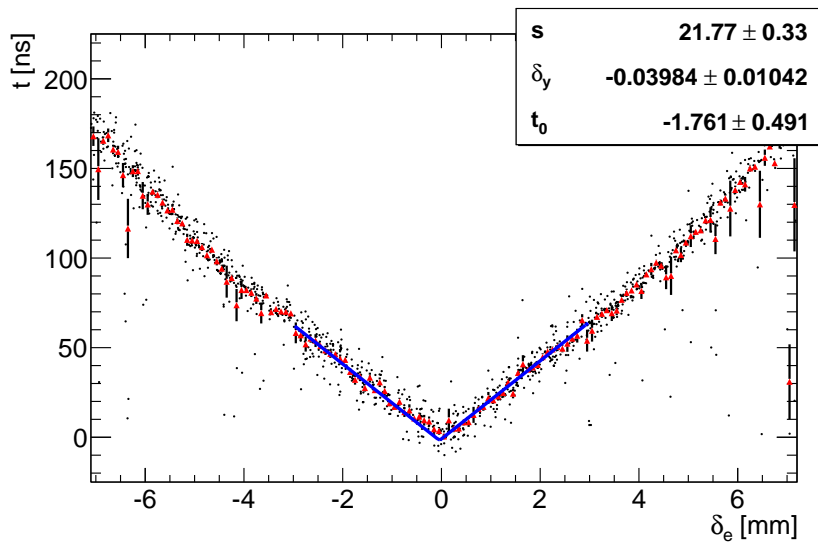


**Figure 7.8:** V-Plot for a tube with no displacement. The red dots are the mean values for slices along the  $t$  axis.

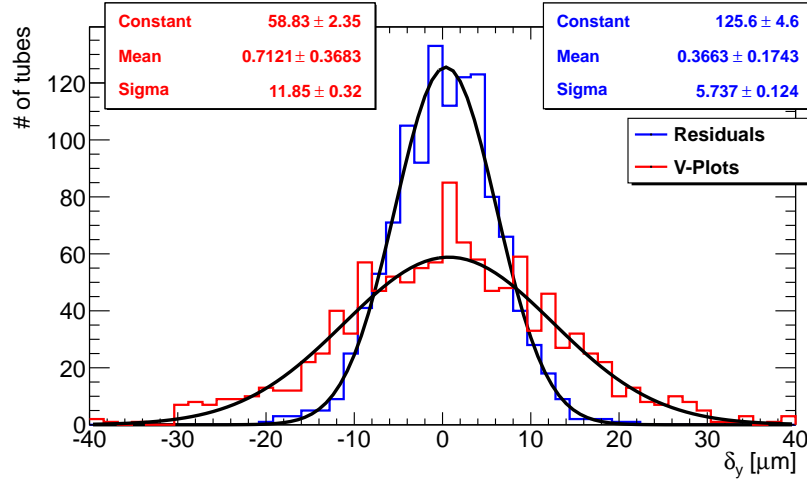


**Figure 7.9:**  $\delta_y$  distributions from method **A** (left fit parameters) and **B** (right fit parameters)

For MC data without wire displacement the mean value of the displacements for all tubes is  $(-0.7 \pm 0.37) \mu\text{m}$  with a resolution of  $(11.9 \pm 0.32) \mu\text{m}$ .

Figure 7.10 shows the distributions of the difference between the wire displacements determined with method **A** and **B**:

$$\Delta\delta_y = \delta_{y,A} - \delta_{y,B} \quad . \quad (7.8)$$

There is no systematic offset between the two methods. In the following method **A** is used to measure  $\delta_y$  and method **B** is only used as cross check. If the difference between the two results is larger than  $50 \mu\text{m}$ , tube is marked and checked separately.

### Monte-Carlo Performance Tests

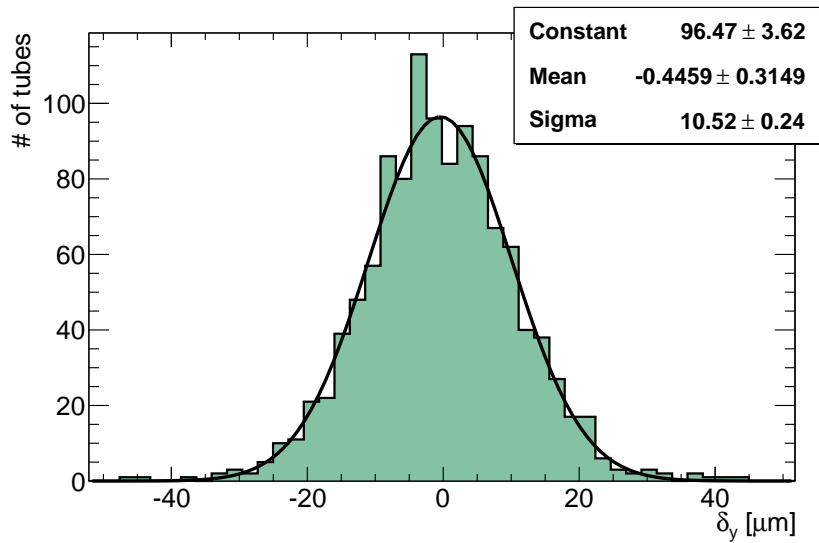
Figure 7.11 shows MC performance tests of the  $\delta_y$  reconstruction algorithm. Artificial shifts in the wire  $y$  coordinate were introduced and the observed  $\delta_y$  compared to the expectation. Induced and reconstructed wire displacements agree perfectly within the measurement errors (see Fig. 7.11(a)).

Figure 7.11(b) shows the effect of vertical wire displacements up to  $\delta_z = 1 \text{ mm}$  on the  $\delta_y$  measurement. As expected there is no dependence of the results on  $\delta_z$ .

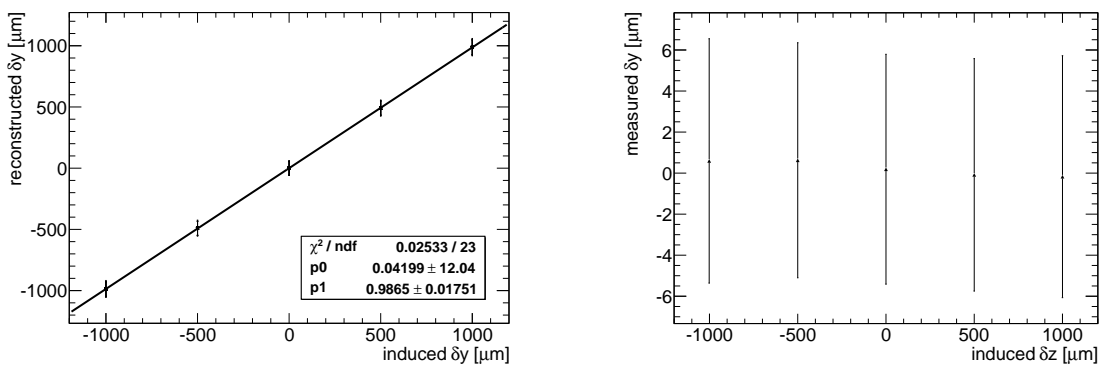
### 7.3.4 Position in vertical direction

To measure the displacement in  $z$  direction, the  $\delta_z$  dependence of the residuals in Equation (7.5) is used. For this analysis no cut on the slope of the muon track is applied to maximise the sensitivity for  $\delta_z$ . Plotting the residuals  $\Delta$  against the slope  $m$  of the muon track and fitting the data points with a linear function allows for extracting  $\delta_z$ .  $\delta_z$  is the slope of the fitted function and  $\delta_y$  the offset which is corrected for. An example of a fit for one tube layer is shown in Figure 7.12(a). The correct position in  $y$  direction is verified if  $\delta_y = 0$  within the errors of the fit.

To test the resolution of the  $\delta_z$  reconstruction the algorithm is applied to MC data with a perfectly aligned wire grid. The width of the  $\delta_z$  distribution is about  $\sigma(\delta_z) = 30 \mu\text{m}$ , not as



**Figure 7.10:** Difference between the wire displacements  $\delta_y$  determined with the two methods using 717837 MC events for 1152 tubes.



(a) Linearity and accuracy of  $\delta_y$  reconstruction (errors multiplied by a factor of 10).

(b) Effect of  $z$  displacements on the  $\delta_y$  measurement.

**Figure 7.11:** Accuracy and robustness of  $\delta_y$  reconstruction from MC simulation.

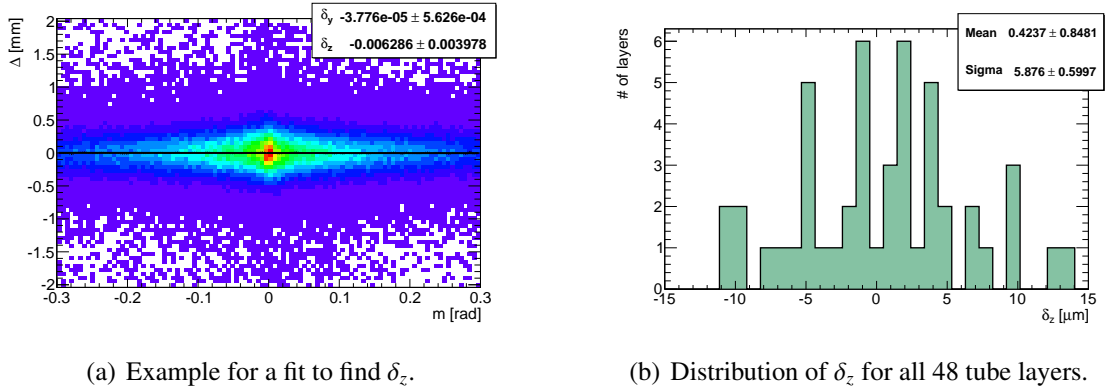


**Figure 7.12:** (a) shows a typical fit to find  $\delta_z$  for a tube layer of MC simulation data and expected wire positions. To measure the resolution of the  $\delta_z$  finding algorithm the value is determined for all 48 tube layers (16 layers in 3 sectors) (b) with respect to the true wire positions and the width of the distribution is determined.

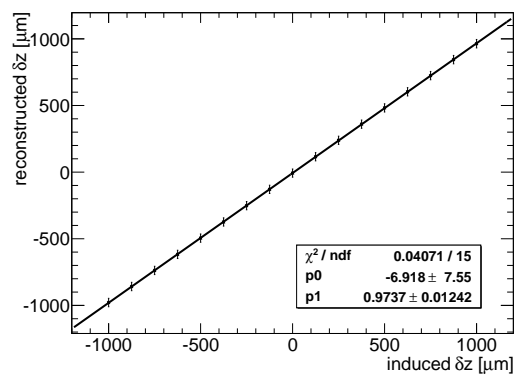


**Figure 7.13:** Linearity and accuracy of  $\delta_z$  reconstruction.

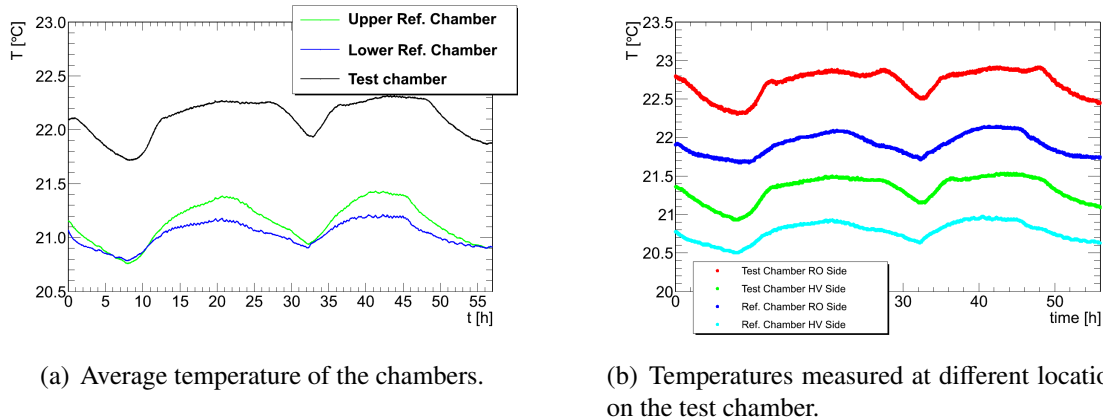


**Figure 7.14:** Temperature measurements in the test-stand as a function of time during the data taking run.

good as for the  $y$  displacements. To improve the accuracy, the average wire displacement for a complete tube layer per section is measured, resulting in a resolution of  $6\ \mu\text{m}$  for 24 tubes combined (see Fig. 7.12(b)).

To test the performance of the  $\delta_z$  reconstruction artificial wire shifts in  $z$  direction were introduced in the MC simulation and reconstructed. The results are shown in Figure 7.13 and prove the good performance of the algorithm.

## 7.4 The Cosmic Ray Data

After the validation of the performance of the algorithm using the Monte-Carlo simulation the experimental data was analysed. Here, in addition, the  $r(t)$  relations of the reference chambers and the test chamber have to be calibrated.

The wire position measurement is based on a data set of 6.0 M triggers during a period with stable operating and environmental conditions. The test chamber is the prototype chamber described in the previous chapter. Due to time constraints it was not possible to equip the whole chamber with readout electronics. Therefore only the tubes in the middle and long tube sectors ( $2\ \text{sectors} \times 16\ \text{layers} \times 24\ \text{tubes per layer} = 768\ \text{tubes in total}$ ) are connected to the readout. The short tubes present in the MC simulation are not included in the analysis.

The average temperatures of the three chambers are shown in Figure 7.14(a), as a function of time. Day–night variations are clearly visible but are no larger than  $0.5^{\circ}\text{C}$ . The rather large temperature difference of about  $2^{\circ}\text{C}$  between the reference chambers and the test chamber can be understood by a more detailed study of the temperature distribution on the test chamber. For the MDT chambers the tubes are warmer on the read-out side compared to the high-voltage side. This effect is most prominent for the test chamber (see Fig. 7.14(b)), since the electronics is much denser.

The signal travel time along the wire to the readout electronics is determined using the second coordinate information from the trigger hodoscope. The second coordinate resolution is only about 5 cm due to the width of the scintillators of 9 cm, but it is enough to achieve a time resolution of better than 0.3 ns.

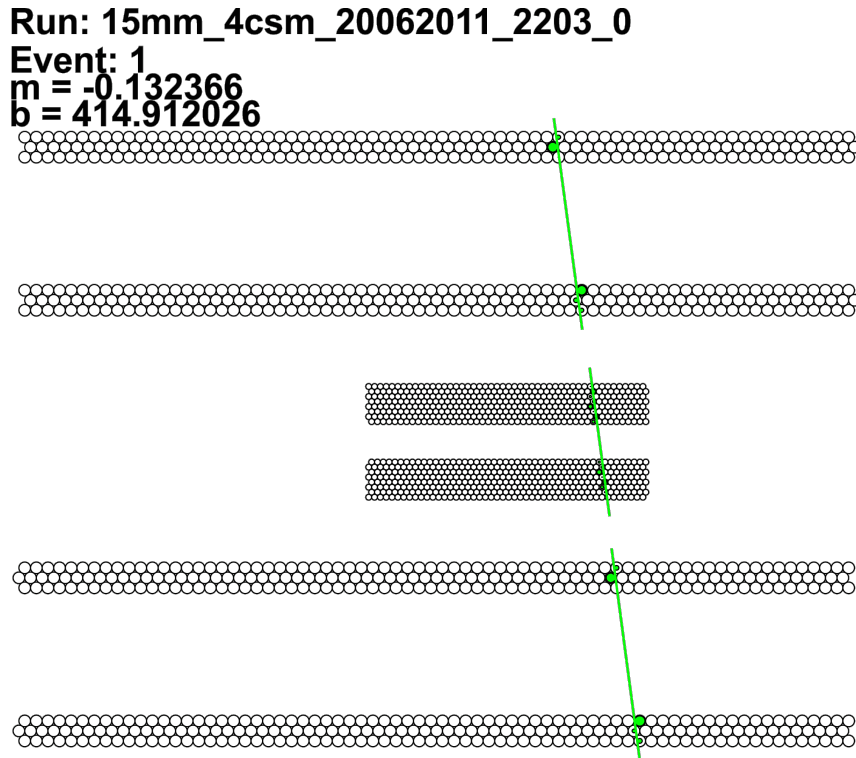


**Figure 7.15:** Event display of a cosmic muon track reconstructed in all three chambers.

### 7.4.1 Drift Tube Calibration

To minimize the influence of temperature variations on the  $r(t)$  relation, the calibration was performed separately for small subsets of the data containing 50 000 triggers in time intervals of approximately 500 s. This corresponds to 15 000 tracks in the reference chambers and more than 5 000 tracks in the smaller test chamber fulfilling the quality criteria. To avoid an influence of potential misalignment and temperature gradients between the two multi-layers of the test chamber, they are calibrated separately.

A test of the performance of the calibration is the flatness of the track-residual distribution as a function of the drift-radius (see section 4.4.3).

The flatness clearly improves after the calibration allowing for reliable and precise track reconstruction. The offset close to the wire is due to geometrical restraints because the drift radius can not be less than zero.

### 7.4.2 Alignment of the Chambers

Using the tracks reconstructed in the teststand, relative rotations and displacements of the chambers can be determined. The relative positions of the reference chambers were determined before and after the data taking with an optical alignment system showing no significant movement between the two measurements. The test chamber mounting frame blocked the optical paths such that alignment monitoring was not possible during the run. Stable relative position of the reference chambers during the whole data taking period is assumed.

The chamber alignment is measured by comparing track segments reconstructed in the three chambers as described in section 4.3. As an example, the rotations around the  $z$  axis are discussed in more detail. One can see in Figure 7.17(a) that the difference  $\Delta$

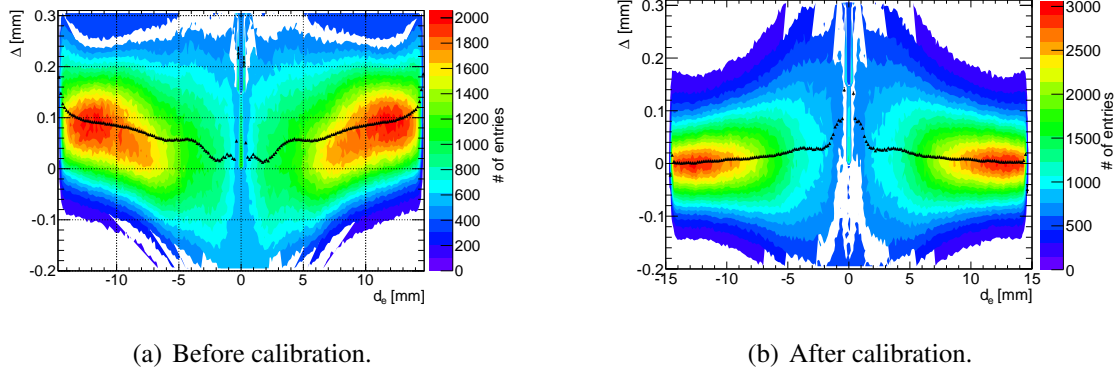


**Figure 7.16:** Track residuals  $\Delta$  as a function of the track distance  $d_e$  to the wire for the bottom reference chamber before and after the  $r(t)$  calibration.

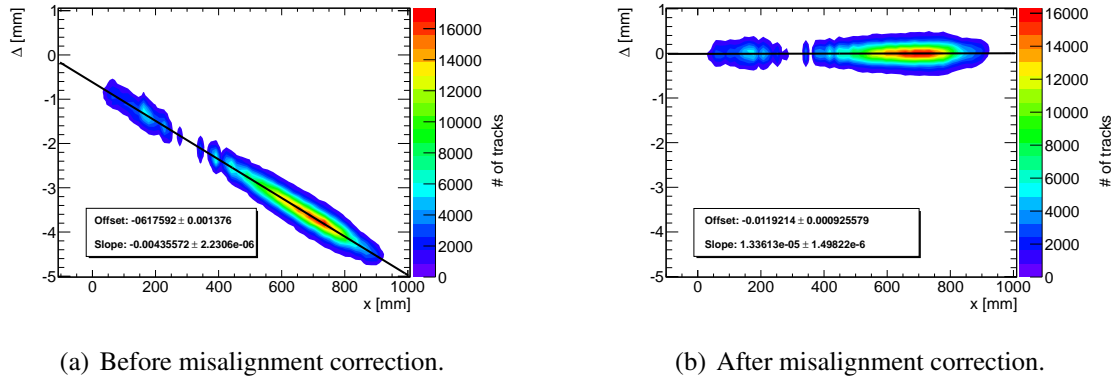


**Figure 7.17:** Measurement and correction of a relative rotation of the test chamber with respect to the reference chambers around the  $z$  axis resulting in a  $x$ -dependent  $y$ -displacement of the wires (see text).

between the reconstructed track position  $y_{\text{ref}}$  extrapolated from the reference chambers into the test chamber and the track position  $y_{\text{test}}$  measured in the test chamber depends linearly on the  $x$  position of the track indicating a relative rotation in the horizontal plane. The maximum deviation over the whole length of the test chamber of 1 m is about  $\Delta_{\text{max}} \approx 4$  mm, corresponding to a rotation angle of about 4 mrad.

After this alignment corrections to the chamber position the residuals are flat over the whole  $x$  range (see Fig. 7.17(b)). The gap in Figure 7.17 for  $225 \text{ mm} < x < 375 \text{ mm}$  is caused by an acceptance gap of the trigger scintilators.

The relative chamber position in  $x$  direction with respect to the hodoscope are needed only with lesser resolution of about 1 cm. They were measured mechanically during the installation of the chambers in the teststand.

After misalignment corrections, all relative rotations are below 0.04 mrad (see Figure 7.18) and all relative shifts in  $y$  direction below  $20 \mu\text{m}$ . The alignment in  $z$  direction can only be measured with a rather large uncertainty of  $100 \mu\text{m}$  using the track based method (see section 4.3) but has also little influence on the track reconstruction. The  $z$  position of the test chamber relative to the reference chambers is investigated in more detail in section 7.5.1.

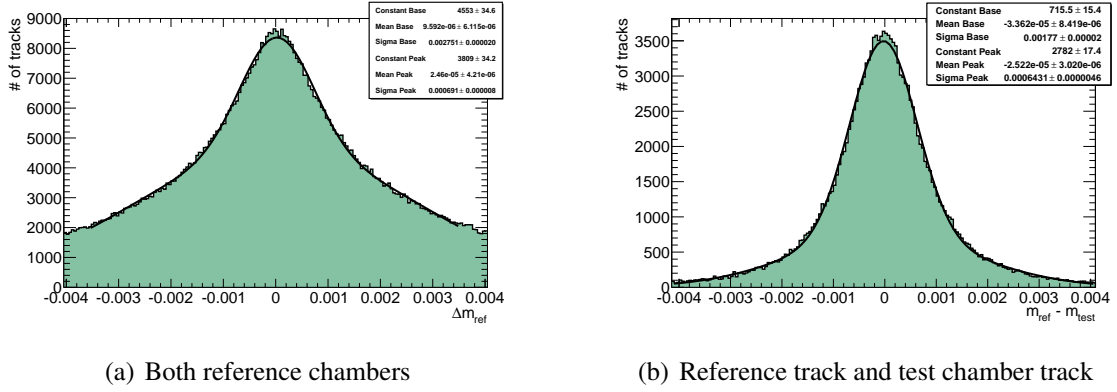


**Figure 7.18:** Relative Rotation around the wire axis (see text).

## 7.5 Horizontal Wire Coordinate Reconstruction

The distributions of the residuals  $\delta_y$  of the measured horizontal wire coordinates with respect to the expected values are shown in Figure 7.19 for the four sectors of the test chamber equipped with readout electronics (see Section 7.4), and in Figure 7.20 for all tubes together.

After the measured position correction is applied to each wire and the displacements of the wires with respect to their measured position are calculated. The width of the  $\delta_y$  distribution (Fig. 7.20) is now  $(5.93 \pm 0.22) \mu\text{m}$  and has within errors the same width as the Monte-Carlo prediction for a perfect alignment of the wires and chambers. Also the distribution of the residuals shows no more dependence on the  $y$  coordinate of the corresponding tube. This proves that the algorithm performs at the desired level of accuracy of better than  $5 \mu\text{m}$  for a single wire end also on the real data.

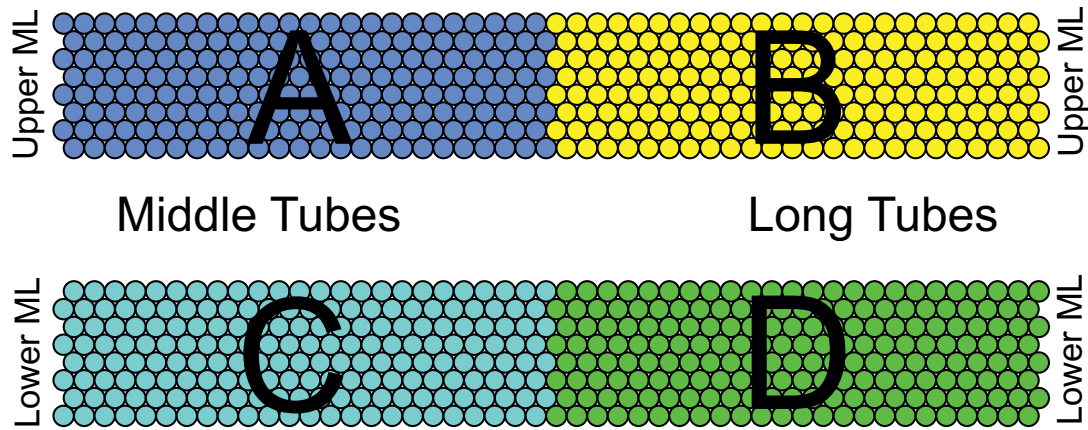
### 7.5.1 Horizontal Wire Grid Reconstruction

The plots in Figure 7.21 show a dependence of  $\delta_y$  on the horizontal position of the tube in the chamber. This is due to deviations of the measured wire grid from the expected grid. The position of a wire  $y_i(y_{0,e}, d_{y,e}, y_{\text{skipp},e})$  in the expected initial grid is calculated from the design parameters (see Fig. 7.22):

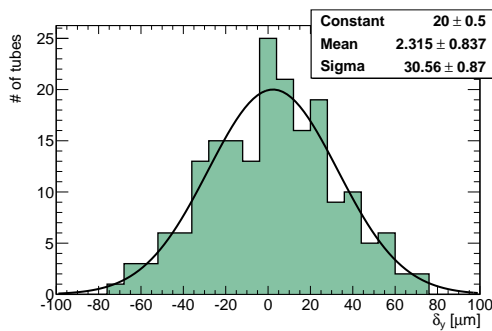
Parameter	Value	Description
$y_{0,e}$	0 mm	$y$ coordinate of the origin (global position with respect to the reference chambers)
$d_{y,e}$	15.10 mm	Wire pitch $y$ direction
$y_{\text{skipp},e}$	7.55 mm	$y$ shift between adjacent tube layers

The wire pitch  $d_{y,e}$  is derived from the outer radius of the tube of  $r_o = 15.0 \text{ mm}$  and a glue gap of  $100 \mu\text{m}$  between the tubes in the chamber. The displacement between two adjacent tube layers  $y_{\text{skipp}}$  is half of the wire pitch.

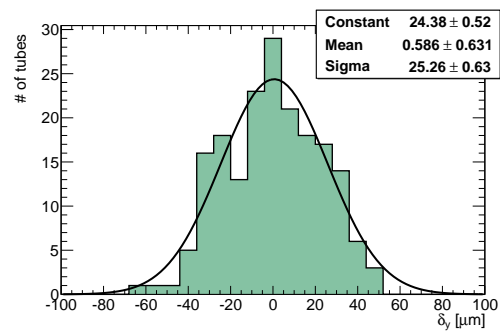
The fit is performed by the Minuit 2 program [MIN] implemented in the ROOT framework [ROO]. The measured wire grid minimizing the  $\chi^2(d_y, d_z, y_{\text{skipp}})$  achieved during



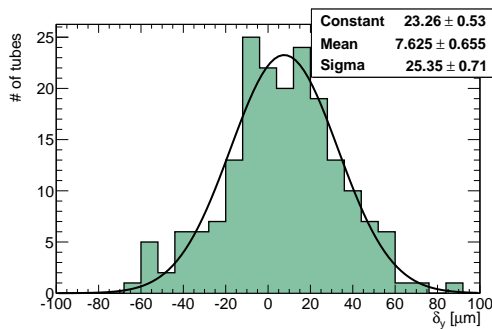
(a) Different sectors of the chamber.



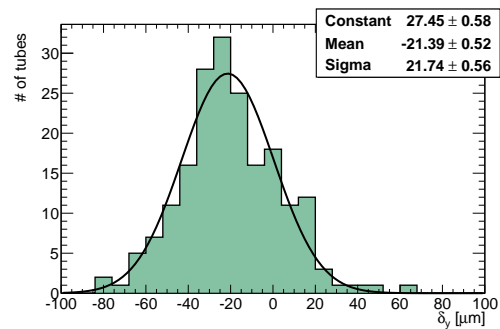
(b) Sector A: middle sector, upper ML.



(c) Sector B: long sector, upper ML.



(d) Sector C: middle sector, bottom ML.



(e) Sector D: long sector, bottom ML.

**Figure 7.19:** Measured residuals  $\delta_y$  with respect to the expected wire y-positions for the four sectors of the test chamber equipped with readout electronics.

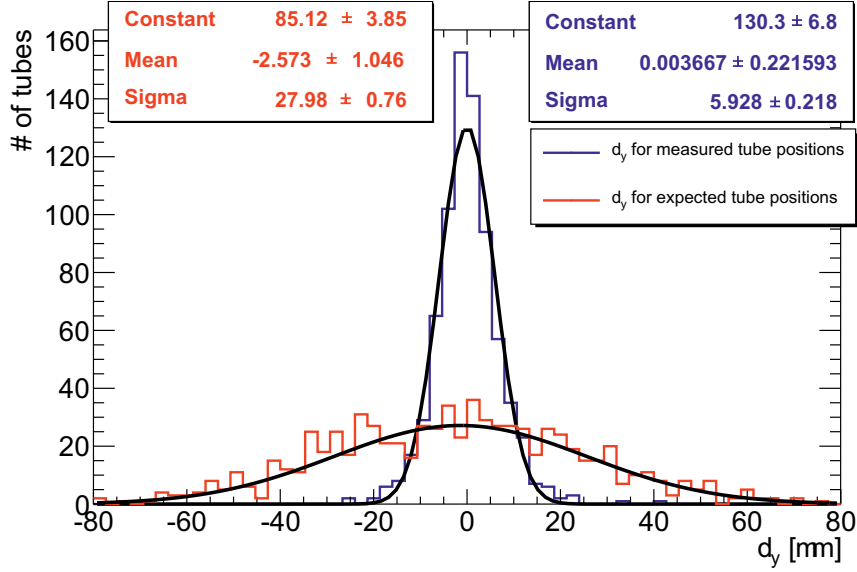


**Figure 7.20:** Residuals  $\delta_y$  distribution for all tubes in the test chamber derived from the expected and measured tube positions, respectively. The width of the distribution derived from the measured tube positions is  $\sigma_m = 5.93 \pm 0.22 \mu\text{m}$  (equivalent to the MC prediction, cp. fig. 7.7) and is limited by the performance of the teststand.

chamber assembly is determined by using the  $\chi^2$  function for

$$\chi^2(y_0, d_y, y_{\text{skipp}}) = \sum_{i=1}^{N_{\text{wires}}} \left( \frac{y_i(y_0, d_y, y_{\text{skipp}}) - y_{i,m}}{\sigma_{y,i}} \right)^2. \quad (7.9)$$

with the measured wire position  $y_{i,m} = y_{i,e}(y_0, d_y, y_{\text{skipp}}) + \delta_{y,i}$ . The errors  $\sigma_{y,i}$  for the individual wire  $y$  positions measurements are assumed to be equal and are estimated from the Monte-Carlo simulation and experimental data to be about  $6 \mu\text{m}$ . Only for outlying wires with very large displacement the error is adjusted. If a wire is displaced by more than  $250 \mu\text{m}$ , the error is scaled up by a factor of 100 to avoid a bias of the grid fit due to this tube. The results for the middle tube sectors are:

Parameter	Upper ML	Lower ML
$y_0$	$2.7 \pm 7 \cdot 10^{-4} \text{ mm}$	$0.4 \pm 3 \cdot 10^{-4} \text{ mm}$
$d_y$	$15.1021 \pm 1.6 \cdot 10^{-4} \text{ mm}$	$15.1009 \pm 1.5 \cdot 10^{-4} \text{ mm}$
$y_{\text{skipp}}$	$7.557 \pm 5 \cdot 10^{-4} \text{ mm}$	$7.550 \pm 2 \cdot 10^{-4} \text{ mm}$

For the sectors with long tubes the fitted parameters are very similar:

Parameter	Upper ML	Lower ML
$y_0$	$54.7 \pm 5 \cdot 10^{-4} \text{ mm}$	$56.8 \pm 6 \cdot 10^{-4} \text{ mm}$
$d_y$	$15.1026 \pm 1.0 \cdot 10^{-4} \text{ mm}$	$15.1017 \pm 2.4 \cdot 10^{-4} \text{ mm}$
$y_{\text{skipp}}$	$7.550 \pm 3 \cdot 10^{-4} \text{ mm}$	$7.543 \pm 3 \cdot 10^{-4} \text{ mm}$

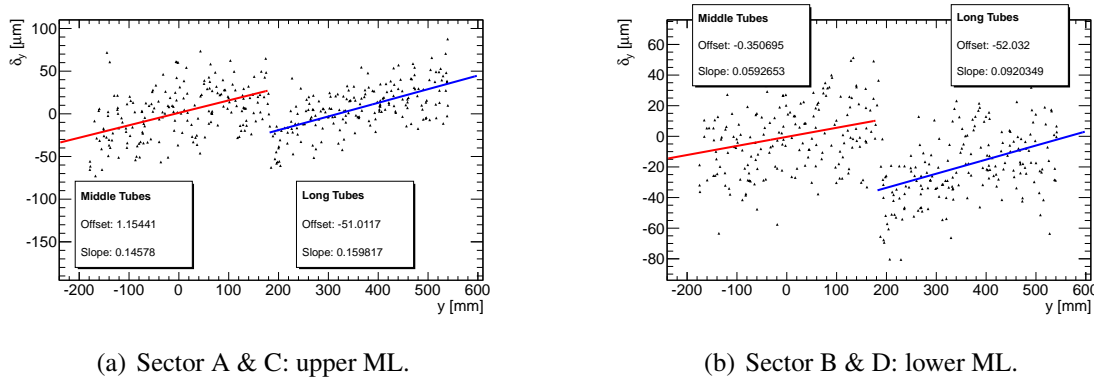


**Figure 7.21:** Residuals  $\delta_y$  as a function of the  $y$  position.

One obvious difference is found in the value of the  $y_0$  parameter. There is a systematic shift of  $55 \mu\text{m}$  of both multilayers in the long sector away from the middle sector. It can be explained by a misplacement of the combs holding the tubes during glueing which are mounted on the granite table separately for each chamber sector (see section 6.2).

The residual distributions for each sector with respect to the fitted grid are shown in Figure 7.23. They are distributed around zero and the widths are considerable smaller than the residuals with respect to the expected grid in Figure 7.19. The upper multilayer shows significantly larger residual width than the lower multilayer in both sectors. The upper ML has been assembled first. It is possible that the second multilayer has higher accuracy because of more experience with the assembly procedure. In particular it is important not to disturb the tube positions during the insertion of the ground pins.

Figure 7.24 shows the residual distributions with respect to the expected and the fitted wire grid combined for all sectors with a width of  $(28.0 \pm 0.8) \mu\text{m}$  and  $(22.4 \pm 0.6) \mu\text{m}$ , respectively. Calculating the positioning accuracy width of only one wire ends gives a positioning accuracy of  $(19.8 \pm 0.8) \mu\text{m}$  with respect to the expected wire grid and  $(15.8 \pm 0.6) \mu\text{m}$  with respect to the fitted grid (see Sec. 7.3.2).

## 7.5.2 Vertical Wire Grid Reconstruction

The vertical wire grid in  $z$  direction is determined by similar parameters as the horizontal grid (see Fig. 7.22):

Parameter	Value	Description
$z_{0,e}$	0.0 mm	$z$ coordinate of the origin (with respect to the reference chambers)
$d_{z,e}$	13.077 mm	Wire pitch in $z$ direction
$s_e$	90.4 mm	Spacer height between the two multilayers (distance between the innermost tube walls)

The expected wire pitch in  $z$  direction for the densest tube package is given by  $d_{z,e} = \sqrt{3}/2 \cdot d_{y,\text{initial}} = 13.077 \text{ mm}$ . The measured track distance to the wires contains information about the  $z$  coordinates of the wires once the  $y$  coordinates have been determined (see previous sections) and are fixed. In addition to the origin and the wire pitch also the vertical separation between the two multilayers, the spacer height  $s$ , can be determined for each sector.

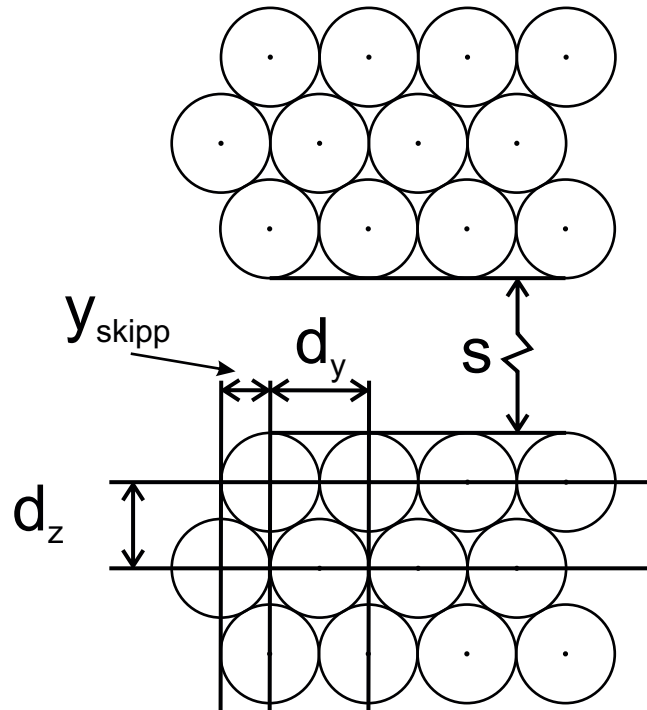
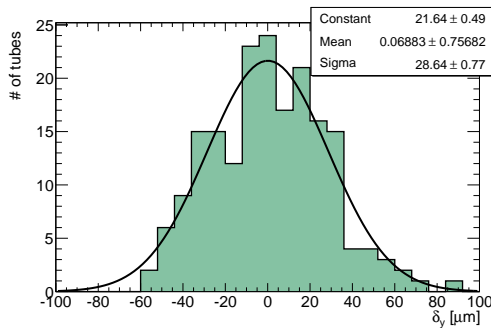
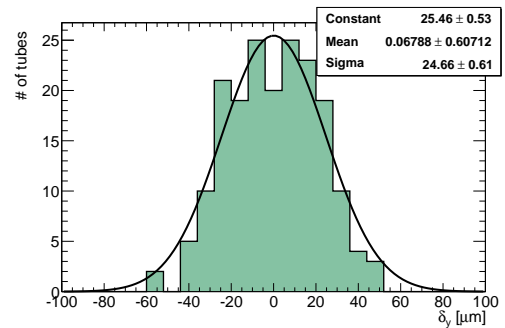


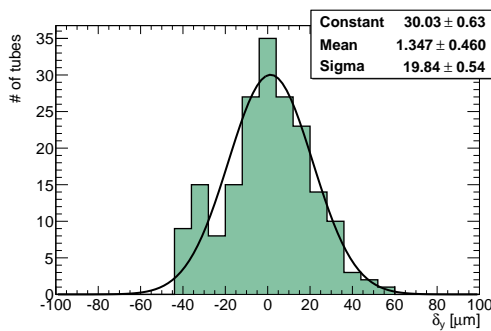
**Figure 7.22:** The wire grid in the MDT chambers is determined by four parameters: the horizontal and vertical wire pitch  $d_y$  and  $d_z$ , the relative horizontal displacement of the tube layers  $y_{\text{skipp}}$  and  $s$ , the width of the spacer between the two multilayers.



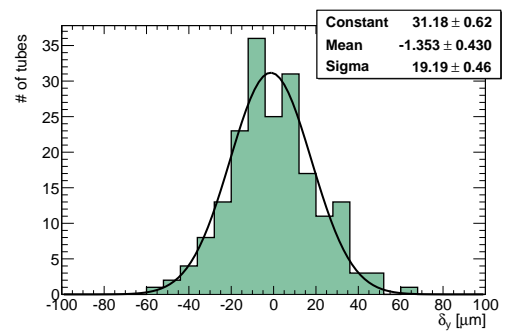
(a) Sector A: middle sector, upper ML.



(b) Sector B: long sector, upper ML.



(c) Sector C: middle sector, lower ML.



(d) Sector D: long sector, lower ML.

**Figure 7.23:** Residuals of the wire  $y$  coordinates with respect to the reconstructed wire grid in the four test chamber sectors.

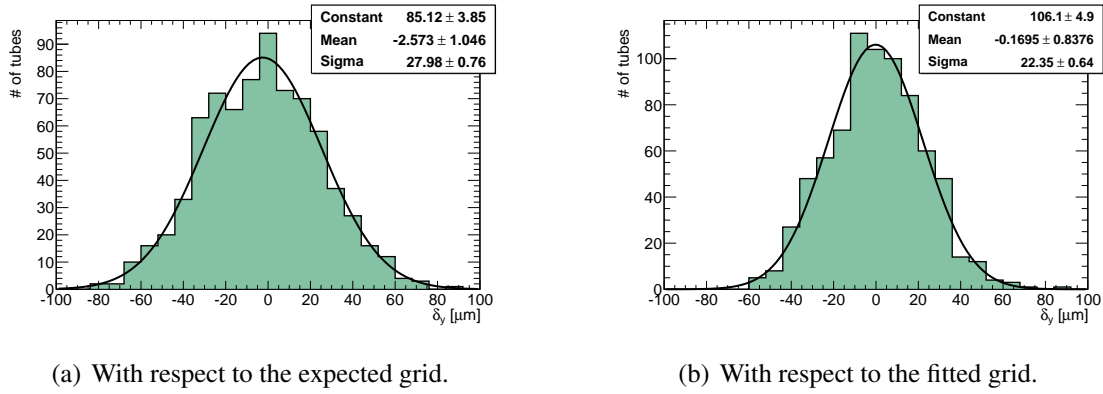


**Figure 7.24:** Residuals  $\delta_y$  of all wire positions with respect to the expected grid (a) and with respect to the fitted grid (b).

The grid is fitted using the  $\chi^2$  function

$$\chi^2 = \sum_{i=1}^{N_{\text{wires}}} \left( \frac{z_i(z_0, d_z, s) - z_{m,i}}{\sigma_{z,i}} \right)^2. \quad (7.10)$$

The results for the wire  $z$ -pitch are separated for each sector:

Sector	Multilayer	$d_z$ [mm]
Middle	Upper	$13.09 \pm 0.03$
Middle	Lower	$13.10 \pm 0.03$
Long	Upper	$13.09 \pm 0.02$
Long	Lower	$13.11 \pm 0.02$

The results show a wire  $z$ -pitch which is  $17 \mu\text{m}$  larger than the design value of  $13.077 \text{ mm}$ . The larger glue gap indicates that the vertical pressure applied by the combs was not quite sufficient to hold the tubes together at the design distance against the viscosity of the glue.

The results for the spacer height, when fitting both multilayers together, are:

	Middle sector	Long sector
Spacer width	$(90.3 \pm 0.2) \text{ mm}$	$(90.4 \pm 0.2) \text{ mm}$

The measurement agrees well with the design value  $s_e = 90.4 \text{ mm}$ , meaning that the mounting of the multilayers on the spacer structure worked perfectly.

## 7.6 Summary

The wire positioning accuracy in  $y$  direction  $\sigma_y^{\text{wire}} = \sigma_{y,\text{res}} / \sqrt{2}$  is in each sector well within the requirement of  $20 \mu\text{m}$ , both with respect to the expected and for the fitted grid. All results are summarized in Table 7.2. The only deviation from the design parameters is the systematic relative displacement between the long and middle tube sectors in  $y$  direction. This effect can be avoided by better alignment of the combs for the assembly of each

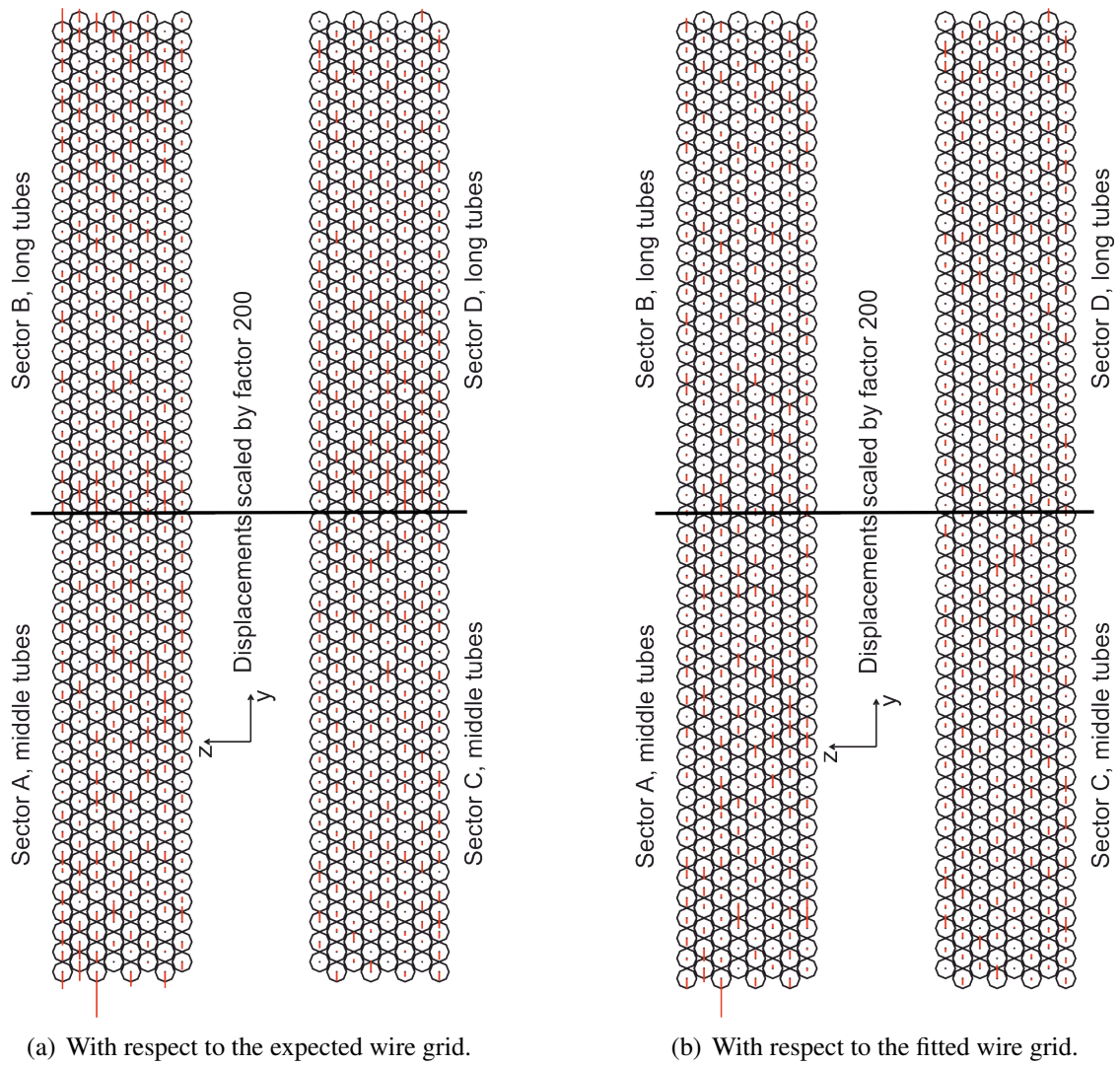


**Figure 7.25:** Individual wire displacements in  $y$  direction for all tubes, determined separately for each tube (enlarged by a factor of 200).

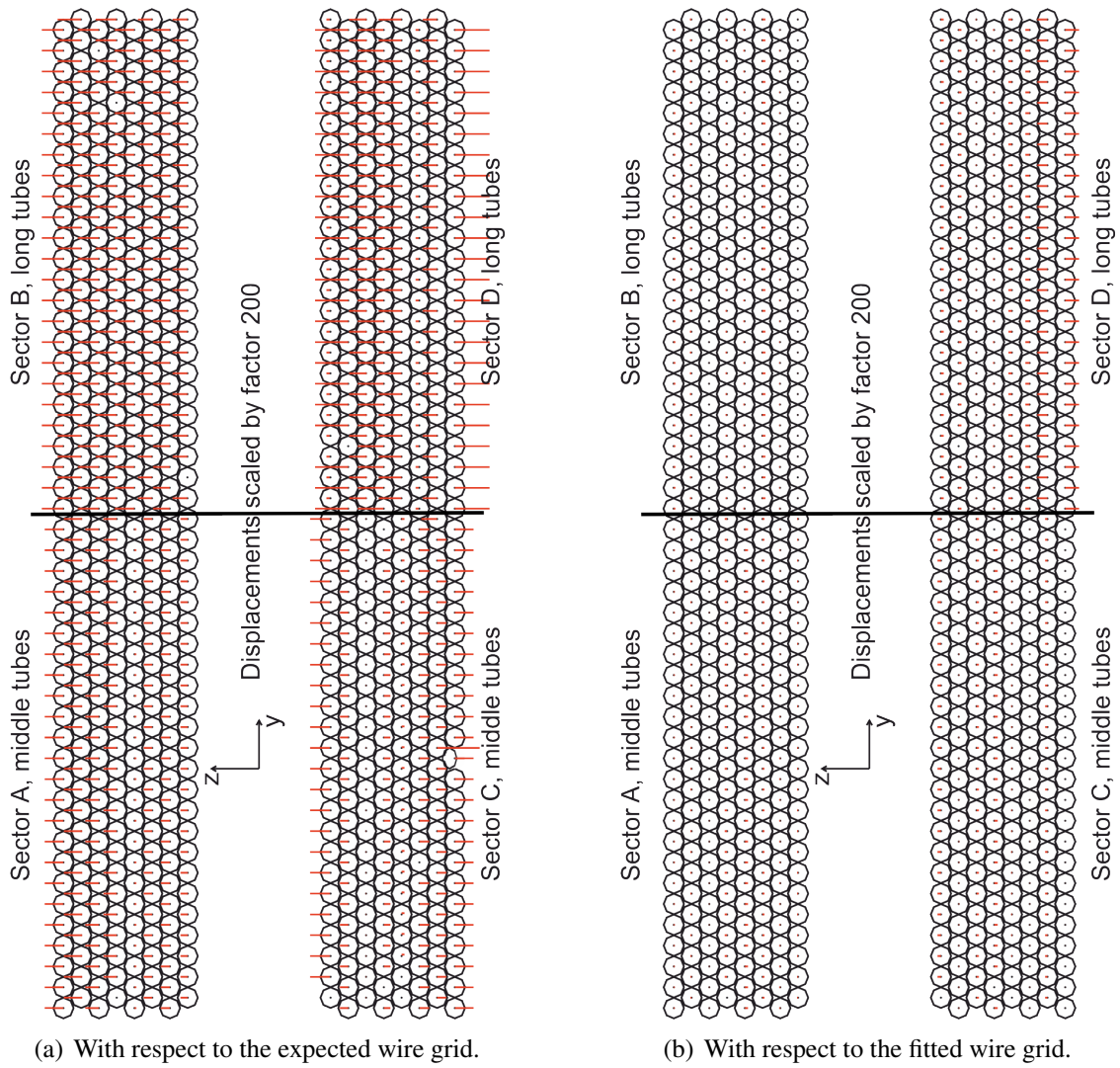


**Figure 7.26:** Layer displacements in  $z$  direction for all tubes determined separately for each layer and sector (enlarged by a factor of 200).

**Table 7.2:** Results from the horizontal and vertical wire grid measurement.  $\sigma_{y,\text{expected}}$  and  $\sigma_{y,\text{fitted}}$  are the width of the  $\delta_y$  distribution with respect to the expected and fitted wire grid, respectively.

Parameter	Value [mm]		Difference [mm]
	design	measured	
$d_y$	15.10	$15.1018 \pm 1 \cdot 10^{-4}$	0.018
$y_{\text{skipp}}$	7.55	$7.5500 \pm 3 \cdot 10^{-4}$	0.004
$\sigma_{y,\text{expected}}$	< 0.020	$0.0198 \pm 6 \cdot 10^{-4}$	–
$\sigma_{y,\text{fitted}}$	< 0.020	$0.0158 \pm 6 \cdot 10^{-4}$	–
$d_z$	13.077	$13.10 \pm 0.02$	0.02
$s$	90.4	$90.4 \pm 0.2$	0.0
$\sigma_{z,\text{expected}}$	< 0.020	$0.016 \pm 2 \cdot 10^{-3}$	–
$\sigma_{z,\text{fitted}}$	< 0.020	$0.013 \pm 2 \cdot 10^{-3}$	–

sector. The values of  $\delta_y$  for each individual wire with respect to the expected and fitted wire grid, respectively, are shown in Figure 7.25.

Figure 7.26 shows the  $\delta_z$  values for each tube layer and sector. Calculating the wire displacements with respect to the fitted wire grid (Fig. 7.26(b)) shows much smaller  $\delta_z$  values compared to the displacements with respect to the expected wire grid with  $d_z = 13.077$  mm (Fig. 7.26(a)). In  $z$  direction the measurement errors are larger due to the almost vertical muon tracks in the teststand. Only global layer displacements in  $z$  direction can be measured. The vertical tube assembly is also more difficult than in  $y$  direction. The glueing of the tubes in  $z$  direction introduces a systematic increase in the  $z$ -pitch which is the same for both MLs. Since they were glued separately, the effect appears to be reproducible. The fitted  $z$ -pitch can be used as new design value for future chamber construction.



# Chapter 8

## Test Beam Measurements

An important requirement for the new drift tube chambers is very high spatial resolution. This is best tested using a high-energy muon beam on order to be unaffected by uncertainties due to multiple scattering like for tests with cosmic ray muons. The H8 muon beam line at CERN has also high intensity in order to collect sufficiency statistics under controlled conditions. This facility has been used for ATLAS muon chambers tests since the beginning.

This chapter discusses the test beam setup and the analysis of the data taken in 2011.

### 8.1 The Beam Line

The SPS<sup>1</sup> was built in 1976 and is the second largest accelerator at CERN with an circumference of 7 km. The accelerator serves a wide range of purposes, from providing the LHC with proton bunches to delivering beams to serve fixed target experiments such as COMPASS<sup>2</sup> or ICARUS<sup>3</sup> and Opera<sup>4</sup> at the CNGS<sup>5</sup>[CER09].

Another important task is to provide test beams for detector research and development. These range from 400 GeV/c protons to a variety of secondary and tertiary particles. Secondary particles are produced when protons interact with a target. The secondary particles are collected by magnets and directed to the experimental sites. Tertiary particles are decay products of secondary particles. The weak leptonic  $\pi$  and  $K$  decays

$$\pi^\pm \rightarrow \mu^\pm + \nu_\mu \quad \text{and} \quad K^\pm \rightarrow \mu^\pm + \nu_\mu \quad (8.1)$$

are of special interest for our tests. After absorbing the remaining hadrons in a beam dump, a clean muon beam is achieved. The beam optics were set for a pion energy of 180 GeV. The decay kinematics of the pions implies a muon momentum distribution between

$$0.57 < \frac{p_\mu}{p_\pi} < 1.0 \quad (8.2)$$

---

<sup>1</sup>Super Proton Synchrotron (<http://user.web.cern.ch/public/en/research/SPS-en.html>)

<sup>2</sup>COmmon MUon Proton Apparatus for Structure and Spectroscopy (<http://wwwcompass.cern.ch/>)

<sup>3</sup>Imaging Cosmic And Rare Underground Signals (<http://icarus.lngs.infn.it/>)

<sup>4</sup>Oscillation Project with Emulsion-tRacking Apparatus (<http://operaweb.lngs.infn.it/>)

<sup>5</sup>CERN Neutrinos to Gran Sasso (<http://proj-cngs.web.cern.ch/>)

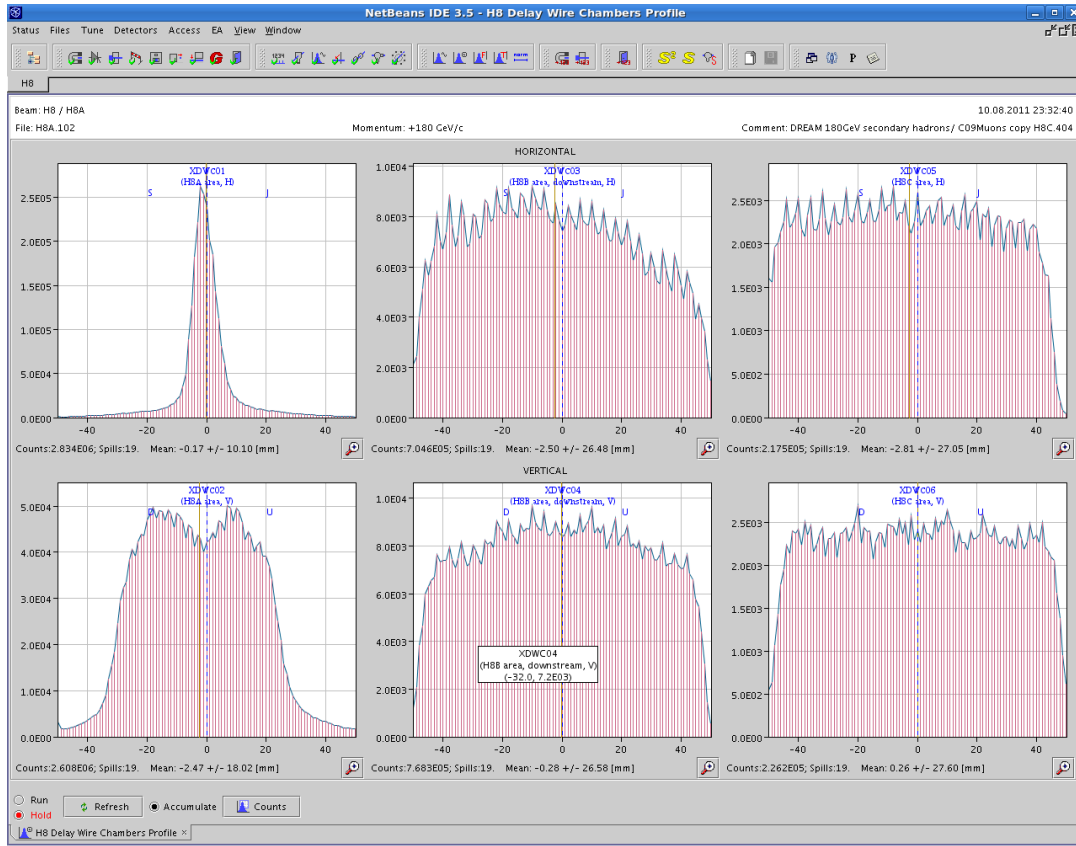


**Figure 8.1:** The beam profile for 180 GeV muons at the H8 beam line at CERN in 2011. See the text for details.

with a peak at about 85% of the pion energy. The momentum of the generated muons is therefore between 103 GeV/c and 180 GeV/c with a peak at 153 GeV/c. This energy is much larger than the average energy of cosmic ray muons of 4 GeV/c. The multiple scattering angle is inversely proportional to the momentum of the particle and is therefore strongly reduced for the beam muons compared to the cosmic ray test stand by a factor of

$$\frac{\theta_{\text{cosmic}}}{\theta_{\text{beam}}} \propto \frac{p_{\text{beam}}}{p_{\text{cosmic}}} = \frac{153 \text{ GeV/c}}{4 \text{ GeV/c}} \approx 38. \quad (8.3)$$

The beam profile is shown in Figure 8.1. One can see that the profile is quite uniform over the 8 cm measurement range of the beam monitoring detectors. The plots on the left-hand side of the figure show that the initial pion beam is more collimated, but during the transport in the beam line and after the decays the beam width is increased. The plots in the middle show the horizontal and vertical distributions of the muon beam measured by wire chambers located about 30 m upstream of the sMDT test chamber. The plots on the right-hand side show measurements of detectors shielded by a 50 cm concrete absorber about 30 m downstream of the sMDT test chamber. The beam profile is very similar to the one upstream of the test chamber indicating that there is little scattering even with the dump inserted in the beam line.

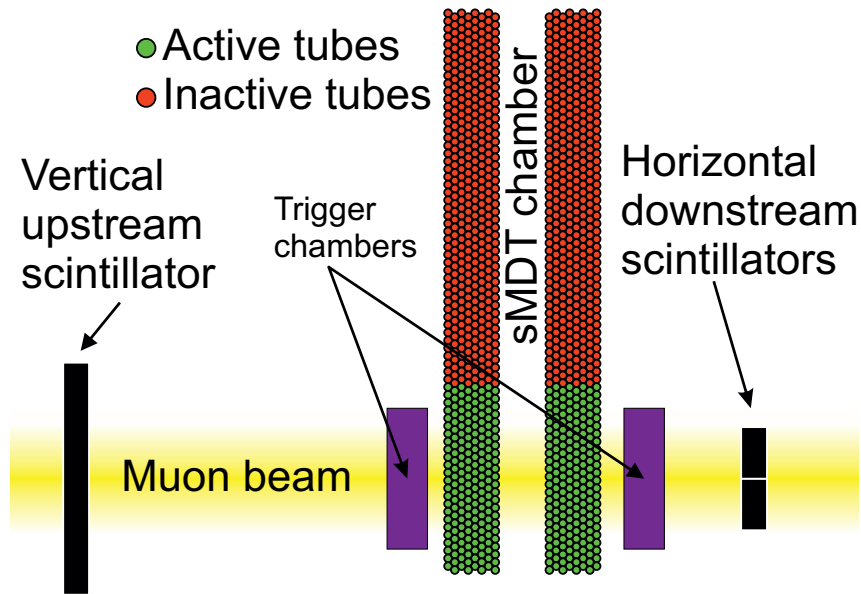


Figure 8.2: Setup for the sMDT chamber tests at the H8 beam line.

## 8.2 Goals of the Beam Test

The goals of the test beam measurement of this sMDT chamber were

- the measurement of the single-tube spatial resolution without background radiation,
- the measurement of the track segment resolution without background radiation,
- the measurement of the single-tube efficiency for varying gas gain and
- performance tests of the system with new trigger chambers (RPC and TGC).

To study the performance with the new trigger chambers, the additional chambers have been included into the readout and the trigger logic was adapted to accept the signals from the trigger chambers.

## 8.3 Experimental Setup

The sMDT prototype chamber described in previous chapters was used for the tests. The setup for the sMDT chamber tests is illustrated in Figure 8.2. Details about the chamber readout system are given in Appendix A. To investigate the effect of different muon incidence angles, the chamber could be rotated by up to  $30^\circ$ . This is also important for the calibration of the  $r(t)$  relation, because the algorithm needs muons at different angles to find the correct solution (cp. Sec. 4.4.3).

Scintillation counters were used for the trigger: one upstream of the chamber oriented vertically and two adjacent ones downstream of the chamber oriented horizontally. The width of the scintillators was 9 cm resulting in a sensitive area of  $9 \times 18 \text{ cm}^2$ , sufficient to cover the core of the beam (cp. Figure 8.1) with about 14 tubes.

The upstream scintillator had a length of 45 cm, the length of the downstream ones of 1 m was long enough to fully cover the longest tubes in the sMDT chamber. This was important for the trigger studies performed with the TGC (see Section 8.8.2).

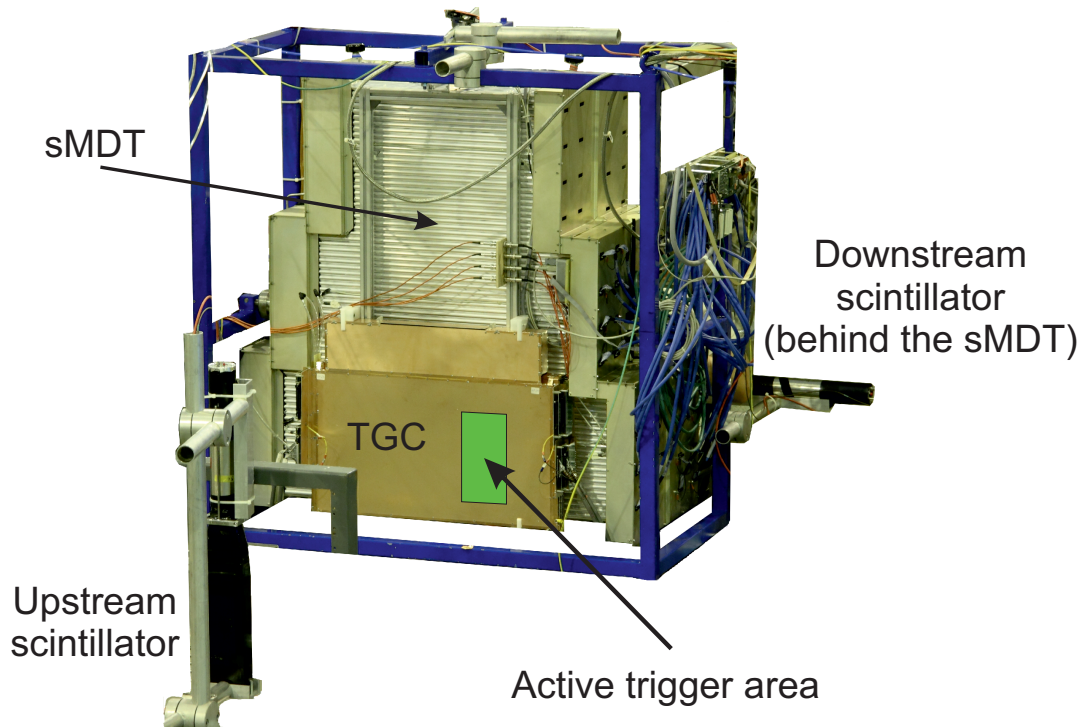


**Figure 8.3:** Photograph of the sMDT chamber test setup in the H8 beam line (see text for details).

## 8.4 Data Taking and Preparation

The data was taken in summer and autumn 2011. During in total 4 weeks more than 100 million events were collected with a stable setup.

Since the sMDT chamber with its 16 precise positioned tube layers serves both as reference and test chamber no relative alignment is needed.

### 8.4.1 Drift Tube Calibration

For the test beam analysis several data taking runs have to be combined. Rotation of the chamber changes the tube position with respect to the stationary trigger scintillator. For the maximum rotation angle of  $22.5^\circ$ , a shift in the start time of the drift time spectrum by more than 1 ns occurs. To correct for this effect, the  $t_0$  is fitted for every geometric setting separately.

The  $r(t)$ -calibration algorithm needs a selection of tracks with different incidence angles [Loe07]. In the test beam setup this is realised by rotating the chamber relative to the beam direction around the wire axis. Several data sets with different rotations were taken and combined for the calibration. The best results are obtained with at least three different muon angles.

Combining the runs is complicated by the fact that the environmental conditions in the H8 beam line vary with time. Temperature variations of up to  $5^\circ\text{C}$  per day were common (see Fig. 8.4). There were also rapid humidity changes.

The environmental conditions were recorded once per minute and written to a data base. Using the time information of the data base and the time stamp of the events from the data acquisition events within a temperature range of  $\pm 0.25^\circ\text{C}$ , but for different incidence

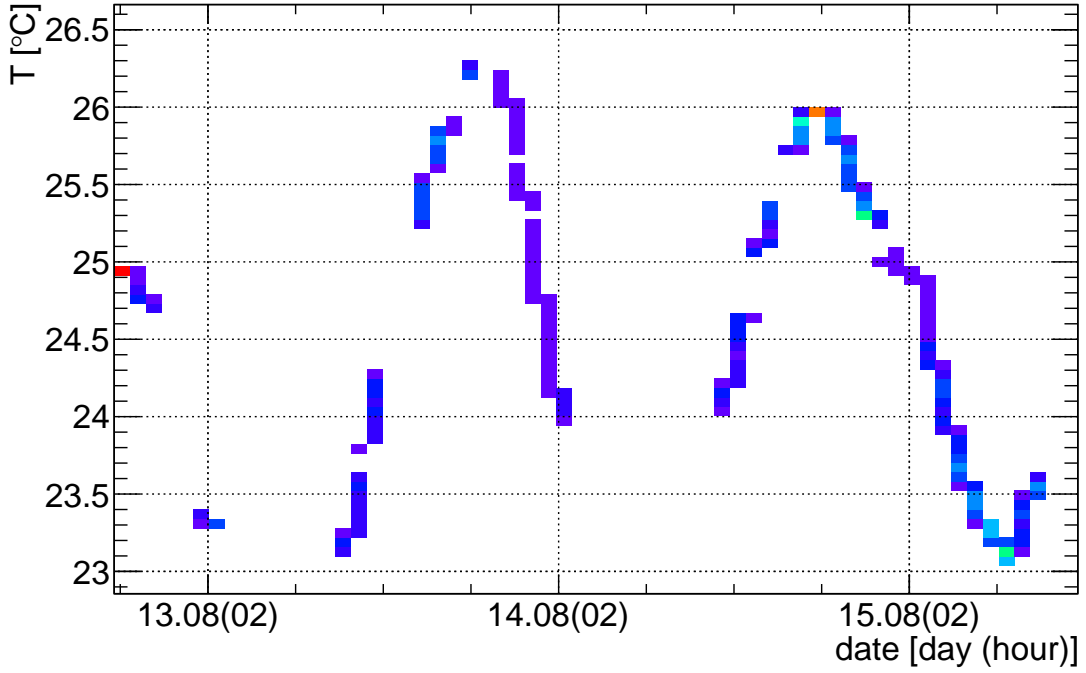


**Figure 8.4:** Temperature of the chamber during 3 days of data taking. Gaps indicate that the DAQ was not running during that time.

angles were selected and used to perform the  $r(t)$  calibration for different temperatures.

### 8.4.2 The Time Slewing Effect

Smaller signal pulses compared to the discriminator threshold tend to have a systematic delay in the threshold crossing time, as illustrated in Figure 8.5, causing a jitter in the time measurement. This time slewing effect is a reason for deterioration of the drift time and therefore the spatial resolution of the drift tubes [Rie00, Ale00]. To correct for this effect, the signal height is measured by an ADC integrated on the readout chip and the time correction corresponding to a certain ADC value is determined. In order to do this, the ADC measurement has to be calibrated to eliminate variations associated to the readout chip production (see Appendix B).

For each event the following procedure is performed:

1. Fit a (straight) track to the drift radii determined from the measurement of the drift times  $t_d$
2. Calculate the distance  $d$  of the track to the wire (see Eq. 7.3)
3. Determine the corresponding drift time  $t_c$  using the  $r(t)$  relation.

As a measure of the signal height, the most probable value  $ADC_m$  is determined from the ADC distribution by fitting it with a combination of a Landau and a Gaussian function constrained to have the same peak value  $ADC_m$  (see Fig. 8.6). There is a clear dependence of the  $ADC_m$  value on the drift time. To avoid a bias from this effect all further calculations involving  $ADC_m$  are done in separate drift time bins. The width of a bin is chosen with the following constraints:

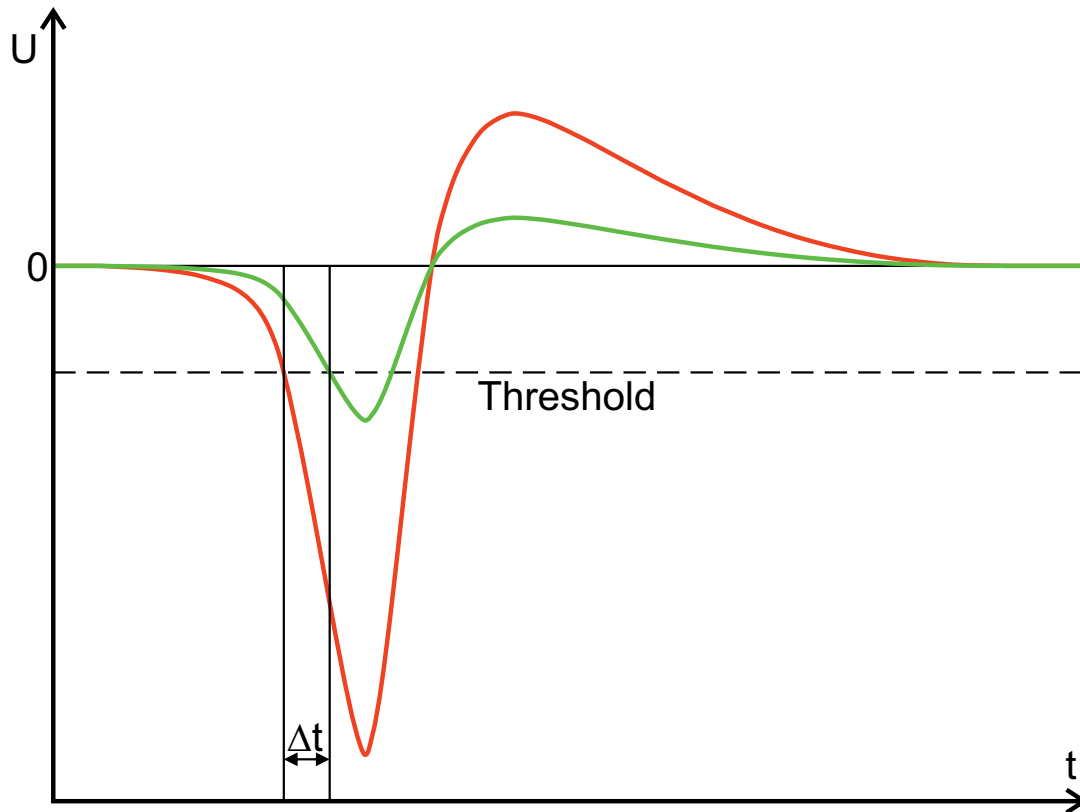
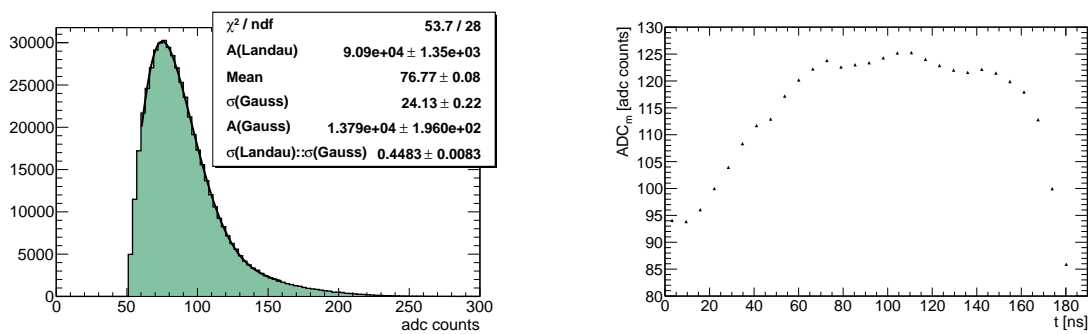


**Figure 8.5:** The time slewing effect: smaller signals tend to cross the discriminator threshold at later times (see text).



(a) ADC counts distribution for the bin  $t_d < 6.67$  ns.

(b) Distribution of the mean ADC value.

**Figure 8.6:** The ADC distribution for one bin and the whole tube.

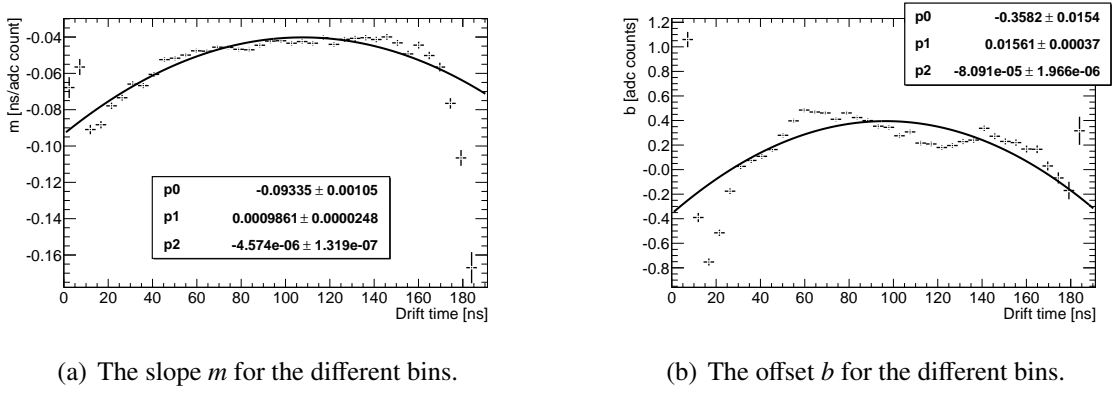


**Figure 8.7:** Slope  $m$  and offset  $b$  as a function of the drift time.

- Not less than 10 and not more than 30 bins,
- At least 2000 entries per bin.

This results in a bin width between 6.67 ns and 20 ns in a time window of 200 ns containing the full drift time spectrum. It is now possible to determine the difference  $\delta t = t_d - t_c$  for each  $ADC_{m,i}$  value and drift time bin  $i$  and determine the correction functions

$$\delta t(ADC, i) = m_i \cdot (ADC - ADC_{m,i}) + b_i \quad (8.4)$$

by fitting the distributions  $\delta t$  vs.  $ADC - ADC_{m,i}$  with a linear function for each bin. The resulting slopes  $m_i$  and offsets  $b_i$  are shown in Figure 8.7 as a function of the drift time bin. The histograms are fitted with parabolas providing a parametrisation of the  $t_d$  dependence of the correction Function (8.4) for the time slewing correction of the drift time measurement.

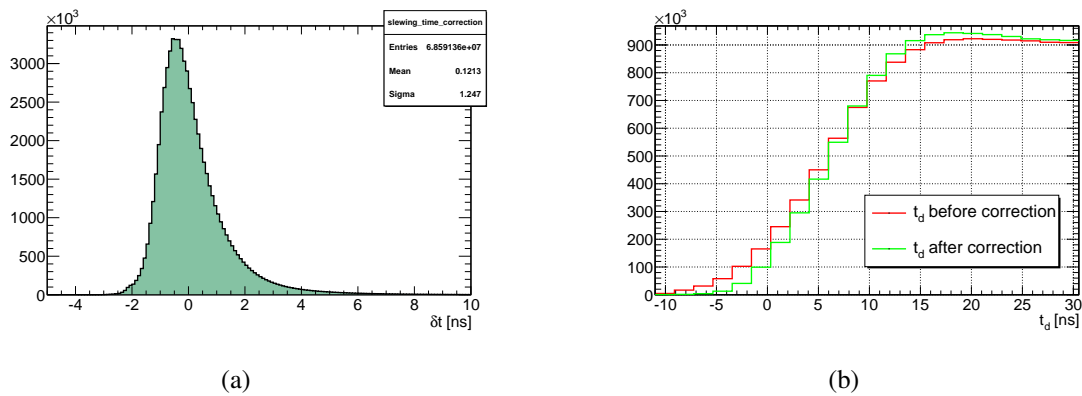
The corrected drift times are used to determine the drift radii. The values of  $ADC_{m,i}$ ,  $m_i$  and  $b_i$  corresponding to the measured drift time  $t_d$  are used to calculate the correction  $\delta t(ADC, i)$  according to Equation (8.4). The correction is applied before the drift radius is calculated from the drift time.

Figure 8.8(a) shows the distribution of  $\delta t$ . The effect of the time slewing correction is also visible in the drift time spectrum. The slope of the rising edge becomes steeper after the correction, corresponding to a better drift time (and therefore spatial) resolution (cp. Sec. 4.4.2). The time slewing correction shifts the  $t_0$  parameter of the drift time spectrum, which has to be refitted. Also the  $r(t)$  calibration has to be redone because of changes in the drift time spectrum.

To study the influence on the  $r(t)$  relation, the track residual distribution is examined. The mean value of the residuals is still zero within  $20 \mu\text{m}$  demonstrating that the  $t_0$  refit and following calibration was successful. Comparing the width of the track residuals before and after the time slewing correction already shows an improvement: the width is clearly reduced (see Fig. 8.9). The improvement of the drift tube resolution is discussed in Section 8.5.

### 8.4.3 Second Coordinate Measurement

The second coordinate along the tubes ( $x$ ) is well defined by the trigger area. The maximum signal travel time difference within the width of the active area of 9 cm is less than



**Figure 8.8:** Distribution of the time slewing correction  $\delta_t$  (a) and its influence on the leading edge of the drift time spectrum (b).

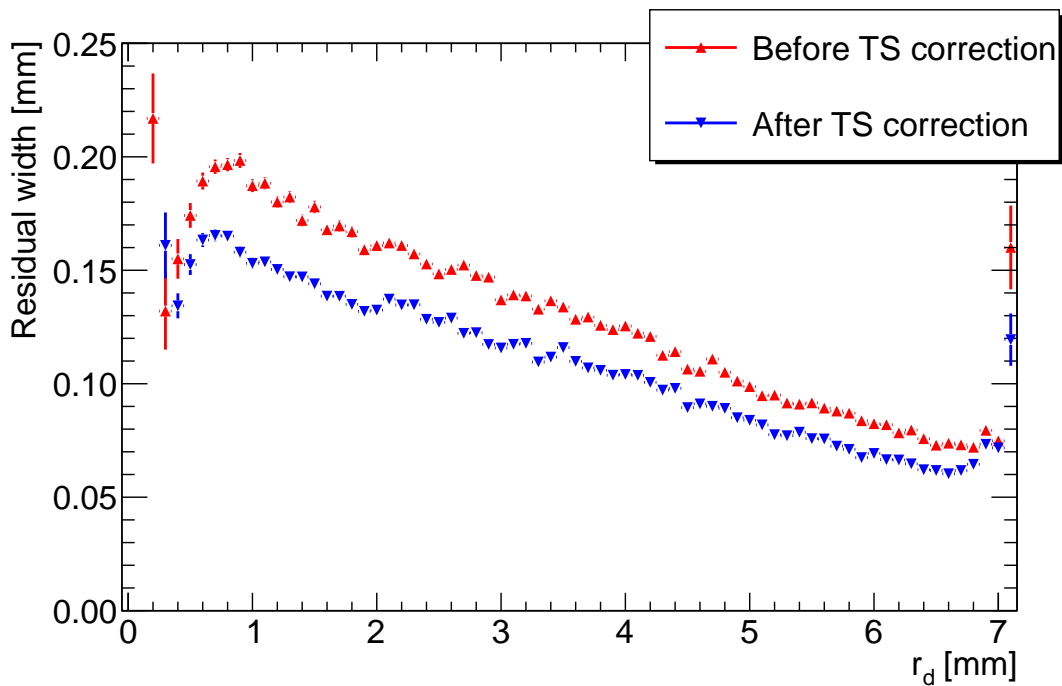


**Figure 8.9:** Effect of the time slewing correction on the track residual width as a function of the drift radius  $r_d$ .

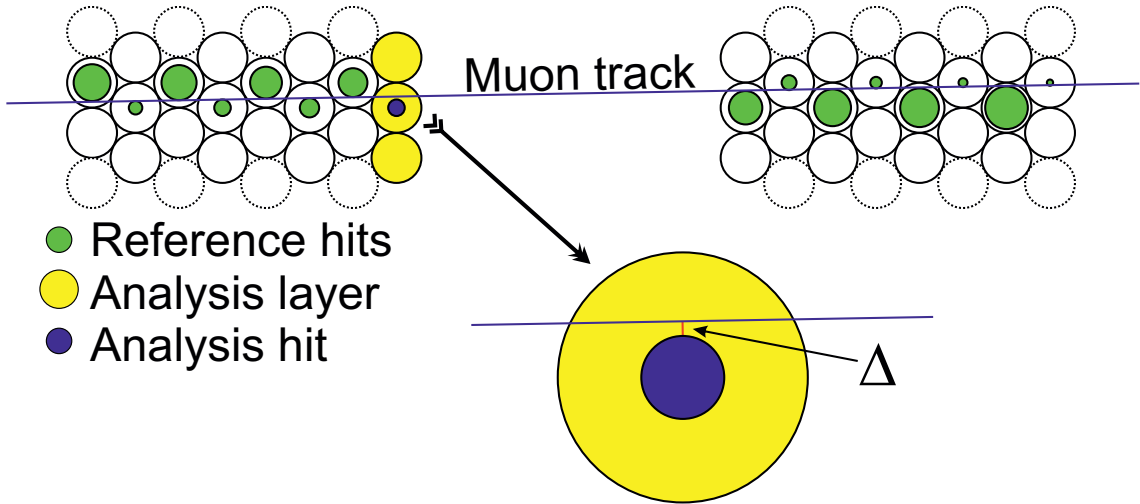


**Figure 8.10:** Finding the track residuals in the analysis layer (see the text).

0.1 ns and therefore negligible.

If the TGC is used for the trigger, the active area is 50 cm wide which would result in an uncertainty of 1.5 ns. However, the TGC measures the second coordinate cathode pads with a width of 9 cm. Adjacent layers are shifted by 4.5 cm. Combining the information of the 8 layers of the TGCs allows reconstruction of the muon position in the  $x$  coordinate with an accuracy of 5 cm by requiring overlapping pads.

## 8.5 Single Tube Resolution

To measure the single tube resolution  $\sigma_s(r)$  the distance  $d$  of a muon to the sense wire is compared to the drift radii  $r_d$ . The drift tube resolution  $\sigma_r(r)$  is the width of the residual distribution  $\sigma_r(r)$  as a function of  $|d|$  corrected for the track extrapolation error  $\sigma_t(r)$  to the respective tube:

$$\sigma_s(r) = \sqrt{\sigma_r^2(r) - \sigma_t^2(r)} . \quad (8.5)$$

Since no external beam telescope was available to measure the muon trajectories the sMDT chamber itself was used to reconstruct the tracks. First a track is reconstructed using the hits in all 16 layers of the test chamber. If this is successful the event is analysed further. The track is reconstructed again, using all tube layers except the layer analysed, in this case the innermost layer of the first multilayer in beam direction (see Figure 8.10). This procedure avoids a bias of the track reconstruction by the analysed tubes.  $\sigma_t(r)$  depends on the spatial resolution of all other hit errors along the track and therefore on the single tube resolution  $\sigma_s(r)$ .  $\sigma_s(r)$  can be extracted from the width of the residual distribution according to Equation 8.5 using the formula derived in [Hor05] to determine the track error at any given position  $(y, z)$  along the track: using the positions  $(y_i, z_i)$  and errors  $\sigma_{r,i}$  of the hits  $i$  used for the track reconstruction:

$$\sigma_t^2(y, z) = \frac{1}{D} \left[ \Lambda_{22} - 2z\Lambda_{12} + z^2\Lambda_{11} \right] \quad (8.6)$$

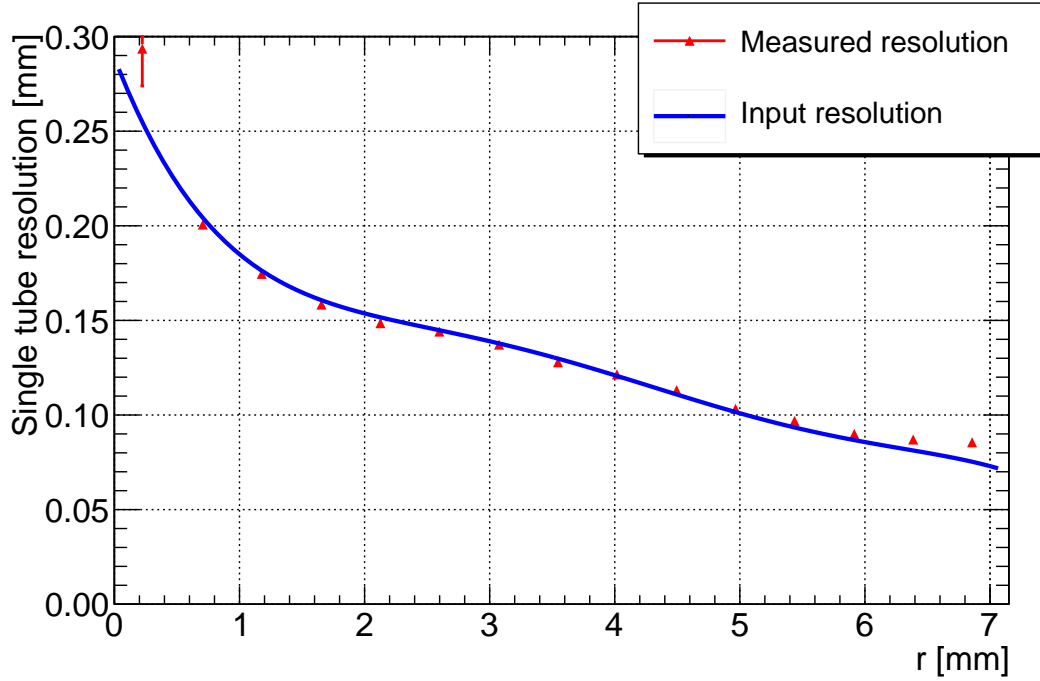


**Figure 8.11:** Single tube resolution measured on the MC data set compared to the true single tube resolution as a function of the track distance to the wire  $r = |d|$ .

with

$$(\Lambda_1, \Lambda_{12}, \Lambda_{22}) = \sum_{i=1}^n \frac{(1, z_i, z_i^2)}{\sigma_{i,r}^2} \quad \text{and} \quad D = \Lambda_{11}\Lambda_{22} - \Lambda_{12}^2 . \quad (8.7)$$

This formula is strictly valid only for tracks with angle zero. For tracks with a different angle, the error estimation for the track position in the analysis layer is not as accurate. One can also see that a larger number of track hits results in a better track accuracy. Therefore only tracks with a hit in every layer are selected for the analysis.

Since  $\sigma_t(r)$  depends on the single tube resolution used in the track fitting and error estimation, the result for  $\sigma_s(r)$  from Equation 8.5 used in the track fit and the whole procedure is iterated. This iteration is terminated when successive results for  $\sigma_s(r)$  remain equal within errors.

### 8.5.1 Monte-Carlo Tests

The procedure has been validated with Monte-Carlo simulation. 6 million muon tracks were simulated. The energy of the muons was fixed at 180 GeV. The angular spread was adapted to the measured width of the muon beam. The chamber and trigger scintillator geometry was the same as in the real setup.

For the MC simulation the true  $r(t)$  relation and single tube resolution are known. This allows for comparison of the results of the algorithm to the true values and for identifying sources for a systematic bias. Figure 8.11 compares the measured and the true single tube resolution. Both agree very well, demonstrating the correct performance of the algorithm.

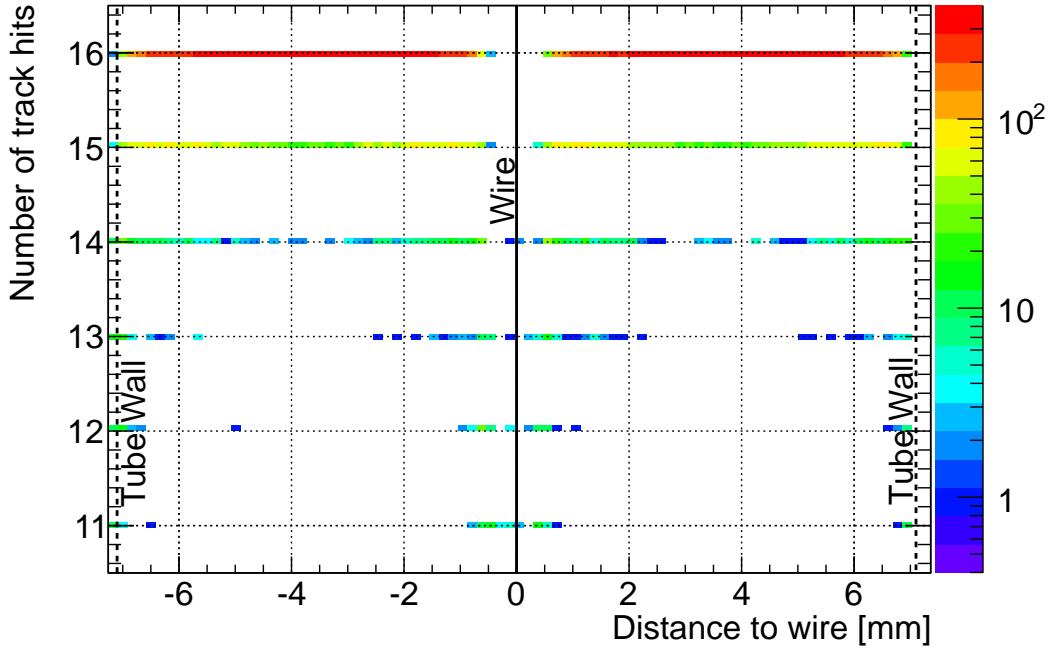


**Figure 8.12:** Number of hits on track for different distances to the wire.

Only close to the wire one sees a disagreement between measurement and input and large errors on the data point. This effect is due to the small number of tracks in this region of the tube. A track with zero impact angle close to the wire in the analysis layer lies between two tubes in every second layer and therefore has too few hits to pass the track quality criteria (see Fig. 8.12). To measure the resolution in the problematic region a different method is chosen.

The slope of the leading edge of the drift time spectrum is related to the time resolution. From the  $r(t)$  relation the drift velocity  $v(r)$  can be determined. The spatial resolution follows from the time resolution according to [Hor05]:

$$\sigma(r) = v(r) \cdot \sigma(t) \quad (8.8)$$

with

$$v(r) = \frac{dr(t)}{dt} . \quad (8.9)$$

Figure 8.13 shows a linear fit to the first  $600 \mu\text{m}$  of the  $r(t)$  relation which gives a drift velocity of  $v = (46.5 \pm 0.5) \mu\text{m}/\text{ns}$ . Comparing calibrations for different temperatures shows that the drift velocity in this region is stable within 5%. The time resolution is estimated as the rise time of the drift time spectrum which is determined as discussed in Section 4.4.2. For the Monte-Carlo data the result is  $t_{\text{rise}} = (5.1 \pm 0.1) \text{ ns}$ . For the spatial resolution follows  $\sigma(r) = (249 \pm 15) \mu\text{m}$  for  $r < 600 \mu\text{m}$ . Comparing the result with the input resolution shown in Figure 8.11 shows good agreement. This method does not require a track in the analysed region.

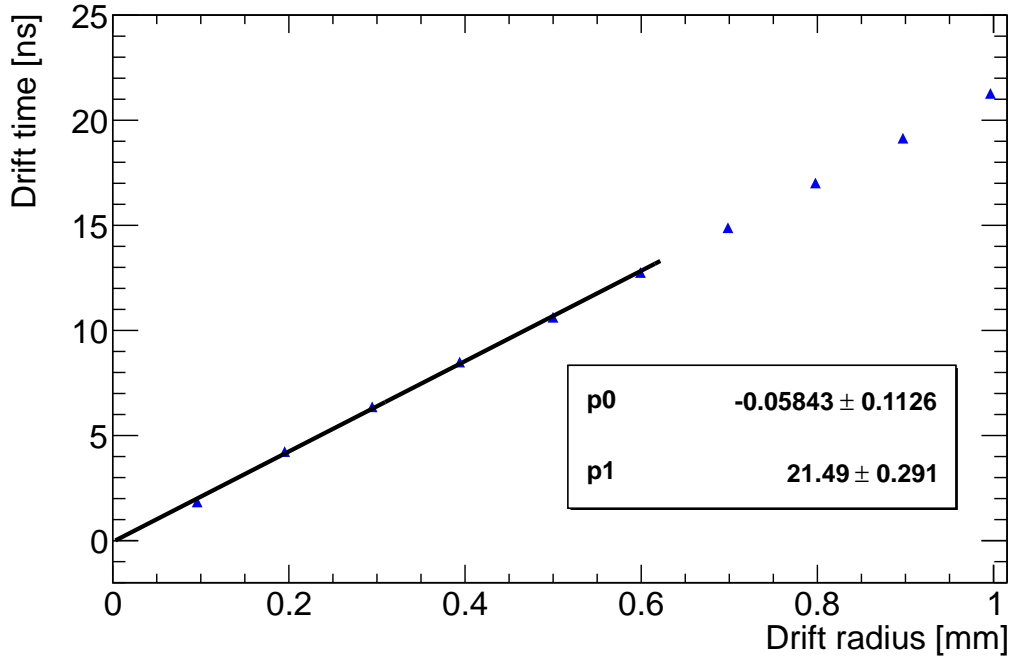


**Figure 8.13:** Determination of the drift velocity from the  $r(t)$  relation.

## 8.5.2 Data Results

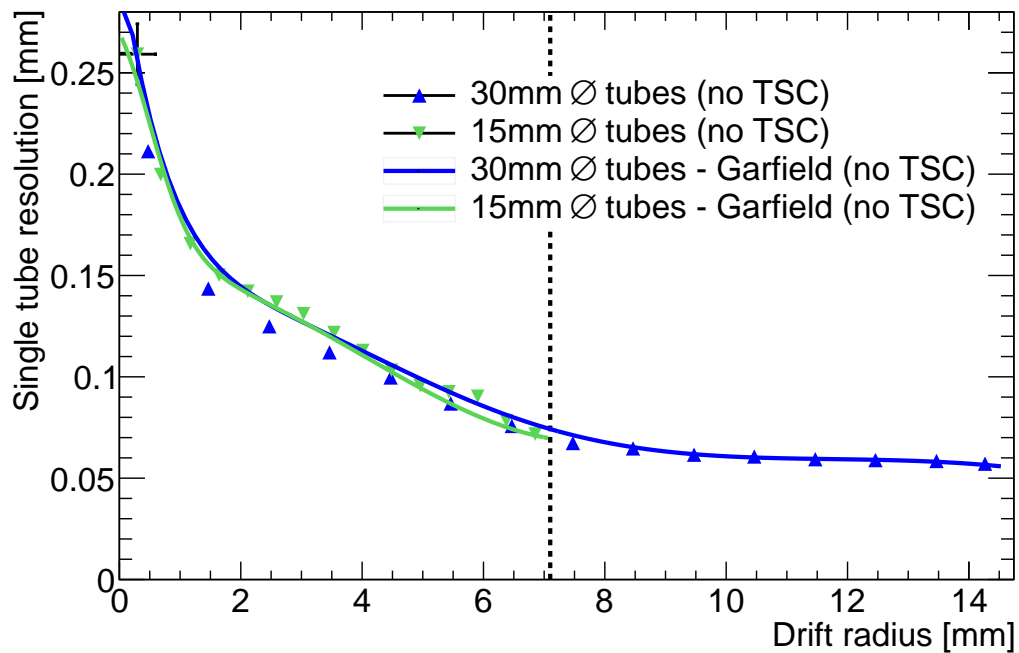
For the analysis a data set of 4.5 million triggers with almost constant temperature of  $(26 \pm 0.25)^\circ\text{C}$  and zero incidence angle and high-quality  $t_0$  fit and  $r(t)$  calibration was used. The next step was to select the tubes in the analysis layer used for the analysis. Only tubes fully covered by the trigger scintillators were selected. This excludes all tubes above and below the downstream scintillator as well as tubes that overlap with the small gap between the two scintillators (cp. Fig. 8.2). Overall, 7 tubes fulfil the quality criteria. Figures 8.14 and Figure 8.15 show the results for the single-tube resolution as function of the track distance to the wire without and with time slewing correction.

The radial dependence for the resolution for both tube diameters without time slewing corrections are in good agreement with the Garfield simulation of the drift properties taken from [Kil10] and with each other in the radial range of  $r < 7.1$  mm. Without time slewing correction the average resolution is  $\sigma_m^{15} = (128 \pm 2) \mu\text{m}$ . This value is consistent with the expectation from the average 30 mm diameter drift tube spatial resolution of  $(128 \pm 2) \mu\text{m}$  [Kor12].

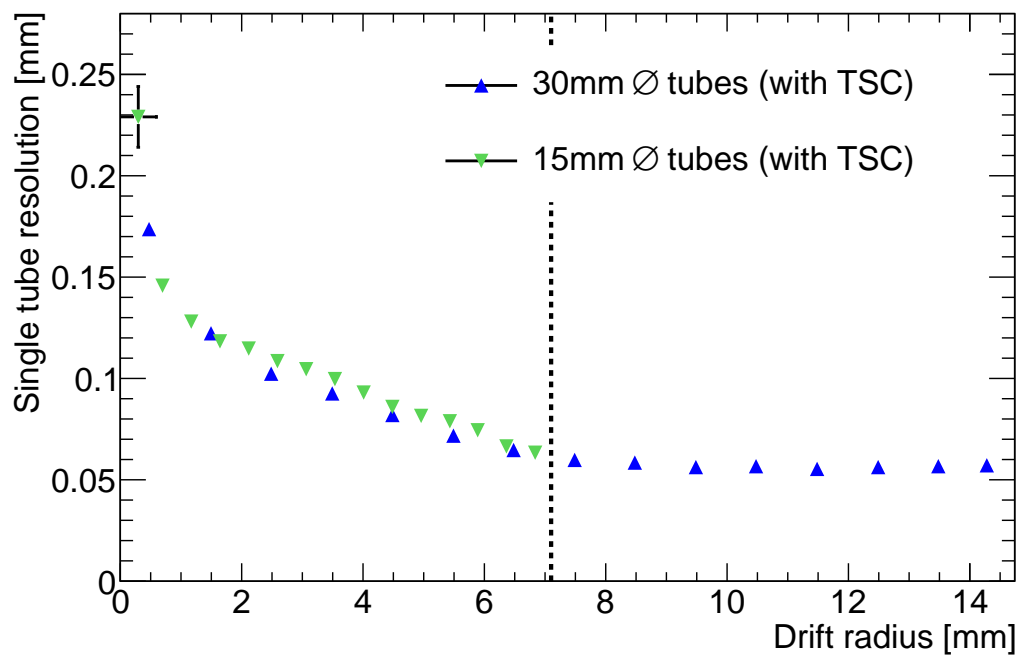
After application of the time slewing correction, the average resolution of the 15 mm diameter tubes is  $\sigma_{m,TS}^{15} = (106 \pm 2) \mu\text{m}$ . This values is in good agreement with the expectation from the average 30 mm diameter tubes resolution of  $(106 \pm 2) \mu\text{m}$  [Kor12]. Figure 8.15 shows that the radial dependence of the resolution of both the 15 mm and 30 mm diameter tubes also agrees well after the time slewing correction in the region  $r < 7.1$  mm.

Figure 8.16 shows  $\sigma_m^{15}(r)$  and  $\sigma_{m,TS}^{15}(r)$ . The effect of the time slewing correction is larger close to the wire where the signal height has a larger variation. Closest to the wire the difference is  $\sigma_m^{15}(0.6 \text{ mm}) - \sigma_{m,TS}^{15}(0.6 \text{ mm}) \approx 350 \mu\text{m}$ .

The resolution in the region close to the wire was analysed separately. From Figure 8.8(b), the rise time of the leading edge of the drift time spectrum decreases by 0.6 ns



**Figure 8.14:** Comparison of the single tube resolution without time slewing correction for the 30 mm $\varnothing$  and the 15 mm $\varnothing$  drift tubes and the corresponding Garfield simulations [Kor12, Kil10].



**Figure 8.15:** Resolution with time slewing correction for the 30 mm $\varnothing$  and the 15 mm $\varnothing$  drift tubes [Kor12].

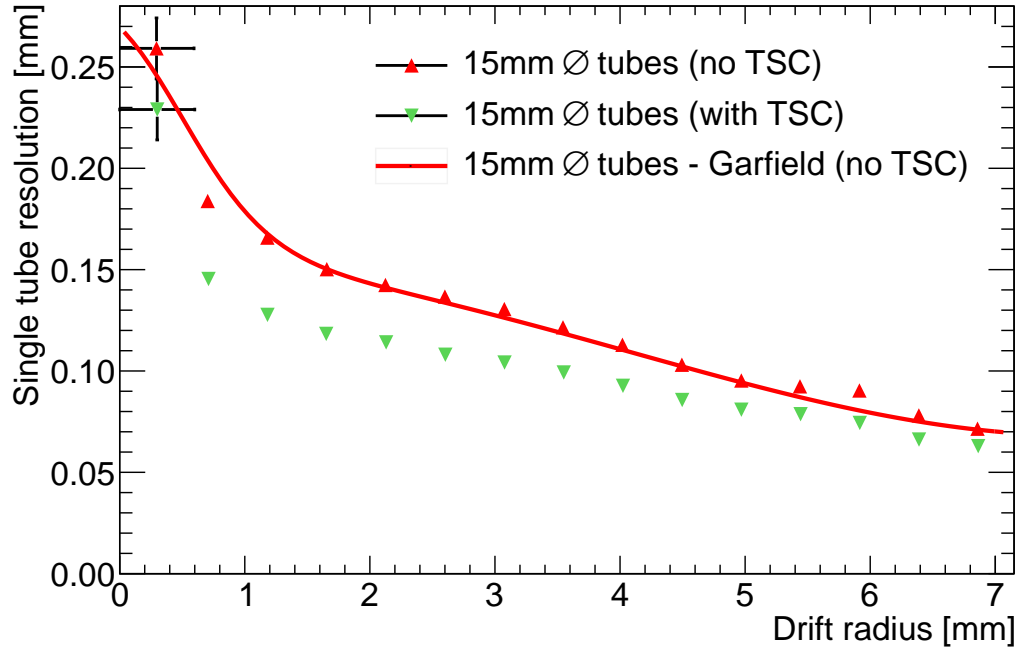


**Figure 8.16:** Single tube resolution with and without applied time slewing correction and the expectation derived from the ATLAS MDT drift tubes.

from  $(5.3 \pm 0.2)$  ns to  $(4.7 \pm 0.2)$  ns after the time slewing correction, resulting in a improvement of the spatial resolution from  $(259 \pm 15)$   $\mu\text{m}$  to  $(229 \pm 15)$   $\mu\text{m}$  for  $r < 600$   $\mu\text{m}$ . Both values are compatible with the measurement of the 30 mm diameter tubes and the Garfield simulation.

## 8.6 Single Tube Efficiency

The  $3\sigma$  detection efficiency of the drift tubes and the effects of high counting rates have been discussed in Section 4.4.4. For the test beam measurement without background radiation there is no limitation of the readout electronics because the muon rate of the beam is well below the limit of 300 kHz per channel and the average time between hits is with about 0.2 ms several orders of magnitude above the 185 ns dead time. Thus the only deteriorating effects on the  $3\sigma$  efficiency are the  $\delta$ -electrons created by the muons and the short path length close to the tube wall.

The measurement of the single-tube efficiency uses a very similar method as for the determination of the spatial resolution. After the resolution measurement has converged, a final iteration is performed with the single tube resolution obtained as input. The muon tracks are reconstructed without using hits in the analysis layer. If a tube in the analysis layer has a hit, the drift radius  $r_d$  is compared to the distance  $r$  between wire and track. If the residual  $\Delta = r - r_d$  is less than three times the single tube resolution  $\sigma(r)$ , the hit is associated to the muon track and the tube responded. If there is no hit in a traversed tube or if the residual is larger than  $3 \cdot \sigma(r)$ , the tube did not respond.

The  $3\sigma$  efficiency  $\varepsilon(r)$  is the fraction of responding tubes for a given track distance  $r$  to the sense wire. The measurement for 30 mm diameter tubes (see Section 4.4.4) is used as reference.

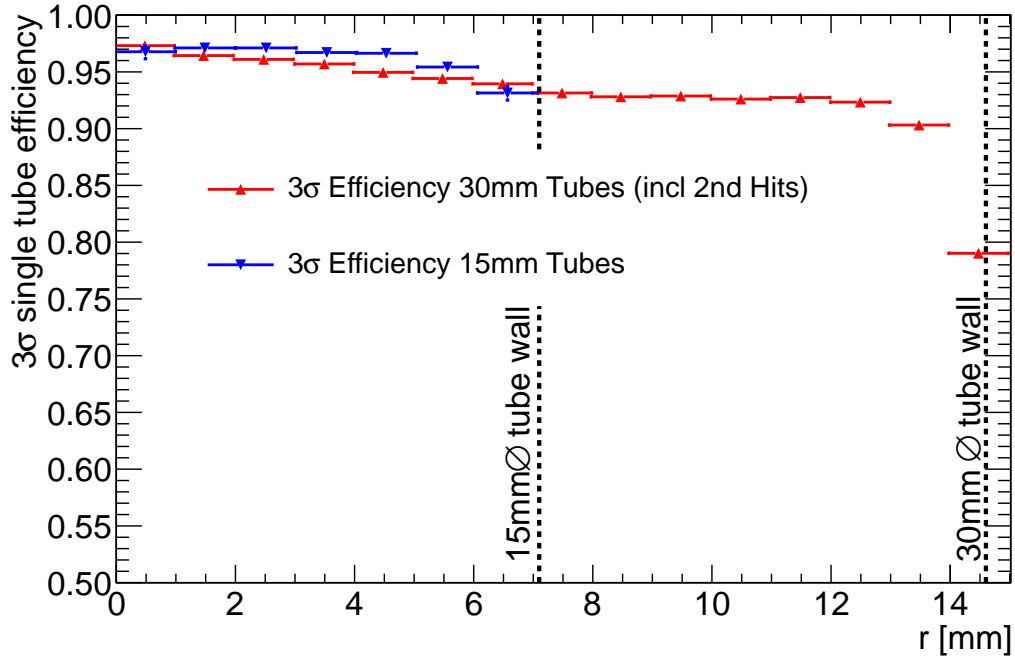


**Figure 8.17:**  $3\sigma$  efficiency for 15 mm and 30 mm [Kor12] diameter drift tubes as a function of the muon track distance to the sense wire without background radiation.

### 8.6.1 Data Results

Figure 8.17 shows the results of the measurement. The average  $3\sigma$  efficiency of the 15 mm diameter tubes is  $(96.3 \pm 0.1)\%$  and therefore slightly larger than for the 30 mm diameter tubes which have an average efficiency of  $(93.8 \pm 0.5)\%$ . The higher average  $3\sigma$  efficiency of the 15 mm diameter tubes is due to the higher efficiency in the radial region  $r < 7.1$  mm and the steadily falling efficiency of the 30 mm diameter tubes. The higher efficiency for the 15 mm  $\varnothing$  tubes compared to the 30 mm  $\varnothing$  tubes in the region close to the wire is most likely due to the smaller influence of  $\delta$ -electrons because of the smaller tube diameter.

The time slewing correction leads to a slight improvement of the average efficiency from  $(96.3 \pm 0.1)\%$  to  $(96.7 \pm 0.1)\%$ , as seen in Figure 8.18. The difference is largest in the region closest to the wire where the time slewing correction is more effective compared to regions close to the tube wall (cp. Fig. 8.16).

## 8.7 Track Segment Resolution

The requirements for new muon detectors for the ATLAS muon spectrometer upgrade are an angular resolution of better than 1 mrad (for use of drift tubes in the muon trigger [ATL11]) and a spatial resolution of better than  $60 \mu\text{m}$  even at a high background rates up to  $14 \text{ kHz/cm}^2$ . Since the resolution of the tubes is decreasing with rising background radiation levels, the chamber resolution without background radiation has to be even better. The dependence of the resolution on the background counting rate is discussed in Section 9.

For a SMDT detector with  $N$  layers of tubes and average single tube resolution  $\sigma_{\text{tube}} =$

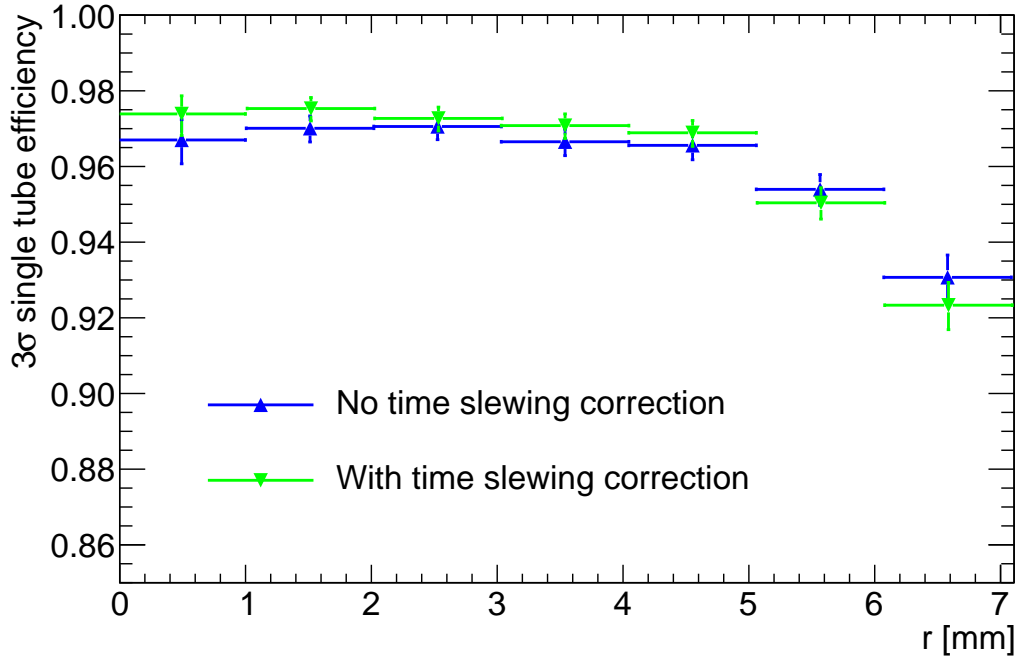


**Figure 8.18:** Effect of the time slewing correction on the  $3\sigma$  efficiency for 15 mm diameter drift tubes without background radiation.

106  $\mu\text{m}$  (after time slewing correction), the track segment resolution is given by

$$\sigma_{\text{track}} = \sqrt{\frac{\sigma_{\text{tube}}^2 + \sigma_{\text{pos}}^2}{N}}, \quad (8.10)$$

with the wire positioning error  $\sigma_{\text{pos}}$  which was measured to be less than 20  $\mu\text{m}$  (see previous chapter) and therefore has a negligible effect. The prototype chamber with 16 layers is expected to provide a track resolution of  $\sqrt{(106 \mu\text{m})^2 + (20 \mu\text{m})^2}/16 = 27 \mu\text{m}$ .

The angular resolution strongly depends on the separation of the multilayers which individually have a spatial resolution of  $\sigma_{ML} = \sqrt{(106 \mu\text{m})^2 + (20 \mu\text{m})^2}/8 = 38 \mu\text{m}$ . With the lever arm  $l = 195 \text{ mm}$  between the two multilayers the angular resolution of the prototype chamber is given by

$$\sigma_{\alpha} = \frac{\sqrt{2} \cdot \sigma_{ML}}{l} = 0.28 \text{ mrad} . \quad (8.11)$$

The measurement of the track segment resolution of the sMDT chamber is affected by the same complication as the resolution and efficiency determination, that there is no external reference system. But again part of the chamber itself can be used as reference.

The chamber is divided into two parts (yellow and blue in Figure 8.19), each consisting of 8 layers, half of them in each multilayer. Figure 8.19 shows the different selections color coded (yellow and blue). Dividing the chamber into alternating layers would have a drawback: the track would always be on the same side of the wire for tracks with a small angle and the reconstruction would have problems to solve this ambiguity. This way of selecting tube layers also ensures that there is always an equal amount of large and small

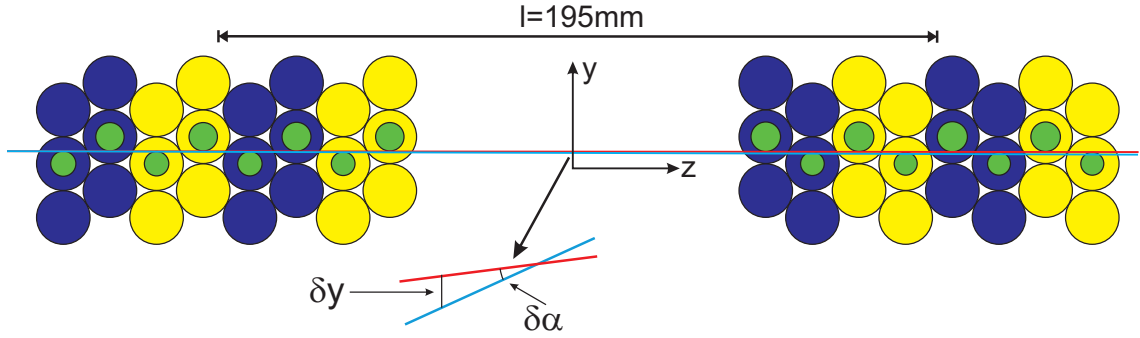


**Figure 8.19:** Selection of 4 layers per multilayer for the tracking studies.

drift radii in both divisions to avoid bias. As discussed in Section 8.5, the single tube resolution depends on the distance of the track to the wire.

For each muon, two tracks are reconstructed, one using the yellow tube layers, the other one using the blue layers, and their parameters are compared. The spatial resolution is evaluated in the centre between the multilayers at  $z = 0$  to minimize extrapolation errors. For a track given by  $y(z) = mz + b$ , the track resolution can be determined from the distribution of the distance  $\Delta b$  of the two track pieces at  $z = 0$ :

$$\Delta y = y_{\text{blue}}(0) - y_{\text{yellow}}(0) = b_{\text{blue}} - b_{\text{yellow}} = \Delta b \quad (8.12)$$

For the estimation of the angular resolution the slopes of the tracks are compared with the small-angle approximation  $m = \tan \alpha \approx \alpha$ :

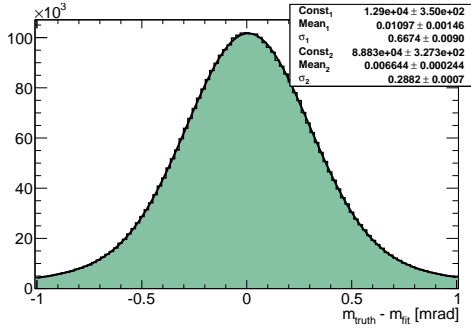
$$\Delta \alpha = m_{\text{blue}} - m_{\text{yellow}} \quad (8.13)$$

The widths of the distributions of  $\Delta y$  and  $\Delta \alpha$  are larger than the real resolution for complete track segments in the chamber because only half of the hits per track contribute with this method (factor of  $\sqrt{2}$ ) and because two measurements are compared (another factor of  $\sqrt{2}$ ). In total the widths of the residuals  $\Delta y$  and  $\Delta \alpha$  are  $\sqrt{2} \cdot \sqrt{2} = 2$  times the track position and angular resolution, respectively.

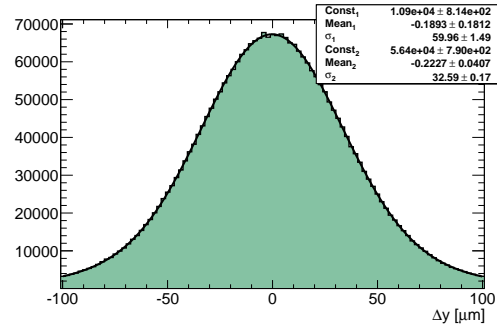
The performance of the method was tested on Monte-Carlo data where the true muon trajectory is known and can be compared to the muon track segment reconstructed in all tube layers. Comparing the true trajectory with the reconstructed muon track allows to measure the track segment reconstruction accuracy, both spatial and angular. Then this value is compared to the results of the algorithm described above.

To do this, tracks are reconstructed using all 16 layers of the chamber and is compared to the true muon track. The distributions of  $\Delta y$  and  $\Delta \alpha$  are shown in Figure 8.20, the histograms are fitted with a double Gaussian to account for a small fraction of badly reconstructed tracks determined from scale factors  $\text{Const}_1$  and  $\text{Const}_2$  of the two Gaussians. With the single tube resolution  $\sigma_{\text{tube}}^{\text{MC}} = 129 \mu\text{m}$  used in the Monte-Carlo simulation a spatial resolution of  $\sigma_y = (32.6 \pm 0.2) \mu\text{m}$  and a angular resolution of  $\sigma_\alpha = (0.288 \pm 0.001) \text{mrad}$  is achieved.

The distributions of  $\Delta y$  and  $\Delta \alpha$  from the two track method are shown in Figure 8.21 and the corresponding resolution results are given in Table 8.1. The result of the two-track method agrees very well with the true track resolution. The method is now applied to the beam data.

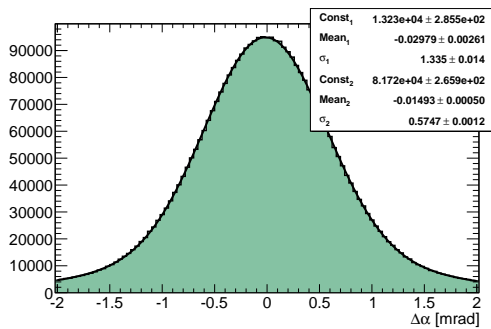


(a) Residuals for true and fitted track slope.

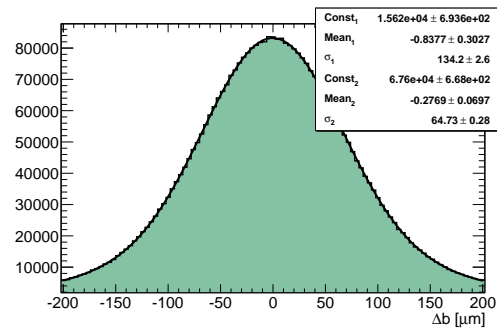


(b) Residuals for true and fitted track position.

**Figure 8.20:** Comparison of the reconstructed track with the truth information about the muon trajectory.



(a) Angular residuals  $\Delta\alpha$

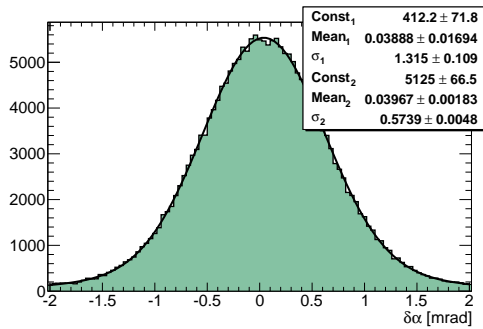
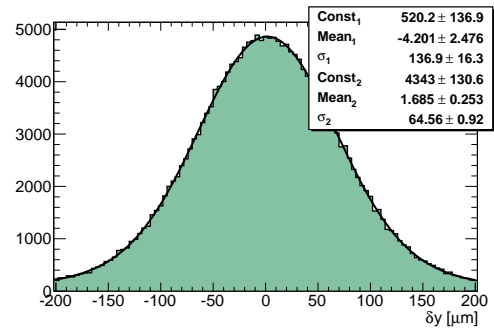


(b) Spatial residuals  $\Delta b$

**Figure 8.21:** Distributions of  $\Delta\alpha$  and  $\Delta b$  for the Monte-Carlo data set.

**Table 8.1:** Comparison of the true track segment resolution with the resolution determined with the two-track method for Monte-Carlo data. Both results agree very well.

	$\sigma_\alpha$ [mrad]	$\sigma_y$ [ $\mu\text{m}$ ]	$\sigma_{\text{tube}}$ [ $\mu\text{m}$ ]
True resolution	$0.288 \pm 0.001$	$32.6 \pm 0.2$	$128.8 \pm 0.2$
Resolution from two-track method	$0.287 \pm 0.002$	$32.4 \pm 0.3$	$128.5 \pm 0.3$

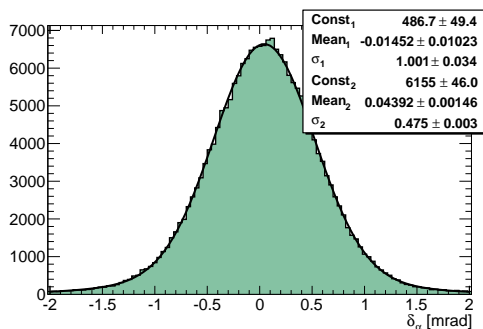
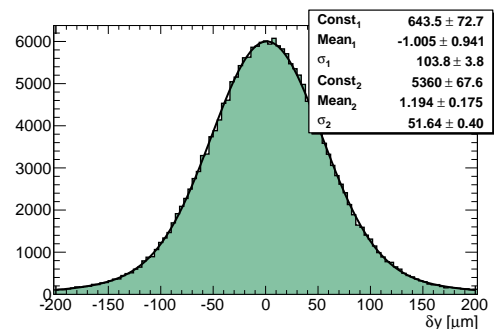
(a) Angular residuals  $\Delta\alpha$ (b) Spatial residuals  $\Delta y$ 

**Figure 8.22:** Distributions of  $\Delta\alpha$  and  $\Delta y$  for the data without time slewing correction.

## Data Results

Since the real single tube resolution is different from the one used in the Monte-Carlo simulation one expects different resolutions. The distributions of  $\Delta m$  and  $\Delta y$  without and with time slewing correction are shown in Figure 8.22 and 8.23, respectively. The calculated track resolutions  $\sigma_\alpha$  and  $\sigma_y$  and the corresponding average single tube resolutions  $\sigma_{\text{tube}}$  reconstructed using equation (8.10) are shown in Table 8.2.

Applying the time slewing correction improves the track angle resolution by 17%, the improvement of the track point resolution is 19%. The average single tube resolution  $\sigma_{\text{tube}}$  calculated from the track resolution is consistent with the direct measurement presented

(a) Angular residuals  $\Delta\alpha$ (b) Spatial residuals  $\Delta y$ 

**Figure 8.23:** Distributions of  $\Delta\alpha$  and  $\Delta y$  after application of the time slewing correction.

**Table 8.2:** Track segment resolution with and without time slewing correction (TSC) and the corresponding average tube resolution  $\sigma_{\text{tube}}$  according to Eq. (8.10).

	$\sigma_{\alpha}$	$\sigma_y$	$\sigma_{\text{tube}}$
Without TSC correction	$0.29 \pm 0.01$ mrad	$32 \pm 1$ $\mu\text{m}$	$128 \pm 2$ $\mu\text{m}$
With TSC correction	$0.24 \pm 0.01$ mrad	$26 \pm 1$ $\mu\text{m}$	$104 \pm 2$ $\mu\text{m}$
Improvement	0.05 mrad	6 $\mu\text{m}$	24 $\mu\text{m}$

in Section 8.5. The estimate of 0.25 rad (0.29 rad) for the track angle resolution with (without) time slewing correction from equation (8.11) agrees well with the measurement.

## 8.8 Tests with Trigger Chambers

For the new Small Wheels of the ATLAS muon spectrometer two different technologies as trigger chambers have been studied: Resistive Plate Chambers (RPC) and Thin Gap Chambers (TGC). Both chamber types are already in use as trigger chambers in the ATLAS muon spectrometer [ATL08]. Details about the two trigger chamber types can be found in [ATL11]. Both technologies were tested together with the sMDT chamber in the test beam. Using the good tracking capabilities of the drift tube chamber the spatial and angular resolutions of the trigger chambers were measured.

### 8.8.1 Test with new RPC Chambers

The sMDT-RPC setup is shown in Figure 8.24. Several different RPC chambers were included. All chambers were read out with the MDT readout electronics (cp. Fig. A.2). Since the chambers were not equipped with trigger electronics, the same scintillators as for the sMDT test were used. Figure 8.25 shows the track residuals measured in the glass-RPC with respect to the sMDT chamber. Deconvoluting the sMDT track extrapolation error results in a RPC spatial resolution of 190  $\mu\text{m}$ . More details about the new RPC chambers developed for the ATLAS muon spectrometer upgrade can be found in [ATL11] and [RPC12].

### 8.8.2 Test with new TGC Chambers

To include the TGC chambers in the test beam setup two additional 128-channel TDCs were installed in the VME crate. The readout scheme is described in detail in Appendix A. The TGC chambers were placed on both sides of the sMDT chamber, at approximately 2 cm distance, as shown in Figure 8.26. Since the TGCs were supported on the sMDT chamber, the whole system could be rotated together.

Only a small part of the readout strips of the TGC was equipped with electronics because of limited availability. The active area was only 5 cm wide making it necessary to adjust the chamber after each rotation to the center of the beam. The trigger was generated by the readout pads in each layer of the TGCs. The trigger logic requires 3 out of 4 pad layers in both TGCs. The pads signals were also used for the second coordinate information in the analysis. The time resolution of the TGCs is about 25 ns. This is not enough to trigger a precise drift time measurement in the sMDT chamber. To get a better

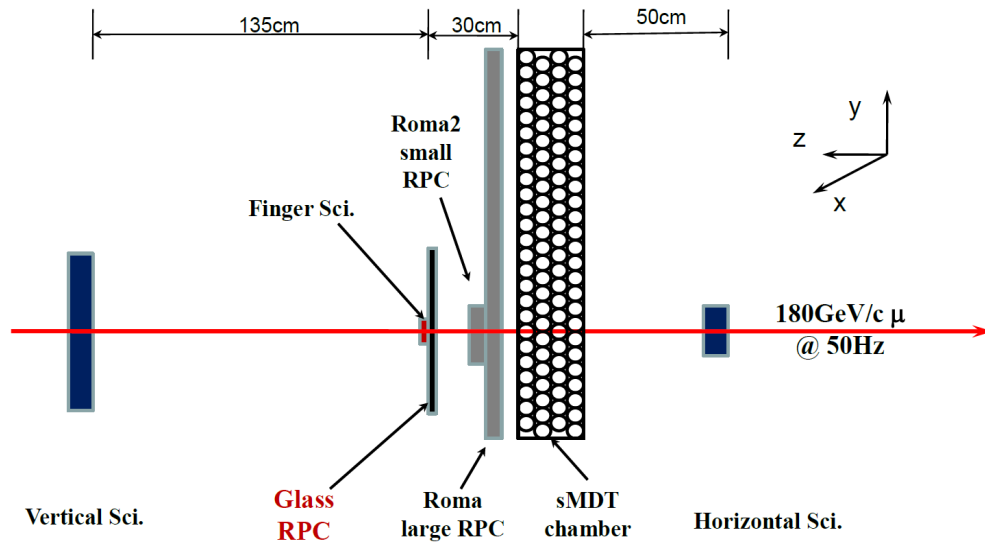


**Figure 8.24:** Overview of the combined sMDT-RPC setup. [Han12]

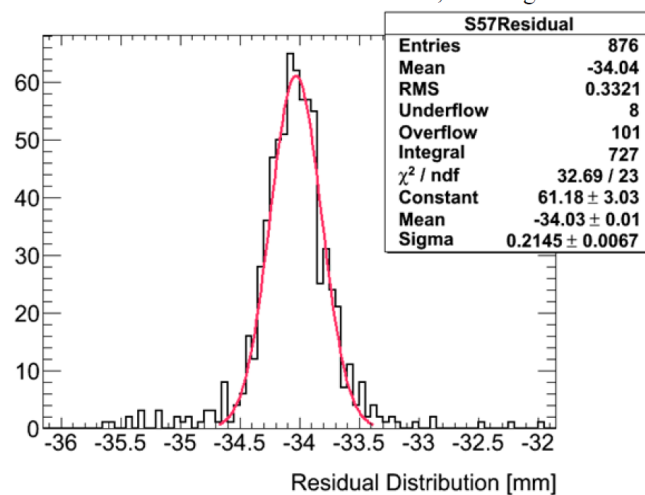


**Figure 8.25:** Residuals of the RPC track position measurement relative to the sMDT track [RPC12].

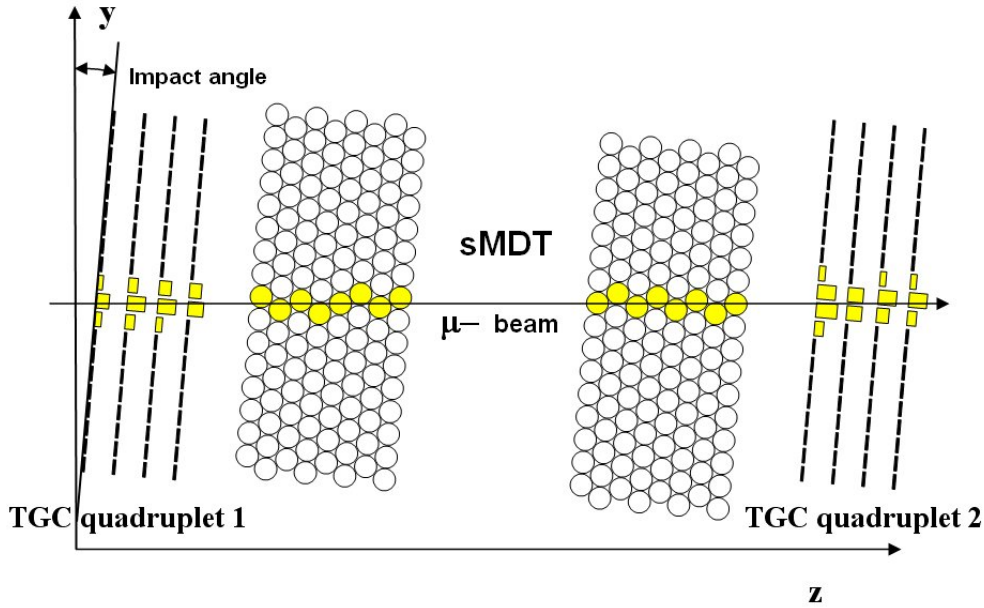
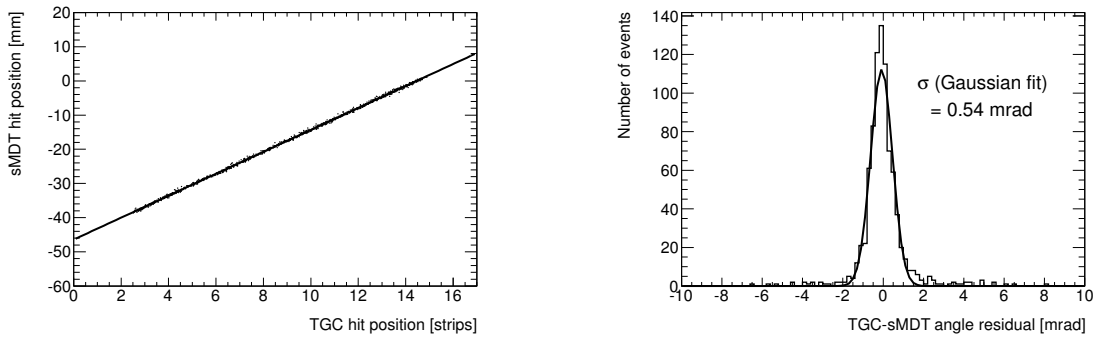


**Figure 8.26:** The combined sMDT-TGC test setup.



(a) Correlation of the track positions measured in the sMDT and TGC chambers.

(b) Residual distribution of the track angles measured in the sMDT and the TGC chambers.

**Figure 8.27:** Comparison of tracks measured in the sMDT and in the TGC chamber in the H8 muon beam.

time resolution, an additional scintillation counter with a time resolution of about 0.3 ns was included in the setup.

An important test of the TGC performance is the measurement of the spatial and angular resolution. The sMDT chamber track measurement was used as reference and compared to the track reconstructed by the two TGCs. Figure 8.27(a) shows the good agreement between the two track position measurements, Figure 8.27(b) shows the angular residuals of the two track measurements giving an angular resolution of the TGC setup of 0.38 mrad. More details of the setup and the analysis can be found in [Ben11].

# Chapter 9

## Performance under Gamma Irradiation

In this chapter the performance of the sMDT chamber technology under high  $\gamma$  irradiation and the tests at the Gamma Irradiation Facility (GIF) [GIF00, Ago00] at CERN are discussed. Such tests have also been performed for the 30 mm diameter drift tube chambers for the ATLAS muon spectrometer and serve as reference [Hor06].

### 9.1 The Gamma Irradiation Facility at CERN

The GIF was built at CERN to investigate the effects of high radiation rates on detectors for the LHC experiments, especially the influence on the spatial resolution and efficiency of the muon chambers [Ago00] as well as the ageing of detectors. The facility allows for testing of large detectors (up to  $3 \times 5 \text{ m}^2$ ) in the irradiation zone. The layout of the GIF is shown in Figure 9.1. The X5 muon beam, similar to the one discussed in the previous chapter, was initially available for the test of the 30 mm diameter tubes providing a high rate of high momentum tracks with small multiple scattering effects. In 2004 the beam line was removed and one now has to rely on tracks from cosmic muons. This results in a much lower event rate and mostly low energy muon tracks which are affected by multiple scattering (see also Chapter 7).

The  $\gamma$  radiation is produced by a high intensity  $^{137}\text{Cs}$  source. It emits  $\gamma$  radiation at an energy of 662 keV. In 1997, when it was installed, the source had an intensity of 740 GBq. With a half life time of 30.17 years [CSI] the activity in 2010 was only 549 GBq. The source can be attenuated by a set of filters mounted directly in front of the source. Attenuation factors between zero and 10000 can be selected. The layout of the source itself is shown in Figure 9.2.

### 9.2 Test Setup for the 15 mm Diameter Drift Tubes

Figure 9.3 shows the sMDT test setup in the GIF in 2010. Data was taken only with the middle part of the sMDT chamber which was equipped with readout electronics (the inactive tubes are marked yellow). Unlike for the wire position measurement, no external reference system was available to determine the muon tracks and one has to rely on the method applied in the test beam using the sMDT prototype chamber itself as tracking reference. For this purpose, the lower part of the chamber is shielded by lead bricks such that it can be used as reliable reference to define the tracks. Hits detected in the irradiated region are compared to the reference muon track segments.

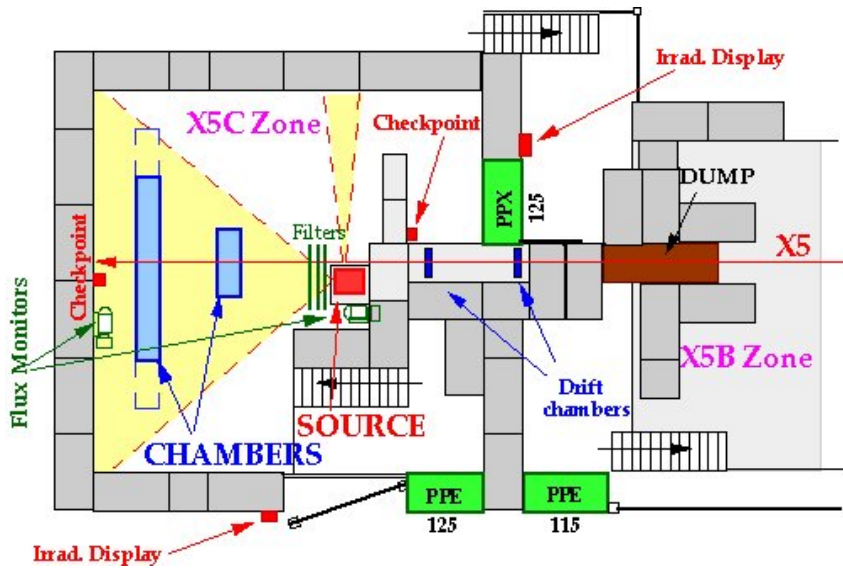


**Figure 9.1:** Layout of the GIF zone at CERN [GIF00]. The X5 muon beam was only available until 2004.

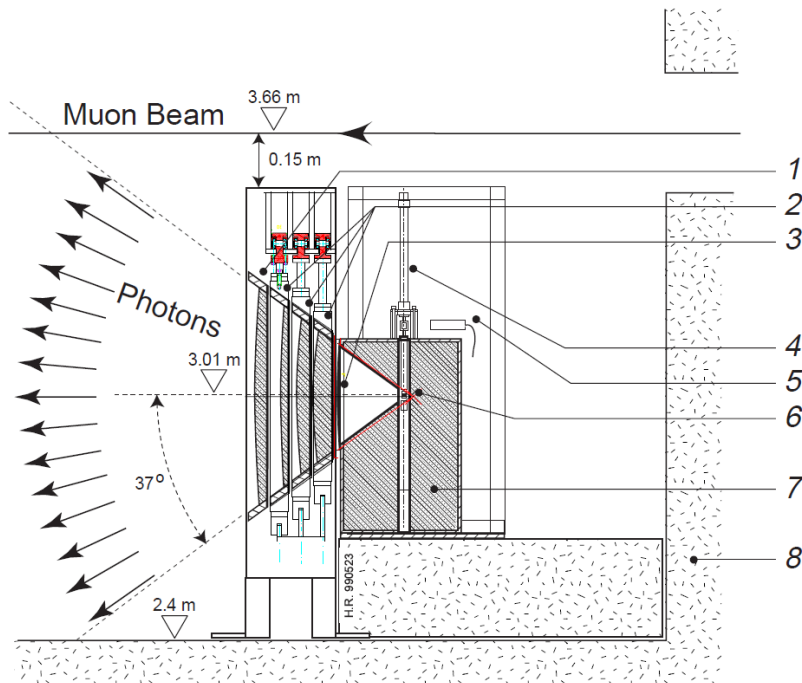


**Figure 9.2:** Vertical cut through the  $\gamma$  irradiation source at the GIF: 1-3: Filters, 4: rod for adjusting the source position, 5: radiation monitor, 6:  $^{137}\text{Cs}$  source. 7: lead housing of source. 8: concrete shielding [Ago00].

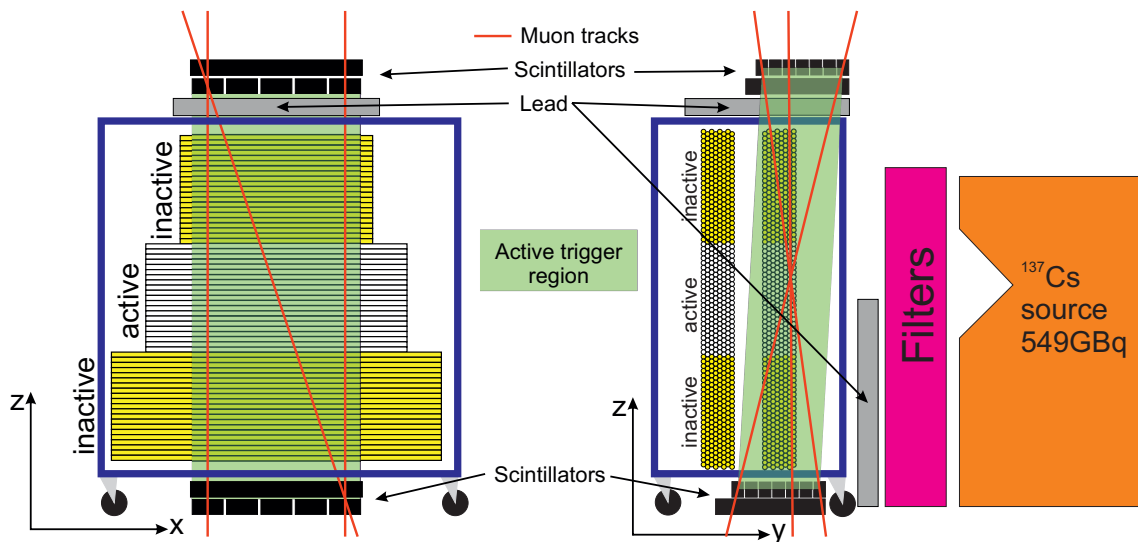


**Figure 9.3:** Test setup of the sMDT chamber at the GIF (left:front view, right side view). The trigger coverage is chosen to maximise the cosmic muon rate with non vertical tracks in the region with the highest achievable counting rate.

To reject muons with very low energies, a lead shielding is mounted underneath the top scintillator that only stops low-energy muons, but unfortunately muons passing the absorber also lose energy. It was not possible to install the lead absorber underneath the sMDT chamber because of space limitations. The multiple scattering effects remain large, especially since the muons have to cross up to 72 tube layers and not only 16 as in the test-beam and for the wire position measurement.

The trigger coverage is defined by two blocks of scintillation counters [Ado10]. The goal was to cover the whole multilayer close to the source and to trigger mostly on muons traversing the region with highest irradiation rate. The geometry of the trigger hodoscope allows for inclined tracks in the interesting region. Problems arising from almost vertical tracks are discussed in section 9.4.

The data taking revealed several problems with the setup. The most important one was the maximum counting rate the MDT electronics can handle. During the design phase of the ATLAS MDT readout, the maximum hit rate per tube was estimated to be 300 kHz. If the rate grows beyond that value, the TDC can still handle the data rate, but the bandwidth of the transfer line between the TDC and the CSM is too small. Not all data in the TDC buffer can be transferred to the readout system and parts of the hits is lost. Figure 9.4 shows the difference between the drift time spectra in the two multilayers. Multilayer 1 is close to the source and shows high counting rate in many channels, multilayer 2 is further away leading to lower hit rates in the tubes. For the  $\gamma$  background a flat time distribution is expected since the arrival of the photons is not related to the cosmic muon trigger. This behaviour is observed in the second multilayer. The first one, however, shows a decrease in the background counting rate for larger times indicating the loss of hits. To solve this problem, two approaches were used to reduce the data rate:

- Shortening of the readout window from 1200 ns to 300 ns and
- Switching off channels on the mezzanine cards in the irradiated region.

Figure 9.5 shows the difference in the number of hits in two typical events with short and with long readout window. Hits outside of the expected time window for muon hits

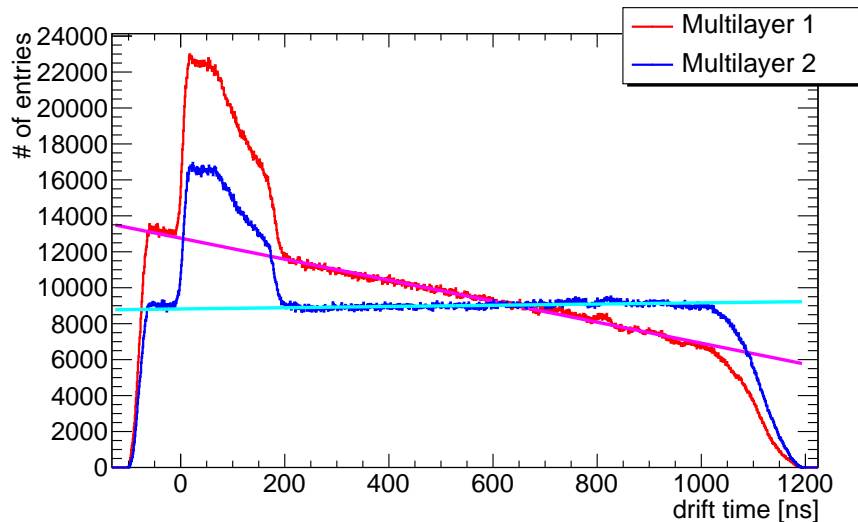


**Figure 9.4:** Drift time spectra in the two multilayers of the sMDT chamber. Multilayer 2 shows the expected flat background hit time distribution on which the triggered muon drift time spectrum sits. Multilayer 1 shows a decreasing background hit time distribution indicating that a fraction of hits is not recorded.

(the maximum drift time after the trigger signal) are marked in red. Their number is reduced significantly for the shorter readout window and the total data volume is much smaller. This is another advantage of the sMDT chambers compared to the ATLAS MDT system: the possibility of using a shorter readout window because of the shorter maximum drift time to reduce the data rate and the required bandwidth of the readout electronics. Unfortunately the reduction in the data rate was not enough for the readout bandwidth.

Switching off channels strongly reduces further the rate per mezzanine card and TDC. 16 of the 24 channels on each mezzanine card in the irradiated region were turned off keeping the tubes with the highest rates in the readout for the performance studies. The shielded part of the chamber already has low counting rate and the amount of data is low enough for the full data transfer at the available bandwidth (below 300 kHz per tube is the design value for the MDT electronics [Pos07]).

The location of the deactivated channels is illustrated in Figure 9.6. The measured counting rate in channels on mezzanine cards with 24 active channels in the irradiated tubes in the multilayer closer to the source, is lower than in the irradiated part of the other multilayer despite the larger distance to the source (see also Figure 9.15(b)). This is an indication that the electronics in this region suffer from saturation of the bandwidth. Channels belonging to a readout board with shielded or disabled tubes show a significantly higher counting rate at the same irradiation flux. The analysis therefore focuses on the small region of the sMDT chamber with high irradiation rate but no bandwidth saturation. 28 000 triggers were taken with the optimum electronics setup.

### 9.3 Data Preparation

Before the data from the sMDT chamber can be analysed, the trigger system and its effect on the time measurement have to be understood.

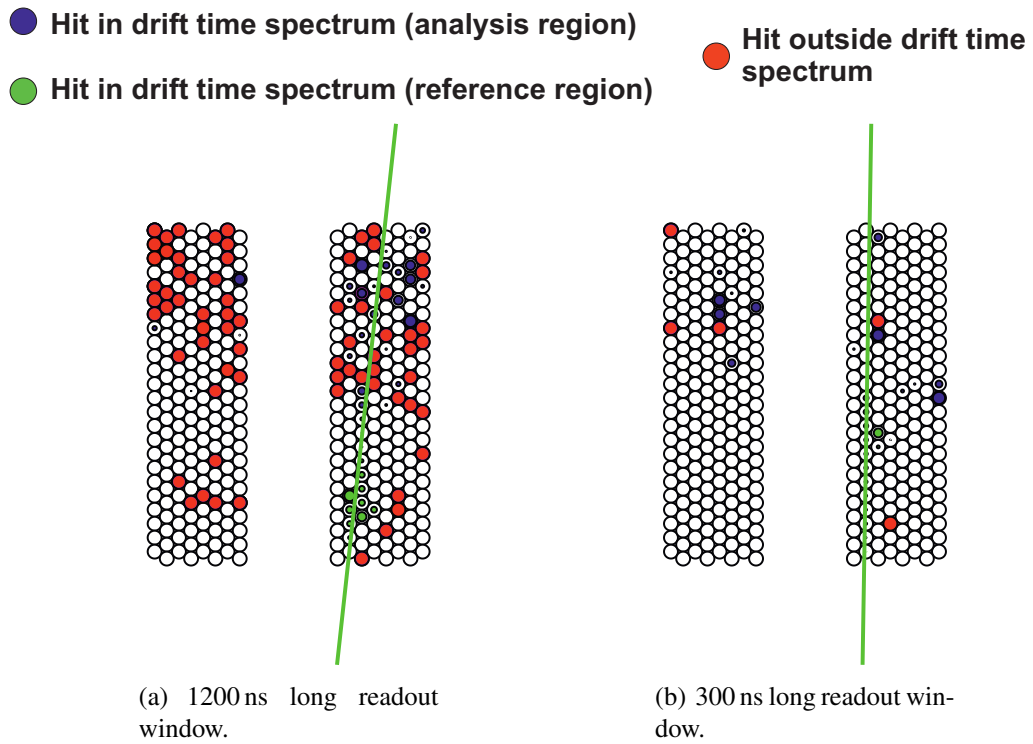


**Figure 9.5:** Occupancy of the chamber for different readout window sizes the same background radiation flux. Each picture shows one event.

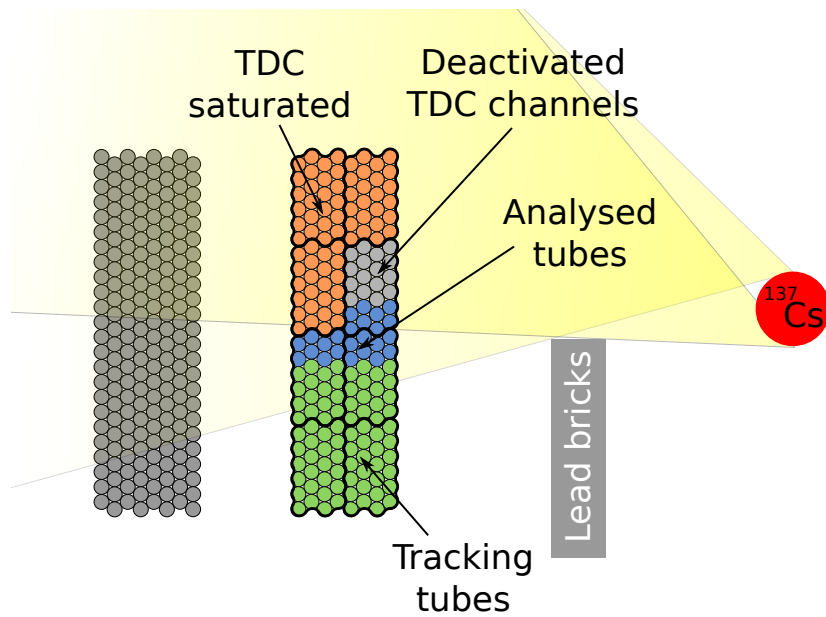


**Figure 9.6:** The different readout regions of the sMDT chamber in the GIF test [Sch10].

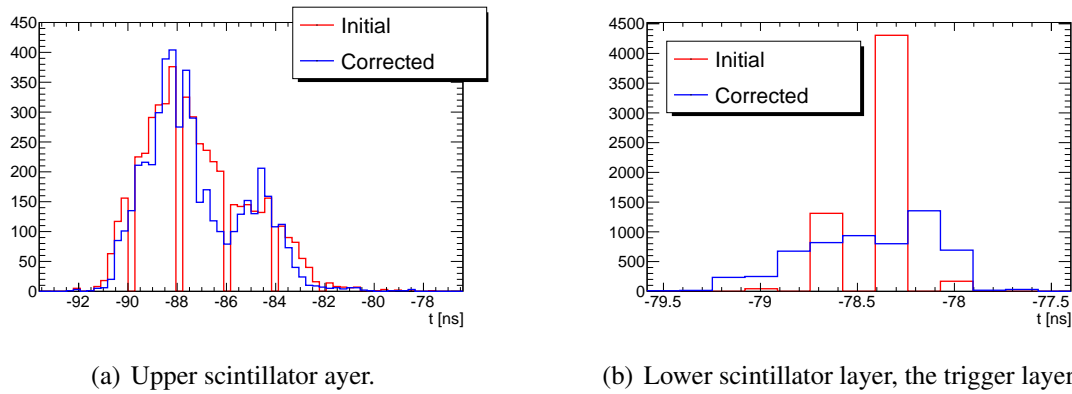


**Figure 9.7:** Time distribution of the signals of the trigger scintillators perpendicular to the tubes before and after correction for the light travel time. Note the different scales on the time axis.

### 9.3.1 The Trigger Hodoscope

Before the data analysis, the timing of the trigger hodoscope and its alignment relative to the test chamber have to be verified. Exactly one hit in each of the four scintillator layers is required for a reliable trigger signal which is not caused by background hits.

The hodoscope consists of two layers of scintillators parallel to the tubes and two layers perpendicular to the tubes as shown in Figure 9.3. The position information of the trigger hits in the parallel scintillators defines a trigger road within which the muon track is expected (for details see next section). The time measurement of these two layers is not used, the perpendicular layers define the trigger timing. They also allow for reconstruction of the second coordinate of the track along the tubes.

The parallel scintillators only have to be aligned relative to the sMDT chamber. This is done by comparing the extrapolated track points from the sMDT chamber to the position of the scintillator layer. The accuracy of the track extrapolation is better than the scintillator width of 4 cm. Combining the track residual information with the constraint that the distance between two adjacent scintillators is known with an accuracy of one millimetre allows for a good alignment accuracy of about 1 mm.

For the scintillators perpendicular to the tubes no alignment with tracks is possible because the sMDT chamber provides no position information along the tubes. Therefore the position of the middle scintillator was chosen to coincide approximately with the centre of the sMDT chamber in  $x$  direction. A relative displacement results in a systematic shift of the drift time in the sMDT tubes. Such a shift is, however, taken into account and corrected by the  $t_0$  determination and thus the absolute alignment does not have to be more accurate than a few centimetres.

The timing for the perpendicular scintillator layer is also important. The red histograms in Figure 9.7 show typical time distributions of the signals of one of the scintillators for the second coordinate information in the upper and in the lower layer. The time spectrum for the upper layer is very broad, whereas the lower layer has a very sharp peak with a width determined by the time resolution of the TDC of about 0.3 ns. The peak in the lower layer is due to the fact that this layer is chosen to define the trigger time. Figure 9.8 illustrates the timing of the trigger input channels. All signals from the hodoscope are routed through a discriminator with a variable output pulse length. The signal from the lower layer at  $t_2$  is delayed relative to the one from the upper layer at  $t_1$ . For the upper

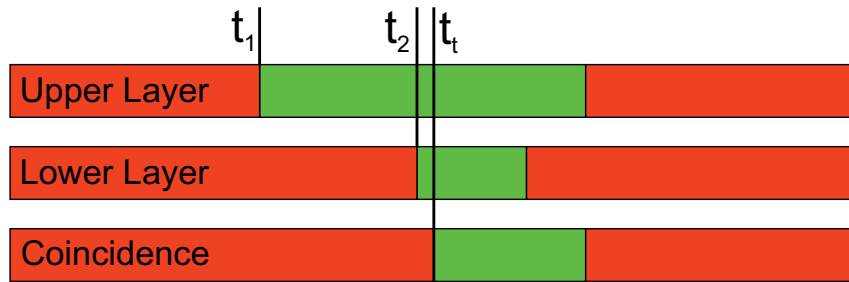


**Figure 9.8:** Timing diagram of the trigger hodoscope (see text).

layer a long output pulse is generated to ensure overlap with the signal from the lower layer. The coincidence unit looks for a signal in both channels and generates the trigger signal at  $t_t$ . The offset  $t_t - t_2$  is due to processing time of the electronics and is constant. The difference  $t_t - t_1$  includes several systematic offsets

- light travel time in the scintillator (variable),
- different cable lengths (constant) and
- influence of which scintillator was hit (constant),

and is not constant.

The light travel time in the scintillator can be corrected for by using the position information from the parallel scintillators with a resolution of about 5 cm corresponding to a time resolution of 0.2 ns which is a factor of 5 smaller than the maximum light travel time of 1.0 ns. Comparing the time spectra from the scintillators in the upper and lower layer before and after the light travel time correction in Figure 9.7 shows that the spectrum for the trigger layer becomes wider while the spectrum for the upper layer starts to show several peaks. This peak structure is caused by different cable lengths connecting lower trigger scintillators to the readout. Plotting the time spectrum for one scintillator in the upper layer versus the corresponding active scintillator in the lower layer (Figure 9.9(a)) shows that the distribution is a combination of several peaks (Figure 9.9(b)). Now it is possible to determine a time correction for every combination of upper and lower scintillators. Figure 9.9(b) shows the effect of this time correction for one scintillator in the upper layer: now the time distribution is independent of which scintillator combination is hit by the muon track.

The final step is to correct the lower trigger scintillators times for different cable lengths. Figure 9.10(a) shows the difference of the measured time in the upper ( $t_1$ ) and lower ( $t_2$ ) hodoscope layer for the different lower scintillators. After correcting for the different cable lengths at the lower scintillators all time differences peak at zero (Fig. 9.10(b)).

The data from the hodoscope used for the analysis are the trigger time correction, the trigger road in the  $y$  direction and the second coordinate measurement in the  $x$  direction along the tubes.

### 9.3.2 sMDT Chamber

The drift time measured in the tubes is corrected for the trigger time correction and the signal travel time along the wire obtained from the second coordinate measurement. Now

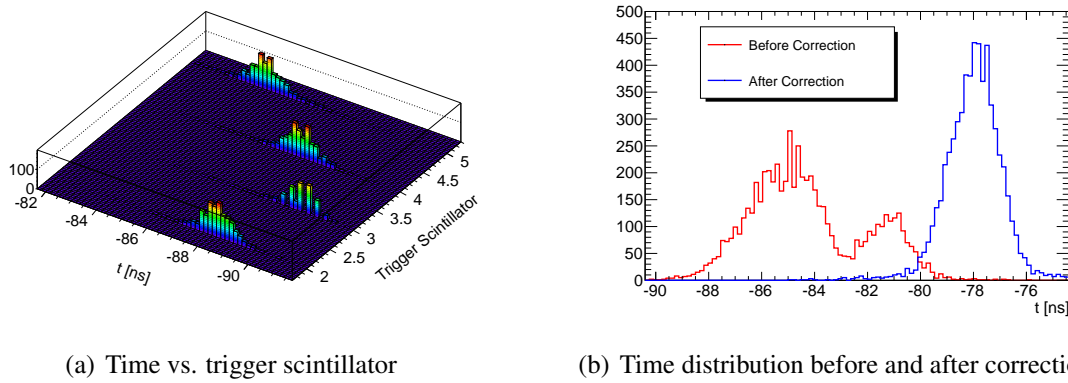


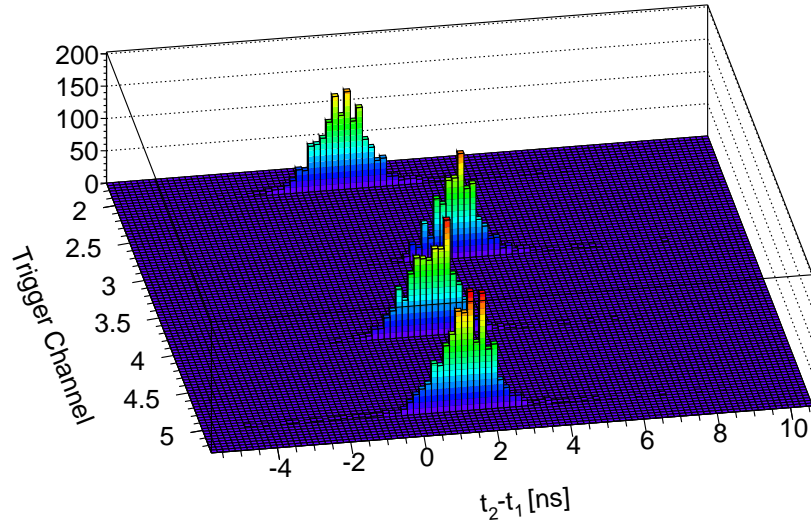
**Figure 9.9:** Correction of the time of one scintillator of the upper layer time for the cable lengths of the lower scintillators.

the  $t_0$  parameters can be determined. Unlike for the test beam measurements, there is now a high background counting rate and a relative small number of hits for each tube from the cosmic ray tracks (see also Fig. 9.11). Therefore it is not possible to fit the drift time spectrum for each tube to determine  $t_0$  and a different approach was chosen. The drift time spectra of all tubes in the reference part (see Fig. 9.15) were combined to determine  $t_0$  of the chamber. Using this method leads to a systematic uncertainty: the flight time of the muon. The active part of the sMDT chamber is 37 cm high corresponding to a flight time difference of 1.2 ns. Using the position information for each tube, this effect can be corrected for.

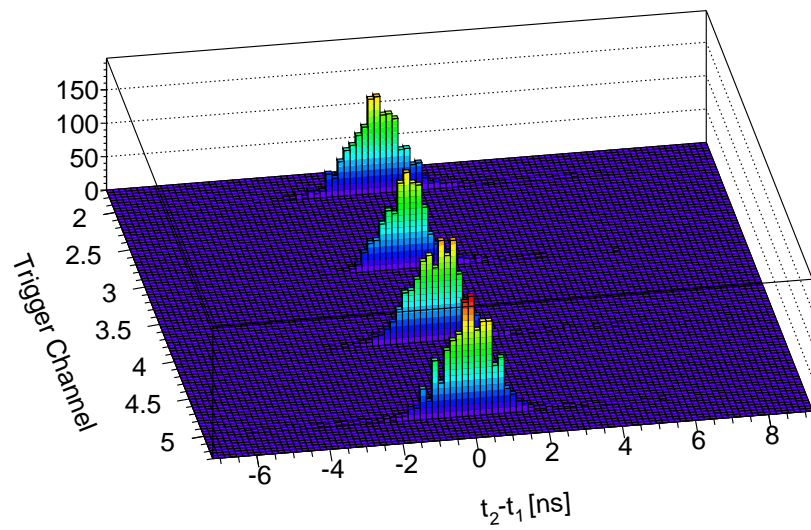
The next step after the measurement of  $t_0$  is the  $r(t)$  calibration. Since the spatial resolution decreases and also the  $r(t)$  relation changes at high background rates, only hits in the reference region were used to fit the tracks used in the calibration algorithm. Cosmic muons have the advantage that the tracks have different incidence angles and a combination of runs like for the test beam measurement is not necessary. To account for varying temperature, the data set was split into blocks of 7 000 events calibrated separately.

To facilitate track reconstruction for the calibration, the information from the trigger hodoscope is used to define a trigger road. If the position of the active scintillators above and below the chamber is known, hits in the sMDT chamber are sorted into two categories: close to the expected path of the muon and outside this region. The second type is neglected for the track fit. Another advantage of the trigger road is the possibility to cross-check the fit result. If the extrapolated track point in the upper or lower hodoscope layer differs from the position of the active scintillators, the reconstruction failed. An example for such an event is shown in Figure 9.12(a). This happens mostly for nearly vertical tracks traversing only one tube layer. In this case there is a left–right ambiguity with respect to the wires the fitter cannot resolve. If also adjacent tube layers are hit, the reconstruction works perfectly as shown in Figure 9.12(b). The possibility to use this constraint is the reason for the already discussed hodoscope alignment. The number of tracks failing the quality criteria is given in Figure 9.17 and is discussed in section 9.4.

Another important ingredient is the determination of the hit rate in the individual tubes. For this measurement one has to rely on the hits recorded in the sMDT chamber. The rate  $\rho$  in one channel is determined by the number of hits  $N_{\text{hits}}$  recorded within a time



(a)



(b)

**Figure 9.10:** Time difference between lower and upper trigger layers for the different lower scintillators before (a) and after (b) correction for different lower scintillator cable lengths.

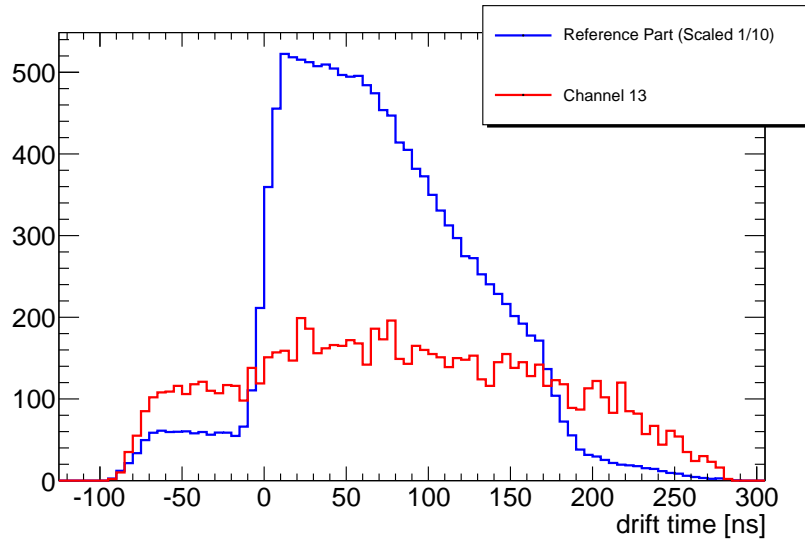


**Figure 9.11:** Combined drift time spectrum for all tubes in the reference part of the sMDT chamber (blue, rescaled by 0.1) and the spectrum of the tube with the highest counting rate (red, channel 13). The muon drift time spectrum is hardly distinguishable in the second case.

window  $\tau$  divided by the total number of events  $N$ .

$$\rho = \frac{N_{\text{hits}}}{\tau \cdot N} . \quad (9.1)$$

Since the hodoscope is triggering on muon signals, the probability of finding a hit within the time window of the drift time spectrum is higher than finding it outside which would bias the measurement towards higher counting rates. The region after the maximum drift time  $t_{\text{max}}$  is also not suitable, because the muon hit induces a dead time in the electronics of about 200 ns and will mask hits arriving shortly after the arrival time of the muons. Therefore the time range before  $t_0$ , from  $t_s = t_0 - 70$  ns to  $t_e = t_0 - 10$  ns, was chosen (cp. the time spectrum in Figure 9.11). The dead time of the electronics can also have an effect on the number of hits registered in this examined time window. Figure 9.13 shows the distribution of the time difference between two successive hits in the same tube.

The dead time of the chips has two contributions: an adjustable dead time and the time the channel is blocked by the incoming pulse and for the ADC measurement of the signal height and can not process the next one. The first part is constant and set to the minimal value of 17 ns for this measurement. The length of the second part varies depending on the signal amplitude. The maximum of the distribution is reached at 200 ns and is used as the electronics dead time for the analysis in agreement with the result for the ATLAS MDT chambers [Hor06].

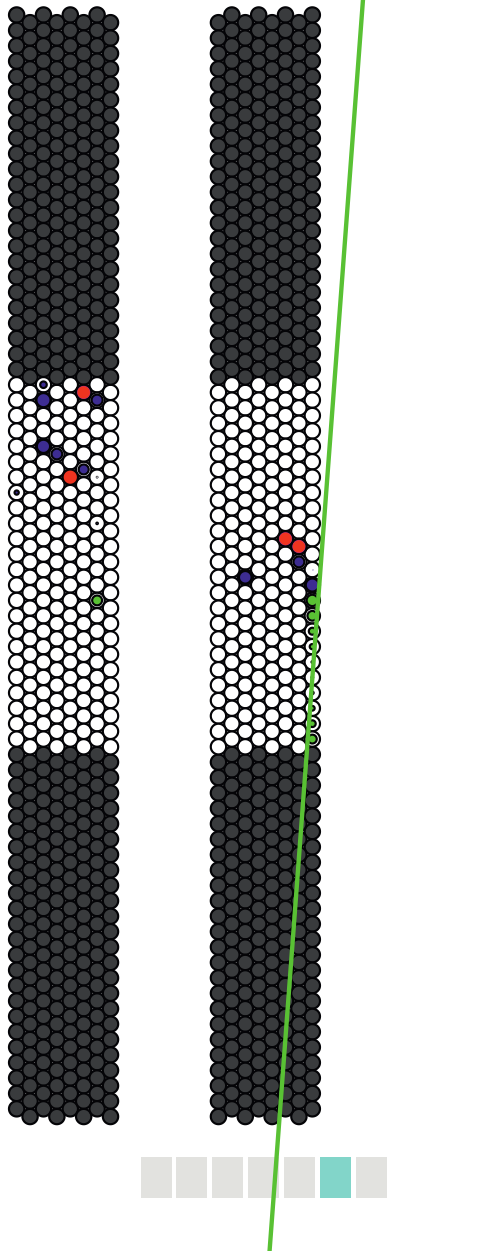
To correct for the loss of hits caused by the dead time, it is assumed that every detected hit causes a fixed dead time  $t_d$ , thus reducing the effective length of the integrated readout window for all events from  $N \cdot \tau$  to  $N \cdot \tau - N_{\text{hits}} \cdot t_d$  resulting in:

$$\rho_{\text{cor}} = \frac{N_{\text{hits}}}{\tau \cdot N - N_{\text{hits}} \cdot t_d} . \quad (9.2)$$

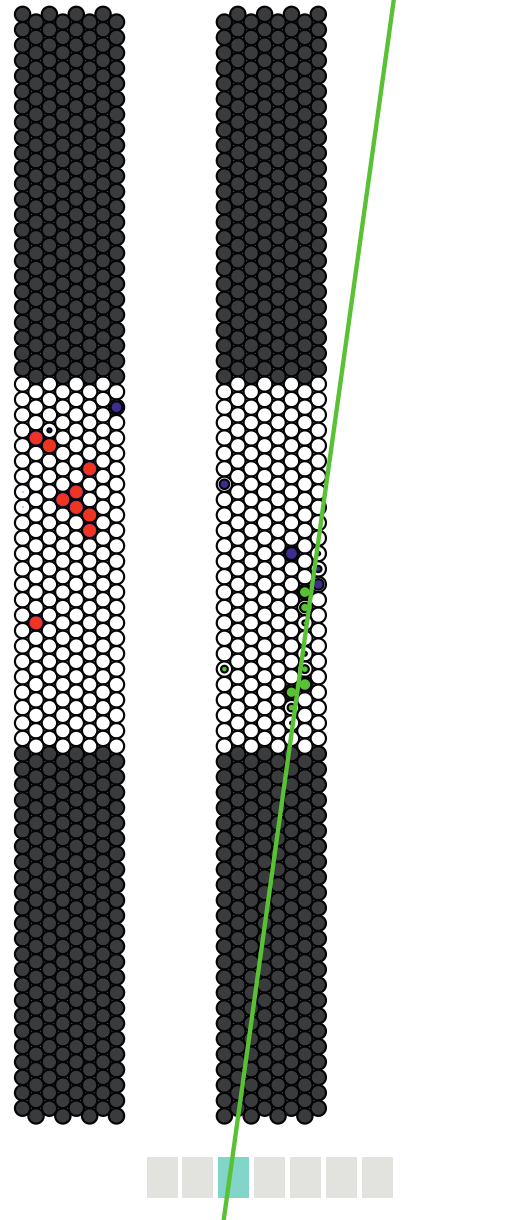
- Hit in drift time spectrum (analysis region)
- Hit in drift time spectrum (reference region)
- Hit outside drift time spectrum

**Event: 106**

$m = 0.074390$   
 $b = 148.801923$   
 $c^2 = 4.026778$

**Event: 160**

$m = 0.138891$   
 $b = 137.382786$   
 $c^2 = 9.786497$



(a) Track reconstructed on the wrong side of the wires pointing far away from the active scintillators. Only the very right tube layer was hit by the muon track in the reference region.

(b) Correctly reconstructed track hitting the active scintillators. Two adjacent tube layers were hit in the reference region.

**Figure 9.12:** Event displays for wrong and correct track reconstruction. The active scintillators are marked in cyan.

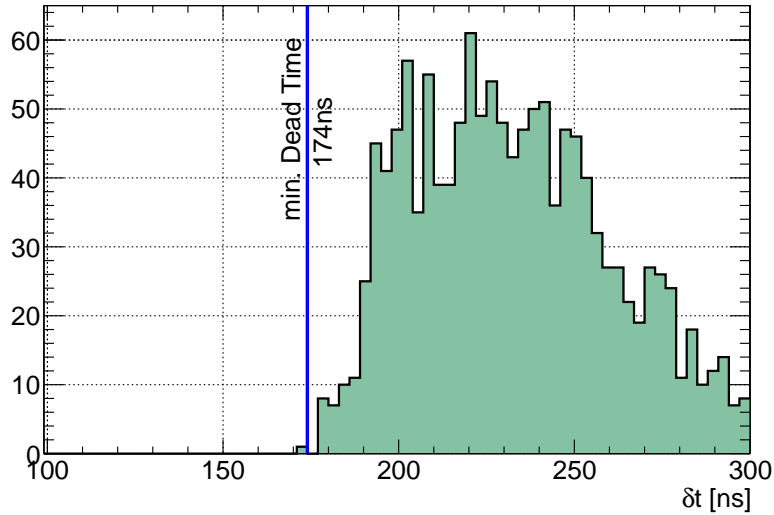


**Figure 9.13:** Time difference between two successive hits in a tube.

Using Equation (9.1), Equation (9.2) can be transformed into:

$$\rho_{\text{cor}} = \frac{\rho}{1 - \rho \times t_d} . \quad (9.3)$$

The validity of this correction for the given values of  $N = 28\,000$  and  $\tau = 60\text{ ns}$  was verified with a toy Monte-Carlo simulation. For input rates in the range of up to  $\rho_{\text{in,max}} = 1\,500\text{ kHz}$ , 28 000 events each were simulated.

The expected number of hits  $\langle N_{\text{hits}} \rangle$  for one event within a  $\tau_f = 4\ \mu\text{s}$  long window starting at  $t_1 = t_0 - 2\ \mu\text{s}$  for the input rates  $\rho_{\text{in}}$  is chosen randomly using a Poisson distribution with mean  $\langle N_{\text{hits}} \rangle$ . The time for each hit is also chosen randomly according to flat distribution. Now the effect of the dead time is simulated. If the time difference  $\delta t$  to the next hit is smaller than  $t_d$ , the second hit is lost. The time difference is always calculated with respect to the last detected hit, since not detected hits will not induce a dead time. The first hit in the event can not be masked by a preceding hit. To avoid a bias of this effect the simulation is started about  $2\ \mu\text{s}$  before the active time window  $\tau$  to allow an equilibrium between detected and masked hits in the examined region.

The active time window used to calculate the rate was set to  $\tau = 60\text{ ns}$  starting at  $t = -70\text{ ns}$ . Counting the number of detected hits  $N_{\text{det}}$  for  $N$  simulated events allows to calculate the detected rate  $\rho_{\text{det}}$  given by

$$\rho_{\text{det}} = \frac{N_{\text{det}}}{N \times \tau} \quad (9.4)$$

and corresponds to the rate detected in a tube. The relative difference  $(\rho_{\text{det}} - \rho_{\text{in}})/\rho_{\text{in}}$  is shown in Figure 9.14. With increasing rate more hits are masked and the difference between  $\rho_{\text{det}}$  and  $\rho_{\text{in}}$  grows. Applying the correction from equation (9.3) eliminates the difference between  $\rho_{\text{in}}$  and the corrected rate  $\rho_{\text{cor}}$  within the error limits, therefore validating the correction function for the given time window and number of events.

Using the verified correction, it is now possible to measure the counting rate in the sMDT tubes. First the rate without any irradiation from the gamma source is measured to

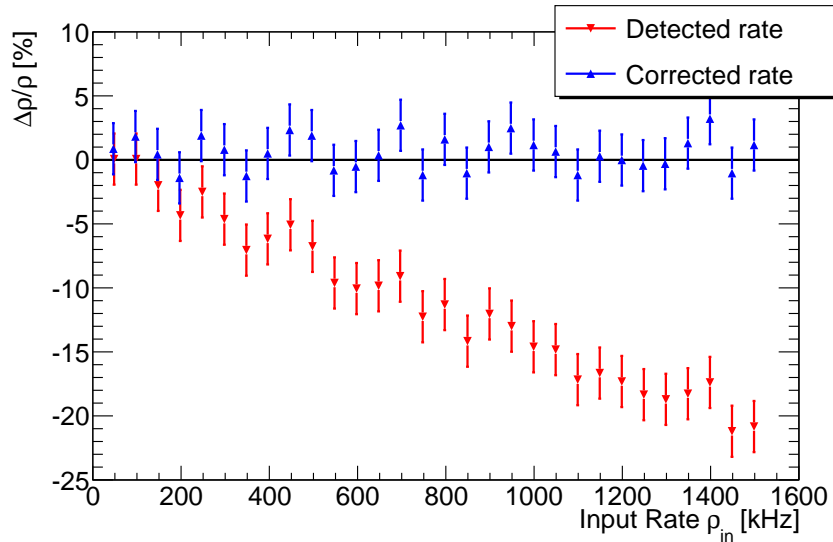


**Figure 9.14:** Red data points show the relative difference to the input rate of the uncorrected measured rate  $(\rho_{\text{det}} - \rho_{\text{in}})/\rho_{\text{in}}$ , blue points the same quantity for the rate corrected according to eq. (9.3)  $(\rho_{\text{cor}} - \rho_{\text{in}})/\rho_{\text{in}}$ .

verify that the electronics is not subject to a high noise rate. These noise hits are produced inside the electronics by thermal noise or from some external source that leaks through the Faraday cage. The maximum noise rate is 17.4 kHz, the distribution of the noisy channels in the chamber is shown in Figure 9.15(a). Tubes with a high noise rate are located outside the analysis and the reference region and will not have any influence on the measurement of the counting rate in the tube or the efficiency.

Figure 9.15(b) shows the different rates for the whole chamber with maximum  $\gamma$  irradiation after the dead time correction. The switched off tubes on the mezzanine card close to the source are marked white. The lower than expected counting rate in the region with bandwidth problems is visible in the upper part in the right multilayer.

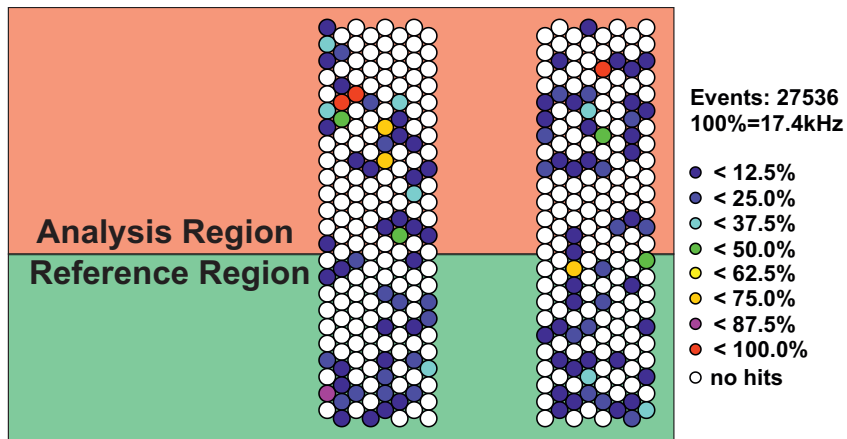
The highest rate measured in the analysis region is  $\rho_{\text{max}} = 1\,363 \pm 27$  kHz. This is equivalent to  $11.95 \pm 0.24$  kHz/cm<sup>2</sup> for the 760 mm long tubes. The rate in the reference region is below 50 kHz per tube and allows a spatial resolution and efficiency at the level of the test-beam measurement.

### 9.3.3 Simulation of the Single Tube Efficiency

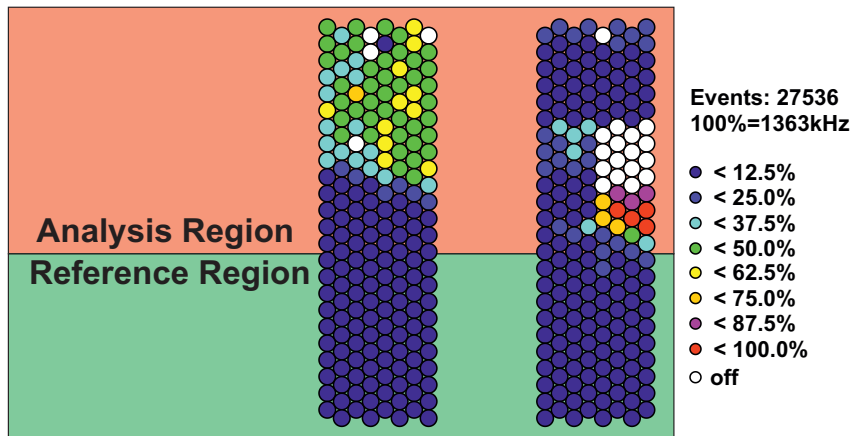
The program used to verify the rate correction factor can also be used to study the influence of the background counting rate on the  $3\sigma$  single tube efficiency. The connection between the dead time and the decrease of the efficiency has already been studied with data in [Rau05]. In this section the assumptions are studied in more detail.

In addition to the background hits, muon hits are simulated. The simulation of these hits takes into account three constrains:

- The maximum efficiency is limited is 94% (96%) for 30 (15) mm diameter tubes due to  $\delta$ -electrons.
- The time distribution is given by the drift time spectrum and

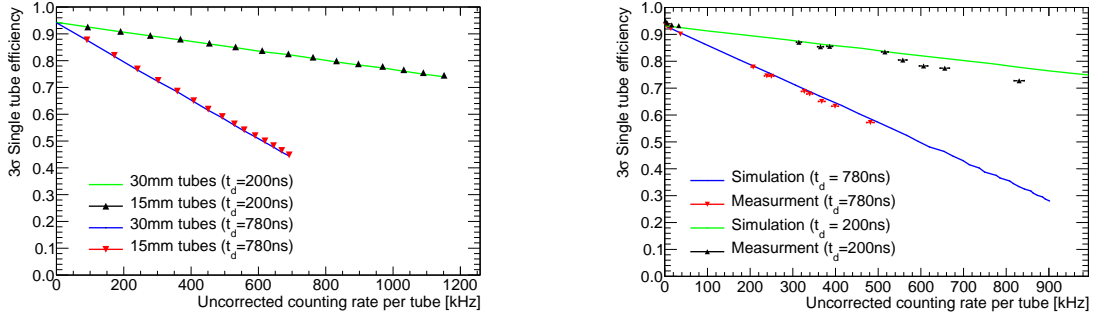


(a) Counting rates for noise hits without photon irradiation.



(b) Counting rates with photon irradiation.

**Figure 9.15:** Counting rate for each tube. Tubes behind the lead shielding (cp. Fig. 9.3 and Fig. 9.6) have a lower rate and are used as reference region. Tubes above this region are combined in the analysis region. White tubes are either switched off ( $4 \times 6$  cluster on the right side) or recorded no hits.



(a) Simulation for 15 mm and 30 mm diameter tubes with different dead times.

(b) Simulation and measurement [Hor06] for the 30 mm diameter tubes with different dead times.

**Figure 9.16:**  $3\sigma$  drift tube efficiency measurements and simulations as a function of the (uncorrected) counting rate for different tube diameters and electronic dead times. All hits in the drift time spectrum are accepted.

- The tube has a limited time resolution.

To simulate the effect of the  $\delta$ -electrons a random number in the interval  $p \in [0, 1]$  is generated. A muon at time  $t_\mu$  chosen according to the drift time spectrum is only generated if  $p \leq 0.94$ . The time resolution of the tube is simulated by smearing out  $t_\mu$  using a random time  $t_r$  generated according to a Gaussian distribution with a width defined by the time resolution of the tube for drift time  $t_\mu$ . The time resolution is calculated from the  $r(t)$  relation and the single tube resolution  $\sigma_s(t)$ . The muon time simulated is therefore

$$t_{\mu,r} = t_\mu + t_r. \quad (9.5)$$

$\sigma(t)$  is calculated using the drift velocity and the spatial resolution  $\sigma_s(t)$  of the tube for a given drift time. The time resolution  $\sigma(t)$  is given by

$$\sigma(t) = \frac{\sigma_s(t)}{v(t)}, \quad (9.6)$$

with the drift velocity  $v(t)$  calculated from the  $r(t)$  relation using

$$v(t) = \frac{dr(t)}{dt}. \quad (9.7)$$

For the application of the dead time the muon hit at  $t_{\mu,r}$  is treated like a background hit and can be masked by an earlier hit. To study the efficiency the number of detected muon hits is counted. Background hits at time  $t < t_\mu$  can fake a detected muon if  $t - t_\mu$  is less than 3 times the time resolution at  $t_\mu$ .

Figure 9.16(a) shows the simulation for 15 mm and 30 mm diameter tubes. For better comparison the efficiency at  $\rho_{in} = 0$  was set to 94% for both diameters. As expected the efficiency does not depend on the properties of the tube as long as the only deteriorating effect is the masking of muon hits.

To verify the simulation, the measurement of the 30 mm diameter tubes with a dead time of 780 ns was simulated. Figure 9.16(b) shows good agreement between the model

and the data points [Hor06]. The amount of background hits being misidentified as muons is below 0.2‰ and therefore completely negligible. The agreement for 200 ns dead time between simulation and measurement is only good for rates up to 500 kHz, the additional efficiency degradation is not covered by this simple model. The most likely explanation is a degradation of the spatial resolution for hits shortly (less than 500 ns) after a preceding hit. Nevertheless the results support the exception that the  $3\sigma$  single tube efficiency for the original MDT tubes and the new sMDT tubes are identical for the same dead time setting and (detected) counting rate in the tube, except a small offset due to the different  $3\sigma$  single tube efficiency at zero background counting rate.

## 9.4 Data Analysis

The analysis follows the same procedure as the test beam analysis. The tracks are reconstructed in the reference region, extrapolated into the analysis region and then compared to the detected hits in the tubes. Compared to the first results presented in [Sch10], the following improvements are made:

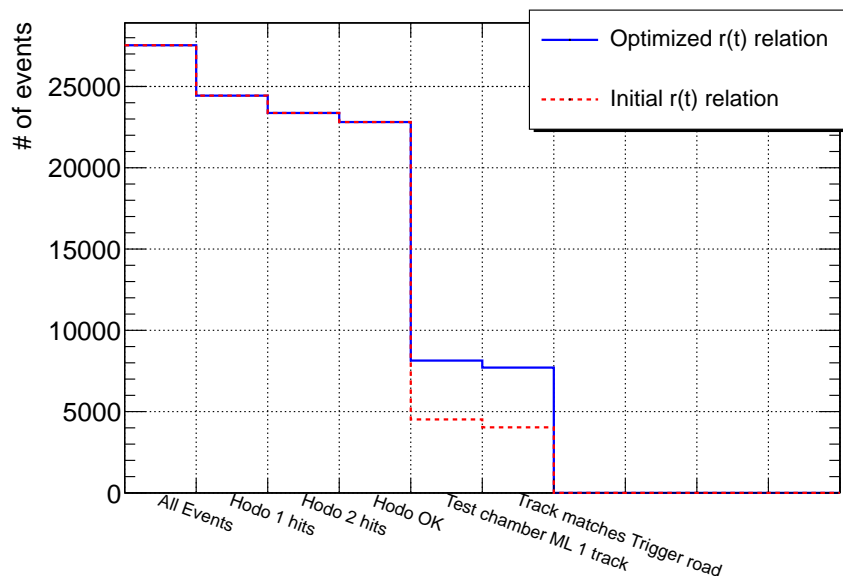
- Improved calibration (temperature and time dependent).
- Known wire position from the cosmic teststand measurement.
- Improved trigger time correction.

Compared to the test beam measurement, the only good data set with high gamma irradiation rates contain a very limited number of good events. Figure 9.17 shows the cut flow for the analysis. Out of about 28 000 events 17% are rejected because of not enough or too many hits per layer in the trigger hodoscope. In only 36% of the events passing the hodoscope selection a track traversing also the reference region is found. Finally 3.3% of the reconstructed tracks are rejected because they do not match the trigger road (see Fig. 9.12).

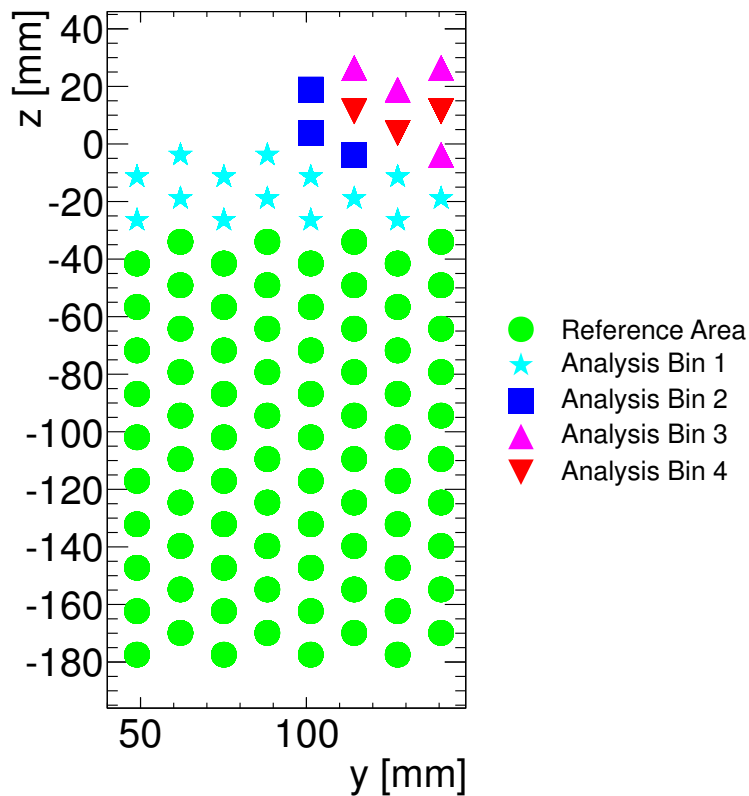
Overall a good track is found in 28% of all events, resulting in 7 711 good tracks usable for the analysis. The cut flow also shows the importance of a good  $r(t)$  calibration: using a non-optimized  $r(t)$  relation reduces the number of tracks found to less than 55% compared to using an optimal calibration because the track fit does not match the quality criteria any more. Since there are 8 tube layers per multilayer in the trigger region each tube will on average be hit by less than 1 000 muon tracks. This does not allow for a detailed analysis of the radial dependence of the resolution and the efficiency.

The location of the analysed tubes is shown in Figure 9.6. To reduce the statistical error, data from tubes with similar background counting rate are combined. Figure 9.18 illustrates the different selections, Table 9.1 lists the criteria for each rate bin.

However, it is not possible to reach the same tracking accuracy as in the test beam because of the smaller number of tube layers in the fit (maximum of 10) and the much lower energy of the muons resulting in a large multiple scattering error. Unlike the wire position measurement, the GIF setup has a much thinner absorber and no possibility to measure the scattering angle in order to reject low energy muons. Also the track extrapolation will have a larger uncertainty because the analysis region is outside of and not embedded in the reference region. The calculated track extrapolation error (cp. sec. 8.5) is shown in Figure 9.19. The track point accuracy decreases with increasing distance to the reference region.



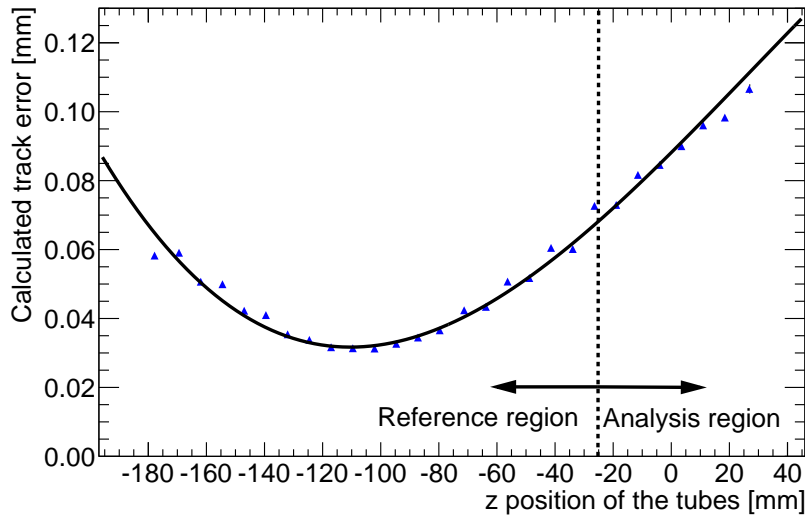
**Figure 9.17:** Cut flow of the analysis before and after application of the optimized  $r(t)$  relation.



**Figure 9.18:** Locations of the tube with comparable background rates belonging to the different analysis regions. The analysis and reference regions of Figure 9.6 are also shown.

**Table 9.1:** Selection criteria for the different analysis bins containing tubes with comparable counting rates.

Bin	Relative rate $\rho/\rho_{\max}$	Rate $\rho$ [kHz/tube]
1	$0\% < \rho/\rho_{\max} < 50\%$	$0 < \rho < 682$
2	$50\% < \rho/\rho_{\max} < 70\%$	$682 < \rho < 954$
3	$70\% < \rho/\rho_{\max} < 90\%$	$954 < \rho < 1227$
4	$90\% < \rho/\rho_{\max} < 100\%$	$1227 < \rho < 1363$

**Figure 9.19:** Position of the different analysis regions.

After the data preparation, first the spatial resolution as a function of the background rate is studied which is then used to measure the  $3\sigma$  efficiency of the irradiated tubes.

## 9.5 Results

The spatial resolution of the tubes in the regions with low background counting rate is taken from the test beam measurement. The large multiple scattering makes it impossible to reach the same accuracy at GIF with cosmic muon tracks and the test beam result from the last chapter is used as reference to estimate the multiple scattering. The widths of the residual distributions for the rate bins and the reference region are shown in Figure 9.20. After subtracting the track extrapolation error the residual width decreases especially for the tubes with large distance to the reference region. To estimate the impact of the multiple scattering, the residual width for the analysis region with the lowest rate is normalized to the expectation for the 15 mm tubes at low rates from the test beam measurement. The corresponding multiple scattering contribution is derived to be  $149.9\ \mu\text{m}$ . Figure 9.21 shows the average spatial resolution (equal to the residual width after corrections) of the 15 mm diameter tubes together with the results for the 30 mm tubes [Kor12] and the predictions (compare Figure 5.6).

The data points are above the expectation for the 15 mm diameter tubes but already show a much smaller increase of the average resolution  $\rho$  compared to the 30 mm diameter

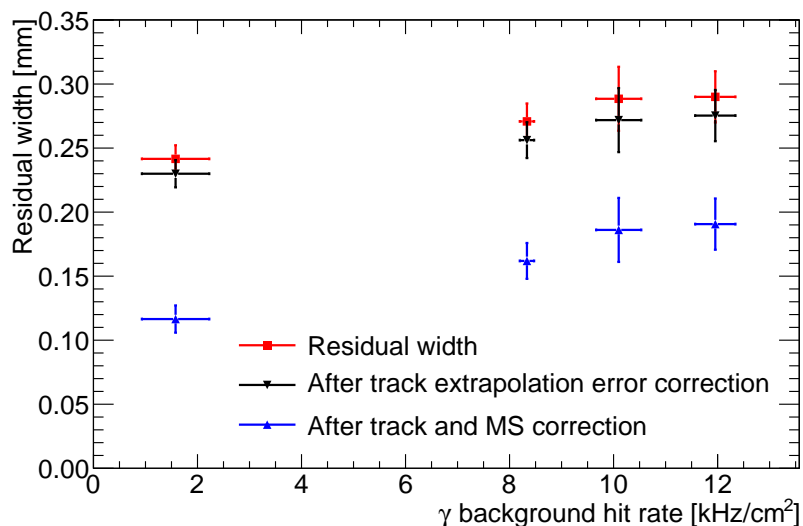


**Figure 9.20:** Measurement of the residual widths for the different rate bins before and after corrections for track extrapolation and multiple scattering errors.

tubes. The relatively large errors are due to the rather low statistics and the uncertainties from the track extrapolation.

Since the multiple scattering contribution was determined from the rate bin with tubes closest to the reference region, the other rate bins have an additional systematic error due to multiple scattering that cannot be determined and is not included in the error bars.

With the measured spatial resolution the  $3\sigma$  efficiency of the tubes under gamma irradiation can be determined. Since the most important effect limiting the  $3\sigma$  efficiency is the masking of muons by background hits, the efficiency is measured as a function of the (uncorrected) counting rate per tube like for the 30 mm $\varnothing$  tubes. For the same dead time one expects the same efficiency for the 15 mm and 30 mm diameter tubes when all hits in the readout window are accepted in both cases (see section 9.3.3).

The test beam result with a value of  $(96.7 \pm 0.1)\%$  was used for the  $3\sigma$  efficiency without radiation background instead of the measurement in the reference region because of the better statistical and systematic precision. The GIF result for the 15 mm diameter drift tubes is shown in Figure 9.22 together with the simulation discussed in Section 9.3.3. As for the 30 mm $\varnothing$  tubes the  $3\sigma$  efficiency is described well by the simulation for background counting rates below 500 kHz per tube. Above that rate the measured efficiency is lower than the simulation (see Sec. 9.3.3 and Fig. 9.16(b)).

Figure 9.23 shows the average  $3\sigma$  tube efficiency of the 15 mm and the 30 mm diameter tubes for different dead time settings and the hit selections as well as the corresponding track segment reconstruction efficiencies for the examples of a 12-layer sMDT chamber and a standard 6-layer ATLAS MDT chamber. The standard ATLAS dead time setting is 780 ns to keep the readout bandwidth required for the transfer of all hits low enough. Changing the dead time to the shortest possible setting of about 200 ns while recording only the first hit in the in the time range of the drift time spectrum increases the efficiency. This setting can only be simulated because the readout electronics always transfers every recorded hit. Using the short dead time and all available hits gives the highest efficiency. These measurements agree very well with the results for the 15 mm $\varnothing$  tubes. These tubes show no difference between using only the first hit or all hits because the dead time is

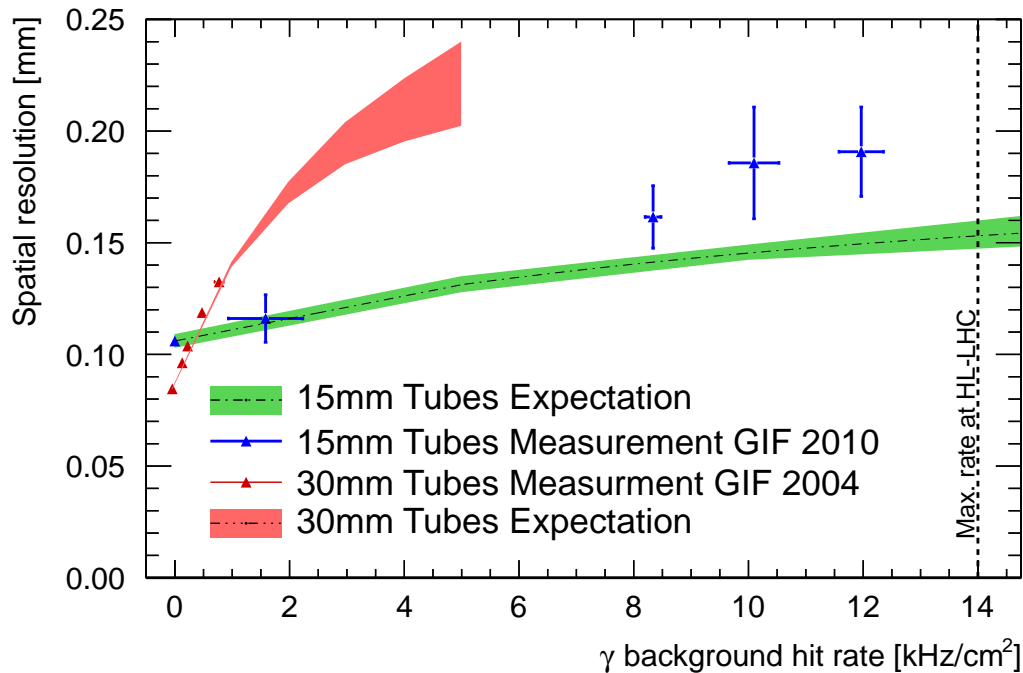


**Figure 9.21:** Average measured resolution of the 15 mm diameter tubes for the different rate bins compared to the results from the 30 mm GIF measurements for the 30 mm $\varnothing$  tubes [Hor06] and the model predictions.

already at the level of the maximum drift time and it is therefore not possible to have a second hit in the tube inside the time range of the drift time spectrum.

The track segment reconstruction efficiency is defined as the probability of finding a given number of hits on a muon track in the chamber within 3 times the drift tube resolution (see Figure 9.23). For a good track one requires at least 4 hits. For the sMDT chambers 6 hits out of 12 layers are required as an example. The standard ATLAS MDT chamber contains only half of this number of tube layers. For both cases the track reconstruction efficiencies as a function of the background hit rate registered in the tubes are shown in Figure 9.24. Here the difference between the new and old technology is even more apparent because of the two times lower exposure of the sMDT tubes to the background radiation. The minimum efficiency 95% requested for ATLAS is reached up to the highest rates expected after the HL-LHC upgrade. For the 30 mm diameter tubes this requirement is already violated at rates of 4 kHz/cm<sup>2</sup> even when using the short dead time. With the long dead time, the limit of the 30 mm $\varnothing$  tubes is at even lower rates.

One problem for the efficiency measurement is the bad tracking resolution in the region with very high background counting rates. This results in a larger error on the single tube efficiency.

## 9.6 Summary and Outlook

The irradiation of the sMDT prototype chamber in the GIF provided a test of the new muon chamber technology under very high background irradiations expected at HL-LHC. The gamma irradiation reached levels of 12 kHz/cm<sup>2</sup>, corresponding to 1.36 MHz/tube. The average  $3\sigma$  single-tube efficiency was measured as a function of the background

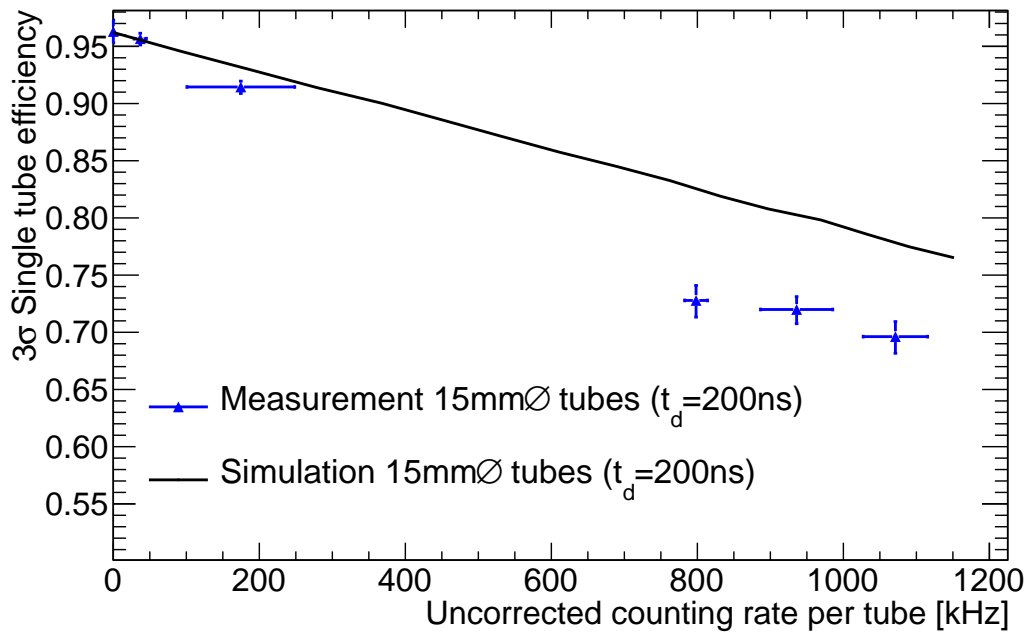


**Figure 9.22:** Comparison of the measured and simulated  $3\sigma$  efficiency for the 15 mm  $\varnothing$  tubes as a function of the background hit rate. The difference between measurement and simulation is expected from the 30 mm  $\varnothing$  tube measurement, see Fig. 9.16(b).

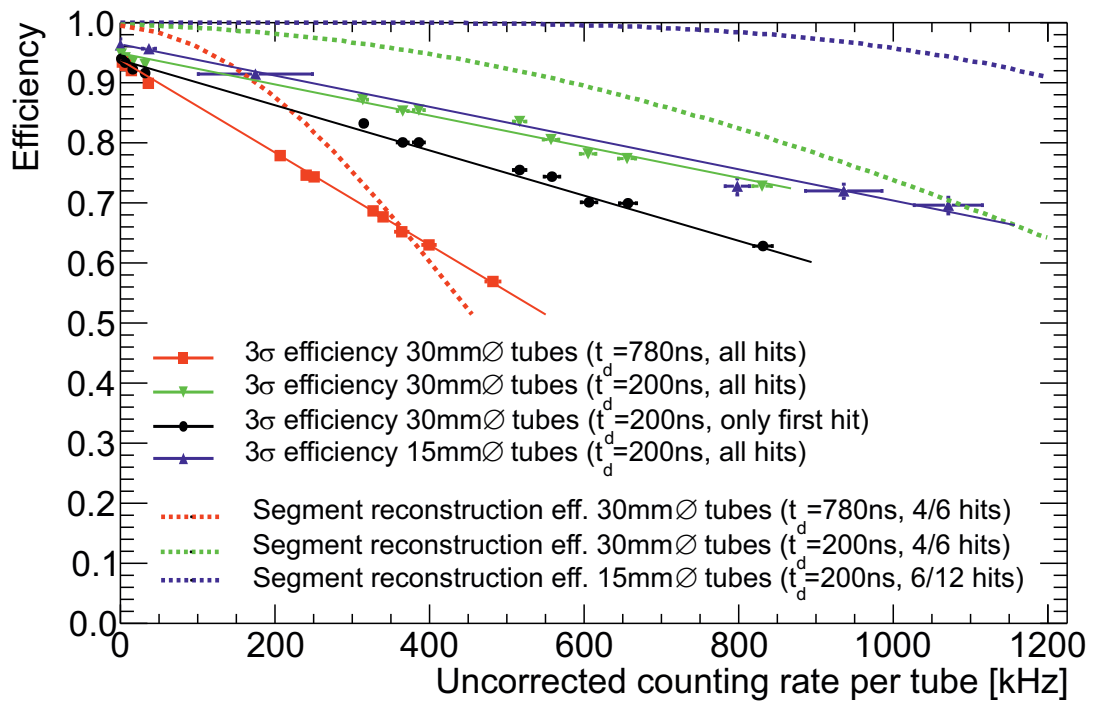


**Figure 9.23:** Mean efficiency of the 15 mm diameter tubes compared to a measurement of the 30 mm diameter tubes with different readout settings.

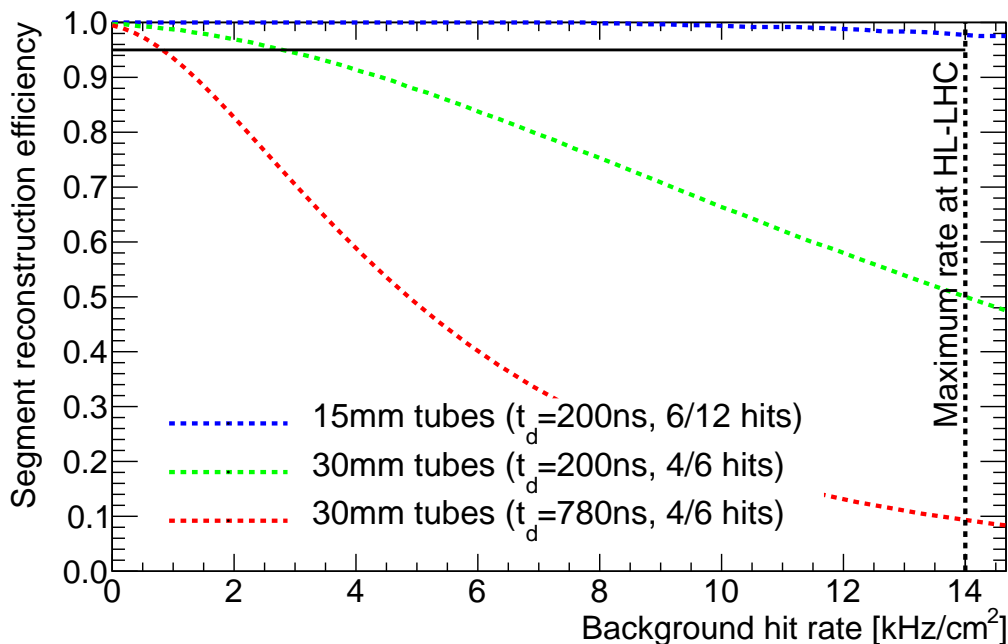


**Figure 9.24:** Segment reconstruction efficiencies in a chamber with 6 layers of 50 cm long tubes of 30 mm diameter and a 12-layer chamber with 50 cm long tubes of 15 mm diameter.

counting rate and is in very good agreement with the expectations from previous tests performed with 30 mm diameter drift tubes. Also the first measurement of the spatial resolution of the 15 mm $\varnothing$  drift tubes at GIF showed the expected behaviour. The deterioration at high background flux follows the expectation, but shows a systematic shift to a higher spatial resolution for high rates. This is most likely caused by a systematic effect caused by problems in the determination of the multiple scattering contribution on the residual with.

The results are still limited by statistics and by systematic constrains from the track extrapolation and multiple scattering corrections. In order to study the drift tube performance in more detail, in particular to perform the resolution and efficiency measurement as a function of the track distance to the wire, an improved setup has been developed taking into account the experience from the presented measurements and has been used for data taking in 2011 (see Figure 9.25).

The test chamber was installed rotated by 90°. The longest tubes, now equipped with readout electronics, could be moved even closer to the source increasing the maximum  $\gamma$  counting rate. The lead absorber placed below the chamber filters more low-energy muons and reduces the multiple scattering effects. The 4 top and 4 bottom tube layers of the chamber are shielded by lead absorbers to act as reference region providing tracks with a lower extrapolation error in the analysis region in the center of the chamber. Furthermore, the bandwidth constrains of the readout electronics have been taken into account from the beginning. To improve the rate measurement, the readout window was extended before the drift time spectrum. This also allows to study the influence on the resolution and efficiency of the time between the muon hit and the preceding background hit. This setup was installed in summer 2011 and a high-statistics data sample has been taken. The analysis is still ongoing and could not be finished within the time-scale of this thesis

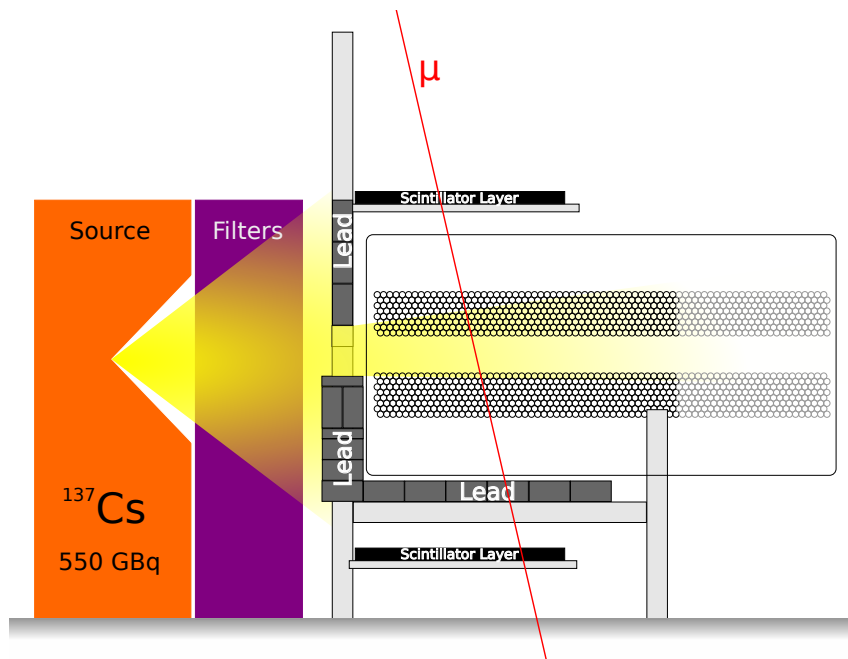


**Figure 9.25:** Improved setup for the 2011 GIF measurement campaign [Sch12b].

[Sch12b], but first results already support the claim that a preceding hit in a tube can have an influence on the resolution of the following hit if the time difference is less than 500 ns.



# Chapter 10

## Conclusions

In order to improve the sensitivity of the LHC experiments for new physics beyond the Standard Model and to study Standard Model parameters even more precise it is planned to increase the LHC luminosity in steps to up to 7 times the design value making it necessary to re-evaluate the performance of the detectors of the expected higher particle and background rates. For the ATLAS muon system, it was found that the innermost detector layer of the forward region will not operate efficiently at the high background rates and has to be replaced. Several detector technologies have been proposed for the replacement. One very promising solution is a modification of the detector system already in use in ATLAS, the Monitored Drift Tube (MDT) chambers. The new sMDT chamber technology contains drift tubes with half the diameter of the ATLAS MDT chambers tubes, i.e. with 15 mm diameter (small), while keeping gas mixture, pressure and gas gain unchanged to allow for easy integration in the existing system. Using the experience with the present system to predict the performance of the new chambers shows that all requirements regarding spatial resolution and efficiency are fulfilled even under the HL-LHC conditions.

To verify these predictions a full sized prototype chamber was built and tested at different  $\gamma$  background irradiation rates in a high energy muon beam and at the Gamma Irradiation Facility GIF at CERN. With straight cosmic ray muon tracks in a cosmic ray test stand at LMU Munich in Garching it was verified that the sense wire positioning accuracy of 20  $\mu\text{m}$  required to provide good spatial track resolution was achieved during prototype chamber construction.

Using the prototype sMDT chamber, the single tube resolution and efficiency without background radiation was studied in a 180 GeV muon beam at CERN. The results agree perfectly with the expectation from the ATLAS MDT chamber performance. The average 15 mm diameter drift tube resolution is  $(106 \pm 2) \mu\text{m}$ , the average  $3\sigma$  efficiency  $(96.7 \pm 0.1)\%$  deviating from 100% because of unavoidable  $\delta$ -rays masking the muon signals.

Tests of the high-rate capability of the new chambers are particularly important for the HL-LHC upgrade. For these measurements, the sMDT prototype chamber was installed in the GIF at CERN and irradiated with a 549 GBq  $^{137}\text{Cs}$   $\gamma$  source. The  $\gamma$ -rates measured in the tubes reached 1.36 MHz/tube corresponding to 12 kHz/cm<sup>2</sup> which is close the maximum expected rates of 14 kHz/cm<sup>2</sup> in the ATLAS muon spectrometer at HL-LHC [Bar05]. The measured efficiency drop is well in agreement with the expectation. The  $3\sigma$  drift tube and track segment reconstruction efficiency as well as the single-tube and chamber spatial resolution fulfil and exceed the ATLAS requirements up to the highest expected background rates of the HL-LHC.



**Part III**  
**Appendix**



# Appendix A

## Readout Scheme of the sMDT Prototype Chamber

This chapter briefly describes the general layout of the readout system used for the sMDT tests. More details and information about the different software packages can be found in [Sch10]. Figure A.1 shows the sMDT chamber and all its connections for data transfer from the chamber to the readout system. The trigger signal is generated by logic modules in the NIM crate looking for hits in the scintillators within a given time window of about 20 ns. This logic can also be adapted to include the trigger signal coming from the TGC electronics.

After trigger generation the information is passed to the VME crate. This crate includes several TDCs<sup>1</sup> and measures the hits from the scintillators and from the TGC. The scintillators are connected to a 16 channel single hit CAEN TDC, the TGCs are connected to two 128 channel multi hit TDCs with the possibility to measure the time of the leading and trailing edge separately. One module translates the trigger signal to the TTC<sup>2</sup> format used for the ATLAS MDT front-end electronics and transfers it via an optical fibre to the CSMs<sup>3</sup> mounted on the chamber. These modules read the TDC and ADC<sup>4</sup> information from the buffers of the mezzanine cards connected to the wires. RPC chambers are also sending their hit information to an mezzanine card connected to one of the CSMs. The information of the CSMs and TDCs in the VME module is collected in the DAQ PC and stored. This data is the basis of the off-line analysis tools and also used to provide an online monitoring of the detector responses.

The parameters for the CSMs and mezzanine cards are set via the JTAG bus serviced by an additional PC. The same bus is also connected to the on chamber temperature sensors used to monitor the environmental conditions. This chamber temperature is sent to the Slowcontrol PC every minute.

Figure A.2 shows all services needed to operate the chamber. The centre of this system is the Slowcontrol PC. It holds the database for the environmental data, controls the HV and gas distribution system and hosts the website displaying the online information from all sensors and detectors. The power supply for the CSMs supplies a low voltage (LV) of 5 V with currents up to 20 A per connection.

---

<sup>1</sup>Time to Digital Converter

<sup>2</sup>Trigger and Timing Control

<sup>3</sup>Chamber Service Module

<sup>4</sup>Analogue to Digital Converter

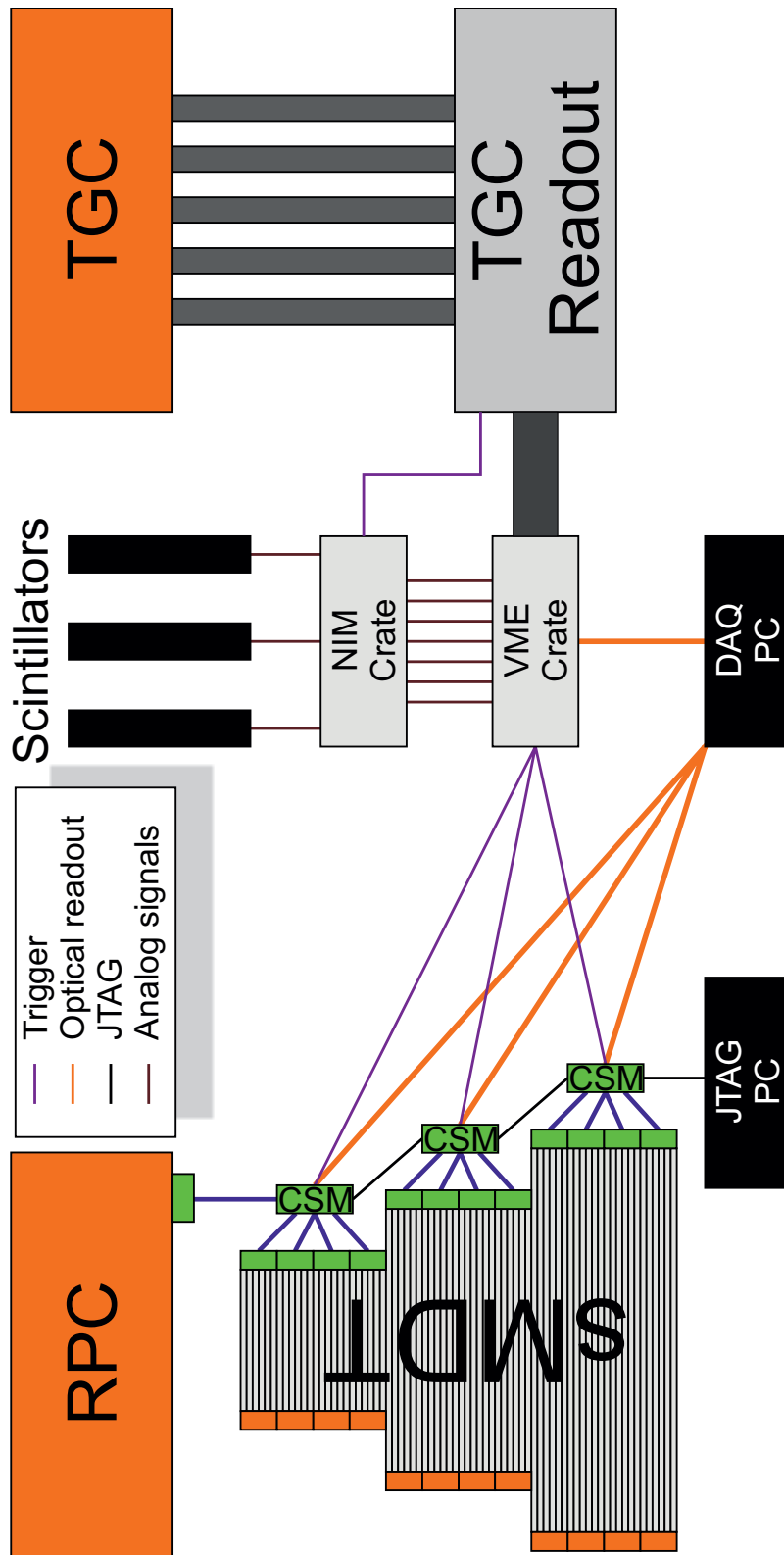
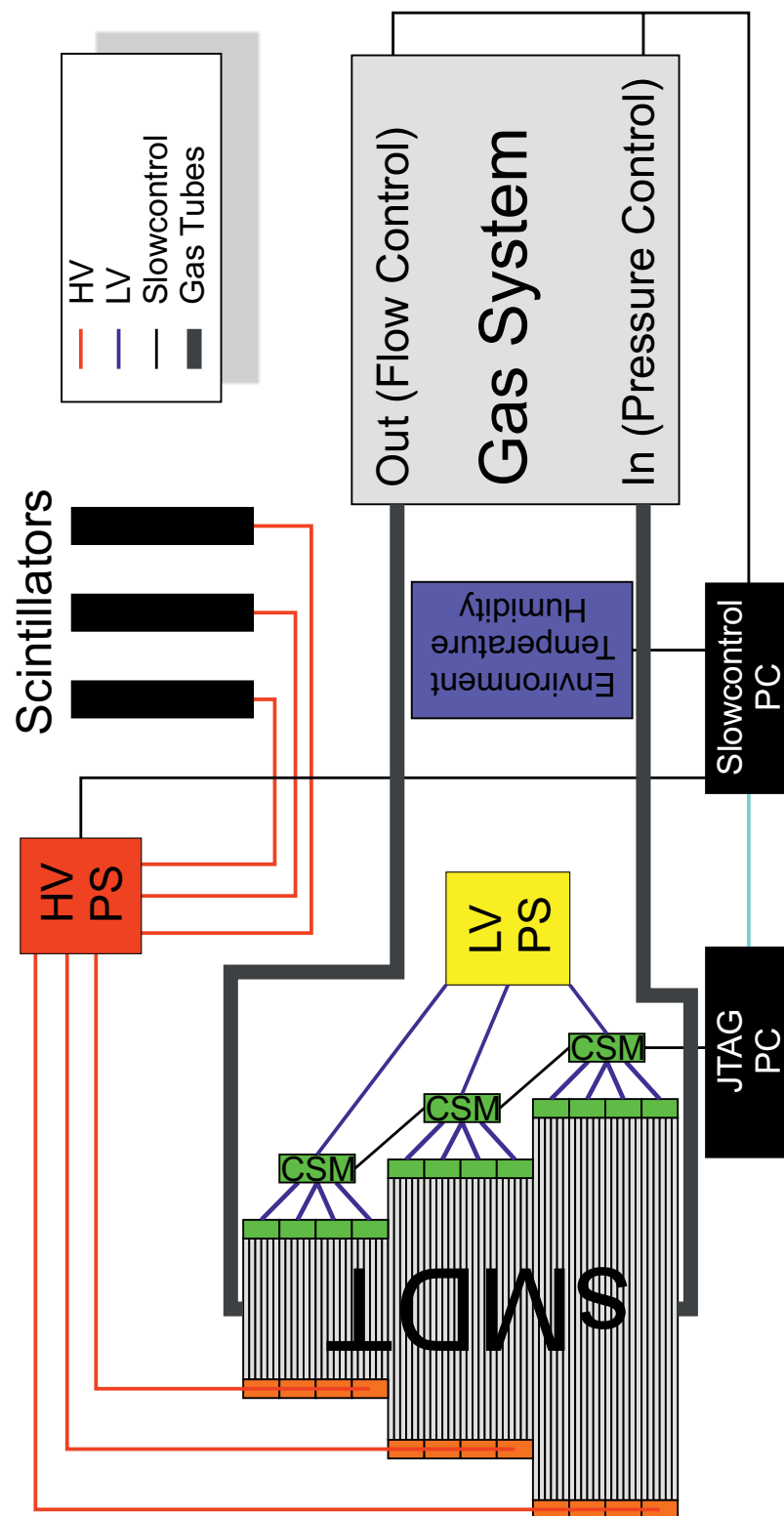


Figure A.1: Overview of the DAQ system used for the tests.



**Figure A.2:** Overview of all connected services.



## Appendix B

# Calibration of the ADC of the MDT Readout Electronics

The response of the ADC<sup>1</sup> is not linear and the response curve has a large spread in the production of the chips. Therefore it is necessary to calibrate the ADC for different input pulses. The technical details can be found in [Pos07].

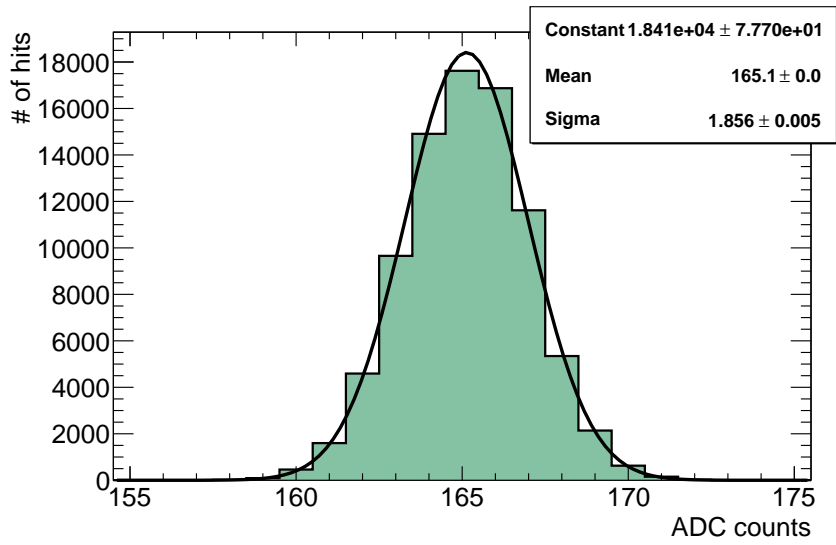
Via the CAN-Bus link (see Appendix A) the calibration mode of the mezzanine cards can be enabled. The chip has 8 built in 50 fF capacitors that can be charged with a fixed voltage of 200 mV, yielding an input signal charge between 10 and 80 fC. The number of capacitors to charge can be selected via the control software. These capacitors are discharged into the ADC when a trigger signal is received. From the response of the ADC to the 8 different charge signals the calibration curve is calculated.

Figure B.1 shows the ADC count distribution for 50 fC (250 fF) input charge for one channel. With a width of  $\sigma = 1.856 \pm 0.005$  counts the response is very uniform. The calibration curve for this channel is shown in Figure B.2. Combining the measurements for different input charges reveals the non-linearity of the ADC to charge conversion. The variation for 24 channels on a single mezzanine card is shown in Figure B.3.

To apply the correction to the data the calibration curves for all channels are read, then the charge corresponding to the ADC counts is determined using the calibration for the active channel. For easier comparison to the raw ADC values the charge is converted back into ADC counts using one specific channel as reference. Figure B.4 shows the width of the overall ADC count distribution before and after the calibration. The width of the distribution is smaller by about 10%, while the mean changes only by less than 3%. The effect is even more apparent when plotting the ADC value against the channel number (Fig. B.5). The mean value of the ADC count distributions before the calibration varies widely, after the calibration the distributions are very similar.

---

<sup>1</sup>Analog to Digital Converter



**Figure B.1:** ADC counts for 250 fF capacity.

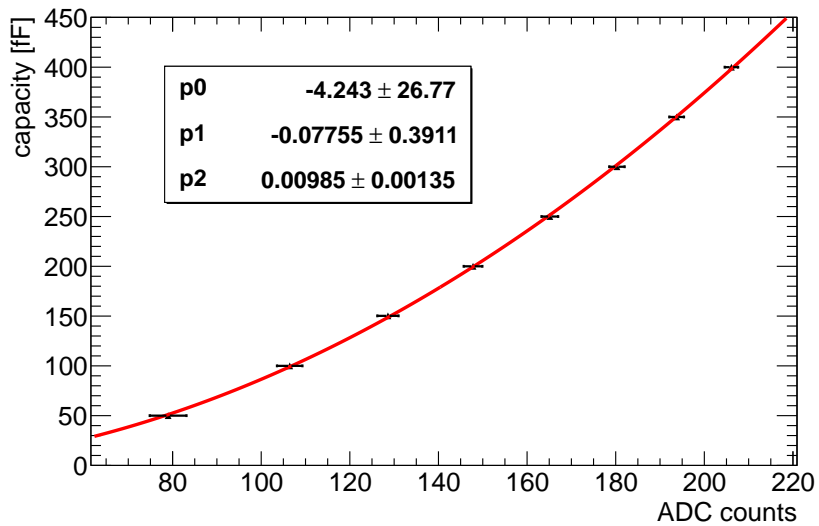


**Figure B.2:** ADC calibration curve for one channel. The measurements for the different input charges are shown.

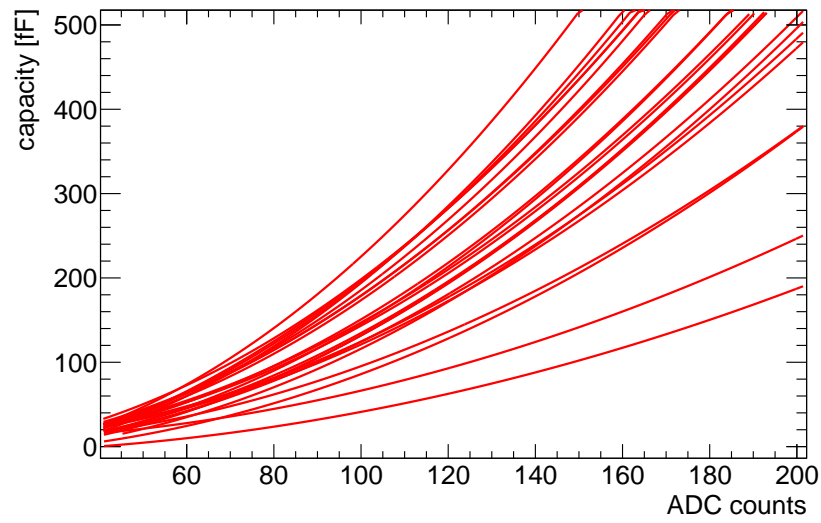


**Figure B.3:** ADC calibration curve for all 24 channels of a mezzanine card. The huge differences of the different response curves are visible.

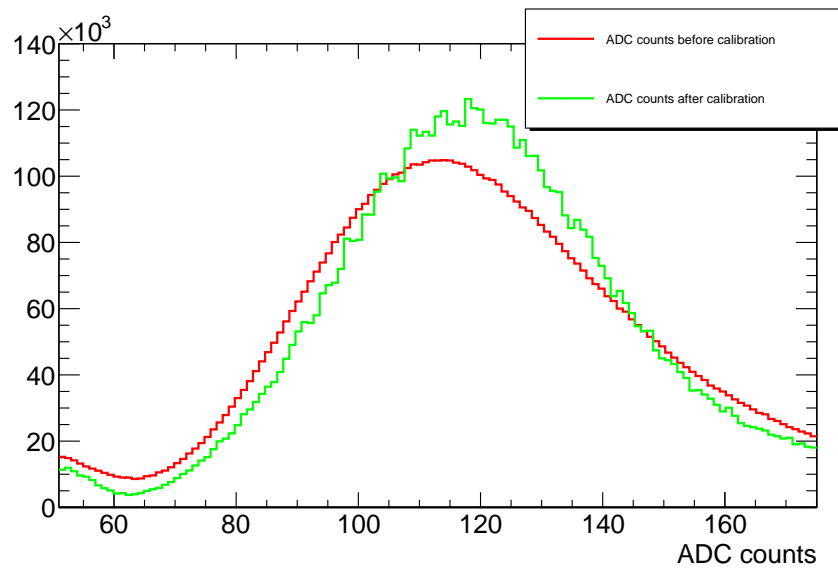


**Figure B.4:** ADC count distribution before and after the calibration.

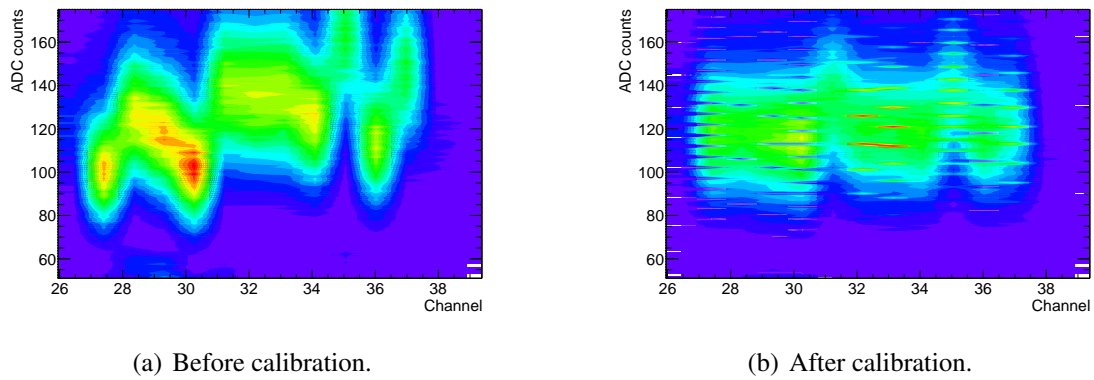


**Figure B.5:** ADC counts for one layer of tubes. The calibration is able to eliminate differences in the ADC count distribution for different channels. The artefacts in (b) are a binning effect.

# Bibliography

- [Ado10] S. Adomeit. *Konstruktion, Bau und Einsatz eines Szintillator-Trigger-Hodoskops*. Diplomarbeit, Ludwig-Maximilians-Universität München, 2010.  
Url: [http://www.etp.physik.uni-muenchen.de/dokumente/thesis/diplom\\_sadomeit.pdf](http://www.etp.physik.uni-muenchen.de/dokumente/thesis/diplom_sadomeit.pdf)
- [Ago00] S. Agosteo, S. Altieri *et al.* *A facility for the test of large-area muon chambers at high rates*. *Nuclear Instruments and Methods in Physics Research Section A: Accelerators, Spectrometers, Detectors and Associated Equipment*, 452(1-2):pages 94 – 104, 2000. ISSN 0168-9002. doi:10.1016/S0168-9002(00)00414-9.  
Url: <http://www.sciencedirect.com/science/article/pii/S0168900200004149>
- [Ago03] S. Agostinelli, J. Allison *et al.* *Geant4 – A Simulation Toolkit*. *Nuclear Instruments and Methods in Physics Research Section A: Accelerators, Spectrometers, Detectors and Associated Equipment*, 506(3):pages 250 – 303, 2003. ISSN 0168-9002. doi:10.1016/S0168-9002(03)01368-8.  
Url: <http://www.sciencedirect.com/science/article/pii/S0168900203013688>
- [Ale99] M. Aleksa. *Performance of the ATLAS Muon Spectrometer*. Ph.D. thesis, Vienna, Tech. U., Wien, 1999. Presented on 11 Sep 1999.  
Url: <https://cdsweb.cern.ch/record/456140>
- [Ale00] M. Aleksa, M. Deile *et al.* *Rate effects in high-resolution drift chambers*. *Nuclear Instruments and Methods in Physics Research Section A: Accelerators, Spectrometers, Detectors and Associated Equipment*, 446(3):pages 435 – 443, 2000. ISSN 0168-9002. doi:10.1016/S0168-9002(99)01016-5.  
Url: <http://www.sciencedirect.com/science/article/pii/S0168900299010165>
- [ATL02] ATLAS Collaboration. *ATLAS Muon Spectrometer Technical Design Report*. Technical report, CERN, 2002.  
Url: <http://atlas.web.cern.ch/Atlas/GROUPS/MUON/TDR/Web/TDR.html>
- [ATL08] ATLAS Collaboration. *The ATLAS Experiment at the CERN Large Hadron Collider*. *Journal of Instrumentation*, 3(08):page S08003, 2008.  
Url: <http://stacks.iop.org/1748-0221/3/S08003>

- [ATL09] ATLAS Collaboration. *Expected performance of the ATLAS experiment: detector, trigger and physics*. CERN, Geneva, 2009.  
Url: <http://cdsweb.cern.ch/record/1125884>
- [ATL11] ATLAS Collaboration. *Letter of Intent for the Phase-I Upgrade of the ATLAS Experiment*. Technical Report CERN-LHCC-2011-012. LHCC-I-020, CERN, Geneva, Nov 2011.  
Url: <https://cdsweb.cern.ch/record/1402470/>
- [Bag08] P. Bagnaia, T. Baroncelli *et al.* *Calibration model for the MDT chambers of the ATLAS Muon Spectrometer*. Technical Report ATL-MUON-PUB-2008-004. ATL-COM-MUON-2008-006, CERN, Geneva, Feb 2008. Backup paper for Atlas Detector paper.
- [Bar05] S. Baranov, M. Bosman *et al.* *Estimation of Radiation Background, Impact on Detectors, Activation and Shielding Optimization in ATLAS*. Technical Report ATL-GEN-2005-001. ATL-COM-GEN-2005-001. CERN-ATL-GEN-2005-001, CERN, Geneva, Jan 2005.  
Url: <http://cdsweb.cern.ch/record/814823>
- [Ben11] Y. Benhammou, B. Bittner *et al.* *Test of spatial resolution and trigger efficiency of a combined Thin Gap and Fast Drift Tube Chambers for high-luminosity LHC upgrades*. In *2011 Nuclear Science Symposium and Medical Imaging Conference*. 2011.
- [Bit08] B. Bittner. *Alignment of the ATLAS Muon Spectrometer Using Muon Tracks*. Diplomarbeit, Tech. U., Munich, 2008. Presented 30 Nov 2008.  
Url: <https://cdsweb.cern.ch/record/1405445/>
- [CER08] CERN/AT/PhL. *Interim Summary Report on the Analysis of the 19 September 2008 Incident at the LHC*. Technical report, CERN, 2008.  
Url: [https://edms.cern.ch/file/973073/1/Report\\_on\\_080919\\_incident\\_at\\_LHC\\_\\_2\\_.pdf](https://edms.cern.ch/file/973073/1/Report_on_080919_incident_at_LHC__2_.pdf)
- [CER09] CERN. *Secondary Beam Areas of the PS and SPS*, 2009.  
Url: <http://sba.web.cern.ch/sba/>
- [CER12] CERN. *LHC Performance Workshop*. CERN, 2012.  
Url: <https://indico.cern.ch/conferenceOtherViews.py?view=standard&confId=164089>
- [CSI] *Radionuclide Half-Life Measurements*.  
Url: <http://www.nist.gov/pml/data/halflife-html.cfm>
- [Dei00] M. Deile. *Optimization and Calibration of the Drift-Tube Chambers for the ATLAS Muon Spectrometer*. Ph.D. thesis, LMU Munich: Faculty of Physics, 2000.
- [Die56] W. Diethorn. *A Methane Proportional Counter System for Natural Radiocarbon Measurements*. Ph.D. thesis, Carnegie Institute of Technology, 1956. USAEC, Rpt. NYO – 6628.

- [Dub10] J. Dubbert, O. Kortner *et al.* *Sharpening the ATLAS muon trigger for high luminosity operation at the LHC*. In *Nuclear Science Symposium Conference Record (NSS/MIC), 2010 IEEE*, pages 843 –846. 30 2010-nov. 6 2010. ISSN 1082-3654. doi:10.1109/NSSMIC.2010.5873880.
- [Eck05] C. Eck, J. Knobloch *et al.* *LHC computing Grid: Technical Design Report. Version 1.06 (20 Jun 2005)*. Technical Design Report LCG. CERN, Geneva, 2005.  
Url: <http://cdsweb.cern.ch/record/840543>
- [GIF00] *The X5 Irradiation Facility*, 2000.  
Url: <http://sl.web.cern.ch/SL/eagroup/irrad.html>
- [Han12] L. Han. *Thin-gap RPC Test Results*. In *RPC2012 - XI Workshop on Resistive Plate Chambers and Related Detectors*. 2012.  
Url: <http://agenda.infn.it/contributionDisplay.py?contribId=76&sessionId=5&confId=3950>
- [Hor04] S. Horvat, D. Kharatchenko *et al.* *Optimization of the ATLAS muon drift-tube chambers at high background rates and in magnetic fields*. In *Nuclear Science Symposium Conference Record, 2004 IEEE*, volume 53, pages 1256 – 1260 Vol. 2. Oct. 2004. ISSN 1082-3654. doi:10.1109/NSSMIC.2004.1462429.
- [Hor05] S. Horvat. *Study of the Higgs Discovery Potential in the Process  $pp \rightarrow H \rightarrow 4\mu$* . Ph.D. thesis, Zagreb Univ., Zagreb, 2005. Presented on 11 Apr 2005.  
Url: <http://cdsweb.cern.ch/record/858509/>
- [Hor06] S. Horvat, D. Khartchenko *et al.* *Operation of the ATLAS muon drift-tube chambers at high background rates and in magnetic fields*. *Nuclear Science, IEEE Transactions on*, 53:pages 562 – 566, April 2006. ISSN 0018-9499. doi: 10.1109/TNS.2006.872636.
- [Kil10] M. Kilgenstein. *Bau und Simulation einer Driftrohrkammer für hohe Zählraten*. Diplomarbeit, Max-Planck-Institut für Physik, Nov. 2010.
- [Kor00] O. Kortner. *MTGEANT-4 - The Munich Test-Stand Simulation Programme*. Technical Report ATL-MUON-2000-021, CERN, Geneva, Sep 2000.  
Url: <https://cdsweb.cern.ch/record/684120>
- [Kor02] O. Kortner. *Schauerproduktion durch hochenergetische Myonen und Aufbau eines Höhenstrahlungsprüfstandes für hochauflösende ATLAS-Myonkammern*. Ph.D. thesis, Ludwig-Maximilians-Universität München, 2002.  
Url: [http://www.etp.physik.uni-muenchen.de/dokumente/thesis/phd\\_kortner.pdf](http://www.etp.physik.uni-muenchen.de/dokumente/thesis/phd_kortner.pdf)
- [Kor12] O. Kortner. *Single Tube Resolution and  $3\sigma$  efficiency of 30 mm diameter ATLAS MDT drift tubes*, 2012. Personal communication.
- [Loe07] J. von Loeben. *Test und Kalibrierung der Präzisionsdriftrohrkammern des ATLAS-Myonspektrometers*. Diplomarbeit, TU München & MPI für Physik, 2007.

- [MIN] *MINUIT 2, a new object-oriented implementation, written in C++, of the popular MINUIT minimization package.*  
Url: [http://root.cern.ch/root/html/MATH\\_MINUIT2\\_Index.html](http://root.cern.ch/root/html/MATH_MINUIT2_Index.html)
- [Pos07] C. Posch, E. Hazen *et al.* *MDT-ASD, CMOS front-end for ATLAS MDT; rev. version 2.1.* Technical Report ATL-MUON-2002-003, CERN, Geneva, Sep 2007. Revised version number 2.1 was submitted on 2007-09-18 19:14:00.  
Url: <http://cdsweb.cern.ch/record/684217>
- [Rau05] F. Rauscher. *Untersuchung des Verhaltens von Driftrohren bei starken Gamma-Bestrahlung sowie Vermessung von Driftrohrkammern mit Hilfe von Myonen der kosmischen Höhenstrahlung.* Ph.D. thesis, Ludwig-Maximilians-Universität München, 2005.  
Url: [http://www.etp.physik.uni-muenchen.de/dokumente/thesis/phd\\_frausch.pdf](http://www.etp.physik.uni-muenchen.de/dokumente/thesis/phd_frausch.pdf)
- [Rie00] W. Riegler, M. Aleksa *et al.* *Resolution limits of drift tubes.* *Nuclear Instruments and Methods in Physics Research Section A: Accelerators, Spectrometers, Detectors and Associated Equipment*, 443(1):pages 156 – 163, 2000. ISSN 0168-9002. doi:10.1016/S0168-9002(99)01014-1.  
Url: <http://www.sciencedirect.com/science/article/pii/S0168900299010141>
- [ROO] ROOT, *An Object-Orientated Analysis Framework.*  
Url: <http://root.cern.ch/>
- [RPC12] RPC Collaboration. *A Major Progress Report on the RPC proposal for the SW upgrade.* Technical report, Rome 2, 2012.  
Url: <https://indico.cern.ch/getFile.py/access?sessionId=4&resId=3&materialId=0&confId=181713>
- [Sch10] P. Schwegler. *Construction and Test of Muon Drift Tube Chambers for High Counting Rates.* Diplomarbeit, Tech. Universität., München, 2010. Presented 30 Nov 2010.  
Url: <https://cdsweb.cern.ch/record/1325103>
- [Sch12a] P. Schwegler. *Gain Drop calculations based on the Diethorn Formula*, 2012. Personal Communication.
- [Sch12b] P. Schwegler and B. Bittner. *GIF 2011 Measurement and Analysis*, 2012. Work in Progress.

# List of Figures

2.1	Overview of the CERN accelerator complex. The year of the first beam and the circumference of the accelerator rings are indicated. . . . .	6
3.1	Cut-away view of the ATLAS detector . . . . .	10
3.2	Magnetic Coils in ATLAS . . . . .	12
4.1	Schematic view of the muon system . . . . .	16
4.2	Simulated flux of photons and neutrons in the ATLAS muon spectrometer for the LHC design luminosity of $10^{34} \text{ cm}^{-2}\text{s}^{-1}$ [Bar05]. . . . .	17
4.3	Effects of chamber misalignment on the track reconstruction. The real chamber positions are marked in gray, the assumed position (if different) is indicated in red. The real muon track has a blue color, the reconstructed segment in the misaligned chamber is red. . . . .	18
4.4	A MDT tube in different views . . . . .	19
4.5	Mechanical structure of a MDT chamber . . . . .	20
4.6	Drift time spectrum of the ATLAS MDT tubes measured in the cosmic ray teststand in Garching. . . . .	21
4.7	Measurement of a typical $r(t)$ relation for an ATLAS MDT tube. . . . .	23
4.8	Influence of the ionisation cluster position on the measured drift radius. $r_{\text{true}}$ is the distance of the muon track from the wire and $r_{\text{drift}}$ the measured drift radius, which can be larger than $r_{\text{true}}$ depending on the cluster position with respect to the wire. . . . .	24
4.9	Spatial resolution of the 30 mm diameter drift tubes before and after the time slewing correction (TSC, cp. Sec. 8.4.2) [Kor12]. . . . .	25
4.10	Masking of muon hits by $\delta$ -electrons. . . . .	26
4.11	$3\sigma$ single tube efficiency for the 30 mm diameter drift tubes for 780 ns and 180 ns dead-time settings of the readout electronics [Kor12]. . . . .	27
4.12	Principle of the track reconstruction in the drift tube chambers. The track is fitted to the measured drift circles. . . . .	27
4.13	The electronic components of a MDT chamber . . . . .	28
4.14	Expected background rates in the muon spectrometer for nominal LHC and maximum HL-LHC luminosity. Where the rates exceed the limit for the MDT chamber operation the chambers are marked with red/orange color. . . . .	30

4.15	Efficiency of the Level-1 muon trigger vs. $p_T$ for three typical trigger thresholds. At the high muon rates from proton–proton collisions at HL-LHC the turn-on ranges of the efficiency curves to the maximum efficiency are too wide in order to sufficiently suppress low $p_T$ muon triggers even at high thresholds. The momentum resolution on the muon trigger chambers needs to be improved [Dub10]. . . . .	31
4.16	Muon production cross-sections and rates in the ATLAS detector as a function of the muon $p_T$ [ATL02]. . . . .	32
5.1	$3\sigma$ efficiency of 30 mm diameter drift tubes as a function of the background counting rate for the maximum deadtime of 780 ns of the readout electronics. The corresponding track segment reconstruction efficiency in MDT chamber with 6 tube layers is also shown. The expected maximum background rate in MDT chambers in ATLAS at the LHC design luminosity is 300 kHz/tube in the Small Wheels of the ATLAS muon spectrometer [Hor06]. . . . .	36
5.2	Effect of the $\gamma$ background hit rate on the spatial resolution for 30 mm $\varnothing$ drift tubes [Hor06]. 500 Hz/cm <sup>2</sup> background flux corresponds to 300 kHz/tube counting rate in 2 m long tubes. . . . .	36
5.3	Spatial resolution of 30 mm $\varnothing$ drift tubes as a function of the drift radius for different $\gamma$ background hit rates [Hor06]. 500 Hz/cm <sup>2</sup> is the maximum expected background hit rate in ATLAS at the LHC design luminosity. . .	37
5.4	Space-to-drift-time relation of the ATLAS MDT drift tubes. The 15 mm $\varnothing$ tubes show the same behaviour at drift radii below 7.1 mm because of the same operating conditions. . . . .	39
5.5	Gas gain $G$ relative to the nominal gain $G_0$ as a function of the background hit rate of $\gamma$ -rays for 15 mm and 30 mm diameter tubes [Sch12a]. The dashed line marks the maximum expected background hit rate in the drift tubes at HL-LHC of 14 kHz/cm <sup>2</sup> [ATL11]. . . . .	41
5.6	Expectation for the average resolution of 15 mm diameter tubes (green) derived from the measurement for the 30 mm diameter tubes (red) as a function of the background hit rate by calculating the average resolution for radii less than 7.1 mm and multiplying the corresponding rates of the 30 mm $\varnothing$ tube measurements by 8.7 (see text) [Sch12a]. . . . .	41
5.7	Track segment reconstruction efficiencies as a function of the $3\sigma$ efficiency for different numbers of tube layers and minimum number of required hits per track segment. . . . .	43
5.8	Comparison of the drift time spectra of 30 mm $\varnothing$ and 15 mm $\varnothing$ tubes. The difference between 100 ns and 160 ns is caused by the different temperatures of the 15 mm $\varnothing$ and 30 mm $\varnothing$ tubes (see Sec. 7.14(a)). . . . .	44
6.1	Blow-up view of the endplug parts and the gas system connection. . . . .	48
6.2	Illustration of the gas distribution system to the individual tubes and connection through an assembled endplug. The hedgehog card is visible on the left-hand side. . . . .	48
6.3	The different hedgehog boards for the ATLAS MDT and the sMDT chambers in comparison. . . . .	49
6.4	The jigs holding the tubes in the grid during chamber assembly. . . . .	50
6.5	The full-size prototype chamber. . . . .	51

7.1	The cosmic ray test setup in the $y$ - $z$ plane. Muons with a momentum of less than 600 MeV/c are stopped in the iron absorber. . . . .	54
7.2	View of the cosmic ray test setup the $x$ - $z$ plane. The 5 trigger towers are visible. . . . .	54
7.3	Difference between the scattering angles between the reference MDT chambers in the teststand from Monte-Carlo prediction ( $\Delta m_{MC}$ ) and from measurement ( $\Delta m_{fit}$ ). . . . .	56
7.4	Comparison of the cut flows for the cosmic MC events set and the data taken with the test cosmic ray teststand. The last step of the event selection is the cut on the scattering angle, the amount of tracks in the test chamber is only shown for comparison. . . . .	57
7.5	Effect of wire displacement on the track coordinate measurement. The drift radius $r_m$ is determined from the measured drift time (see text). . . . .	57
7.6	Track residual distribution for one tube in the Monte-Carlo simulation. The shift of the distribution is determined from a Gaussian fit. . . . .	59
7.7	Distribution of $\delta_y$ , the horizontal wire displacement, for Monte-Carlo data with ideal wire positions. . . . .	60
7.8	V-Plot for a tube with no displacement. The red dots are the mean values for slices along the $t$ axis. . . . .	60
7.9	$\delta_y$ distributions from method <b>A</b> (left fit parameters) and <b>B</b> (right fit parameters) . . . . .	61
7.10	Difference between the wire displacements $\delta_y$ determined with the two methods using 717837 MC events for 1152 tubes. . . . .	62
7.11	Accuracy and robustness of $\delta_y$ reconstruction from MC simulation. . . . .	62
7.12	(a) shows a typical fit to find $\delta_z$ for a tube layer of MC simulation data and expected wire positions. To measure the resolution of the $\delta_z$ finding algorithm the value is determined for all 48 tube layers (16 layers in 3 sectors) (b) with respect to the true wire positions and the width of the distribution is determined. . . . .	63
7.13	Linearity and accuracy of $\delta_z$ reconstruction. . . . .	63
7.14	Temperature measurements in the test-stand as a function of time during the data taking run. . . . .	64
7.15	Event display of a cosmic muon track reconstructed in all three chambers. . . . .	65
7.16	Track residuals $\Delta$ as a function of the track distance $d_e$ to the wire for the bottom reference chamber before and after the $r(t)$ calibration. . . . .	66
7.17	Measurement and correction of a relative rotation of the test chamber with respect to the reference chambers around the $z$ axis resulting in a $x$ -dependent $y$ -displacement of the wires (see text). . . . .	66
7.18	Relative Rotation around the wire axis (see text). . . . .	67
7.19	Measured residuals $\delta_y$ with respect to the expected wire $y$ -positions for the four sectors of the test chamber equipped with readout electronics. . . . .	68
7.20	Residuals $\delta_y$ distribution for all tubes in the test chamber derived from the expected and measured tube positions, respectively. The width of the distribution derived from the measured tube positions is $\sigma_m = 5.93 \pm 0.22 \mu\text{m}$ (equivalent to the MC prediction, cp. fig. 7.7) and is limited by the performance of the teststand. . . . .	69
7.21	Residuals $\delta_y$ as a function of the $y$ position. . . . .	70

7.22	The wire grid in the MDT chambers is determined by four parameters: the horizontal and vertical wire pitch $d_y$ and $d_z$ , the relative horizontal displacement of the tube layers $y_{\text{skipp}}$ and $s$ , the width of the spacer between the two multilayers. . . . .	71
7.23	Residuals of the wire $y$ coordinates with respect to the reconstructed wire grid in the four test chamber sectors. . . . .	71
7.24	Residuals $\delta_y$ of all wire positions with respect to the expected grid (a) and with respect to the fitted grid (b). . . . .	72
7.25	Individual wire displacements in $y$ direction for all tubes. determined separately for each tube (enlarged by a factor of 200). . . . .	73
7.26	Layer displacements in $z$ direction for all tubes determined separately for each layer and sector (enlarged by a factor of 200). . . . .	74
8.1	The beam profile for 180 GeV muons at the H8 beam line at CERN in 2011. See the text for details. . . . .	78
8.2	Setup for the sMDT chamber tests at the H8 beam line. . . . .	79
8.3	Photograph of the sMDT chamber test setup in the H8 beam line (see text for details). . . . .	80
8.4	Temperature of the chamber during 3 days of data taking. Gaps indicate that the DAQ was not running during that time. . . . .	81
8.5	The time slewing effect: smaller signals tend to cross the discriminator threshold at later times (see text). . . . .	82
8.6	The ADC distribution for one bin and the whole tube. . . . .	82
8.7	Slope $m$ and offset $b$ as a function of the drift time. . . . .	83
8.8	Distribution of the time slewing correction $\delta_t$ (a) and its influence on the leading edge of the drift time spectrum (b). . . . .	84
8.9	Effect of the time slewing correction on the track residual width as a function of the drift radius $r_d$ . . . . .	84
8.10	Finding the track residuals in the analysis layer (see the text). . . . .	85
8.11	Single tube resolution measured on the MC data set compared to the true single tube resolution as a function of the track distance to the wire $r =  d $ . . . . .	86
8.12	Number of hits on track for different distances to the wire. . . . .	87
8.13	Determination of the drift velocity from the $r(t)$ relation. . . . .	88
8.14	Comparison of the single tube resolution without time slewing correction for the 30 mm $\varnothing$ and the 15 mm $\varnothing$ drift tubes and the corresponding Garfield simulations [Kor12, Kil10]. . . . .	89
8.15	Resolution with time slewing correction for the 30 mm $\varnothing$ and the 15 mm $\varnothing$ drift tubes [Kor12]. . . . .	89
8.16	Single tube resolution with and without applied time slewing correction and the expectation derived from the ATLAS MDT drift tubes. . . . .	90
8.17	$3\sigma$ efficiency for 15 mm and 30 mm [Kor12] diameter drift tubes as a function of the muon track distance to the sense wire without background radiation. . . . .	91
8.18	Effect of the time slewing correction on the $3\sigma$ efficiency for 15 mm diameter drift tubes without background radiation. . . . .	92
8.19	Selection of 4 layers per multilayer for the tracking studies. . . . .	93
8.20	Comparison of the reconstructed track with the truth information about the muon trajectory. . . . .	94

8.21	Distributions of $\Delta\alpha$ and $\Delta b$ for the Monte-Carlo data set. . . . .	94
8.22	Distributions of $\Delta\alpha$ and $\Delta y$ for the data without time slewing correction. . . . .	95
8.23	Distributions of $\Delta\alpha$ and $\Delta y$ after application of the time slewing correction. . . . .	95
8.24	Overview of the combined sMDT-RPC setup. [Han12] . . . . .	97
8.25	Residuals of the RPC track position measurement relative to the sMDT track [RPC12]. . . . .	97
8.26	The combined sMDT-TGC test setup. . . . .	98
8.27	Comparison of tracks measured in the sMDT and in the TGC chamber in the H8 muon beam. . . . .	98
9.1	Layout of the GIF zone at CERN [GIF00]. The X5 muon beam was only available until 2004. . . . .	100
9.2	Vertical cut through the $\gamma$ irradiation source at the GIF: 1-3: Filters, 4: rod for adjusting the source position, 5: radiation monitor, 6: $^{137}\text{Cs}$ source. 7: lead housing of source. 8: concrete shielding [Ago00]. . . . .	100
9.3	Test setup of the sMDT chamber at the GIF (left:front view, right side view). The trigger coverage is chosen to maximise the cosmic muon rate with non vertical tracks in the region with the highest achievable counting rate. . . . .	101
9.4	Drift time spectra in the two multilayers of the sMDT chamber. Multilayer 2 shows the expected flat background hit time distribution on which the triggered muon drift time spectrum sits. Multilayer 1 shows a decreasing background hit time distribution indicating that a fraction of hits is not recorded. . . . .	102
9.5	Occupancy of the chamber for different readout windows sizes the same background radiation flux. Each picture shows one event. . . . .	103
9.6	The different readout regions of the sMDT chamber in the GIF test [Sch10].	103
9.7	Time distribution of the signals of the trigger scintillators perpendicular to the tubes before and after correction for the light travel time. Note the different scales on the time axis. . . . .	104
9.8	Timing diagram of the trigger hodoscope (see text). . . . .	105
9.9	Correction of the time of one scintillator of the upper layer time for the cable lengths of the lower scintillators. . . . .	106
9.10	Time difference between lower and upper trigger layers for the different lower scintillators before (a) and after (b) correction for different lower scintillator cable lengths. . . . .	107
9.11	Combined drift time spectrum for all tubes in the reference part of the sMDT chamber (blue, rescaled by 0.1) and the spectrum of the tube with the highest counting rate (red, channel 13). The muon drift time spectrum is hardly distinguishable in the second case. . . . .	108
9.12	Event displays for wrong and correct track reconstruction. The active scintillators are marked in cyan. . . . .	109
9.13	Time difference between two successive hits in a tube. . . . .	110
9.14	Red data points show the relative difference to the input rate of the uncorrected measured rate $(\rho_{\text{det}} - \rho_{\text{in}})/\rho_{\text{in}}$ , blue points the same quantity for the rate corrected according to eq. (9.3) $(\rho_{\text{cor}} - \rho_{\text{in}})/\rho_{\text{in}}$ . . . . .	111

9.15	Counting rate for each tube. Tubes behind the lead shielding (cp. Fig. 9.3 and Fig. 9.6) have a lower rate and are used as reference region. Tubes above this region are combined in the analysis region. White tubes are either switched off ( $4 \times 6$ cluster on the right side) or recorded no hits. . . . .	112
9.16	$3\sigma$ drift tube efficiency measurements and simulations as a function of the (uncorrected) counting rate for different tube diameters and electronic dead times. All hits in the drift time spectrum are accepted. . . . .	113
9.17	Cut flow of the analysis before and after application of the optimized $r(t)$ relation. . . . .	115
9.18	Locations of the tube with comparable background rates belonging to the different analysis regions. The analysis and reference regions of Figure 9.6 are also shown. . . . .	115
9.19	Position of the different analysis regions. . . . .	116
9.20	Measurement of the residual widths for the different rate bins before and after corrections for track extrapolation and multiple scattering errors. . . . .	117
9.21	Average measured resolution of the 15 mm diameter tubes for the different rate bins compared to the results from the 30 mm GIF measurements for the 30 mm $\varnothing$ tubes [Hor06] and the model predictions. . . . .	118
9.22	Comparison of the measured and simulated $3\sigma$ efficiency for the 15 mm $\varnothing$ tubes as a function of the background hit rate. The difference between measurement and simulation is expected from the 30 mm $\varnothing$ tube measurement, see Fig. 9.16(b). . . . .	119
9.23	Mean efficiency of the 15 mm diameter tubes compared to a measurement of the 30 mm diameter tubes with different readout settings. . . . .	119
9.24	Segment reconstruction efficiencies in a chamber with 6 layers of 50 cm long tubes of 30 mm diameter and a 12-layer chamber with 50 cm long tubes of 15 mm diameter. . . . .	120
9.25	Improved setup for the 2011 GIF measurement campaign [Sch12b]. . . . .	121
A.1	Overview of the DAQ system used for the tests. . . . .	128
A.2	Overview of all connected services. . . . .	129
B.1	ADC counts for 250 fF capacity. . . . .	132
B.2	ADC calibration curve for one channel. The measurements for the different input charges are shown. . . . .	132
B.3	ADC calibration curve for all 24 channels of a mezzanine card. The huge differences of the different response curves are visible. . . . .	133
B.4	ADC count distribution before and after the calibration. . . . .	133
B.5	ADC counts for one layer of tubes. The calibration is able to eliminate differences in the ADC count distribution for different channels. The artefacts in (b) are a binning effect. . . . .	134

# List of Tables

4.1	Different types and sources of misalignment. For 2D plots the distributions are fitted with a polynomial $y = m \cdot x + b$ , the interesting variable is then represented by $m$ . . . . .	18
4.2	Parameters of the drift tubes in the ATLAS MDT chambers. . . . .	19
5.1	Comparison of the parameters of the drift tubes in the ATLAS MDT and in the sMDT chambers. . . . .	45
7.1	Monte-Carlo data sets used for studying the teststand data analysis. . . . .	55
7.2	Results from the horizontal and vertical wire grid measurement. $\sigma_{y,\text{expected}}$ and $\sigma_{y,\text{fitted}}$ are the width of the $\delta_y$ distribution with respect to the expected and fitted wire grid, respectively. . . . .	75
8.1	Comparison of the true track segment resolution with the resolution determined with the two-track method for Monte-Carlo data. Both results agree very well. . . . .	95
8.2	Track segment resolution with and without time slewing correction (TSC) and the corresponding average tube resolution $\sigma_{\text{tube}}$ according to Eq. (8.10). . . . .	96
9.1	Selection criteria for the different analysis bins containing tubes with comparable counting rates. . . . .	116



# Acknowledgements

After the amazing time during my diploma thesis I wanted to continue working in the ATLAS MPI group. Hubert Kroha was so kind to offer me the possibility to do my PhD thesis in his group. His strong interest in my work and the many discussions helped me to keep the overview and focus on the important tasks. I'm also very grateful for all the time I could spend at CERN or at Summer Schools and conferences all over the world.

Furthermore I want to thank Oliver Kortner and Jörg Dubbert for all the time they spend discussing and solving problems. Oliver always found the time to discuss all aspects of the analysis, whether it was the already existing framework or ideas for the new code, and with his vast experience and knowledge about the MDT chambers never failed to point in the right direction. Without Jörg and his Slowcontrol software not a single test beam or GIF measurement would have been possible. Not only did he provide on call and on site support during any time of the day (or night), he also always knew where to find the right parts or tools to solve any hardware related problem. A very huge thanks goes to Federica Legger for all the explanations and help during the first part of the thesis and the very good introduction to the whole sMDT system.

Another person who made the enormous task of preparing the tests, taking the data and extracting some meaningful results much more pleasant and easy is Philipp Schwegler who already was a huge help during his diploma thesis and even more since he started his PhD. Many thanks go also to the sMDT crew, especially Alessandro Manfredini, Daniele Zanzi and Andre Zibell. Not only were they helping during the tests, but I was also able to enjoy the short intervals of free time with all of them in the mountains or other nice locations. This crew was completed by all my friends from all over the world, especially the 2007 summer students. No matter when I came to CERN or any conference & summer school, they always knew how to have a good time and how to make the best pasta!

Without the huge efforts by the MPI workshop and electronics department in Munich and at CERN there would have been no chambers to test, no support structures, no readout boards, no nothing. No matter what crazy requests we had, they were always able to solve the problem, most of the time even faster and better than what we could have asked for.

Letztendlich aber wäre all dies nicht möglich gewesen ohne die Unterstützung und Ermutigungen von meinen Freunden und besonders meiner Familie. Auch wenn ich einmal wieder mehr als die Hälfte eines Jahres unterwegs gewesen bin und nur wenig Zeit für alle Leute in und um München finden konnte haben sie immer Interesse an meiner Arbeit gezeigt und geholfen wo immer sie nur konnten.

Die wichtigste Person ist und bleibt allerdings meine Freundin Lili. Ihr Rückhalt und ihre Unterstützung während des letzten Jahres haben mir immer wieder Kraft und Motivation gegeben und oft dabei geholfen auch mal abschalten zu können wenn die Analyse mal wieder nicht so wollte wie ich.